Ministry of Education and Science of the Russian Federation
Saint Petersburg National Research University of Information Technologies, Mechanics, and Optics

NANOSYSTEMS:
PHYSICS, CHEMISTRY, MATHEMATICS

2019, volume 10(4)

Наносистемы: физика, химия, математика
2019, том 10, № 4

NANOSYSTEMS:

PHYSICS, CHEMISTRY, MATHEMATICS

Address: University ITMO, Kronverkskiy pr., 49, St. Petersburg 197101, Russia.
Phone: +7(812)312-61-31, **Journal site:** http://nanojournal.ifmo.ru/,
E-mail: popov1955@gmail.com

AIM AND SCOPE

The scope of the journal includes all areas of nano-sciences. Papers devoted to basic problems of physics, chemistry, material science and mathematics inspired by nanosystems investigations are welcomed. Both theoretical and experimental works concerning the properties and behavior of nanosystems, problems of its creation and application, mathematical methods of nanosystem studies are considered.

The journal publishes scientific reviews (up to 30 journal pages), research papers (up to 15 pages) and letters (up to 5 pages). All manuscripts are peer-reviewed. Authors are informed about the referee opinion and the Editorial decision.

CONTENT

NANOSYSTEMS: PHYSICS, CHEMISTRY, MATHEMATICS, 2019, 10 (4), P. 391–397

Stability of intersite dark solitons in a parametrically driven discrete nonlinear Schrödinger equation

O. P. Swami[1], V. Kumar[2], B. Suthar[3], A. K. Nagar[2]

[1]Department of Physics, Government College, Loonkaransar, Bikaner, Rajasthan, 334603, India
[2]Department of Physics, Government Dungar College, Bikaner, Rajasthan, 334001, India
[3]Department of Physics, MLB Government College, Nokha, Bikaner, Rajasthan, 334803, India

omg1789@gmail.com, vijendrasaini2009@gmail.com, bhuvneshwer@gmail.com, ajaya.nagar@gmail.com

PACS 05.45.Yv, 42.65.Tg, 63.20.Pw, 11.15.Bt **DOI 10.17586/2220-8054-2019-10-4-391-397**

In this paper, a parametrically driven discrete nonlinear Schrödinger equation will be considered for defocusing case. Analytical and numerical calculations will be performed to determine the existence and stability of intersite dark discrete solitons admitted by discrete nonlinear Schrödinger equation. It will be shown that a parametric driving can stabilizes intersite discrete dark solitons. Stability windows of all the fundamental solitons will be presented and approximations to the onset of instability will be derived using perturbation theory, with accompanying numerical results.

Keywords: soliton, discrete nonlinear Schrödinger equation, parametrically driven, instability, perturbation theory.

Received: 4 May 2019

Revised: 26 May 2019

1. Introduction

We consider a parametrically driven discrete nonlinear Schrödinger (PDNLS) equation for defocusing case:

$$i\dot{\varphi}_n = -C\Delta_2\varphi_n + |\varphi_n|^2\varphi_n - \omega\varphi_n - \gamma\bar{\varphi}_n, \tag{1}$$

where, $\varphi_n \equiv \varphi_n(t)$ is a real-valued wave function at site n, the overdot and the overline indicates to time derivative and complex conjugation, respectively. The coupling constant between two adjacent sites is represented by C. $\Delta_2\varphi_n = \varphi_{n+1} - 2\varphi_n + \varphi_{n-1}$ is the one-dimensional (1D) discrete Laplacian, γ is the parametric driving coefficient with frequency ω. In the absence of parametric driving, i.e., for $\gamma = 0$, Eq. (1) is reduced to the standard discrete nonlinear Schrödinger (DNLS) equation which appears in a wide range of important applications [1–5] and admits dark solitons with defocusing nonlinearities, respectively.

With a focusing nonlinearity and finite C PDNLS has been studied first by Susanto *et al*. [6, 7, 9]. The PDNLS model was also derived for coupled arrays of nonlinear resonators in micro and nano-electromechanical systems [8,10]. The same equation also applies to the study of Bose–Einstein condensates and long bosonic Josephson junctions [11, 12]. Dynamics of the parametrically driven NLS solitons beyond the onset of the oscillatory instability was studied by N. V. Alexeeva *et al*. [13]. Bright and dark solitons in optical media with intensity-dependent non-linear response as well as two-component solitary waves supported by parametric wave mixing in quadratic or cubic media was studied by Yu. S. Kivshar [14]. Theory of stationary solitary waves generated by optical parametric interactions in the presence of Kerr-type nonlinearities and dissipations was studied by K. Hayata and M. Koshiba [15].

In this study, the existence and stability of the fundamental intersite dark solitons in the defocusing PDNLS is examined analytically and numerically. The method of perturbation theory for small C is adopted in analytical calculation. Numerical comparisons are made by solving a corresponding eigenvalue problem.

Stationary solution of system (1) is in the form of $\varphi_n = Z_n$, where Z_n is a real-valued and time independent, satisfy the following stationary equation:

$$-C\Delta_2 Z_n + Z_n^3 - \omega Z_n - \gamma Z_n = 0. \tag{2}$$

The solution of Eq. (1) is the form of solitonic and its linear stability is determined by solving a corresponding eigenvalue problem. A linearization ansatz is introduced as follows

$$\varphi_n = Z_n + \delta\rho_n,$$

where $\delta \ll 1$, and substitute this into the defocusing Eq. (1), to yield the following linearized equation at $O(\delta)$:

$$i\dot{\rho}_n = -C\Delta_2\rho_n - 2|Z_n|^2\rho_n - Z_n^2\bar{\rho}_n + \omega\rho_n + \gamma\bar{\rho}_n, \tag{3}$$

by writing $\rho_n = \eta_n + i\zeta_n$, equation (3) can be transformed into the eigenvalue problem:

$$\begin{pmatrix} \dot{\eta}_n \\ \dot{\zeta}_n \end{pmatrix} = M \begin{pmatrix} \eta_n \\ \zeta_n \end{pmatrix}, \tag{4}$$

where:

$$M = \begin{pmatrix} 0 & L_+(C) \\ L_-(C) & 0 \end{pmatrix}, \tag{5}$$

and the operators $L_+(C)$ and $L_-(C)$ are defined by

$$L_+(C) \equiv -C\Delta_2 + (3Z_n^2 - \omega - \gamma),$$
$$L_-(C) \equiv -C\Delta_2 - (Z_n^2 - \omega + \gamma).$$

By the eigenvalues of M the stability of Z_n is determined. Let the eigenvalues of M is denoted by id, which implies that Z_n is stable if $\mathrm{Im}(d) = 0$. Because the Eq. (5) is linear then one of the 'eigenvectors', for instance ζ_n, can be eliminated, from which following eigenvalue problem is obtained

$$L_+(C)L_-(C)\eta_n \equiv \mathrm{d}^2\eta_n = \Omega\eta_n. \tag{6}$$

2. Analytical calculations

To perform analytical calculations of the existence and stability of the intersite dark solitons for small coupling constant C, a perturbation analysis is used. By expanding Z_n in powers of C, the $O(1)$ and $O(C)$ equations are obtained, which give the solutions Z_n at order C as:

$$Z_n^{(1)} = \frac{\Delta_2 Z_n^{(0)}}{3\left(Z_n^{(0)}\right)^2 - (\omega + \gamma)}. \tag{7}$$

Using a perturbative expansion, the configuration of intersite dark soliton in AC limit $C = 0$ is given by:

$$Z_n^{(0)} = \begin{cases} -\sqrt{\omega + \gamma}, & n = 0, -1, ..., \\ \sqrt{\omega + \gamma}, & n = 1, 2, ... \end{cases} \tag{8}$$

To study the eigenvalue(s) analytically, η_n and ω are expanded in power of C as

$$\eta_n = \eta_n^{(0)} + C\eta_n^{(1)} + O(C^2), \tag{9}$$

$$\omega = \omega^{(0)} + C\omega^{(1)} + O(C^2). \tag{10}$$

Then equation (6) can be written at $O(1)$ and $O(C)$ as

$$\left[L_+(0)L_-(0) - \Omega^{(0)}\right]\eta_n^{(0)} = 0, \tag{11}$$

and

$$\left[L_+(0)L_-(0) - \Omega^{(0)}\right]\eta_n^{(1)} = f_n, \tag{12}$$

where

$$f_n = \left[(\Delta_2 - 2Z_n^{(0)}Z_n^{(1)})L_-(0) + L_+(0)(\Delta_2 - 6Z_n^{(0)}Z_n^{(1)}) + \Omega^{(1)}\right]\eta_n^{(0)}. \tag{13}$$

To perform a stability analysis, firstly the significance of continuous spectrum for a intersite dark soliton is investigated by substituting a plane-wave expansion:

$$\eta_n = ae^{ikn} + be^{-ikn}. \tag{14}$$

From this, the dispersion relation for an intersite dark soliton is obtained as

$$\Omega = [2C(\cos k - 1) - (\omega + 2\gamma)]^2 - \omega^2, \tag{15}$$

thus the continuous band lies between

$$\Omega_L = 4(\omega + \gamma)\gamma, \tag{16}$$

when $k = 0$, and

$$\Omega_U = 4(\omega + \gamma)\gamma + 8C(\omega + 2\gamma) + O(C^2), \tag{17}$$

when $k = \pi$.

It is shown from above analysis that there are only three possibilities for parameter values γ and ω in the continuous spectrum above, i.e., either $\omega \geq \gamma > 0$, $\gamma > \omega > 0$ or $\gamma > -\omega \geq 0$. However, this paper is restricted to the first case only.

In this case, the leading order solution is given by the configuration (8) and the next correction can be obtained from Eq. (7) resulting

$$u_n^{(1)} = \begin{cases} 0, & n = -2, -3, ..., \\ \dfrac{1}{\sqrt{\omega+\gamma}}, & n = -1, \\ -\dfrac{1}{\sqrt{\omega+\gamma}}, & n = 0, \\ 0, & n = 1, 2, ... \end{cases} \tag{18}$$

Thus the intersite discrete dark soliton is given, with errors of $O(C^2)$, by

$$u_n = \begin{cases} -\sqrt{\omega+\gamma}, & n = -2, -3, ..., \\ -\sqrt{\omega+\gamma} + \dfrac{C}{\sqrt{\omega+\gamma}}, & n = -1, \\ \sqrt{\omega+\gamma} - \dfrac{C}{\sqrt{\omega+\gamma}}, & n = 0, \\ \sqrt{\omega+\gamma}, & n = 1, 2, ..., \end{cases} \tag{19}$$

and for this configuration Eq. (6) can be written as

$$L_+(0)L_-(0) = 4\omega\gamma + 4\gamma^2 \quad \text{for all } n, \tag{20}$$

from which it is concluded that there is a single leading order eigenvalue, given by $\Omega^{(0)} = 4\omega\gamma + 4\gamma^2$, with infinite multiplicity. Then a continuous spectrum for nonzero C is formed by the expansion of that eigenvalue.

From the fact of a single eigenvalue above, nothing can be said about the discrete eigenvalue(s) yet. However, its continuation still can be calculated as the coupling constant is turned on, which can be carried out from Eq. (12). Because

$$L_+(0)L_-(0) - \Omega^{(0)} = 0 \quad \text{for all } n, \tag{21}$$

the solvability condition for Eq. (12) has required $f_n = 0$ for all n. Then after a simple calculation:

$$f_n = \begin{cases} \left[4\omega + 16\gamma + 2(\omega+2\gamma)\Delta_2 + \Omega^{(1)}\right]\eta_n^{(0)}, & n = -1, 0, \\ \left[2(\omega+2\gamma)\Delta_2 + \Omega^{(1)}\right]\eta_n^{(0)}, & n \neq -1, 0. \end{cases} \tag{22}$$

Notice that the eigenvector for a localized mode in which there is only one eigenvalue with infinite multiplicity is also localized and decaying exponentially (see, e.g., Baesens *et al.* [16] for a justification). Thus, a suitable ansatz for $\eta_n^{(0)}$ can be chosen as

$$\eta_n^{(0)} = \begin{cases} Pe^{c(n+1.5)}, & n \leq -2, \\ P_0, & n = -1, \\ Q_0, & n = 0, \\ Qe^{-c(n+1.5)}, & n \geq 1, \end{cases} \tag{23}$$

for P, P_0, Q, $Q_0 \neq 0$ and $c > 0$. Substituting Eq. (23) in Eq. (22) and after applying solvability condition $f_n = 0$ for all n, following Eqs. are obtained:

$$\begin{aligned} Pe^{-0.5c}\left[2(\omega+2\gamma)(e^{-c}-2) + \Omega^{(1)}\right] + 2P_0(\omega+2\gamma) = 0, \quad & n = -2, \\ P_0(8\gamma + \Omega^{(1)}) + 2Q_0(\omega+2\gamma) + 2P(\omega+2\gamma)e^{-0.5c} = 0, \quad & n = -1, \\ Q_0(8\gamma + \Omega^{(1)}) + 2P_0(\omega+2\gamma) + 2Q(\omega+2\gamma)e^{-2.5c} = 0, \quad & n = 0, \\ Qe^{-2.5c}\left[2(\omega+2\gamma)(e^{-c}-2) + \Omega^{(1)}\right] + 2Q_0(\omega+2\gamma) = 0, \quad & n = 1, \\ 2(\omega+2\gamma)(e^{c} - 2 + e^{-c}) + \Omega^{(1)} = 0, \quad & n \neq -2, -1, 1, 0. \end{aligned} \tag{24}$$

It is clear from above first four equations that either $P_0 = Q_0$ or $P_0 = -Q_0$. From which it is obtained respectively, either

$$c = \ln\left(\frac{3\omega + 10\gamma}{\omega + 2\gamma}\right), \quad \Omega^{(1)} = \frac{-8(\omega + 4\gamma)^2}{3\omega + 10\gamma}, \tag{25}$$

or

$$c = \ln\left(\frac{\omega + 6\gamma}{\omega + 2\gamma}\right), \quad \Omega^{(1)} = \frac{-32\gamma^2}{\omega + 6\gamma}. \tag{26}$$

Therefore, the bifurcating discrete eigenvalues of an intersite dark soliton for small C are respectively given by

$$\Omega_{E,1} = 4\gamma\omega + 4\gamma^2 - \frac{8(\omega + 4\gamma)^2}{3\omega + 10\gamma}C + O(C)^2, \tag{27}$$

$$\Omega_{E,2} = 4\gamma\omega + 4\gamma^2 - \frac{32\gamma^2}{\omega + 6\gamma}C + O(C)^2. \tag{28}$$

In the AC limit $C = 0$, the above eigenvalues correspond, respectively, to the following normalized eigenvectors

$$\eta_n^{(0)} = \begin{cases} \dfrac{2\sqrt{(\omega + 3\gamma)(\omega + 4\gamma)}}{\omega + 2\gamma}\left(\dfrac{3\omega + 10\gamma}{\omega + 2\gamma}\right)^n, & n \le -2, \\ \dfrac{2\sqrt{(\omega + 3\gamma)(\omega + 4\gamma)}}{3\omega + 10\gamma}, & n = -1, \\ \dfrac{2\sqrt{(\omega + 3\gamma)(\omega + 4\gamma)}}{3\omega + 10\gamma}, & n = 0, \\ \dfrac{2\sqrt{(\omega + 3\gamma)(\omega + 4\gamma)}}{3\omega + 10\gamma}\left(\dfrac{3\omega + 10\gamma}{\omega + 2\gamma}\right)^{-n}, & n \ge 1, \end{cases} \tag{29}$$

and

$$\eta_n^{(0)} = \begin{cases} \dfrac{2\sqrt{\gamma(\omega + 4\gamma)}}{\omega + 2\gamma}\left(\dfrac{\omega + 6\gamma}{\omega + 2\gamma}\right)^n, & n \le -2, \\ \dfrac{2\sqrt{\gamma(\omega + 4\gamma)}}{\omega + 6\gamma}, & n = -1, \\ -\dfrac{2\sqrt{\gamma(\omega + 4\gamma)}}{\omega + 6\gamma}, & n = 0, \\ -\dfrac{2\sqrt{\gamma(\omega + 4\gamma)}}{\omega + 6\gamma}\left(\dfrac{\omega + 6\gamma}{\omega + 2\gamma}\right)^{-n}, & n \ge 1. \end{cases} \tag{30}$$

It is clear from Eq. (28) that when $C > 0$ the eigenvalue $\Omega_{E,2}$ is always less than Ω_L. As C is increased, both $\Omega_{E,1}$ and $\Omega_{E,2}$ are decreased to zero but $\Omega_{E,2} > \Omega_{E,1}$ (note that $\Omega_{E,2}$ is decreased more slowly than $\Omega_{E,1}$). Therefore, it is concluded that the instability may occur due to $\Omega_{E,1}$ becoming negative as illustrated in Fig. 1. The critical value of C can be found by equating $\Omega_{E,1} = 0$ as

$$C_{cr} = \frac{\gamma(3\omega + 10\gamma)(\omega + \gamma)}{(\omega + 4\gamma)^2}, \tag{31}$$

which approximate the onset of instability.

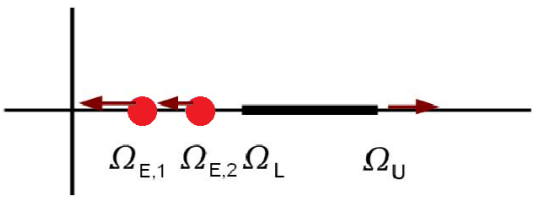

FIG. 1. A sketch of the dynamics of the eigenvalues and the continuous spectrum of a stable intersite dark soliton in the $(\mathrm{Re}(\Omega), \mathrm{Im}(\Omega))$-plane. The arrows indicate the direction of movement as the coupling constant C increases. Note that a soliton is unstable if there is some Ω with either $\Omega < 0$ or $\mathrm{Im}(\Omega) \neq 0$

3. Comparison with numerical computations

In this section, the numerical results are compared with the analytical calculation for previous section. The steady-state equation (2) is solved numerically by using Newton–Rapson method. Stability of this numerical solution is analyzed by solving the eigenvalue problem (4). ω is taken 0.9 in all the examples.

The comparisons between analytical predictions for the critical eigenvalues, given by equations (27)–(28) and corresponding numerical results are presented in Fig. 2. One should not be surprised by the appearance of the branching curves in the figure as they reveal the bifurcation of the critical eigenvalues from the inner edge of the continuous spectrum as soon as C is turned on from which they then split into two distinct eigenvalues. It is seen that the approximations given by Eqs. (27)–(28) are in good agreement with the numerics. The range of validity of these approximations is wider for the upper branches in each branching curve.

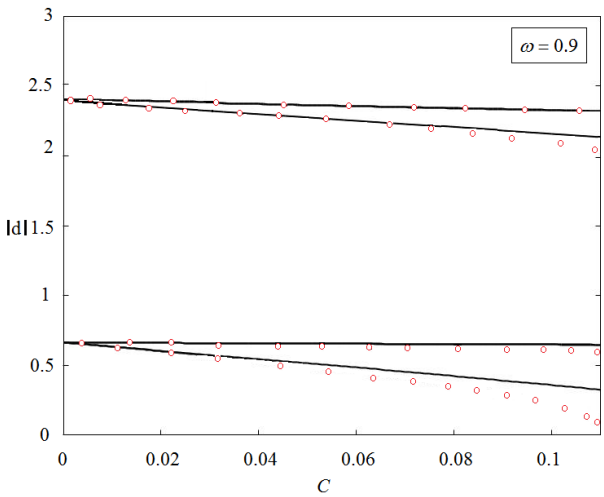

FIG. 2. Comparisons between the critical eigenvalue of intersite dark solitons obtained numerically (solid lines) and analytically (red dots) for two values of γ. The upper branching curves correspond to $\gamma = 0.8$ while the lower ones to $\gamma = 0.1$. The analytical approximations for the lower-upper branches in each branching curve are given by Eqs. (27)–(28)

The eigenvalue structures and corresponding soliton profiles of two values of $\gamma = 0.1, 0.8$ are plotted in Fig. 3. For $\gamma = 0.1$, when $C = 0.04$ the eigenvalues d lie in the gap between the two parts of the continuous spectrum, therefore no instability is obtained (Fig. 3(a)). For $\gamma = 0.1$, when $C = 0.5$ the instability is caused by a collision between one of the critical eigenvalues and its twin at the origin (Fig. 3(b)) (in Fig. 2, this eigen-value corresponds to the lower branch of the lower branching curves). If the value of C is taken greater than 0.05 (taking $\gamma = 0.1$ constant) the intersite dark solitons are remained always stable. It is interesting to note that the oscillatory instability can be fully suppressed by the presence of parametric driving, which has been appeared in onsite dark soliton [8]. As shown in the bottom panels of Fig. 3, there are values of the parameter γ for which no instability-inducing collision ever occurs. The (in)stability region of this configuration as well as the analytical prediction for the onset of instability are summarised in Fig. 4. It is seen from the figure that for any C and $\gamma > 0.31$ an intersite dark soliton is remained always stable. By contrast, it is also seen that the intersite dark soliton is remaining always unstable for $\gamma < 0$. The instability, in this case, is caused by the fact that the lower band of the continuous spectrum ($d = \sqrt{\Omega_L}$) lies on the imaginary axis.

4. Conclusions

In this paper, analytical and numerical calculations are performed to determine the existence and stability of intersite dark discrete solitons in the parametrically driven discrete nonlinear Schrödinger equation. It has been shown that the presence of a parametric driving can stabilize intersite dark discrete solitons. An interval has been found in γ for which a discrete dark soliton is stable for any value of the coupling constant, i.e., a parametric driving can suppress oscillatory instabilities. Stability windows for all the fundamental solitons have been presented and approximations using perturbation theory have been derived to accompany the numerical results.

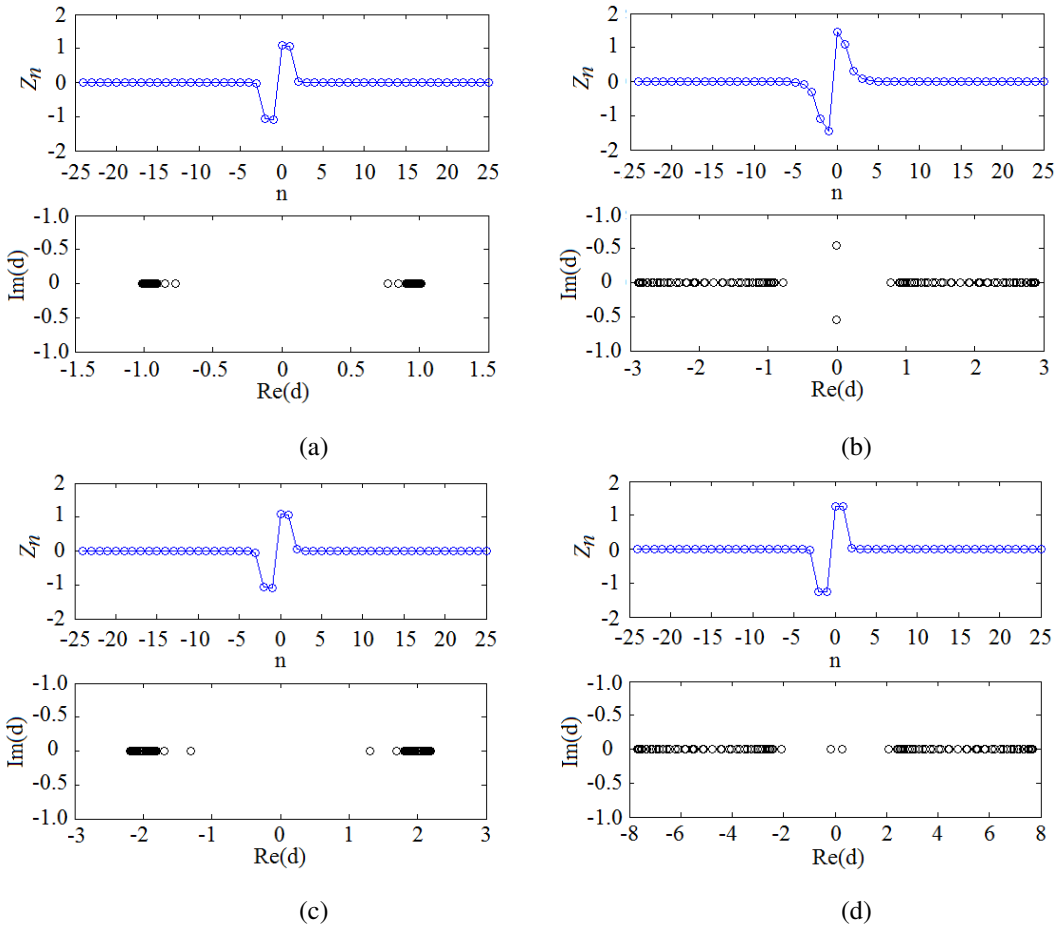

FIG. 3. The eigenvalue structures and soliton profiles of intersite dark solitons with parameter values as indicated in the caption for each panel. $\gamma = 0.1$, $C = 0.04$ (a); $\gamma = 0.1$, $C = 0.5$ (b); $\gamma = 0.8$, $C = 0.5$ (c); $\gamma = 0.8$, $C = 1.7$ (d)

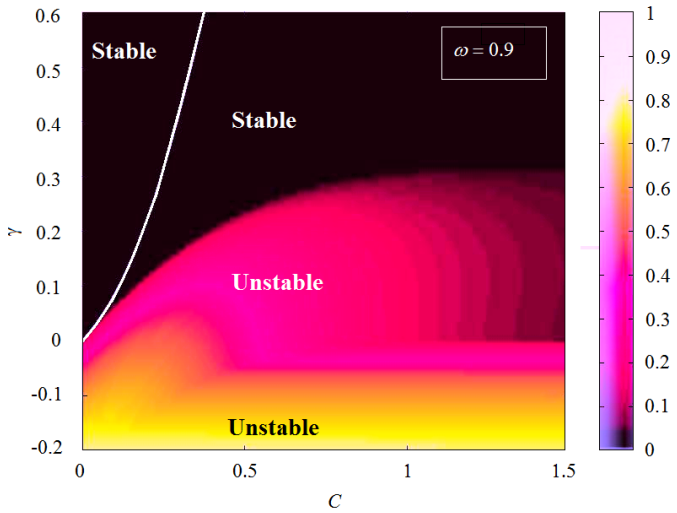

FIG. 4. The (in)stability region of intersite dark solitons in (C, γ)-space. For each value of C and γ, the corresponding colour indicates the maximum value of $|\,\mathrm{Im}(d)|$ (over all eigenvalues d) for the steady-state solution at that point. Stability is therefore indicated by the region in which $\mathrm{Im}(d) = 0$, namely the black region. Analytical approximation of Eq. (31) is given by white line.

References

[1] Kevrekidis P.G. *The Discrete Nonlinear Schr"odinger Equation: Mathematical Analysis, Numerical Computations and Physical Perspectives*. Berlin, Springer, 2009.

[2] Lederer F., Stegeman G.I., et al. Discrete solitons in optics. *Phys. Rep.*, 2008, **463**, P. 1.

[3] Scott A. *Encyclopedia of Nonlinear Science*. New York and London, Routledge, 2005.

[4] Christinsen P.L., Scott A.C. *Devydon's Soliton revisited, Self-tarpping of vibrational energy in protein*. Denmark, Springer Science, 1989.

[5] Christodoulides D.N., Joseph R.I. Discrete self-focusing in nonlinear arrays of coupled waveguides. *Optics Letters*, 1988, **13** (9), P. 794–796.

[6] Susanto H., Johansson M. discrete dark solitons with multiple holes. *Phys. Rev. E*, 2005, **72**, 016605(1–8).

[7] Syafwan M., Susanto H., Cox S.M. Discrete solitons in electromechanical resonators. *Phys. Rev. E*, 2010, **81** (2), 026207(1–14).

[8] Syafwan M. *The existence and stability of solitons in discrete nonlinear Schrdinger equations*. Ph.D. Thesis, University of Nottingham, 2012.

[9] Susanto H., Hoq Q.E., Kevrekidis P.G. Stability of discrete solitons in the presence of parametric driving type nonlinear Schrödinger lattices. *Phys. Rev. E*, 2006, **74**, 067601(1–4).

[10] Swami O.P., Kumar V., Nagar A.K. Bright Solitons In A Parametrically Driven Discrete Nonlinear Schrödinger Equation. *Int. J. Mod. Phys.*, 2013, **22**, P. 570–575.

[11] Kaurov V.M., Kuklov A.B. Josephson vortex between two atomic Bose-Einstein condensates. *Phys. Rev. A*, 2005, **71**, 011601(1–4).

[12] Kaurov V.M., Kuklov A.B. Atomic Josephson vortices. *Phys. Rev. A*, 2006, **73**, 013627(1–8).

[13] Alexeeva N.V., Barashenkov I.V., Pelinovsky D.E. Dynamics of the parametrically driven NLS solitons beyond the onset of the oscillatory instability. *Nonlinearity*, 1999, **12**, P. 103–140.

[14] Kivshar Yu.S. Bright and dark spatial solitons in non-Kerr media. *Optical and Quantum Electronics*, 1998, **30**, P. 571–614.

[15] Hayata K., Koshiba M. Theory of stationary solitary waves generated by optical parametric interactions in the presence of Kerr-type nonlinearities and dissipations. *J. Opt. Soc. Am. B*, 1995, **12**, P. 2288–2295.

[16] Baesens C., Kim S., MacKay R.S. localised modes on localised equilibria. *Physica D*, 1998, **133**, P. 242.

NANOSYSTEMS: PHYSICS, CHEMISTRY, MATHEMATICS, 2019, 10 (4), P. 398–401

Analysis of the unambiguous state discrimination with unequal a priori probabilities

A. A. Gaidash, S. S. Medvedeva, G. P. Miroshnichenko

ITMO University, Kronverkskiy, 49, St. Petersburg, 197101, Russia

andrewdgk@gmail.com, mdvdv.svt@gmail.com

PACS 42.50.Dv **DOI 10.17586/2220-8054-2019-10-4-398-401**

In this paper, we study unambiguous state discrimination regarding advanced attack on phase-coded quantum key distribution protocol. We propose the method of optimal unambiguous state discrimination probability derivation as a function of *a priori* probabilities for signal states. The expression obtained as an example in case of two signal states explicitly demonstrates the additional term dependent on small deviations from equal *a priori* probabilities that may take place in real quantum key distribution implementations. Precise estimation of optimal unambiguous state discrimination probability is significant for complete evaluation of quantum key distribution security.

Keywords: quantum key distribution, unambiguous state discrimination.

Received: 13 May 2019

Revised: 28 June 2019

1. Introduction

Throughout the last few decades the field of quantum cryptography has been rapidly developing and advancing. It has emerged with the first papers [1, 2] dedicated to the descriptions of protocols which allow secure distribution of a finite bit sequence between legitimate partners, and it is still in the focus of research groups, for instance [3–5]. Not only the protocols are of special interest, but also different types of attacks are studied in order to find successful countermeasures.

In this work we would like to concentrate on zero-error unambiguous state discrimination (USD) attack that is a considerable threat for protocols utilizing weak coherent states. USD attack requires eavesdropper (Eve) tapping into quantum channel of legitimate parties (Alice and Bob), errorlessly measuring the states and resending the modified states to Bob in order to preserve detection statistics [6]. We explore the phase-coded protocol which utilizes several pairs weak coherent states sent with unequal *a priori* probability. Imperfect state preparation that can result in the sending probabilities' inequality is the immanent part of every practical set-up. For example, quantum random number generator may cause unequal probability of state preparation [7–9]. Hence we examine the influence of unequal *a priori* probability on the discrimination probability.

USD measurement is subject of research for almost three decades. General approach to discrimination between linearly independent states was introduced in [10, 12, 13]. The solution for minimum achievable probability of inconclusive outcome for three states was given by [11]. The method of minimizing the probability for N symmetric states was considered in [12]. The special case of equal *a priori* probabilities for N states was discussed in [13]. Bounds of unambiguous state discrimination probabilities have been studied for the case of N linearly independent states in [14–16]. Several approaches to numerical optimization were proposed as well in [16, 17]. Implementations of USD in field of quantum computations also take place, e.g. for purpose of quantum cloning operation [18] or USD between oracle operators [19].

2. Method description

To perform unambiguous discrimination of the N signal states $|f_i\rangle$ Eve determines special positive-operator valued measure (POVM). It consists of projection operators $\hat{A}_i$ which are related to probabilities of successful state discrimination P_i (for each state) and operator $\hat{A}_0$ that is related to obtaining inconclusive result which is always present due to the nonorthogonality of the states and introduced in order to make the sum of the projection operators satisfy the decomposition of the identity:

$$\sum_{i=0}^{N} \hat{A}_i = \hat{I}. \tag{1}$$

Extracted from (1) the operator $\hat{A}_0$ is expressed as:

$$\hat{A}_0 = \hat{I} - \sum_{i=1}^{N} \hat{A}_i, \tag{2}$$

and according to [11] $\hat{A}_0$ is subject to condition:

$$\det[\hat{A}_0] = 0. \tag{3}$$

The latter provides maximal allowed values for probabilities P_i. We specify operators $\hat{A}_i$ as follows:

$$\hat{A}_i = P_i \left|v_i\right\rangle \left\langle v_1\right|, \tag{4}$$

where $|v_i\rangle$ is state that forms biorthogonal basis with the signal states $|f_i\rangle$ (i.e. $\langle v_i|f_j\rangle = \delta_{ij}$, where δ_{ij} is Kronecker delta).

Thus one needs to optimize the average probability of USD:

$$P = \sum_{i=1}^{N} p_i P_i, \tag{5}$$

where p_i is *a priori* probability of sending each state. One may use Lagrange multiplier method in order to do so. Hence, the function to be optimized is P from expression (5) and the following expression is bound [11]:

$$\det \hat{A}_0 = \det \left(\hat{I} - \sum_{i=1}^{2N} P_i |v_i\rangle\langle v_i| \right) = 0. \tag{6}$$

Let us introduce orthogonal basis $|u_i\rangle$ obtained by, for instance, Gram–Schmidt process. For simplicity let us denote matrix of the operator $\hat{A}_0$ (inconclusive result) as A in this orthonormal basis, and operators $|v_k\rangle\langle v_k|$ as $V^{(k)}$ respectively.

Thus system of equations is as follows:

$$\begin{gathered} \frac{d}{dP_n} \sum_{k=1}^{N} p_k P_k - \lambda \frac{d}{dP_n} \det A = 0, \\ \det A = 0, \end{gathered} \tag{7}$$

where λ is Lagrange multiplier. Insofar as

$$\frac{d}{dP_n} \det(A) = \mathrm{Tr} \left(\mathrm{adj}(A) \frac{d}{dP_n} \left(I - \sum_{k=1}^{N} P_k V^{(k)} \right) \right) = \mathrm{Tr} \left(- \mathrm{adj}(A) V^{(n)} \right), \tag{8}$$

where, $\mathrm{Tr}(X) = \sum_i X_{ii}$ is trace of arbitrary matrix X, $\mathrm{adj}(A)$ is adjoint matrix of matrix A, I is identity matrix, hence

$$\begin{gathered} p_n + \lambda \, \mathrm{Tr} \left(\mathrm{adj}(A) V^{(n)} \right) = 0, \\ \det A = 0. \end{gathered} \tag{9}$$

Since sum of p_i is equal to unit than Lagrange multiplier is as follows:

$$\lambda = - \frac{1}{\mathrm{Tr} \left(\mathrm{adj}(A) \sum_k V^{(k)} \right)}, \tag{10}$$

and consequently p_i is expressed as

$$p_i = \frac{\mathrm{Tr} \left(\mathrm{adj}(A) V^{(i)} \right)}{\mathrm{Tr} \left(\mathrm{adj}(A) \sum_k V^{(k)} \right)}. \tag{11}$$

One needs to derive P_i as function p_i in order to obtain expression of optimal USD as function of p_i.

3. Example

As an example let us consider two signal states. Their overlapping is denoted as B. Thus signal states can be described in terms of orthonormal basis (obtained by Gram–Schmidt process) as follows:

$$|f_1\rangle = \begin{pmatrix} 1 \\ 0 \end{pmatrix}, \quad |f_2\rangle = \begin{pmatrix} \dfrac{-B}{\sqrt{1-B^2}} \\ \dfrac{1}{\sqrt{1-B^2}} \end{pmatrix}. \tag{12}$$

Considering

$$|v_1\rangle = \begin{pmatrix} 1 \\ \dfrac{-B}{\sqrt{1-B^2}} \end{pmatrix}, \quad |v_2\rangle = \begin{pmatrix} 0 \\ \dfrac{1}{\sqrt{1-B^2}} \end{pmatrix}, \tag{13}$$

condition (6) may be derived in the following form:

$$\begin{aligned} \det \hat{A}_0 &= \det \left(\begin{bmatrix} 1 & 0 \\ 0 & 1 \end{bmatrix} - \begin{bmatrix} 1 & \dfrac{-B}{\sqrt{1-B^2}} \\ \dfrac{-B}{\sqrt{1-B^2}} & \dfrac{B^2}{1-B^2} \end{bmatrix} P_1 - \begin{bmatrix} 0 & 0 \\ 0 & \dfrac{1}{1-B^2} \end{bmatrix} P_2 \right) \\ &= \det \begin{bmatrix} 1-P_1 & \dfrac{BP_1}{\sqrt{1-B^2}} \\ \dfrac{BP_1}{\sqrt{1-B^2}} & \dfrac{1-B^2-B^2P_1-P_2}{1-B^2} \end{bmatrix} = \frac{1-B^2-P_1-P_2+P_1P_2}{1-B^2} = 0, \end{aligned} \tag{14}$$

thereby the probability P_1 can be denoted as

$$P_1 = \frac{1-B^2-P_2}{1-P_2}. \tag{15}$$

Lagrange multiplier is as follows:

$$\lambda = \frac{1-B^2}{(P_1+P_2)-2}, \tag{16}$$

and probabilities p_1 and p_2 are as

$$p_1 = \frac{1-P_2}{2-(P_1+P_2)}, \tag{17}$$

$$p_2 = \frac{1-P_1}{2-(P_1+P_2)}. \tag{18}$$

By substituting expression (15) in expression (17) we find

$$p_1 = \frac{(1-P_2)^2}{(1-P_2)^2+B^2}, \tag{19}$$

and consequently:

$$P_2 = 1 - B\sqrt{\frac{p_1}{1-p_1}} = 1 - B\sqrt{\frac{p_1}{p_2}}. \tag{20}$$

Taking into account symmetry of expressions (15), (17), (18) with respect to P_1 and P_2 following expression for P_1 is derived analogously:

$$P_1 = 1 - B\sqrt{\frac{p_2}{p_1}}. \tag{21}$$

By substituting expressions (20) and (21) in (5) we obtain optimized USD probability:

$$P = p_1\left(1 - B\sqrt{\frac{p_2}{p_1}}\right) + p_2\left(1 - B\sqrt{\frac{p_1}{p_2}}\right) = 1 - 2B\sqrt{p_1p_2}. \tag{22}$$

This result has well-known form [11] if $p = p_1 = p_2 = \dfrac{1}{2}$. Defining $p_1 = \dfrac{1}{2} + \Delta p$ and $p_2 = \dfrac{1}{2} - \Delta p$, where Δp is considerably small deviation from equal *a priori* probabilities, we get

$$P = 1 - 2B\sqrt{\left(\frac{1}{2} + \Delta p\right)\left(\frac{1}{2} - \Delta p\right)} \approx 1 - B + 2B(\Delta p)^2. \tag{23}$$

Therefore, the value of P has quadratic term dependent on small deviations from equal *a priori* probabilities.

4. Discussion and conclusion

In this work we analyze the probability of unambiguous discrimination for arbitrary number of states with unequal *a priori* probabilities. The proposed method provides system of equations (expressions (11) and (3)) that can be solved in order to find optimized USD probability as function of *a priori* probabilities. We consider rather simple and well-studied example for two states; the result is the same as in [20]. However, the authors of that paper obtain result only for two states. Concerning the method described in this paper it is unfortunate that the amount of calculations for higher number of states grows rapidly so it might be rather difficult to obtain analytical expressions similar to expression (22).

The results are important mostly in the field of quantum key distribution. In order to achieve certain level of security, one should consider various attacks, estimate probabilities of their success, and apply corresponding countermeasures to them. Thus estimation of optimal USD probability is crucial for bounding Eve's information during, for instance, advanced USD attack [6]. However consideration of an ideal case is not enough in this instance since there is an additional quadratic term related to slightly unequal (e.g. due to the bias in quantum random number generator) *a priori* probabilities in expression (23) that might provide additional information to Eve. Precise estimation of optimal USD probability is a significant step towards complete evaluation of quantum key distribution security.

Acknowledgements

This work was financially supported by the Ministry of Education and Science of Russian Federation (contract No. 03.G25.31.0229).

References

[1] Bennett C.H., Brassard G. Quantum Cryptography: Public Key Distribution and Coin Tossing. *Proceedings of "International Conference on Computers, Systems and Signal Processing"*, Bangalore, India, 09.12.1984, P. 17.
[2] Ekert A. Quantum cryptography based on Bell's theorem. *Physical review letters*, 1991, **67** (6), P. 661–663.
[3] Vazirani U., Vidick T. Fully device independent quantum key distribution. *Communications of the ACM*, 2019, **62** (4), P. 133–133.
[4] Minder M., Pittaluga M., et al. Experimental quantum key distribution beyond the repeaterless secret key capacity. *Nature Photonics*, 2019, **13**, P. 334–338.
[5] Razavi M., Leverrier A., et al. Quantum key distribution and beyond: introduction. *JOSA B*, 2019, **36** (3), P. QKD1–QKD2.
[6] Ko H., Choi B.S., Choe J.S., Youn C.J. Advanced unambiguous state discrimination attack and countermeasure strategy in a practical B92 QKD system. *Quantum Information Processing*, 2018, **17** (17), P. 1–14.
[7] Ivanova A.E., Chivilikhin S.A., Gleim A.V. Quantum random number generator based on homodyne detection. *Nanosystems: Physics, Chemistry, Mathematics*, 2017, **8** (2), P. 239–242.
[8] Ivanova A.E., Chivilikhin S.A., Gleim A.V. The use of beam and fiber splitters in quantum random number generators based on vacuum fluctuations. *Nanosystems: Physics, Chemistry, Mathematics*, 2016, **7** (2), P. 378–383.
[9] Ivanova A.E., Egorov V.I., Chivilikhin S.A., Gleim A.V. Investigation of quantum random number generation based on space-time division of photons. *Nanosystems: Physics, Chemistry, Mathematics*, 2013, **4** (4), P. 550–554.
[10] Barnett S.M., Croke S. Quantum state discrimination. *Advances in Optics and Photonics*, 2009, **1** (2), P. 238–278.
[11] Peres A., Terno D.R. Optimal distinction between non-orthogonal quantum states. *Journal of Physics A: Mathematical and General*, 1998, **31** (34), P. 7105–7111.
[12] Chefles A., Barnett S.M. Optimum unambiguous discrimination between linearly independent symmetric states. *Physics letters A*, 1998, **250** (4–6), P. 223–229.
[13] Chefles A. Unambiguous discrimination between linearly independent quantum states. *Physics Letters A*, 1998, **239** (6), P. 339–347.
[14] Zhang S., Feng Y., Sun X., Ying M. Upper bound for the success probability of unambiguous discrimination among quantum states. *Physical Review A*, 2001, **64** (6), 062103, P. 1–3.
[15] Duan L.M., Guo G.C. Probabilistic cloning and identification of linearly independent quantum states. *Physical review letters*, 1998, **80** (22), P. 4999–5002.
[16] Sun X., Zhang S., Feng Y., Ying M. Mathematical nature of and a family of lower bounds for the success probability of unambiguous discrimination. *Physical Review A*, 2002, **65** (4), 044306, P. 1–3.
[17] Eldar Y.C. A semidefinite programming approach to optimal unambiguous discrimination of quantum states. *IEEE Transactions on information theory*, 2003, **49** (2), P. 446–456.
[18] Galvao E.F., Hardy L. Cloning and quantum computation. *Physical Review A*, 2000, **62** (2), 022301, P. 1–5.
[19] Chefles A., Kitagawa A., et al. Unambiguous discrimination among oracle operators. *Journal of Physics A: Mathematical and Theoretical*, 2007, **40** (33), P. 10183–10213.
[20] Jaeger G., Shimony A. Optimal distinction between two non-orthogonal quantum states. *Physics Letters A*, 1995, **197** (2), P. 83–87.

NANOSYSTEMS: PHYSICS, CHEMISTRY, MATHEMATICS, 2019, 10 (4), P. 402–409

On a possibility to develop a full-potential orbital-free modeling approach

V. G. Zavodinsky[1], O. A. Gorkusha[2]

[1]Institute for Material Science, Tikhookeanskaya str., 153, Khabarovsk, 680042, Russia

[2]Institute of Applied Mathematics, Khabarovsk Division, Dzerzhinsky, 54, Khabarovsk, 680000, Russia

vzavod@mail.ru

PACS 03.65.-w **DOI 10.17586/2220-8054-2019-10-4-402-409**

We studied a principal opportunity to develop a full–potential orbital–free method for modeling of multi–atomic systems using results of Kohn–Sham calculations for single atoms. We have obtained equilibrium bond lengths and binding energies for homoatomic dimers Li_2, Be_2, B_2, C_2, N_2, O_2, F_2, Na_2, Mg_2, Al_2, Si_2, P_2, S_2, and Cl_2 as well as for heteroatomic dimers CSi, CB, CN, CO, SiO, NO, AlO, AlC, and NaCl. We analyzed our results and concluded that they are coordinated with experimental data not worse, than the results received by means of full-electrons calculations by the Kohn–Sham method.

Keywords: orbital-free, density functional, full-potential.

Received: 25 May 2019

Revised: 17 July 2019, 17 August 2019

1. Introduction

Modern technologies – nanotechnologies, bio-engineering, drug production and so on – need powerful tools to predict properties of systems containing hundreds of thousands and millions of atoms. Traditional quantum–mechanical approaches, such as Hartree–Fock theory, Quantum Chemistry methods and the Kohn–Sham version of Density Functional Theory (DFT), do not provide an opportunity to operate with large amounts of atoms; their limits do not exceed thousand atoms, even using pseudopotentials. Methods of empirical potentials and Monte–Carlo allow operation with large systems but they do not provide reliability of results. On the other hand, opportunities for increaseing computer speed are near their physical limit, thus it is useless to hope for solution of the problem by this way. An imperative need is a new modeling method, which would combine quantum-mechanical accuracy with a possibility of operating with enormous number of atoms. The idea of such method has arisen in 1964 when Hohenberg and Kohn formulated the theorem [1] that the ground state energy of any quantum system is completely defined by its electronic density. In the same work, they have declared that there is a certain universal functional $E[\rho]$, which minimization has to lead to the equilibrium the electronic density ρ and total electron energy E. The functional $E[\rho]$ has been written in the following form:

$$E[\rho] = \int \varepsilon(\rho) d\mathbf{r} = \int V(\mathbf{r})\rho(\mathbf{r}) d\mathbf{r} + \frac{1}{2}\int \varphi(\mathbf{r})\rho(\mathbf{r}) d\mathbf{r} + \int \varepsilon_{ex-c}(\rho) d\mathbf{r} + \int \varepsilon_{kin}(\rho) d\mathbf{r}, \tag{1}$$

where $\varepsilon(\rho)$ is the density of total electron energy, $V(\mathbf{r})$ is an external potential, $\varphi(\mathbf{r}) = \int \frac{\rho(\mathbf{r}')}{|\mathbf{r}-\mathbf{r}'|} d\mathbf{r}'$ is the electrostatic electron Hartree potential, $\varepsilon_{ex-c}(\rho)$ and $\varepsilon_{kin}(\rho)$ are exchange-correlation and kinetic energies (per electron). Minimization of (1) means solution has the following equation:

$$\delta E[\rho] = \int \frac{\partial \varepsilon(\rho)}{\partial \rho} \delta\rho(\mathbf{r}) = 0, \tag{2}$$

from where, according to the general variation theory, it follows:

$$\frac{\partial \varepsilon(\rho)}{\partial \rho} = V(\mathbf{r}) + \varphi(\mathbf{r}) + \mu_{ex-c}(\rho) + \mu_{kin}(\rho) = 0 \tag{3}$$

with the condition $\int \rho(\mathbf{r}) d\mathbf{r} = N$, where N is the number of electrons in the system,

$$\mu_{kin}(\rho) = \frac{\partial \varepsilon_{kin}(\rho)}{\partial \rho},\ \mu_{ex-c}(\rho) = \frac{\partial \varepsilon_{ex-c}(\rho)}{\partial \rho} \tag{4}$$

are so called kinetic and exchange-correlation potentials.

The Hartree potential $\varphi(\mathbf{r})$ may be calculated using Fourier transformations or Poisson equations, the external potential $V(\mathbf{r})$ usually consists of atomic potentials or pseudopotentials. There are some realistic approximations

for the exchange-correlation potential $\mu_{ex-c}(\rho)$ (for example [2–4]). The only real problem is the kinetic potential $\mu_{kin}(\rho)$, or the kinetic energy $\varepsilon_{kin}(\rho)$.

There were attempts to use the Thomas and Fermi (TF) approximation [5, 6] based on the free electron approach:

$$\varepsilon_{kin}^{TF}(\rho) = \frac{3}{10}\left(3\pi^2\right)^{2/3}\rho^{5/3}, \quad \mu_{kin}^{TF}(\rho) = \frac{1}{2}\left(3\pi^2\right)^{2/3}\rho^{1/3}. \tag{5}$$

This functional was found to be absolutely inadequate (all molecules were unstable); the von Weizsacker (vW) correction $\Delta\varepsilon_{kin}^{W}(\rho)$ [7] added to the TF:

$$\Delta\varepsilon_{kin}^{W}(\rho) = \frac{1}{8}\int \frac{|\nabla\rho(\mathbf{r})|^2}{\rho(\mathbf{r})}d\mathbf{r} \tag{6}$$

also did not solve the problem (binding energies were incorrect).

There were no other serious innovations in this area therefore Kohn and Sham have offered a compromise approach [8]. They have proposed to find the kinetic energy E_{kin} by solving some one-electron equation, the Hamiltonian of which depended only on the electronic density:

$$-\frac{1}{2}\Delta\psi_i(\mathbf{r}) + V_{eff}(\mathbf{r})\psi_i(\mathbf{r}) = \varepsilon_i\psi_i(\mathbf{r}), \tag{7}$$

$$V_{eff}(\mathbf{r}) = V(\mathbf{r}) + \varphi(\mathbf{r}) + \mu_{ex-c}(\rho), \tag{8}$$

$$E_{kin} = -\frac{1}{2}\int\sum_i \psi_i(\mathbf{r})\Delta\psi_i(\mathbf{r})d\mathbf{r} = \sum_i \varepsilon_i - \int\sum_i \psi_i(\mathbf{r})V_{eff}(\mathbf{r})\psi_i(\mathbf{r})d\mathbf{r}, \tag{9}$$

where $\rho(\mathbf{r}) = \sum_i |\psi_i(\mathbf{r}|^2$, $\psi_i(\mathbf{r})$ are wave functions, or orbitals, ε_i – energy of $i-$state. Equation (7) is called the Kohn–Sham (KS) equation.

The KS equation has become widely known, on its basis, many effective computing programs were created, many tasks of modeling of polyatomic systems were solved; however, as has been mentioned above, its opportunities are currently exhausted. The orbital-free (OF) approach as a version of the density functional theory could present an alternative to the KS method. It is a consecutive development of the idea of Hohenberg–Kohn [1] that the basic state of a quantum system can be completely described by means of electronic density. The advantage of this approach is obvious: operating only with an electronic density instead of numerous wave functions, it allows to increase sharply the speed of calculations and to include in consideration huge number of atoms.

The first attempts to develop an OF method of modeling began about 20 years ago. Those were simulations of liquid metals in the jellium approximation [9, 10]. Then works of other researchers (see for example reviews and original articles [11–14]) were applied to some simple molecules and solids. All of these were based on the use of special pseudopotentials, with most of them trying to use the TF and vW approximations for the kinetic energy in different combinations. However, these attempts did not have a large degree of success and were not widely adopted. It seems to us that the main reason for their inadequate efficiency is that they try to use some universal functional of kinetic energy for all systems. However, it was recently shown [15, 16], the Hohenberg–Kohn idea about existence of the universal density functional leading to the energy minimum was not strictly proved. Therefore, the search of specific types of kinetic potentials is necessary and justified.

In our recent works [17–21], we described an orbital-free pseudopotential approach for modeling of nanosystems containing atoms with s, p and d electrons. The key point of the approach was finding of the kinetic energy using some functions special for each type of atoms. This approach was tested on clusters contained C, Al, Si, O, Ti, and Cu atoms and demonstrated good agreement with Kohn–Sham method and experimental data. However, construction of pseudopotentials is a rather ambiguous operation and brings this method closer to the category of semi-empirical ones. In our present work, we describe an attempt of the orbital-free full-potential approach working without pseudopotentials.

2. General points of the approach

First, let us consider a single atom of any type A, which equilibrium total electron density $\rho(\mathbf{r})$ may be calculated easily by the KS method. According to (3), we can write an equation for finding the single-atom kinetic potential $\mu_{kin}^{(1)}$:

$$\mu_{kin}^{(1)}(\mathbf{r}; A) = -\frac{Z(A)}{|\mathbf{r}-\mathbf{R}|} - \varphi(\mathbf{r}) - \mu_{ex-c}(\mathbf{r}), \tag{10}$$

where $Z(A)$ is the total nuclear charge, $\mathbf{R}$ is an atomic position. If we know $\mu_{kin}^{(1)}$ as a function of $\mathbf{r}$ and ρ as a function of $\mathbf{r}$ we can find $\mathbf{r}(\rho)$, substitute it into $\mu_{kin}^{(1)}(\mathbf{r})$ and obtain $\mu_{kin}^{(1)}(\rho)$. Using $\rho(\mathbf{r})$ obtained from total potential KS calculations (FHI98pp [22]), we constructed kinetic potentials for B, C, N, O. They are plotted in Fig. 1.

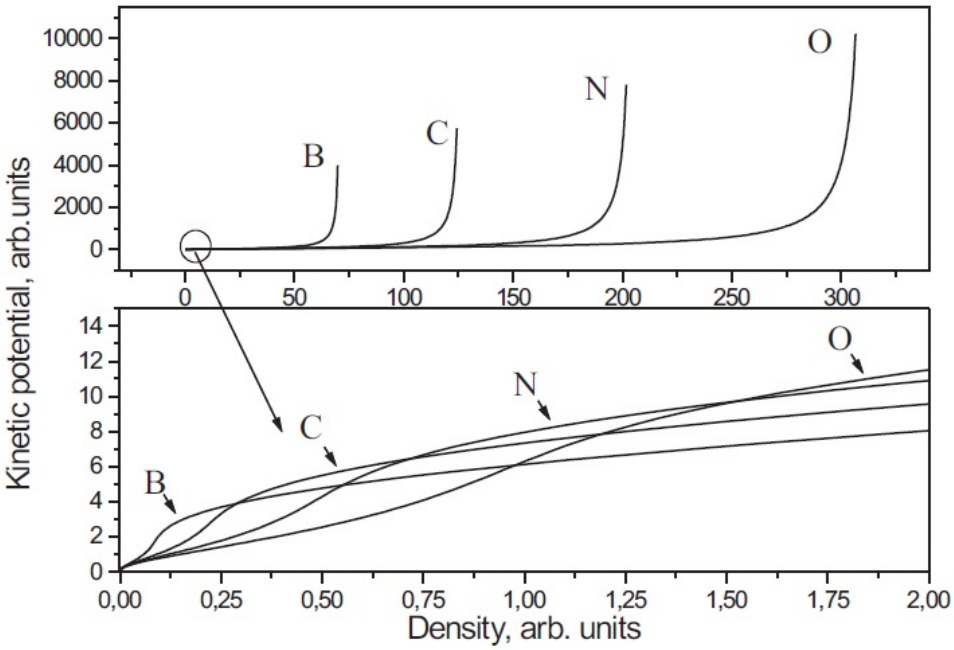

FIG. 1. Kinetic potentials calculated for equilibrium single-atomic full-electrons densities. The top panel demonstrates the total view of $\mu_{kin}^{(1)}(\rho)$ for different atoms; the down panel shows $\mu_{kin}^{(1)}(\rho)$ for small densities

One can see that plotted curves differ from each other's very much. In accordance with works [15, 16], there is no universal kinetic potential for different quantum systems. However, a question arises: If we have the single-atomic kinetic potentials for an each kind of atoms why we cannot use them for polyatomic systems? What is the difference between a single atom and for example a dimer?

Let us consider a dimer consisted of two boron atoms using the full-potential KS code Elk [23]. The equilibrium electron density of this dimer is plotted in Fig. 2.

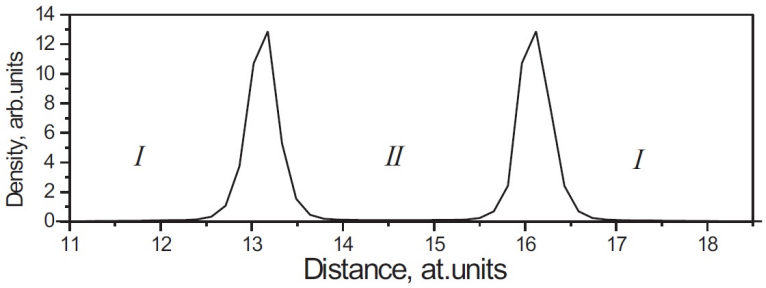

FIG. 2. The equilibrium electron density of the boron dimer. The interatomic distance is 3.0 Å

The kinetic potential isn't calculated in the KS approach. But we can determine it. Because we have the equilibrium KS density, we can find the two-atomic kinetic potential $\mu_{kin}^{B_2-KS}(\mathbf{r})$ for the boron dimer, according to (3):

$$\mu_{kin}^{B_2-KS}(\mathbf{r}) = -\frac{Z(boron)}{|\mathbf{r}-\mathbf{R}_1|} - \frac{Z(boron)}{|\mathbf{r}-\mathbf{R}_2|} - \varphi(\mathbf{r}) - \mu_{ex-c}(\mathbf{r}), \tag{11}$$

where $Z(boron) = 5$; $\mathbf{R}_1$, $\mathbf{R}_2$ are coordinates of 1 and 2 atoms of a dimer; $\varphi(\mathbf{r})$, $\mu_{ex-c}(\mathbf{r})$ are calculated using the equilibrium KS density.

It is clear from Fig. 2 that in the case of the dimer the two different types of regions exist. In the first one (I) the density grows from zero at the large distance from the atom to the maximum value at the atomic nuclear. The second region type (II) means the space between the atoms. Our calculations showed (Fig. 3) that in the I region the two-atomic kinetic potential behaves identically the one-atomic potential. It is naturally because an electron in this

region is far from the atom 2 and interacts with the atom 1 only. In the II region an electron interacts with the both atoms; the kinetic potential decreases, and the level of the decreasing depends on the interatomic distance: less the distance less the kinetic potential.

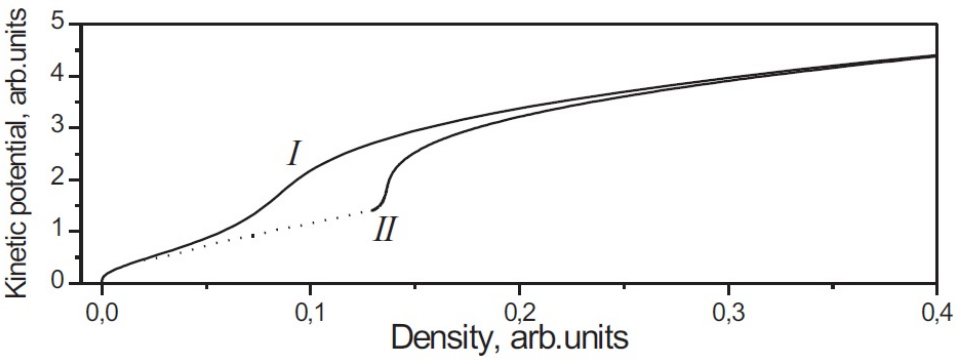

FIG. 3. Behavior of the kinetic potential in different regions of the boron dimer

Obviously, the direct way to provide correct results for orbital-free calculations is to fulfill KS calculations for different atomic positions, to find the kinetic potential in the each space points, and to use it for OF calculations. However, such way is very expensive and has no sense. It seems to us, the optimal method is to find some regularities from the KS calculations on the dimer level and extend them to polyatomic systems in the OF approach. The simplest way is to introduce some median kinetic potential acting in the multi-atomic system, leading to the correct binding energy and atomic configuration. We constructed the following fitting expression for the kinetic potentials for any homoatomic dimers :

$$\mu_{kin}^{homo\ dimer}(\mathbf{r};A) = \mu_{kin}^{(1)}(\mathbf{r};A)\cdot\left[1.0 - \frac{\alpha}{d}\exp(-\beta\cdot Z_{val}^2(A))\right], \tag{12}$$

where A is the type atoms, d is the dimer length, α and β are fitting constants, $Z_{val}(A)$ is the number of valence electrons in the dimer atom. Parameters α and β control values of the binding energy and the bond length. If they are fitted for one system (for B_2 for example) and are satisfied then for other dimers, this stage of our approach will be successful and we can pass to modeling more complicated systems.

As different atoms have different functions for kinetic energy, some procedure to calculate the total kinetic functions in the space of the atomic system has to be developed. Near each atom it has to be approximately equal to its specific function, but it has to be equal to mixture of the specific atomic functions between atoms. It seems that, in the case of a heteroatomic dimer, the simple way to construct the total function $\mu_{kin}^{hetero\ dimer}(\mathbf{r})$ is to summarize the specific atomic kinetic functions with some weights:

$$\mu_{kin}^{hetero\ dimer}(\mathbf{r}) = W_1(\mathbf{r})\cdot\mu_{kin}^{homo\ dimer}(\mathbf{r};A_1) + W_2(\mathbf{r})\cdot\mu_{kin}^{homo\ dimer}(\mathbf{r};A_2), \tag{13}$$

$$W_1(\mathbf{r}) = \frac{\exp\left(-\frac{(\mathbf{r}-\mathbf{R}_1)^2}{B_1}\right)}{\exp\left(-\frac{(\mathbf{r}-\mathbf{R}_1)^2}{B_1}\right)+\exp\left(-\frac{(\mathbf{r}-\mathbf{R}_2)^2}{B_2}\right)}, \tag{14}$$

$$W_2(\mathbf{r}) = \frac{\exp\left(-\frac{(\mathbf{r}-\mathbf{R}_2)^2}{B_2}\right)}{\exp\left(-\frac{(\mathbf{r}-\mathbf{R}_1)^2}{B_1}\right)+\exp\left(-\frac{(\mathbf{r}-\mathbf{R}_2)^2}{B_2}\right)}, \tag{15}$$

where A_1, A_2 are the types of atoms in the dimer, $\mathbf{R}_1$, $\mathbf{R}_2$ are coordinates of 1 and 2 atoms, B_1, B_2 are parameters, with which the Gauss functions limit areas of valence electrons, and the equilibrium values of d are used for $\mu_{kin}^{homo\ dimer}(\mathbf{r};A_1)$ and $\mu_{kin}^{homo\ dimer}(\mathbf{r};A_2)$ here.

3. Details of calculations

The full-electrons consideration of atoms meets some peculiarities, which makes it rather difficult. One of them is a sharp intensive peak of the electron density centered on the atomic nucleus. These peaks correspond to localized core states, which do not participate in interatomic interactions and usually are considered as "frozen" (for example in the package Elk [23]. Such dividing of electron density helps to avoid awful operations with intensive sharp peaks and to construct realistic computer codes. Here, we also follow that technique and divide the atomic density to core

and valent components. In particularly, we consider that the B atom has two core electrons and three valence ones and their densities distributions are shown in Fig. 4.

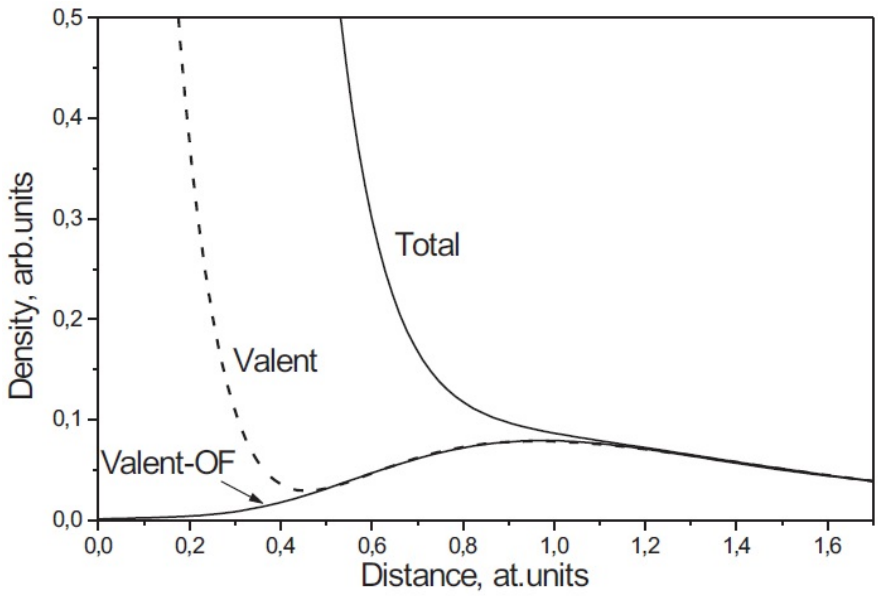

FIG. 4. Electron density of a single boron atom. The solid line (Total) demonstrates the total atomic density, the dashed line presents the density of the $2s^2 2p^1$ electrons, the Valent-OF line shows the valent density used in our OF approach

Let us introduce a function $F_{12}(\mathbf{r})$ for a homoatomic dimer:

$$F_{12}(\mathbf{r}) = \frac{Z(A)}{|\mathbf{r}-\mathbf{R}_1|} + \frac{Z(A)}{|\mathbf{r}-\mathbf{R}_2|} + \varphi_{12}(\mathbf{r}) + \mu^{(2)}_{kin}(\rho_{12}) + \mu_{ex-c}(\rho_{12}), \tag{16}$$

where $Z(A)$ is an atomic nuclear charge, $\rho_{12}(\mathbf{r}) = \rho_1^{core}(\mathbf{r}) + \rho_2^{core}(\mathbf{r}) + \rho_{12}^{val}(\mathbf{r})$, $\varphi_{12}(\mathbf{r}) = \int \frac{\varphi_{12}(\mathbf{r}')}{|\mathbf{r}-\mathbf{r}'|}$, $\mu_{ex-c}(\rho_{12})$ is calculated using some well-known approaches (LDA in our case).

Because we started with equilibrium states for single atoms 1 and 2 we can, according (10), write

$$\frac{Z(A)}{|\mathbf{r}-\mathbf{R}_1|} = -\varphi_1^a(\mathbf{r}) - \mu^{(1)}_{kin}(\rho_1^a) - \mu_{ex-c}(\rho_1^a), \tag{17}$$

$$\frac{Z(A)}{|\mathbf{r}-\mathbf{R}_2|} = -\varphi_2^a(\mathbf{r}) - \mu^{(1)}_{kin}(\rho_2^a) - \mu_{ex-c}(\rho_2^a), \tag{18}$$

where ρ_1^a and ρ_2^a are equilibrium electron densities of the 1 and 2 atoms, φ_1^a and φ_2^a are electrostatic potentials formed by these densities.

Substituting (17) and (18) into (16) we obtain

$$F_{12}(\mathbf{r}) = \varphi_{12}(\mathbf{r}) - \varphi_1^a(\mathbf{r}) - \varphi_2^a(\mathbf{r}) + \mu^{(2)}_{kin}(\rho_{12}) - \mu^{(1)}_{kin}(\rho_1^a) - \mu^{(1)}_{kin}(\rho_2^a) + \mu_{ex-c}(\rho_{12}) - \mu_{ex-c}(\rho_1^a) - \mu_{ex-c}(\rho_2^a). \tag{19}$$

Our purpose is to find such density ρ_{12}, which would turn (19) into zero.

Taking into account that the core densities do not change due to the interatomic interactions, we can write the iteration equation for valent density ρ_{12}^{val} in any point $\mathbf{r}$.

$$\rho_{12}^{val}(\mathbf{r};i) = \rho_{12}^{val}(\mathbf{r};i-1) + K_{iter} \cdot F_{12}(\mathbf{r};i-1)\rho_{12}^{val}(\mathbf{r};i-1), \tag{20}$$

where K_{iter} is an iteration parameter controlling the procedure convergence. The start step $(i = 0)$ means that the density $\rho_{12}^{val}(\mathbf{r};0)$ is a sum of equilibrium atomic valence densities: $\rho_{12}^{val}(\mathbf{r};0) = (\rho_1^{val}(|\mathbf{r}\text{-}\mathbf{R}_1|))^a + (\rho_1^{val}(|\mathbf{r}\text{-}\mathbf{R}_2|))^a$.

If we have found the equilibrium electron density we can calculate all components of the total energy. Let us remind that the total energy of the dimer $(E_{tot})_{12}$ is a sum of the nuclear-nuclear repulsive energy $(E_{rep})_{12}$, the

Coulomb energy $(E_C)_{12}$, the Hartree energy $(E_H)_{12}$, the exchange-correlation energy $(E_{ex-c})_{12}$ and the kinetic energy $(E_{kin})_{12}$:

$$(E_{rep})_{12} = \frac{Z(A) \cdot Z(A)}{|\mathbf{R}_1 - \mathbf{R}_2|}, \tag{21}$$

$$(E_C)_{12} = -\int \left(\frac{Z(A)}{|\mathbf{r} - \mathbf{R}_1|} + \frac{Z(A)}{|\mathbf{r} - \mathbf{R}_2|} \right) \cdot \rho_{12}(\mathbf{r}) d\mathbf{r}, \tag{22}$$

$$(E_H)_{12} = \frac{1}{2} \int \varphi(\rho_{12}) \cdot \rho_{12}(\mathbf{r}) d\mathbf{r}, \tag{23}$$

$$(E_{ex-c})_{12} = \int \varepsilon_{ex-c}(\rho_{12}) d\mathbf{r},\ \varepsilon_{ex-c}(\rho_{12}) = \int \mu_{ex-c}(\rho_{12}) d\rho_{12}, \tag{24}$$

$$(E_{kin})_{12} = \int \varepsilon^{(2)}_{kin}(\rho_{12}) d\mathbf{r},\ \varepsilon^{(2)}_{kin}(\rho_{12}) = \int \mu^{(2)}_{kin}(\rho_{12}) d\rho_{12}. \tag{25}$$

4. Calculations and discussions

4.1. Homoatomic dimers

Let us not foorget that we chose the B_2 dimer as a test object. We have found for it the binding energy $E_b = 1.8$ eV and the equilibrium length $d = 1.59$ Å taking parameters $\alpha = 1.08$, and $\beta = 0.13$. Then we used these values for all dimers of the Li–F and the Na–Cl rows. Results for binding energies are shown in Fig. 5; the dimer lengths are collected in Table 1. Experimental data are taken from the book [24]. The cited book contains experimental data taken from different sources; they often differ from each other very significantly. In these cases we averaged them and gave average values with two numbers after a decimal point. Our results are yielded with one number after a decimal point, because now we cannot guarantee higher precision for technical reasons. First of all, it is connected with the fact that the equilibrium states of the modeled systems are found by "manual" change of distance between atoms. In this work, we changed interatomic distances by the increments of 0.01 Å and we observed that we cannot guarantee the energy accuracy more than 0.1 eV. We supposed that such accuracy is sufficient for comparing our results with experimental data and the KS results.

We calculated mean absolute energy and distance deviations of OF and KS approaches with respect to reference experimental data. They are 0.6 eV, 1.2 eV and 0.09 Å, 0.03 Å for OF and KS, respectively. Thus we see that our approach provides better energy accuracy than the KS approach, however it is less accurate when finding interatomic distances.

We did not attract the published data to comparison with our results. The matter is that these data, as a rule, significantly differ from each other because they were obtained by different methods within different approaches and approximations. Instead of this, we took a modern code (Elk [23]) based on the full-electrons KS–DFT approach and fulfilled calculations for systems of interest to us using the same approach for the exchange-correlation interaction that we used in our OF calculations.

Table 1. Equilibrium bond lengths $d(\mathring{A})$ for studied dimers

Method	**Li**$_2$	**Be**$_2$	**B**$_2$	**C**$_2$	**N**$_2$	**O**$_2$	**F**$_2$	**Na**$_2$	**Mg**$_2$	**Al**$_2$	**Si**$_2$	**P**$_2$	**S**$_2$	**Cl**$_2$
OF	3.02	2.43	1.59	1.16	1.00	1.16	1.59	3.02	4.02	2.33	2.16	1.91	1.91	1.85
KS	3.07	2.46	1.63	1.23	1.11	1.18	1.37	3.07	3.89	2.54	2.22	1.83	1.90	1.96
Exp. [24]	3.09	2.47	1.59	1.24	1.10	1.15	1.417	3.07	3.891	2.56	2.32	1.90	1.88	1.99

Notations : "OF" are our OF calculations,

"KS" means full–potential calculations using the Elk [23]

It is clear from Fig. 5 that our OF energy results are in good agreement with the experimental data in many cases, they demonstrate even better agreement than KS calculations. The OF dimer lengths (see Table 1) also agree well with experimental ones, although this agreement is sometimes worse than in the case of the KS calculations. In general, we can say that our OF approach demonstrates a rather good ability to describe the interaction of atoms, especially taking into consideration the fact that parameters α and β were fitted only for one type of dimers (B_2).

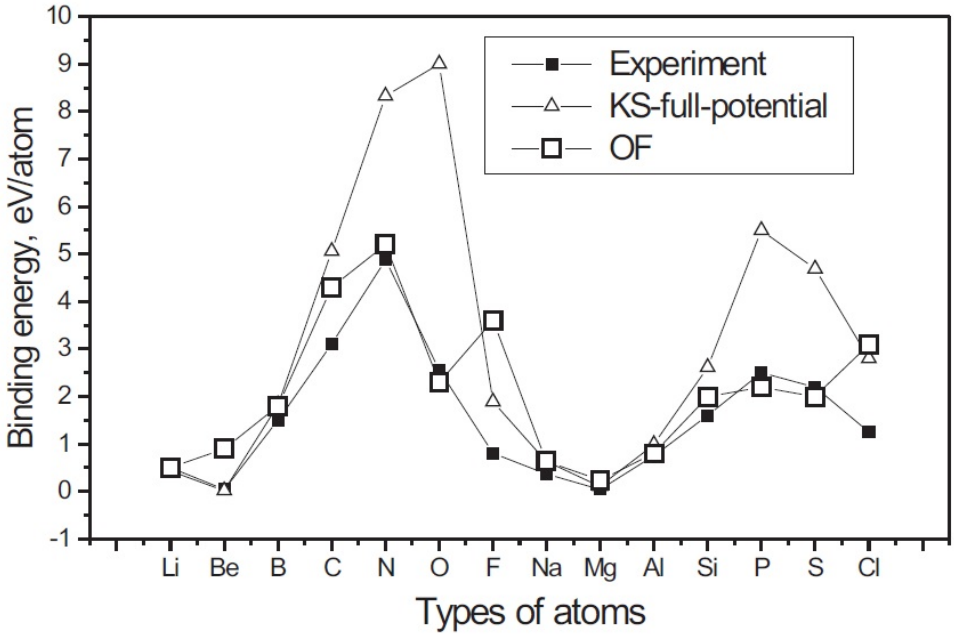

FIG. 5. Binding energies for studied dimers. "Experiment" [24], "KS-full-potential" means calculations using the Elk code [23], "OF" are our OF calculations

4.2. Heteroatomic dimers

The dimers CSi, CB, CN, CO, SiO, NO, AlO, AlC, NaCl were taken as heteroatomic pairs interesting for technical and chemical applications. The Gaussian weight parameters B for corresponding atoms are shown in Table 2. Calculated equilibrium bond lengths and dissociation energies are collected in Table 3. As in the case of homoatomic dimers, we compare our results with experimental data and results of KS full-electrons calculations (Elk code [23]).

Table 2. The values of the parameters B for weight functions

	C	**Si**	**B**	**N**	**O**	**Al**	**Na**	**Cl**
$B\ (a.u.)^2$	1.5	3.0	1.6	1.3	1.3	4.0	7.0	2.6

Table 3. Dissociation energies E_d and bond lenghts d for heteroatomic dimers

	Source	**C–Si**	**C–B**	**C–N**	**C–O**	**Si–O**	**N–O**	**Al–O**	**Al–C**	**Na–Cl**
E_d, eV	OF	5.7	6.4	12.9	12.7	6.7	7.9	4.9	3.9	4.2
	KS	5.9	6.32	13.35	14.7	15.55	10.95	2.3	1.69	5.07
	Exp. [24]	4.6	4.6	7.7	11.09	8.26	6.5	5.2	2.8	4.23
d, Å	OF	1.8	1.4	1.2	1.3	1.7	1.1	1.7	1.9	2.4
	KS	1.74	1.43	1.11	1.15	1.53	1.08	1.64	1.90	2.41
	Exp. [24]	1.7	1.49	1.15	1.11	1.60	1.15	1.62	1.96	2.36

Analysis of Table 3 shows that our OF approach describes interactions of studied atoms not worse than KS Elk-code.

5. Conclusions

In this work, we demonstrated that it is possible to design a full-potential orbital-free approach for modeling of atomic systems using one-atomic kinetic potentials obtained from Kohn–Sham calculations. We proposed a practical way to construct the two-atomic kinetic potential for the B_2 dimer and used successfully this way for dimers from

Li_2 up to Cl_2. We have generalized our OF method on heteroatomic systems. For this purpose, we used some weight functions and calculated equilibrium energies and bond lengths for dimers CSi, CB, CN, CO, SiO, NO, AlO, AlC, NaCl. The analysis of our results shows that they will be coordinated with experiments not worse than results of full-electrons KS calculations. Certainly, for development of this method in full, it is necessary to overcome a set of difficulties: namely, to construct kinetic potentials for multi-atomic systems, to develop a relaxation procedure, to develop a spin dependent version of the orbital free approach and the OF approach atoms with d-electrons. However, these problems seems to us surmountable, and an opportunity to model very big nanosystems – of hundreds thousands atoms and more – will be as a result had as an award.

References

[1] Hohenberg H., Kohn W. Inhomogeneous Electron Gas. *Physical Review*, 1964, **136**, P. B864–B871.

[2] Perdew J. P., Zunger A. S. Self-interaction correction to density functional approximation for many-electron systems. *Physical Review*, 1981, **23**, P. 5048–5079.

[3] Ceperley D. M., Alder B. J. Ground state of the electron gas by a stochastic method. *Physical Review*, 1980, **45**, P. 566–569.

[4] [4] Perdew J. P., Wang Y. Accurate snd simple density functional for the electronic exchange energy. *Physical Review*, 1986, **33**, P. 88008802.

[5] Thmas L. H. The calculation of atomic field. *Proc. Cambr. Phil. Soc.*, 1927, **23**, P. 542–548.

[6] Fermi E. Un metodo statistic per la determinazione di alcune priorieta dell'atomo. *Rend. Accad. Lincei.*, 1927, **6**, P. 602607.

[7] v. Weizsacker C. F. Theorie de Kernmassen. *Z. Physik*, 1935, **96**, P. 431458.

[8] Kohn W., Sham J. L. Self-consistent equations including exchange and correlation effects. *Phys. Rev.*, 1965, **140**, P. A1133–A1138.

[9] Garciá- González P., Alvarellos J. E., Chacón E. Nonlocal symmetrized kinetic- energy density functional: Application to simple surfaces. *Phys. Rev.*, 1998, **57**, P. 48574862.

[10] Gomez S., Gonzalez L. E., Gonzalez D. J., Stott M. J., Dalgic S., Silbert M. J. Orbital free ab initio molecular dynamic study of expanded liquid Cs. *Non-Cryst. Solids*, 1999, **250-252**, P. 163–167.

[11] Wang Y. A, Carter E. A. Orbital- free kinetic- energy density functional theory. In: *Theoretical Methods in Condensed Phase Chemistry*. Schwartz, S.D., Ed. Springer, Dordrecht.: 2002, P. 117–184.

[12] Huajie Chen, Aihui Zhou. Orbital- free density functional theory for molecular structure calculations. *Numerical Mathematics: Theory, Methods and Applications*, 2008, **1**, P. 1–28.

[13] Hung L., Carter E. A. Accurate Simulations of Metals at the Mesoscale: Explicit Treatment of 1 Million Atoms with Quantum Mechanics. *Chemical Physics Letters*, 2009, **475**, P. 163–170.

[14] Karasiev V. V., Chakraborty D., Trickey S. B. Progress on New Approaches to Old Ideas:Orbital-Free Density Functionals. In: *Many-Electron Approaches in Physics, Chemistry and Mathematics. Mathematical Physics Studies.* Eds: Bach V, Delle S. L. Ed. Springer, Dordrecht.: 2014, P. 113–135.

[15] Sarry A. M., Sarry M. F. To the density functional theory. *Physics of Solid State*, 2012, **54(6)**, P. 1315–1322.

[16] Bobrov V. B., Trigger S. A. The problem of the universal density functional and the density matrix functional theory. *Journal of Experimental and Theoretical Physics*, 2013, **116(4)**, P. 635–640.

[17] Zavodinsky V. G., Gorkusha O. A. A new Orbital-Free Approach for Density Functional Modeling of Large Molecules and Nanoparticles. *Modeling and Numerical Simulation of Material Science*, 2015, **5**, P. 39–47.

[18] Zavodinsky V. G., Gorkusha O. A. Development of an orbital free approach for simulation of multiatomic nanosystems with covalent bonds. *NANOSYSTEMS: PHYSICS, CHEMISTRY, MATHEMATICS*, 2016, **7(3)**, P. 427–432.

[19] Zavodinsky V. G., Gorkusha O. A. Development of the orbital free approach for heteroatomic systems.*NANOSYSTEMS: PHYSICS, CHEMISTRY, MATHEMATICS*, 2016, **7(6)**, P. 1010–1016.

[20] Zavodinsky V. G., Gorkusha O. A. New Orbital Free Simulation Method Based on the Density Functional Theory. *Applied and Computational Mathematics*, 2017, **6(4)**, P. 189–195.

[21] Zavodinsky V. G., Gorkusha O. A. Orbital- free modelling method for materials contained atoms with d- electrons. *International Journal of Scientific Research in Computer Science, Engineering and Information Technology*, 2018, **3(7)**, P. 57–62.

[22] Fuchs M., Scheffler M. Ab initio pseudopotentials for electronic structure calculations of poly-atomic systems using density-functional theory. *Computational Physics Communications*, 1999, **119**, P. 67–98.

[23] URL: http://elk.sourceforge.net.

[24] Huber K. R., Herzberg G. *Molecular Spectra and Molecular Structure. IV. Constants of Diatomic Molecules*. Litton Educational Publishing, N.Y.: 1979. 732 p.

NANOSYSTEMS: PHYSICS, CHEMISTRY, MATHEMATICS, 2019, 10 (4), P. 410–414

Quantum image transmission based on linear elements

P. A. Gilev, I. Y. Popov

ITMO University, Kronverkskiy, 49, St. Petersburg, 197101, Russia

grandarchtemplar@gmail.com, popov1955@gmail.com

PACS 03.67.Hk, 42.50.Ex **DOI 10.17586/2220-8054-2019-10-4-410-414**

Modeling of image transmission with a classic quantum computer interpreter is suggested. The transmission algorithm from the paper (Lemos G.B., et.al. Quantum Imaging with Undetected Photons, *Nature*, 2014, **512**, P. 409–412) is modified to reduce the complexity of the quantum circuit. Simplification was done by replacing the non-linear optical elements with a conventional quantum entanglement operator. The obtained results show expected efficiency of data transmission with Gaussian beam by hypothesis test and calculation error function. This error function is used for quality measurement. The interpreter is written in Kotlin language.

Keywords: quantum imaging, quantum communication, image restoration.

Received: 7 June 2019

Revised: 3 August 2019

1. Introduction

The production of a working quantum computer has become a real possibility thanks to recent developments in the field of nanotechnology but there is still a long way to go [1]. Optical channels are preferable in quantum communications (see, e.g., [2, 3]). The idea of quantum signal transportation appeared at the very beginning of quantum algorithms research or even earlier. The AbbeRayleigh diffraction limit constrains spatial resolution for classical imaging methods. Quantum imaging exploits correlations between photons to reproduce structures with higher resolution. Quantum-correlated N-photon states were shown to potentially surpass the classical limit by a factor of $1/N$, corresponding to the Heisenberg limit, using a method known as optical centroid measurement [4–6]. Quantum imaging found many applications in communications, material investigation, biology, etc. [7–10].

The measurement problem discovered by Steven Weinberg in 1998 [11] does not give one the ability to use full information contained in a quantum-entangled system. Thus, measurement avoidance is the main vector of quantum algorithm development, including quantum information transfer algorithm. This leads to the use of an uncontrollably big system in transport system. Other problem is overwhelming difficulty of maintaining an exclusive measurement system. In this way, the measurement of high frequency waves is more difficult than the measurement of low frequency waves. In [12], an example is given of a quantum circuit which transmits information using a wave twice as high frequency as the measured. But this scheme has a problem, elements used in the suggested circuit are difficult for expected behavior simulation. In the present work, we suggest to change all non-linear components by a linear quantum entanglement operator.

2. Quantum imaging

2.1. Classic quantum computer interpreter

A modified quantum imaging algorithm is implemented with classic quantum computer interpreter. The main element of the quantum algorithm is *unitary* operators. Operator A is called unitary operator if $AA^+ = A^+A = E$ where E is the identity operator and A^+ is the adjoint operator. Each unitary operator corresponds to some quantum operation (quantum gate) applied to quantum system. A composition of two unitary operators is consequent application of each one. A sequence of quantum gates forms a quantum algorithm.

Qubit is the main object for quantum computing. A physical qubit is a quantum system which can be in a superposition of two states. In quantum informatics, any system has 2^n states where n is the number of qubits. Each qubit is a complex 2-vector

$$|\phi\rangle = \begin{pmatrix} \alpha \\ \beta \end{pmatrix}, \quad \alpha, \beta \in \mathbb{C},$$

where $|\alpha|^2, |\beta|^2$ are the probabilities of observing the qubit in the corresponding state, respectively, $|\alpha|^2 + |\beta|^2 = 1$.

The state space for a multiqubit system is the tensor product of the state spaces for separate qubits. Let A be the operator acting on the first qubit $|\phi\rangle$ and B be the operator acting on the second qubit $|\psi\rangle$. Then,

$$(A \otimes B)(|\phi\rangle \otimes |\psi\rangle) = A(|\phi\rangle) \otimes B(|\psi\rangle),$$

where $\otimes$ is the tensor product of operators (in matrix case, it is the Kronecker product of matrices). Particularly, the tensor product of two vectors $|\phi\rangle, |\psi\rangle$ of sizes $n \times 1, m \times 1$ is the vector ξ of size $nm \times 1$, where:

$$\xi_{ni+j} = \phi_i \psi_j \ \forall i \in (1 \dots n), \forall j \in (1 \dots m).$$

The tensor product of two matrices A, B of sizes $n \times n, m \times m$ is the block matrix C with the following block entries

$$C_{ij} = A_{ij} B \ \forall i, j \in (1 \dots n).$$

So for implementation of a classic quantum interpreter, the following operations should be implemented:

(1) Algebra of application of matrix to vectors,
(2) Algebra of multiplication between two matrices,
(3) Algebra of tensor products between two vectors,
(4) Algebra of tensor products between two matrices.

2.2. Implementation features

In the current work some data structures were recreated to fulfill the requirements of clean functional style code. Thus, the vector is linked list with generalized typing. Also the full experimental model used complex number type which does not exist in vanilla Kotlin. The main idea is to use only recursive types with single exit point for tail-optimization provided by JVM environment. These types of structures also solve the problem of state mutation, as, all elements are made immutable objects.

Because the Kotlin sealed class model does not allow to extend them beyond this class, there are some features such as boxed types. Any type used for this interpreter are boxed. So, formally, there are no outer usage of standard types.

Finally, there is a problem that Kotlin does not have an apparatus for contract checking, as for pure functions so for impure. Also, it can not guarantee that all objects are linear-typing. So, the usage of this interpreter is non-verified and thus, there is a need for large test coverage or in formal verification. For image processing the standard java library is used.

2.3. Gaussian beam model

The main transmitter is a laser with Gaussian beam characteristics. A Gaussian beam is one in which there is a superposition of coherent waves each of which has special distribution of amplitudes:

$$H_{ij}(x, y) = H_i(\frac{x\sqrt{2}}{\rho}) H_j(\frac{y\sqrt{2}}{\rho}) e^{-\frac{x^2+y^2}{\rho}},$$

where ρ is related to the width of the beam, $H_i(x)$ is the Hermitian polynomial

$$H_i(x) = \sum_{j=0}^{\lceil n/2 \rceil} (-1)^j \frac{n!}{j!(n-2j)!} (2x)^{n-2j}.$$

Examples of the amplitude distributions can be found below. In Figs. 2–5 one can see the amplitude distributions for main gaussian beam modes which contribute the most important modes for the image.

Also for improvement of statistics, one uses relative distribution without any mode except $|00\rangle, |01\rangle, |10\rangle, |11\rangle$. In the present work, there are attempts to use different sets of Gaussian beams, but it does not confer an essential effect for the quality of the restored image.

The rotation operator is, usually, described by the following matrix in standard basis:

$$T(\phi) = \begin{pmatrix} \cos(\phi) & -\sin(\phi) \\ \sin(\phi) & \cos(\phi) \end{pmatrix},$$

however, we will use another, more convenient, representation:

$$T(t)(\alpha |0\rangle + \beta |1\rangle) = \xi |0\rangle + \zeta |1\rangle,$$

where

$$\xi = \alpha t - \beta \dot{t}, \zeta = \beta t + \alpha \dot{t}, \dot{t} = \sqrt{1 - t^2}$$

Thus, the object can be transformed from a constant matrix to a functional matrix. Here, t is "the rotation function" which is given by location of our beam. In this way, $t : \mathbb{R} \times \mathbb{R} \to \mathbb{R}$. This leads to the final representation of the rotation operator as the following matrix:

$$T(x,y) = \begin{pmatrix} t(x,y) & -\dot{t}(x,y) \\ \dot{t}(x,y) & t(x,y) \end{pmatrix}$$

This rotation operator is a one-qubit operator, but for many-qubit systems, one can consider the corresponding tensor product:

$$T_{k+1} = T \otimes T_k, \quad T_1 = T.$$

Also, one can construct T, not for each pixel (or other atomic element), but for a cluster. This solves a problem of transmission because we can easily facilitate data volume transmitted by classic channel.

Using this operator, one comes to the final representation of the quantum algorithm (the corresponding circuit is shown in Fig. 5):

$$Q = (NL1_{n+n} \otimes E_n) \circ (E_n \otimes T_n(x,y)) \circ (E_n \otimes NL2_{n+n}).$$

Here $NL1$ and $NL2$ elements are non-linear crystals which splits the laser beam in two beams of single frequency. These elements are not simple both for implementation and for computer modelling. We replace it by a linear optical elements (CNOT-gates):

$$Q' = (CNOT_{n+n} \otimes E_n) \circ (E_n \otimes T_n(x,y)) \circ (E_n \otimes CNOT_{n+n})$$

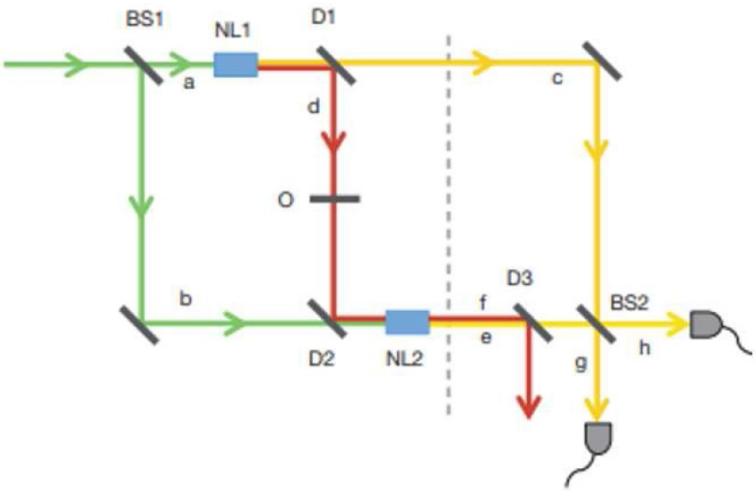

FIG. 1. The main circuit used in [12]

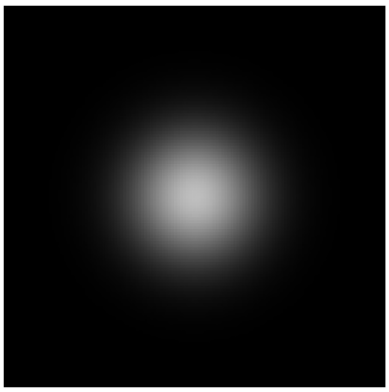

FIG. 2. H_{00} mode distribution

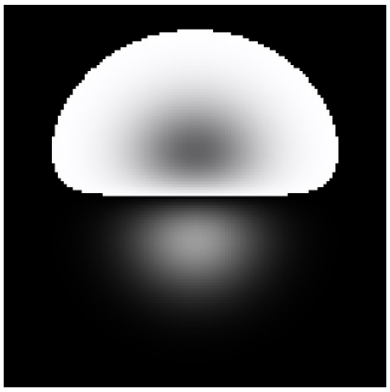

FIG. 3. H_{01} mode distribution

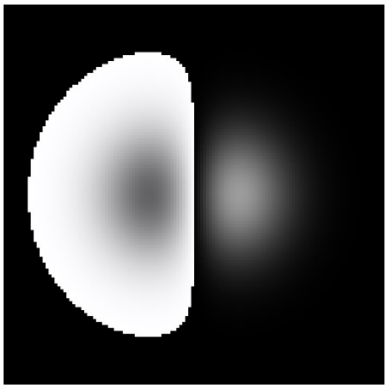

FIG. 4. H_{10} mode distribution

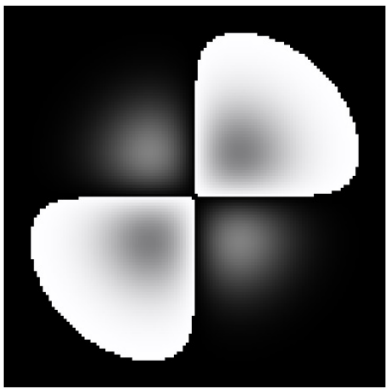

FIG. 5. H_{11} mode distribution

2.4. Measurements with interference model

The measurements are particle numbers which are recorded by the sensors. It is important that the sensors detect only low frequency signals which match them before they have an interference. Taking into account the distribution for the modes, one can calculate the interference between them with simple addition:

$$A(x,y)\dot{+}B(x,y) = I(x,y),$$

where $A(x,y)$ is the distribution after entanglement with modified high-frequency, $B(x,y)$ is the distribution after entanglement with non-modified high-frequency and $\dot{+}$ is the binary operator which sums only projection with right angle. Thus there are two different interference pictures:

$$I_A(x,y) = A(x,y) + T^{+}(x,y)B(x,y),$$

$$I_B(x,y) = T^+(x,y)A(x,y) + B(x,y).$$

Let us perform some pre-transformations. Let $P_h(x,y)$ be the initial high frequency distribution, $P_l(x,y)$ be the initial low frequency distribution, $Z(x,y)$ be the constant zero distribution, $H(x,y)$ be the high frequency after-processed distribution,

$$Q'(P_h \otimes P_l \otimes P_l) = (A \otimes B \otimes H),$$
$$TI_A = TA + TT^+B = TA + B.$$

As A, B are real scalars, their conjugation does not change the inner structure of them.

$$T^+I_A = T^+A + B = I_B,$$

or

$$TI_B = I_A.$$

In this way, we can get A, B if we know nature of T. Keeping in mind the known values of A and B, one can obtain the approximate picture.

Let us estimate the error. MSE (mean squared error) is a metrics for quality of the transmitted image ($I1, I2$ are the initial and the transmitted signals).

$$MSE(I1, I2) = \frac{1}{mn}\sum_{x=1}^{n}\sum_{y=1}^{m}|I1(x,y) - I2(x,y)|^2.$$

The corresponding results for different number of bits is presented in Table 1.

TABLE 1. Results

Size	16	32	64	128	256	512
MSE	0.5601	0.5559	0.5612	0.5603	0.5600	0.5603

3. Conclusion

Finally, the quantum image transmission method was suggested with use of linear elements in quantum circuit (without non-linear ones). This scheme is simpler for implementation than the analogous non-linear ones. It shows an appropriate quality of transmission. But there are two unsolved problems: strong blur on image and the need for classic channel usage (moreover, with no constant size of data). The strong blur may be partially solved by other non-quantum methods or with additional classical data transfer. This need in classic channel, unfortunately, can not currently be resolved by this algorithm without additional complication of the scheme.

Acknowledgements

This work was partially financially supported by the Government of the Russian Federation (grant 08-08), by grant 16-11-10330 of Russian Science Foundation.

References

[1] Milburn G.J., Woolley M.J. Quantum nanoscience. *Contemporary Physics*, 2008, **49**(6), P. 413-433.
[2] Pathak A., Banerjee A. *Optical Quantum Information and Quantum Communication*. SPIE Spotlight, NY, 2016.
[3] Sheremetev V.O., Rudenko A.S., Trifanov A.I. Testing Bell inequalities for multi-partite systems with frequency-encoded photonic qubits. *Nanosystems: Phys. Chem. Math.*, 2018, **9**(4), P. 484–490.
[4] Pittman T.B., Shih Y.H., Strekalov D.V., Sergienko A.V. Optical imaging by means of two-photon quantum entanglement. *Phys. Rev. A.*, 1995, **52**(5), P. R3429–R3432.
[5] Morris P.A., Aspden R.S., Bell J.E.C., Boyd R.W., Padgett M.J. Imaging with a small number of photons. *Nature Commun.*, 2015, **6**, P. 5913/1–6.
[6] Unternahrer M., Bessire B., Gasparini L., Perenzoni M., Stefanov A. Super-resolution quantum imaging at the Heisenberg limit. *Optica*, 2018, **5**(9), P. 1150–1154.
[7] Tenne R. et al. Super-resolution enhancement by quantum image scanning microscopy. *Nat. Photonics*, 2019, **13**, P. 116-122.
[8] Schnell Ch. Quantum imaging in biological samples. *Nature Methods*, 2019, **16**, P. 214–214.
[9] Genovese M. Real applications of quantum imaging. *Journal of Optics*, 2016, **18**, P. 073002.
[10] Kolobov M. (Ed.). *Quantum imaging*. Berlin, Springer, 2007, 111 p.
[11] Weinberg S. The Great Reduction: Physics in the Twentieth Century. In Michael Howard & William Roger Louis (eds.). *The Oxford History of the Twentieth Century*. Oxford University Press, 1998, P. 26
[12] Lemos G.B., Borish V., Cole G.D., Ramelow S., Lapkiewicz R. and Zeilinger A. Quantum Imaging with Undetected Photons. *Nature*, 2014, **512**, P. 409–412.

NANOSYSTEMS: PHYSICS, CHEMISTRY, MATHEMATICS, 2019, 10 (4), P. 415–419

On formal asymptotic expansion of resonance for quantum waveguide with perforated semitransparent barrier

A. M. Vorobiev, A. S. Bagmutov, A. I. Popov

ITMO University, Kronverkskiy, 49, Staint Petersburg, 197101, Russia

lenden31@yandex.ru, bagmutov94@mail.ru, popov239@gmail.com

DOI 10.17586/2220-8054-2019-10-4-415-419

A quantum waveguide with a semitransparent barrier, placed across it, is considered. It is assumed that the barrier has a small window. This local perturbation of the waveguide causes the appearance of resonance states localized near the barrier with the window. The asymptotics (in small parameter – the window width) of the resonances (quasi-bound states) is obtained. The procedure of construction of full formal asymptotic expansion is described. The first two terms of the asymptotic expansion are obtained explicitly. These terms describe the shift of the resonance from the threshold and the life time of the corresponding resonance state.

Keywords: quantum waveguide, resonance, asymptotics, scattering.

Received: 15 January 2019

Revised: 17 June 2019

1. Introduction

Problems concerning the small coupling window became interesting for mathematicians and theoretical physicists after Rayleigh's work in 1916 [1]. He considered the Helmholtz resonator and calculated the real part of the smallest quasi-eigenfrequency. Actually, it was not very significant result because calculating the imaginary part of quasi-eigenfrequencies and functions is a key point in such problems. For the first time, the imaginary part was calculated by Morse and Feshbach [2] using the Rayleigh method in 1960. They found a simple algebraic equation, which made it possible to approximately describe both components of this frequency – real and imaginary.

Related problems were widely studied in the second half of the 20-th century in connection with the development of nanotechnology and are quite popular currently. Now, these problems concern asymptotic analysis, resonances and resonance states. Such problems are characterized by a large number of different factors. The first factor is the system itself, which can contain different units like Helmholtz resonator, quantum waveguides, angles and so on. Of course we can consider systems with combination of such units; this may be system of two connected resonators [3], single resonator opened to space [4], pair of waveguides with common boundary [5] or even system of waveguides with resonators [6].

There are several other geometric factors characterizing such systems: shape of the resonator (it can be ideal square, circle or just some domain) [7], amount of dimensions (we can consider both two-dimensional and three-dimensional problems or even something else) [8], the window position (this can be significant, as a window on the side of square resonator and window right on its angle is quite different) [9] and the number of windows [10]. There are also works related to eigenstates and resonances induced by coupling window between waveguides [11–13].

One more fundamental factor is type of boundary conditions. Actually, we consider the Helmholtz equation in most parts of problems, so we need to set up boundary conditions. Standard options are Dirichlet and Neumann conditions, but there are cases when more complicated conditions are considered. Borisov and Gadylshin studied changing conditions in the process of the problem [14] (see also another approach in [15]). This point is also important for the subject of this work, because we will consider semitransparent boundary with specific condition on it, depending on transparency parameter. Thus, this wide class of similar problems is very popular for mathematicians all over the world [16–19]. The last introductory word brings us to the subject of this work – the transparency of the barriers is one not so popular, but more important factor . A system of two waveguides with common semitransparent wall was studied by Exner and Kreicirik in [20].

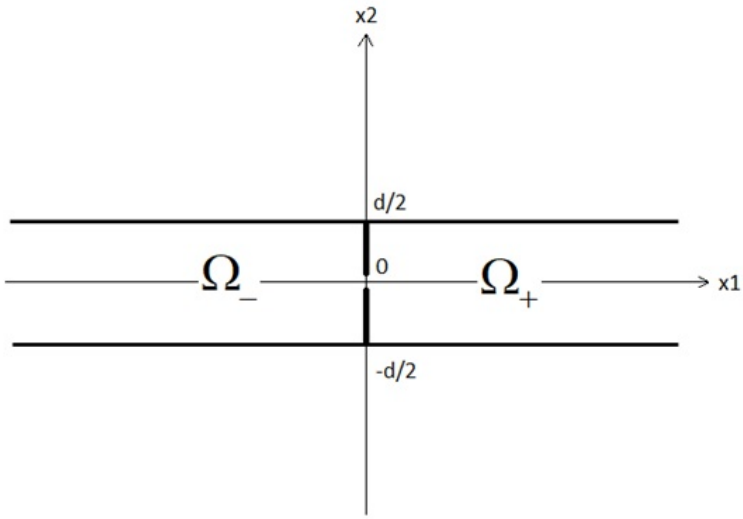

FIG. 1. The geometry of the system

2. Asymptotics construction

We will consider similar system, but with semitransparent barrier placed across the waveguide.

Let us set introductory formulas. α-transparency parameter. $\alpha = 0$ means no barrier, $\alpha = \infty$ – nontransparent barrier. Boundary conditions on the both waveguide walls are those of Dirichlet. But for barrier, there are specific conditions:

$$\begin{cases} u_+ = u_-, \\ u'_+ - u'_- = \alpha u. \end{cases} \tag{1}$$

The second condition characterizes the "jump" of the derivative on the barrier, α is a real constant. The conditions of such type appear if one considers singular potential supported on hypersurface. These potentials have been intensively investigated during last two decades (see, e.g., [21–25]).

The window size is 2ε, which is placed at the center of the barrier. For the corresponding unperturbed system (i.e., without coupling window), one can perform a separation of variables. Eigenvalues and orthonormal eigenfunctions for Laplacian (i.e. the second derivative) in the waveguide cross-section are as follows:

$$\psi_n(x_2) = \sqrt{\frac{2}{d}} \sin \frac{\pi n x_2}{d}, \quad \lambda_n = \left(\frac{\pi n}{d}\right)^2.$$

These eigenvalues play the role of the thresholds for the corresponding branches of the continuous spectrum for the waveguide Hamiltonian. The lower bound of the continuous spectrum of the Dirichlet Laplacian is greater than zero. We seek the main terms of the asymptotic expansion of a quasieigenvalues close to the first threshold:

$$\sqrt{\left(\frac{\pi}{d}\right)^2 - \tau_\varepsilon^2} = \sum_{j=2}^{\infty} \sum_{i=0}^{[j/2]-1} \tau_{ji} \varepsilon^j \left(\ln \frac{\varepsilon}{\varepsilon_0}\right)^i. \tag{2}$$

It's not the only possible expansion, but it's convenient for this case. Asymptotic series for the corresponding eigenfunctions are the following:

$$\psi_\varepsilon(x) = \sqrt{\left(\frac{\pi}{d}\right)^2 - \tau_\varepsilon^2} \cdot \sum_{j=0}^{\infty} \varepsilon^j \; P_{j+1}\left(D_y, \ln \frac{\varepsilon}{\varepsilon_0}\right) G^-(x,y,k)\Big|_{y=0}, \quad x \in \Omega^- \backslash S_{\varepsilon_0(\varepsilon/\varepsilon_0)^{1/2}}, \tag{3}$$

$$\psi_\varepsilon(x) = \sum_{j=1}^{\infty} \sum_{i=0}^{[(j-1)/2]} v_{ji}\left(\frac{x}{\varepsilon}\right) \varepsilon^j \ln^i \frac{\varepsilon}{\varepsilon_0}, \quad x \in S_{2\varepsilon_0(\varepsilon/\varepsilon_0)^{1/2}}, \tag{4}$$

$$\psi_\varepsilon(x) = -\sqrt{\left(\frac{\pi}{d}\right)^2 - \tau_\varepsilon^2} \cdot \sum_{j=0}^{\infty} \varepsilon^j \; P_{j+1}\left(D_y, \ln \frac{\varepsilon}{\varepsilon_0}\right) G^+(x,y,k)\Big|_{y=0}, \quad x \in \Omega^+ \backslash S_{\varepsilon_0(\varepsilon/\varepsilon_0)^{1/2}}. \tag{5}$$

Here, ε_0 is natural unit of length, for example d, S_t is the circle of radius t with the center at the center of the window,

$$v_{ji} \in W^1_{2,loc}(\Omega^- \cup \Omega^+),$$

$$P_1\left(D_y, \ln\frac{\varepsilon}{\varepsilon_0}\right) = c^{(1)}_{10}\frac{\partial}{\partial n_y},$$

n_y is normal to barrier in y,

$$P_m\left(D_y, \ln\frac{\varepsilon}{\varepsilon_0}\right) = \sum_{q=1}^{m-1}\sum_{i=0}^{[(q-1)/2]} c^{(m)}_{qi}\left(\ln\frac{\varepsilon}{\varepsilon_0}\right) D_y^{m-q+1}, \quad m \geq 2,$$

$$D_y^{2j+1} = \frac{\partial^{2j+1}}{\partial n_y^{2j+1}}, \quad D_y^{2j} = \frac{\partial^{2j}}{\partial n_y^{2j-1}\partial l_y}.$$

The first thing we're going to calculate is Green's function for such system. Green's function for standard planar quantum waveguide is well known [26] and is written as:

$$G(x,y,k) = \sum_{n=1}^{\infty}\frac{\psi_n(x_2)\cdot\psi_n(y_2)}{2p_n}\cdot e^{-p_n\cdot|x_1-y_1|}.$$

Here, x_1 and y_1 are coordinates on waveguide axis, ψ are orthonormal eigenfunctions for non-perturbed case, $p_n = \sqrt{\lambda_n - k^2}$ and for $n = 1$ it is exactly the left part of the asymptotic expansion given before.

Let's consider our case, where waveguide is placed as in the Figure, x_0 is the abscissa of the barrier, and two arguments of Green's function are x and y. One can write down Green's function with some coefficients considering three subdomains:

$$G(x,y,k) = \sum_{n=1}^{\infty}\frac{\psi_n(x_2)\cdot\psi_n(y_2)}{2p_n}\cdot\phi(x_1,y_1,k),$$

where

$$\phi(x_1,y_1,k) = \begin{cases} a_n\cdot e^{-p_n\cdot(x_1-y_1)}, & y_1 < x_1,\\ b_n\cdot e^{-p_n\cdot(x_1-y_1)} + c_n\cdot e^{p_n\cdot(x_1-y_1)}, & x_0 < x_1 < y_1,\\ d_n\cdot e^{p_n\cdot(x_1-y_1)}, & x_1 < x_0.\end{cases}$$

Coefficients are calculated using conditions (1):

$$\begin{cases} a_n\cdot e^{-p_n\cdot(x_1-y_1)}\Big|_{x_1=y_1} = b_n\cdot e^{-p_n\cdot(x_1-y_1)}\Big|_{x_1=y_1} + c_n\cdot e^{p_n\cdot(x_1-y_1)}\Big|_{x_1=y_1},\\ -p_na_n\cdot e^{-p_n\cdot(x_1-y_1)}\Big|_{x_1=y_1} + p_nb_n\cdot e^{-p_n\cdot(x_1-y_1)}\Big|_{x_1=y_1} - p_nc_n\cdot e^{p_n\cdot(x_1-y_1)}\Big|_{x_1=y_1} = 1,\\ b_n\cdot e^{-p_n\cdot(x_1-y_1)}\Big|_{x_1=y_1} + c_n\cdot e^{p_n\cdot(x_1-y_1)}\Big|_{x_1=y_1} = d_n\cdot e^{p_n\cdot(x_1-y_1)}\Big|_{x_1=y_1},\\ -p_nb_n\cdot e^{-p_n\cdot(x_1-y_1)}\Big|_{x_1=y_1} + p_nc_n\cdot e^{p_n\cdot(x_1-y_1)}\Big|_{x_1=y_1} - p_n\, d_n\cdot e^{p_n\cdot(x_1-y_1)}\Big|_{x_1=y_1} = \alpha\cdot d_n\cdot e^{p_n\cdot(x_1-y_1)}\Big|_{x_1=y_1}\end{cases} \Leftrightarrow$$

$$\begin{cases} a_n = b_n + c_n,\\ p_n(b_n - a_n - c_n) = 1,\\ b_n\dfrac{1}{\gamma} + c_n\gamma = d_n\gamma,\\ 2c_np_n = d_n(\alpha + 2p_n)\end{cases} \Leftrightarrow \begin{cases} a_n = \dfrac{\alpha\gamma^2 - \alpha - 2p_n}{2p_n(\alpha + 2p_n)},\\ b_n = \dfrac{\alpha\gamma^2}{2p_n(\alpha + 2p_n)},\\ c_n = -\dfrac{1}{2p_n},\\ d_n = -\dfrac{1}{\alpha + 2p_n},\end{cases}$$

where $\gamma = e^{p_n\cdot(x_0-y_1)}$. Let's notice that for no-barrier case ($\alpha = 0$) we will obtain coefficients which satisfy conventional formulas:

$$a_n = c_n = d_n = -\frac{1}{2p_n}, \quad b_n = 0.$$

The derivative of Green's function is used in (3) and (5), thus we need the following representation:

$$D_y^jG^{\pm}(x,0,k) = \frac{1}{d}\sin\frac{\pi x_2}{d}\sin\frac{\pi y_2}{d}D_y^j\left(\phi(x_1,y_1,k)\right)\Big|_{y_1=y_0}\left(\left(\frac{\pi}{d}\right)^2 - k^2\right)^{-1/2} + \Phi_j(x,k)\ln\frac{r}{\varepsilon_0} + g_j^{\pm}(x,k),$$

where $g_j^{\pm}(x,k)$ has no singularity at $x = 0$.

Boundary problems for coefficients v_{ji} can be obtained by the following manner. Let's consider asymptotic series of τ_ε^2 based on (2):

$$\tau_\varepsilon^2 = \sum_p \sum_q \Lambda_{pq} \varepsilon^p \ln^q \frac{\varepsilon}{\varepsilon_0}, \tag{6}$$

where coefficients Λ_{pq} are polynomials of τ_{ji} which can be easily calculated. Then, one can substitute (4) and (6) into the Helmholtz equation, change variables $\xi = \dfrac{x}{\varepsilon}$ and match terms of corresponding orders in the both series. Hence, one obtains the following equation:

$$\begin{aligned} &\Delta_\xi v_{ji} = -\sum_{p=0}^{j-3} \sum_{q=0}^{[p/2]-1} \Lambda_{pq} v_{j-p-2,i-q}, \quad \xi \in R^2 \backslash \Gamma_1, \\ &v_{ji} = 0, \ \ \xi \in \Gamma_1, \end{aligned} \tag{7}$$

where

$$\Gamma_1 = \{\xi | \xi_1 = 0 \wedge \xi_2 \in (-\infty; -1] \cup [1; +\infty)\}.$$

Let us define operator K_{pq} for sums $S(x, \varepsilon)$ like (3) and (5) by the following method: if $S(x, \varepsilon)$ has coefficient $\mu(\xi)$ for $\varepsilon^p \ln^q \dfrac{\varepsilon}{\varepsilon_0}$ in asymptotic expansion, then $\mathrm{K}_{pq}(S) = \mu$. Also let's define $\mathrm{K}_p = \sum\limits_q \mathrm{K}_{pq}$.

Taking into account Green's function derivative representation, we can use a procedure analogous to that in [27] and [28] and obtain:

$$\lim_{k \to \frac{\pi}{d}} \left(\sqrt{\left(\frac{\pi}{d}\right)^2 - k^2} P_1 G^-(x, 0, k) \right) = -\frac{\pi}{d^2} c_{10}^{(1)} \sin \frac{\pi x_2}{d},$$

$$\lim_{k \to \frac{\pi}{d}} \left(\sqrt{\left(\frac{\pi}{d}\right)^2 - k^2} P_1 G^+(x, 0, k) \right) = 0,$$

$$\begin{aligned} &\varepsilon^{-1} \mathrm{K}_1 \left(\sqrt{\left(\frac{\pi}{d}\right)^2 - \tau_\varepsilon^2} \cdot P_1 G^+(x, 0, \tau_\varepsilon) \right) = \\ &= \varepsilon^{-1} c_{10}^{(1)} \mathrm{K}_1 \left(\left(\tau_{20} \varepsilon^2 + \tau_{30} \varepsilon^3 + \tau_{40} \varepsilon^4 + \tau_{41} \varepsilon^4 \ln \frac{\varepsilon}{\varepsilon_0} + \ldots \right) \cdot \frac{\partial}{\partial x_1} \left(\frac{1}{\pi} \ln \rho + g(x, 0, \tau_\varepsilon) \right) \right) = \\ &= \varepsilon^{-1} c_{10}^{(1)} \cdot \tau_{20} \cdot \frac{x_1}{\pi \rho^2} = \xi_1 \cdot c_{10}^{(1)} \cdot \tau_{20} \cdot \pi^{-1} \rho^{-2}. \end{aligned}$$

Lemma. There exist harmonic functions $Y_q(\xi)$ which have the following differentiable asymptotics in $\rho \to \infty$:

$$Y_q = \begin{cases} -\sum\limits_{j=1}^{\infty} \rho^{-j} (a_{qj}^+ \cos j\theta + b_{qj}^+ \sin j\theta), \quad \xi_1 > 0; \\ \rho^q (a_q^0 \cos q\theta + b_q^0 \sin q\theta) + \sum\limits_{j=1}^{\infty} \rho^{-j} (a_{qj}^- \cos j\theta + b_{qj}^- \sin j\theta), \quad \xi_1 < 0. \end{cases}$$

To match terms from (8), we can choose v_{10} as follows:

$$v_{10}(\xi) = c_{10}^{(1)} \sum_{j=1}^{\infty} \rho^{-j} (a_{qj}^+ \cos j\theta + b_{qj}^+ \sin j\theta). \tag{8}$$

Now, we can equate coefficients of $\rho^{-1} \cos\theta$ in (8) and (9) to obtain τ_{20}:

$$\xi_1 \cdot c_{10}^{(1)} \cdot \tau_{20} \cdot \pi^{-1} \rho^{-2} = \rho \cos\theta \cdot c_{10}^{(1)} \cdot \tau_{20} \cdot \pi^{-1} \rho^{-2} = \rho^{-1} \cos\theta \cdot c_{10}^{(1)} \cdot \tau_{20} \cdot \pi^{-1} \Rightarrow$$

$$\tau_{20} \cdot \pi^{-1} = a_{q1}^+ \Rightarrow \tau_{20} = \pi \cdot a_{q1}^+.$$

3. Conclusion

The suggested procedure can be continued to obtain terms of the asymptotic expansion of any order. The results concerning the real part of the resonance, give one an estimation of the shift of resonance with respect to the threshold. As for the last formula for τ_{20} , it shows the imaginary part of the resonance which corresponds to the decay rate for the resonance state, i.e. to the lifetime of the quasi-bound state. These results can be useful for the description of "quantum waveguide – quantum dot – quantum waveguide" systems. One can find such systems in different nanotechnology-based applications.

Acknowledgment

This work was partially financially supported by the Government of the Russian Federation (grant 08-08), by grant 16-11-10330 of Russian Science Foundation.

References

[1] Lord Rayleigh O.M. The theory of Helmholtz Resonator. *Proceeding of Royal Society*, 1916, **638**, P. 265–275.
[2] Morse F.M., Feshbach G. *Methods of theoretical physics*, V. 2. .: Foreign Literature Publishing House, 1960, 986 p.
[3] Kiselev A.A., Pavlov B.S. The eigenfrequencies and eigenfunctions of the Laplace operator of the Neumann problem in a system of two coupled resonators. *Theor. Math. Phys.*, 1994, **100**(3), P. 354–366.
[4] Gadylshin R.R. The existence and asymptotics of poles with a small imaginary part for the Helmholtz resonator. *Uspekhi of Mathematical Sciences*, 1997, **52**(313), P. 71–72.
[5] Borisov D.I. Discrete spectrum of an asymmetric pair of waveguides coupled through a window. *Sb. Math.*, 2006, **197**(4), P. 475–504.
[6] Achilleos V., Richoux O., et.al. Acoustic solitons in waveguides with Helmholtz resonators: Transmission line approach. *Phys.Rev. E.*, 2015, **91**, P. 023204.
[7] Martinez A., Nédélec L. Optimal lower bound of the resonance widths for a Helmoltz tube-shaped resonator. *J. Spectral Th.*, 2012, **2**, P. 203–223.
[8] Gadyl'shin R.R. A two-dimensional analogue of the Helmholtz resonator with ideally rigid walls. *Diff. Uravn.*, 1994, **30**(2), P. 221–229. Translation in Diff. Eq., 1994, **30**(2), P. 201–209.
[9] Gadyl'shin R.R. Influence of the position of the opening and its shape on the properties of a Helmholtz resonator. *Theor. Math. Phys.*, 1992, **93**, P. 1151–1159.
[10] Borisov D., Exner P. Distant perturbation asymptotics in window-coupled waveguides. I. The non-threshold case. *J. Math. Phys.*, 2006, **47**(11), P. 113502(1-24).
[11] Exner P., Seba P., Tater M., Vanek D. Bound states and scattering in quantum waveguides coupled laterally through a boundary window. *J. Math. Phys.*, 1996, **37**, P. 4867–4887.
[12] Exner P., Vugalter S.A. Asymptotic estimates for bound states in quantum waveguides coupled laterally through a narrow window. *Ann. Inst. H. Poincare*, 1996, **65**, P. 109–123.
[13] Popov I.Y. Asymptotics of bound state for laterally coupled waveguides. *Rep. Math. Phys.* 1999, **43**, P. 427–437.
[14] Borisov D.I., Gadyl'shin R.R. On the spectrum of the Laplacian with frequently alternating boundary conditions. *Theor. Math. Phys.*, 1999, **118**(3), P. 272–277.
[15] Botman S.A., Leble S.B. Kinetic model of electron transport in cylindrical nanowire with rough surface. *Nanosystems: Phys. Chem. Math.*, 2018, **9**(2), P. 206–211.
[16] Popov I.Yu. The operator extension theory, semitransparent surface and short range potential. *Math. Proc. Cambridge Phil. Soc.*, 1995, **118**, P. 555–563.
[17] Popov I.Yu. The extension theory and the opening in semitransparent surface. *J. Math. Phys.*, 1992, **33**(5), P. 1685–1689.
[18] Ikebe T., Shimada S. Spectral and scattering theory for the Scgrödinger operator with penetrable wall potentials. *J.Math. Kyoto Univ.*, 1991, **31**(1), P. 219–258.
[19] Popov I.Yu. The extension theory, domains with semitransparent surface and the model of quantum dot. *Proc. Royal Soc. London A.*, 1996, **452**, P. 1505–1515.
[20] Exner P., Kreicirik D. Waveguides coupled through a semitransparent barrier: a Birman-Schwinger analysis. *Rev. Math. Phys.*, 2001, **13**, P. 307–334.
[21] Behrndt J., Langer M., Lotoreichik V. Boundary triples for Schrödinger operators with singular interactions on hypersurfaces. *Nanosystems: Phys. Chem. Math.*, 2016, **7**(2), P. 290–302.
[22] Mantile A., Posilicano A. Laplacians with singular perturbations supported on hypersurfaces. *Nanosystems: Phys. Chem. Math.*, 2016, **7**(2), P. 315–323.
[23] Exner P., Kondej S., Lotoreichik V. Asymptotics of the bound state induced by delta-interaction supported on a weakly deformed plane. *J. Math. Phys.*, 2018, **59**, P. 013051.
[24] Behrndt J., Exner P., et.al. Approximation of Schroedinger operators with delta-interactions supported on hypersurfaces. *Math. Nachr.*, 2017, **290**, P. 12151248.
[25] Popov I.Yu. The operator extension theory, semitransparent surface and short range potential. *Math. Proc. Cambridge Phil. Soc.*, 1995, **118**, P. 555–563.
[26] Tikhonov A.N., Samarskii A.A. *Equations of Mathematical Physics*. M.: Science, 1972, 531 p.
[27] Frolov S.V., Popov I.Yu. Resonances for laterally coupled quantum waveguides. *J. Math. Phys.*, 2000, **41**, P. 4391–4405.
[28] Gadyl'shin R.R. Surface potentials and the method of matching asymptotic expansions in the Helmholtz resonator problem. *Algebra i Analiz*, 1992, **4**(2), P. 88–115; translation in *St. Petersburg Math. J.*, 1993, **4**(2), P. 273–296.

NANOSYSTEMS: PHYSICS, CHEMISTRY, MATHEMATICS, 2019, 10 (4), P. 420–427

Thermodynamics of H–T phase transition in MoS_2 single layer

I. S. Popov, A. N. Enyashin

Institute of Solid State Chemistry UB RAS, Ekaterinburg, Russia

popov@ihim.uran.ru

PACS 64.70.Kb, 62.20.Fe, 61.72.Bb, 61.50.Ah **DOI 10.17586/2220-8054-2019-10-4-420-427**

Molybdenum disulfide is a title compound among the layered metal dichalcogenides, being a prominent tribological agent and vital platform for catalysts. The properties of a MoS_2 layer can vary widely, depending upon polymorphic composition. Here, using the density-functional theory calculations, the potential energy surfaces for polymorphic H- and T-MoS_2 layers are mapped. While the energy barriers for H→T and T(T′)→H transitions are found to be in fair agreement with previous studies which employed the nudged elastic band method, the bird's-eye view at the energy landscape of MoS_2 layer has disclosed the as-yet undescribed energy plateau attributed to an intermediate – square lattice of MoS_2 layer (S-MoS_2). The stability, structural and electronic properties of S-MoS_2 are discussed in comparison with those for H- and T-MoS_2 layers.

Keywords: layered chalcogenides, molybdenum sulfide, phase transition, DFT calculations.

Received: 13 August 2019

1. Introduction

Molybdenum disulfide MoS_2 yields a wealth of crystalline and nanostructured materials, well respected in numerous tribological applications [1] and promising in the fields of nanoelectronics [2, 3], photovoltaics [4] and photodetectors [5]. This compound under normal conditions crystallizes in the layered $2H_b$-MoS_2 phase, which hexagonal unit cell includes two anti-parallel layers held together by van der Waals' interactions [6]. The S atoms in every layer (henceforth, H-layer) are arranged in trigonal prisms with the bases forming two S atom planes, while the Mo atoms are located in the centers of these prisms. Related 3R-MoS_2 polytype, containing three parallel H-layers in the hexagonal unit cell, was also found in nature [7]. $2H_b$-MoS_2 modification is a semiconductor with an indirect intrinsic band gap (E_g) equal to 1.2 eV [2]. The exfoliation of either $2H_b$-MoS_2 or 3R-MoS_2 crystals into individual monolayers leads to the rise of a direct intrinsic band gap of material E_g = 1.8 eV [2].

Increasing of the pressure to ∼20 GPa initiates emergence of another polytypic form – $2H_a$-MoS_2 [8, 9]. This phase differs from $2H_b$-MoS_2 by a shift of two H-layers relative to each other and a decrease in the interlayer distance. The compound $2H_a$–MoS_2 exhibits metallic properties [9].

A heavy doping of the MoS_2 lattice by electrons stimulates stabilization of another polymorph – the layered 1T-MoS_2 phase – regardless of the source of excessive electrons [10–14]. The S atoms in the single layer of 1T-MoS_2 (henceforth, T-layer) are arranged as octahedra with Mo atoms in the center. 1T-MoS_2 is characterized by the absence of the band gap [15]. This phase is of interest in the development of supercapacitors [16, 17] and memristors [18, 19]. Due to natural metal-like character the catalytic properties of 1T-MoS_2 in the hydrogen evolution reaction may be significantly stronger than those of semiconducting $2H_b$-MoS_2 [10, 20].

A spontaneous reconstruction of the ideal hexagonal 1T-MoS_2 monolayer results in several superstructures, collectively designated as the T′ phase [21]. According to quantum-chemical calculations, 1T′-MoS_2 superstructures have a lower energy than the energy of hexagonal 1T-MoS_2 crystals, since a band gap E_g = 50 meV is open in the band structure of the precursor 1T-MoS_2, due to the spin-orbit coupling (SOC) at the Dirac cone [22]. The band gap opening due to SOC is of particular interest, as it is related to 2D topological insulators [22, 23].

A mixture of the H, T, and T′ phases within single MoS_2 layer was observed in experiments on stabilization of the T-phase by intercalating alkali metals into the interlayer space, followed by exfoliation [24, 25]. Due to the vital potential of a metal-like MoS_2 for practical applications, the evaluation of its controlled fabrication is of greatest importance. Hence, a deep understanding of the phase transition from a stable $2H_b$-MoS_2 polymorph to a metastable 1T-MoS_2 polymorph is required. The mechanism of the H-T phase transition was suggested earlier, as the one involving the gliding of atomic S planes [22,26–29]. The magnitude of the energy barrier for H→T and T(T′)→H transitions was estimated using the DFT calculations with the nudged elastic band (NEB) method as 1.5–1.9 and 0.7–1.0 eV, respectively. According to [27], the magnitude of the energy barrier can drop from 1.6 to 0.3 eV, when $4e^-$ are injected per MoS_2 unit. The formation energy of 1T-MoS_2 gradually decreases from +0.8 eV in neutral state to −0.3 eV in such extremely charged $4e^-$ state. The decrease of both the energy barrier and the formation energy of the T-phase by the charging have also been obtained using the DFT calculations [22]. Experimentally, the H→T phase transition was registered in Re-doped molybdenum disulfide using the method of scanning transmission electron microscopy [28].

The mechanism observed in [28] involves the gliding of atom planes of sulfur and/or molybdenum and requires an intermediate phase (so-called α-phase) as a precursor. A seed of the T-phase originates from the appearance of two α-phase bands that are located relative to each other at an angle of 60°.

Structural phase transition can significantly alter the properties of solids without modifying their chemical composition. Understanding the mechanisms of phase transitions and the formation of possible structural defects thereof is the key to the synthesis of materials with desired and regulated properties. In this paper, we propose another mechanism for the H–T phase transitions in MoS_2 layer, which might be realized not only under electron doping, but under shock-wave propagation, too. Namely, the H–T transition is considered as an in-plane compression of a monolayer along *armchair* and/or *zigzag* directions via formation of an intermediate metastable "square" phase (S-phase) not yet disclosed on the minimum energy paths using DFT NEB method [26, 27, 29]. In addition, a relationship is established between the different scenarios of subsequent structure relaxations of S-phase into H-phase and the experimentally observed grain boundaries within the H-phase [30–35].

2. Computational details

As the basic models for the study of the H–T phase transition the supercells of both polymorphic single H- and T-layers of MoS_2 in rectangular $a\sqrt{3}\times a = b\times a$ representation were employed, where a is the in-plane lattice parameter (Fig. 1). The atomic positions within supercells were optimized, while their lattice parameters were fixed and varied using the step 1% within 85%–150% a_0 and 65%–120% b_0, where a_0 and b_0 are equilibrium lattice parameters.

All quantum-chemical calculations were performed within the framework of the density-functional theory (DFT) using the SIESTA 4.0 implementation [36]. The exchange-correlation potential was described within the Generalized Gradient Approximation (GGA) in the Perdew-Burke-Ernzerhof parametrization. The core electrons were treated within the frozen core approximation, applying norm-conserving Troullier–Martins pseudopotentials. The valence electrons were taken as $4d^5 5s^1 5p^0$ for Mo and $3s^2 3p^4 3d^0$ for S. The pseudopotential core radii were chosen as 2.43 a_B for Mo4d and Mo5s, 2.62 a_B for Mo5p states, and 1.69 a_B for all S states, respectively. In all calculations, a double-ζ polarized basis set was used. The k-point mesh was generated by the method of Monkhorst and Pack. For k-point sampling, a cutoff of 15 Å was used. The real-space grid used for the numeric integrations was set to correspond to the energy cutoff of 300 Ry. The calculations of the pristine MoS_2 structures were performed using variable-cell and atomic position relaxations, with convergence criteria corresponding to the maximum residual stress of 0.1 GPa for each component of the stress tensor, and the maximum residual force component of 0.01 eV/Å.

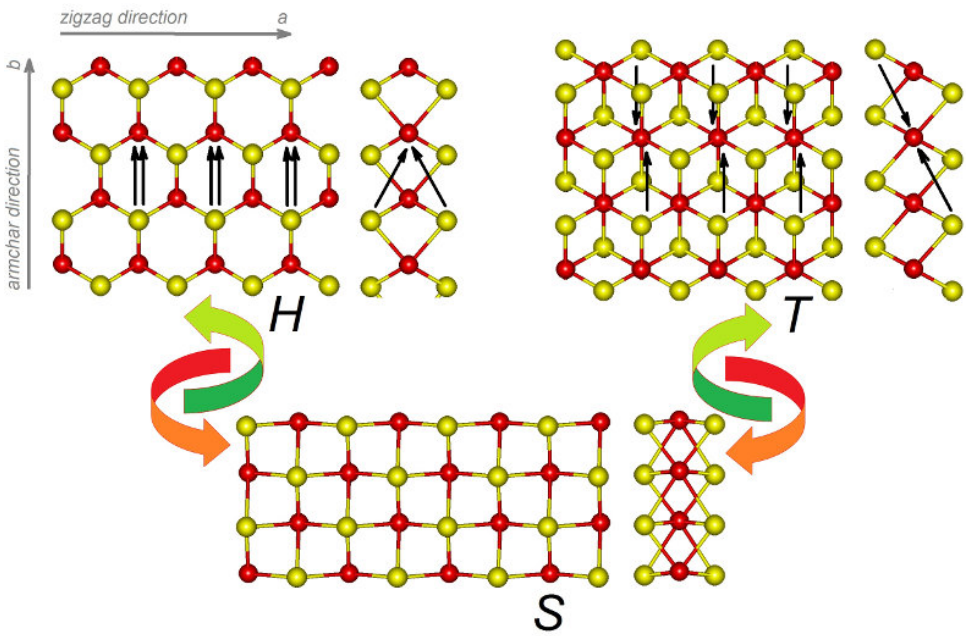

FIG. 1. Relation between H- and T-layers of MoS_2 established via in-plane compression along *armchair* direction of the layers suggests an existence of two-dimensional MoS_2 transition state with square lattice (S-phase). Ball-and-stick models represent the top and the side views on the structures with the DFT optimized geometries (Mo and S atoms are painted in red and yellow, respectively)

3. Results and Discussion

3.1. S-phase of MoS_2: a possible intermediate between H- and T-MoS_2

Our main methodology for the study of H-T phase transition within individual MoS_2 monolayer involved the brute-force scan of the potential energy surface (PES) for both H- and T-phases depending on the imposed in-plane strain along two directions. Hence, a function of the potential energy can be simply mapped as a three-dimensional surface. Intuitively, the energy surfaces of both 2D polymorphs should share at least one joint point, when simply considering the deformation of 2D structures (Fig. 1). The in-plane compression of H-layer along *armchair* direction leads to rapprochement between a Mo atom and two S atoms opposing it as a couple within the same hexagonal ring. The similar compression of T-layer also leads to rapprochement between a Mo atom and two S atoms opposing it already as loners from two different hexagonal rings. One of the final common stages for both processes could be represented as a phase with regular square-like atom ordering – henceforth, S-phase. Apart of the lattice symmetry, the surmised intermediate S-phase should possess such coordination numbers of Mo and S atoms as 8 and 4, which are drastically different to the coordination in both known hexagonal phases. Therefore, we have preliminary examined by DFT calculations a possible stability and the properties of S-phase in comparison to those for the parent H- and T-MoS_2 layers.

The equilibrium lattice parameters a obtained in the present work for H- and T-layers are found equal 3.21 and 3.20 Å, respectively, which is in fair agreement with experimental and previous theoretical data [7, 37]. The geometry of the ideal S-MoS_2 with square lattice has not been reported before. It is found preserved after full optimization, yielding the lattice parameter $a_0 = 2.99$ Å. The distances between sulfur planes within H-, T- and S-layers are equal to $w_0 = 3.21$, 3.27 and 2.98 Å, respectively. Hence, while the surface area of unit cells remains roughly the same for all three polymorphs, a contraction of S-layer is observed in out-plane direction. The cubic MoS_8 polyhedra within S-layer are slightly distorted with distribution of Mo-S bond lengths l = 2.46–2.74 Å, which fits at the lower bound $l = 2.45$ and 2.47 Å within MoS_6 prisms and MoS_6 octahedra.

According to our calculations, T-MoS_2 is expectedly less stable, than H-MoS_2 on 0.85 eV/MoS_2 The corresponding relative energy of S-MoS_2 was found to be close to this value and is 1.04 eV/MoS_2. Since the stability difference between H- and T-MoS_2 is ruled mostly by electronic factor, T- and S-MoS_2 could share common features in electronic structure. The calculated electronic band structures for all three MoS_2 layers are drawn on Fig. 2. H-MoS_2 is semiconductor with the direct K–K band gap of 1.63 eV. The top edge of the valence band at $-2\ldots-1$ eV relative the Fermi level as well as the bottom of conduction band are presented by Mo4d-states. The valence band below -2 eV is mostly composed of S3p-states. In contrast, both T- and S-MoS_2 layers have a metal-like character. Like in the case of H-MoS_2 the valence band of occupied S3p states can be found below -3 eV, while Mo4d-states form the bands hosting the Fermi level.

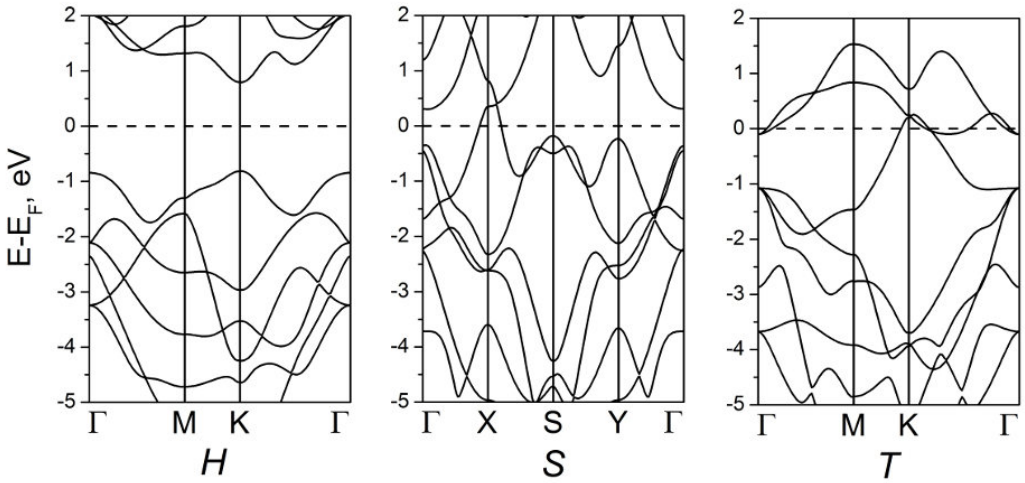

FIG. 2. Electronic band structures for H-, S- and T-layers of MoS_2. DFT calculations

In terms of ligand field theory the semiconducting nature of H-MoS_2 is caused by the splitting of the Mo4d levels within trigonal prismatic field into the levels of the fully occupied Mo4d_{z^2} orbital and the unoccupied Mo4d_{xy}, Mo4$d_{x^2-y^2}$, Mo4d_{xz} and Mo4d_{yz} orbitals. Octahedral crystal field in T-MoS_2 splits the Mo4d levels into three

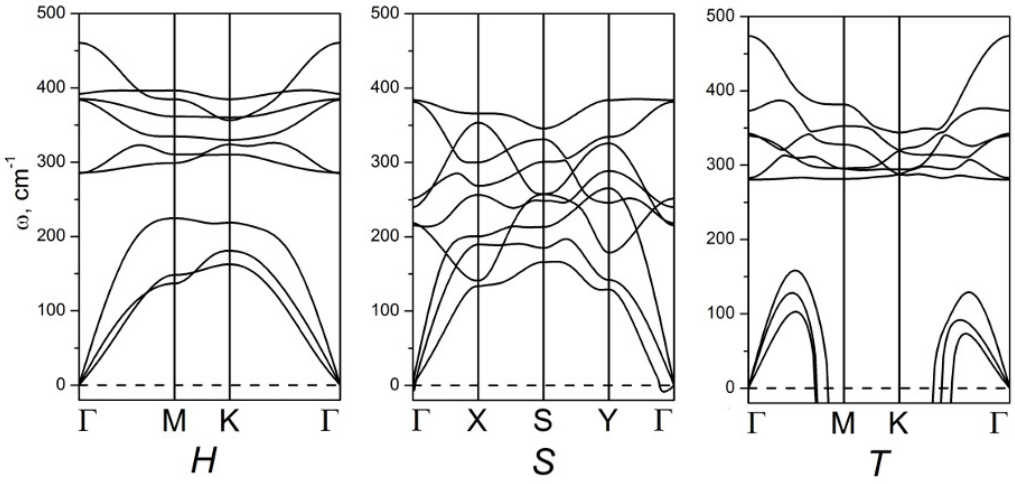

FIG. 3. Phonon band structures for H-, S- and T-layers of MoS_2. DFT calculations

degenerate Mo$4d_{xy,yz,xz}$ levels occupied with only two electrons and the unoccupied Mo$4d_z^2$ and Mo$4d_{x^2-y^2}$ levels. Such partial population is not beneficial, hence, stimulating the Jahn-Teller distortion of MoS_6 octahedron and the reconstruction of T-MoS_2 into a T′-MoS_2 phase. The splitting of the Mo$4d$ levels in cubic field of S-MoS_2 is opposite to the former: every Mo$4d_{z^2}$ and Mo$4d_{x^2-y^2}$ level is occupied by single electron, while Mo$4d_{xy,yz,xz}$ levels are unoccupied. Such electron configuration should be more resistant against the Jahn-Teller distortion, inhibiting a reconstruction and, possibly, prolonging the life-time of intermediate S-MoS_2 phase. To establish a dynamic stability of the intermediate the phonon band structures have been calculated for all three MoS_2 phases (Fig. 3). No imaginary frequency is obtained for the kinetically stable H-MoS_2. In contrast, a part of the Brillouin zone in the band structure of T-MoS_2 contains a deep "pocket" of negative dispersion curves, which should be attributed to kinetic instability of the compound. The phonon band structure of S-MoS_2 is reminiscent of that for H-MoS_2, yet, demonstrating the crossing of acoustic and optical modes. Here, a single phonon dispersion curve forms a small "pocket" of negative values at Γ-point. If not related to a numerical error of DFT calculation, it may refer to a long-living state.

3.2. Energy landscape of MoS_2 monolayer

The potential energy surfaces of H- and T-layers of MoS_2 have been calculated as the total energies relative to the total energy of H-layer at equilibrium. PES for T-layer lies mostly above PES of H-layer. Therefore, the former is mapped in the mirror a/a_0 coordinates for a better perception (Fig. 4). PES of H-layer is characterized by single global minimum and a continuous up-hill energy valley along the decrease of b lattice parameter (i.e. upon shrinkage along *armchair* direction of the layer). The valley egresses a plateau of energies corresponding to S-MoS_2 layer. PES of T-layer unveils the presence of three minima in accordance to the three known monoclinic T′-phases of MoS_2 [21], arising from the reconstructions of hexagonal T-layer. Therefore, in addition to kinetic instability, the perfect environment of Mo atoms within T-layer is not the most thermodynamically stable one among octahedral coordinations.

The minimal energy paths plotted on the PES's of H- and T-layers (closed circles, Fig. 4) demonstrate that the global minima are separated by an energy barrier. Though, these paths are not strictly aligned along a/a_0 coordinate and should be connected via the energy plateau of S-layer. The cross section of both PES's along these paths yields a classical picture of the transition between two states, requiring the passage of an energy barrier (Fig. 5). The energy barriers estimated using our brute-force scan of the MoS_2 energy map are equal to 1.66 eV for H→T transition, 0.83 eV and 1.06 eV for T→H and T′ →H transitions, respectively, which are in-between the values found from the DFT-based NEB approach [29] and from the DFT analysis of consecutive transition states [26]. However, the energy path established here demonstrates the existence of a flattened part of the energy barrier, related to the S-MoS_2 phase as the transition state.

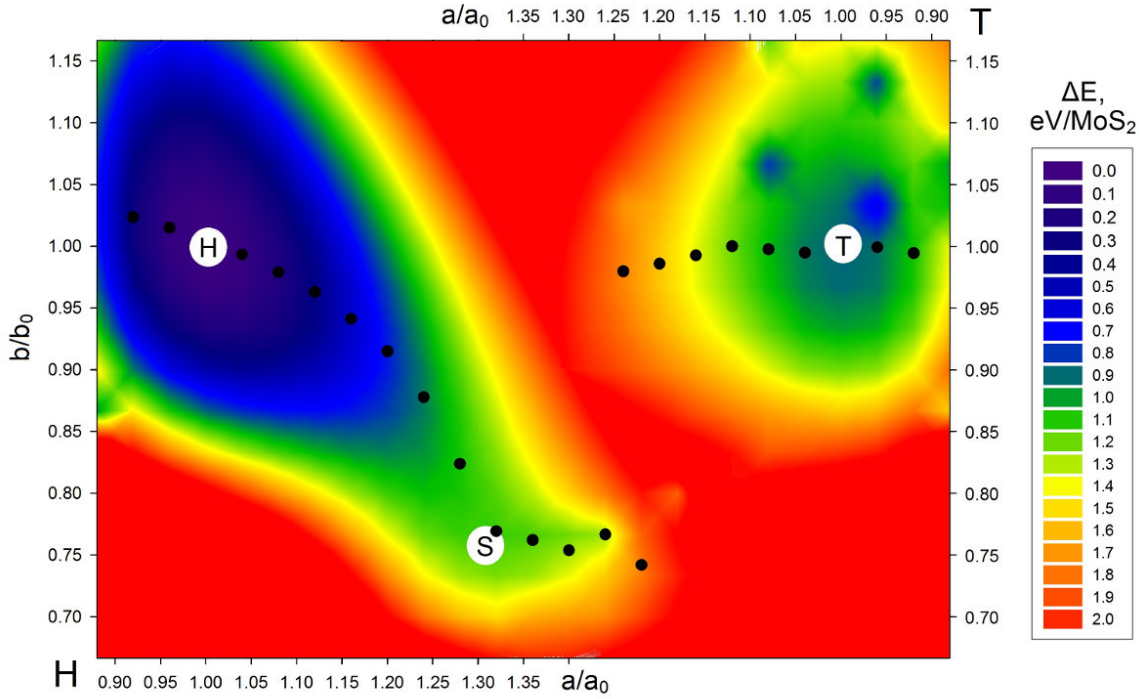

FIG. 4. Energy landscape depending on the lattice parameters for single MoS_2 layer unveils the equilibrium positions of H-, T- and S-phases (large open circles) and the minimal energy path between H and T phases (small closed circles). All energies ΔE are given relative to the most stable H-MoS_2 phase. DFT calculations

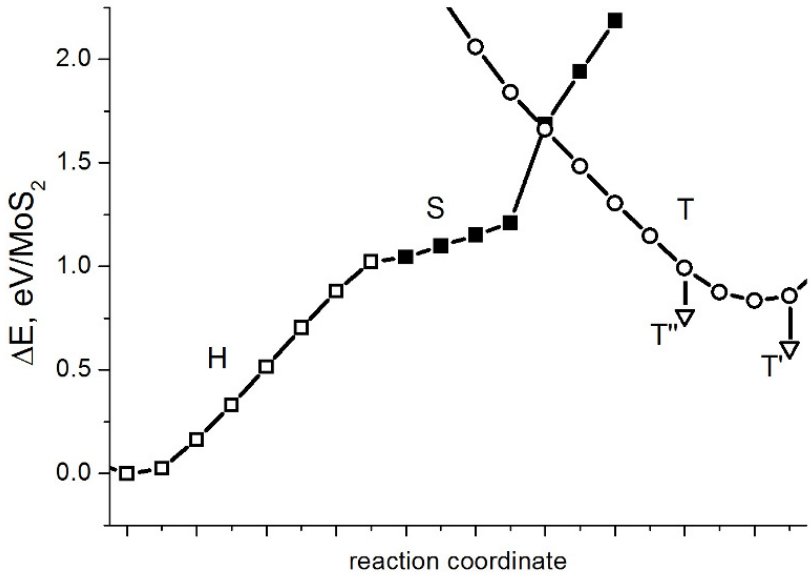

FIG. 5. Energy path during H↔T transition within a MoS_2 monolayer as derived from energy maps for both H- and T-phases (Fig. 4). ΔE values for hexagonal H- and T-phases are plotted using open squares and circles, for square S-phase using closed squares, for reconstructed monoclinic T′-, T″-phases using open triangles. DFT calculations

4. Summary

The full energy mapping has disclosed a complicated energy landscape for MoS_2 layer, including the field of intermediate state of square lattice S-MoS_2 between hexagonal lattices of H- and T-MoS_2. Hence, the phase transitions of MoS_2 between H- and T-phases or these in related MX_2 compounds may be not considered as a simple gliding of X planes within the molecular MX_2 layer. While the direct registration of S-MoS_2 remains an open problem, the traces of the manifestation of this state can be searched, analyzing the structural chemistry of two-dimensional MoS_2 booming in the recent years.

Several possible defect types have been visualized within the molecular layers of MoS_2 and related dichalcogenides: point vacanices within metal or chalcogen sublattices, point-like reconstructions and extended line defects, grain boundaries, doping or adsorbed atoms, which can affect the electronic, transport, optical properties of the compounds [38]. Much attention was paid to the grain boundaries and line defects. One of the scenarios of their origin is regarded to a merging of two growing nanoplates oriented relative to each other at a certain angle. According to [29], the grain boundary with the lowest formation energy in H-MoS_2 is the linear defect 4|4P consisting of four-membered cycles. A similar type of defect was observed at the junction of the H and T phases [30]. Other types of linear defects are also observed in the experiment, for example, squares and octagons or pentagons and heptagons among the hexagonal pattern of H-MoS_2 (4|8|4 and 5|7 defects) [31, 32].

However, the rise of these extended and perfectly organized grain boundaries in MoS_2 can also be related to the different tracks of relaxation of intermediate S-MoS_2 layer once appeared. A few examples are depicted on Fig. 6. The synchronous dissociation of cubic units MoS_8 within S-MoS_2 layer into distorted prisms MoS_6 gives a characteristic parquet-like pattern, which relaxes into perfect hexagonal H-MoS_2 layer (1, Fig. 6). The violations during such dissociation, e.g. due to a local mechanical strain or due to a substrate underneath, can finalize in various point-like or linear defects, including the grain boundaries observed in experiments [32, 33].

Therefore, irrespective the direct observation of intermediate S-MoS_2 layer, its model can serve as a useful tool for the construction of model defective MoS_2 layers.

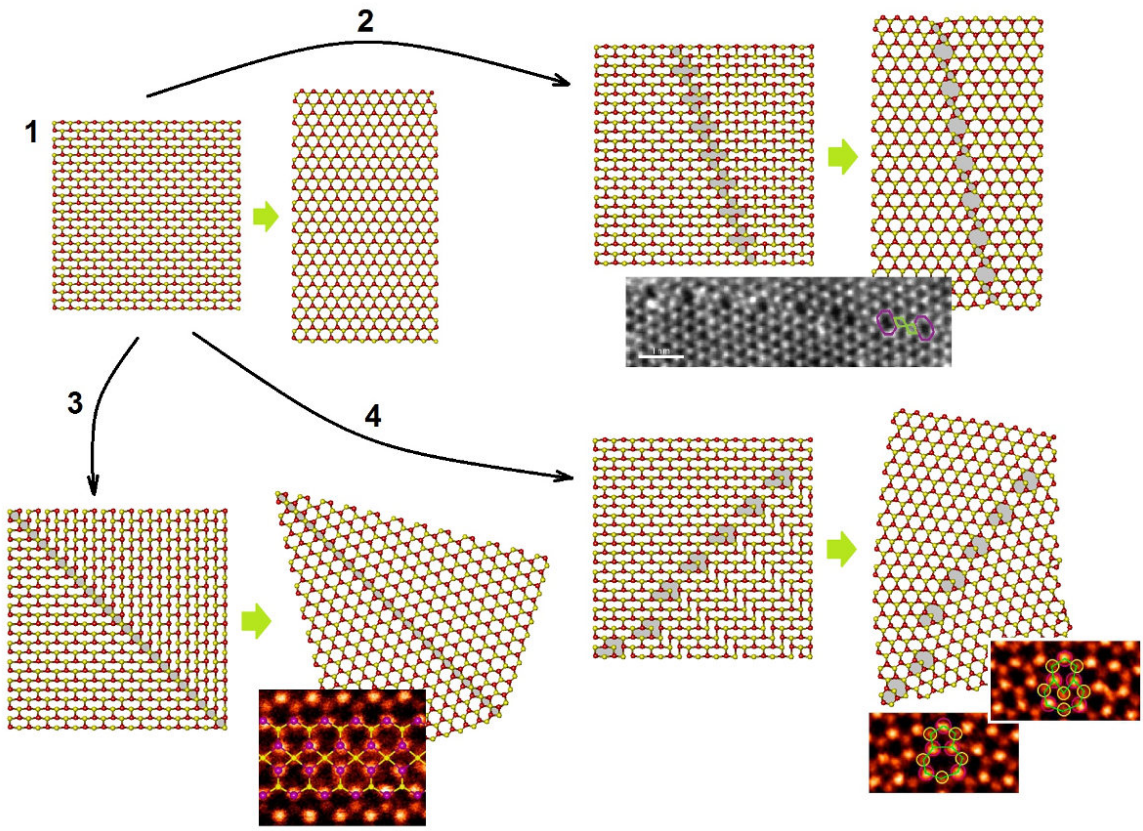

FIG. 6. The reconstruction tracks of S-MoS_2 layer can lead not only to the perfect H-MoS_2 layer (1), but to a wealth of line defects like these observed experimentally [32,33]: 4|4|8 grain boundary (2), 4|4 grain boundary (3), 6|8 and 5|7 grain boundaries (4) etc.

Acknowledgment

The work was performed within the order from Ministry of Science and Higher Education of the Russian Federation (No. 0397-2019-0003).

References

[1] Chen Z., Liu X., Liu Y., Gunsel S., Luo J. Ultrathin MoS_2 Nanosheets with Superior Extreme Pressure Property as Boundary Lubricants. *Sci. Rep.*, 2015, **5**, P. 12869.

[2] Radisavljevic B., Radenovic A., Brivio J., Giacometti V., Kis A. Single-layer MoS_2 transistors. *Nat. Nanotechnol.*, 2011, **6**, P. 147–150.

[3] Desai S.B., Madhvapathy S.R., Sachid A.B., Llinas J.P., Wang Q., Ahn G.H., Pitner G., Kim M.J., Bokor J., Hu C., Wong H.-S.P., Javey A. MoS_2 transistors with 1-nanometer gate lengths. *Science*, 2016, **354**(6308), P. 99–102.

[4] Guan Z., Lian C.-S., Hu S., Ni S., Li J., Duan W. Tunable Structural, Electronic, and Optical Properties of Layered Two-Dimensional C_2N and MoS_2 van der Waals Heterostructure as Photovoltaic Material. *J. Phys. Chem. C*, 2017, **121**(6), P. 3654–3660.

[5] Yore A.E., Smithe K.K.H., Jha S., Ray K., Pop E., Newaz A.K.M. Large array fabrication of high performance monolayer MoS_2 photodetectors. *Appl. Phys. Lett.*, 2017, **111**, P. 043110.

[6] Bergmann, H.; Czeska, B.; Haas, I.; Mohsin, B.; Wandner, K.-H. Gmelin Handbook of Inorganic and Organometallic Chemistry. *Springer-Verlag*, Berlin, 1992, Vol. B7.

[7] He Z., Que W. Molybdenum disulfide nanomaterials: Structures, properties, synthesis and recent progress on hydrogen evolution reaction. *Appl. Mater. Today*, 2016, **3**, P. 23–56.

[8] Cao Z-Y., Hu J.-W., Goncharov A.F., Chen X.-J. Nontrivial metallic state of MoS_2. *Phys. Rev. B*, 2018, **97**, P. 214519.

[9] Zhuang Y., Dai L., Wu L., Li H., Hu H., Liu K., Yang L., Pu C. Pressure-induced permanent metallization with reversible structural transition in molybdenum disulfide. *Appl. Phys. Lett.*, 2017, **110**, P. 122103.

[10] Liu Q., Li X., He Q., Khalil A., Liu D., Xiang T., Wu X., Song L. Gram-Scale Aqueous Synthesis of Stable Few-Layered 1T-MoS_2: Applications for Visible-Light-Driven Photocatalytic Hydrogen Evolution. *Small*, 2015, **11**, P. 5556–5564.

[11] Xie X., Kang J., Cao W., Chu J.H., Gong Y., Ajayan P.M., Banerjee K. Designing artificial 2D crystals with site and size controlled quantum dots. *Scientific Reports*, 2017, **7**, P. 9965.

[12] Enyashin A.N., Seifert G. Denisty-functional study of Li_xMoS_2 intercalates ($0 \leq x \leq 1$). *Comp. Theor. Chem.*, 2012, **999**, P. 13–20.

[13] Enyashin A.N., Yadgarov L., Houben L., Popov I., Weidenbach M., Tenne R., Bar-Sadan M., Seifert G. New Route for Stabilization of 1T-WS_2 and MoS_2 Phases. *J. Phys. Chem. C*, 2011, **115**, P. 24586–24591.

[14] Kim S., Song S., Park J., Yu H.S., Cho S., Kim D., Baik J., Choe D.-H., Chang K.J., Lee Y.H., Kim S.W., Yang H. Long-Range Lattice Engineering of $MoTe_2$ by 2D Electride. *Nano Lett.*, 2017, **17**(6), P. 3363–3368.

[15] Kvashnin D.G., Chernozatonskii L.A. Electronic and Transport Properties of Heterophase Compounds Based on MoS_2. *JETP LETTERS*, 2017, **105**(4), P. 250–254.

[16] Acerce M., Voiry D., Chhowalla M. Metallic 1T phase MoS_2 nanosheets as supercapacitor electrode materials. *Nat. Nanotechnol.*, 2015, **10**, P. 313–318.

[17] Jiang L., Zhang S., Kulinich S.A., Song X., Zhu J., Wang X., Zeng H. Optimizing Hybridization of 1T and 2H Phases in MoS_2 Monolayers to Improve Capacitances of Supercapacitors. *Mater. Res. Lett.*, 2015, **3**, P. 177–183.

[18] Cheng P., Sun K., Hu Y.H. Memristive Behavior and Ideal Memristor of 1T Phase MoS_2 Nanosheets. *Nano Lett.*, 2016, **16**(1), P. 572–576.

[19] Cheng P., Sun K., Hu Y.H. Mechanically-induced Reverse Phase Transformation of MoS_2 from Stable 2H to Metastable 1T and Its Memristive Behavior. *RSC Adv.*, 2016, **6**, P. 65691–65697.

[20] Sun T., Zhang H., Wang X., Liu J., Xiao C., Nanayakkara S.U., Blackburn J.L., Mirkin M.V., Miller E.M. Nanoscale mapping of hydrogen evolution on metallic and semiconducting MoS_2 nanosheets. *Nanoscale Horiz.*, 2019.

[21] Heising J., Kanatzidis M.G. Structure of Restacked MoS_2 and WS_2 Elucidated by Electron Crystallography. *J. Am. Chem. Soc.*, 1999, **121**, P. 638–643.

[22] Zhuang H.L., Johannes M.D., Singh A.K., Hennig R.G. Doping-controlled phase transitions in single-layer MoS_2. *Phys. Rew. B*, 2017, **96**, P. 165305.

[23] Wang Z.F., Jin K.-H., Liu F. Computational design of two-dimensional topological materials. *WIREs Comput. Mol. Sci.*, 2017, **7**, P. e1304.

[24] Eda G., Fujita T., Yamaguchi H., Voiry D., Chen M., Chhowalla M. Coherent Atomic and Electronic Heterostructures of Single-Layer MoS_2. *ACS Nano*, 2012, **6**, P. 7311–7317.

[25] Eda G., Yamaguchi H., Voiry D., Fujita T., Chen M., Chhowalla M. Photoluminescence from Chemically Exfoliated MoS_2. *NanoLett.*, 2011, **11**, P. 5111–5116.

[26] Ryzhikov M.R., Slepkov V.A., Kozlova S.G., Gabuda S.P., Fedorov V.E. Solid-State Reaction as a Mechanism of 1T$\leftrightarrow$2H Transformation in MoS_2 Monolayers. *J. Comput. Chem.*, 2015, **36**, P. 2131–2134.

[27] Gao G., Jiao Y., Ma F., Jiao Y., Waclawik E., Du A. Charge Mediated Semiconducting-to-Metallic Phase Transition in Molybdenum Disulfide Monolayer and Hydrogen Evolution Reaction in New 1T′ Phase. *J. Phys. Chem. C*, 2015, **119**(23), P. 13124–13128.

[28] Lin Y.-C., Dumcenco D.O., Huang Y.-S., Suenaga K. Atomic mechanism of the semiconducting-to-metallic phase transition in single-layered MoS_2. *Nat. Nanotechnol.*, 2014, **9**, P. 391–396.

[29] Guo Y., Sun D., Ouyang B., Raja A., Song J., Heinz T.F., Brus L.E. Probing the Dynamics of the Metallic-to-Semiconducting Structural Phase Transformation in MoS_2 Crystals. *Nano Lett.*, 2015, **15**, P. 5081–5088.

[30] Komsa H.-P., Krasheninnikov A.V. Engineering the Electronic Properties of Two-Dimensional Transition Metal Dichalcogenides by Introducing Mirror Twin Boundaries. *Adv. Electron. Mater.*, 2017, **3**, P. 1600468.

[31] Lin Y.-C., Yeh C.-H., Lin H.-C., Siao M.-D., Liu Z., Nakajima H., Okazaki T., Chou M.-Y., Suenaga K., Chiu P.-W. Stable 1T WS_2 monolayer and its junctions: growth and atomic structures. *ACS Nano*, 2019, **12**, P. 12080–12088.

[32] Najmaei S., Liu Z., Zhou W., Zou X., Shi G., Lei S., Yakobson B.I., Idrobo J.-C., Ajayan P.M., Lou J. Vapour phase growth and grain boundary structure of molybdenum disulphide atomic layers. *Nat. Mater.*, 2013, **12**, P. 754.

[33] van der Zande A.M., Huang P.Y., Chenet D.A., Berkelbach T.C., You Y., Lee G.-H., Heinz T.F., Reichman D.R., Muller D.A., Hone J.C. Grains and grain boundaries in highly crystalline monolayer molybdenum disulphide. *Nat. Mater.*, 2013, **12**, P. 554–561.

[34] Ghorbani-Asl M., Enyashin A.N., Kuc A., Seifert G., Heine T. Defect-induced conductivity anisotropy in MoS_2 monolayers. *Phys. Rev. B*, 2013, **88**, P. 245440.

[35] Taha D., Mkhonta S.K., Elder K.R., Huang Z.-F. Grain Boundary Structures and Collective Dynamics of Inversion Domains in Binary Two-Dimensional Materials. *Phys. Rev. Lett.*, 2017, **118**, P. 255501.

[36] Soler J.M., Artacho E., Gale J.D., Garcia A., Junquera J., Ordejon P., Sanchez-Portal D. The SIESTA method for *ab initio* order-N materials simulation. *J. Phys. Condensed Matter*, 2002, **14**, P. 2745–2779.

[37] Kan M., Wang J.Y., Li X.W., Zhang S.H., Li Y.W., Kawazoe Y., Sun Q., Jena P. Structures and Phase Transition of a MoS_2 Monolayer. *J. Phys. Chem. C*, 2014, **118**, P. 1515–1522.

[38] Enyashin A.N., Seifert G. Electronic properties of MoS_2 monolayer and related structures. *Nanosystems: physics, chemistry, mathematics*, 2014, **5**, P. 517–539.

NANOSYSTEMS: PHYSICS, CHEMISTRY, MATHEMATICS, 2019, 10 (4), P. 428–437

The minimum size of oxide nanocrystals: phenomenological thermodynamic vs crystal-chemical approaches

O. V. Almjasheva[1,2], N. A. Lomanova[2], V. I. Popkov[2], O. V. Proskurina[2,3], E. A. Tugova[2], V. V. Gusarov[2]

[1]Saint Petersburg Electrotechnical University "LETI", St. Petersburg, 197376 Russia
[2]Ioffe Institute, Politekhnicheskaya St. 26, St. Petersburg, 194021, Russia
[3]St. Petersburg State Institute of Technology, Moskovsky Pr., 26, St. Petersburg, 190013, Russia

almjasheva@mail.ru, nat-lomanova@yandex.ru, vadim.i.popkov@technolog.edu.ru, proskurinaov@mail.ru, katugova@inbox.ru, victor.v.gusarov@gmail.com

PACS 61.46.+w, 64.60.Qb **DOI 10.17586/2220-8054-2019-10-4-428-437**

The minimum crystallite size in a group of oxides has been analyzed as a function of their synthesis conditions, critical nucleus size and the crystal structure parameters. Nanocrystals were synthesized by solution combustion, hydrothermal synthesis and heat treatment in air of the precipitated hydroxides. Aluminum and iron oxides, titania and zirconia, cobalt ferrite, $AFeO_3$ ferrites (A = Bi, RE), Aurivillius phases $Bi_{m+1}Ti_3Fe_{m-3}O_{3m+3}$ ($m = 3 - 9$), as well as solid solutions based on these phases were chosen as the objects of the study. The presence of a correlation between the crystalline oxide unit cell parameters and the synthesized crystals minimum size is shown. A conclusion was made about the impossibility to use only the thermodynamic concept of the critical nucleus for determining the minimum possible particle size of a new phase in some cases of oxide nanocrystals synthesis. The paper demonstrates a necessity to use crystal-chemical criteria that complement the methods of phenomenological thermodynamics and kinetics for determining the minimum possible particle size of the resulting crystalline oxide phases synthesized under the considered conditions.

Keywords: nucleation, nanocrystals, oxides, crystal structure, soft chemistry, solution combustion.

Received: 3 December 2018

Revised: 1 August 2019

1. Introduction

Though the methods based on phenomenological thermodynamics and on macrokinetic models of phase formation processes [1–22] are widely used for determining the minimum limit size of crystallites [1–22], these approaches encounter a series of problems when describing the formation of nanocrystals. Some possibilities to expand these methods are based on determining how thermodynamic model parameters, in particular, the specific surface energy, depend on particle size [23–30]. Another possibility is to describe the features of nucleation taking into account the presence in the reaction system of the variously shaped and sized subcritical clusters, which determine the high rate of stable nanoparticles formation in a new phase [10, 31–48]. However, these approaches do not solve all the problems of describing nucleation processes in the case of a crystalline phase formation. For example, at certain ratios of specific surface energy values for the new phase particles and the Gibbs energy of their formation, cases are possible when the calculated size of the crystal critical nucleus is smaller or comparable with the size of its unit cell. Such cases are presented, e.g., in [47]. Since the unit cell of a crystal is its minimum structural element, the translation of which builds a crystalline particle, the above hypothetical cases cannot exist in reality, as the very principle of a crystalline body formation will be violated. Consequently, the minimum size of the forming particles in the case of crystallite formation should be determined not only by the thermodynamically-determined critical nuclei size, but also by other reasons. For example, the minimum size of crystals may be related to the dependence of the crystal structure stability on the number of the minimum building blocks in the crystal lattice, i.e., on the elementary cells that form the crystalline particles, and also, apparently, on the crystalline particles morphology, and on the unit cell composition and structure. Experimental determination of the crystalline particles minimum size dependence on these factors is complicated by a number of issues. First of all, it is not always possible to calculate the values of the critical nucleus size for particular phase formation conditions. This means that it is impossible to attribute the experimentally-obtained dimensions of the synthesized crystal particles to a factor associated with the nucleation process, or to a factor determined by the dependence of the forming phase crystalline structure stability on the number of unit cells contained by this crystalline particle, and on their crystal-chemical features. On the other hand, as a rule, it is very difficult to experimentally register the minimum possible values of the crystalline particle size due to the rapid growth of nanoscale crystals during phase formation [49–52], which depends on the conditions of their synthesis [38, 42, 43, 46, 52–59]. Crystal growth can be reduced by using special synthetic methods, which include, in particular, soft chemistry methods,

when synthesis proceeds at relatively low temperatures [36–48, 52–59]. Another group of methods that includes, for example, solution combustion, self-propagating high-temperature synthesis (SHS), autocatalytic and other fast solid-state reactions, is based on the use of rapid synthesis [49–51, 60–71]. Crystal growth can often be restricted by using nano- and microreactors, or synthesis methods that use spatial constraints [63, 64, 72–82].

The interest in determining the minimum possible size of crystals is determined by the possibility of creating promising functional and structural nanomaterials based on such crystalline particles [83–87]. One such widely used class of nanomaterials is represented by oxide nanocrystalline materials [35–58, 83–87]. At the same time, literature offers no systematic analysis of the influence of chemical composition, features of the crystal structure, and of the methods and conditions of the nanocrystals synthesis on the possible limit values of their size.

The listed reasons show the relevance for the problem of determining the effect of methods and synthetic conditions, and of thermodynamic and crystal-chemical characteristics on the production of oxide nanocrystals with the smallest possible size.

2. Methods

2.1. Calculations and modeling

The sizes of critical nuclei were calculated for the methods of solid phase synthesis that were used in the work, and for the cases when it was possible to obtain information on the specific surface energy of the particles and on thermodynamic properties of the phases required for calculating the Gibbs energy of the corresponding reactions. The data for thermodynamic properties of the phases were taken mainly from the databases listing the thermodynamic properties of substances [88, 89]. In some cases, when the necessary experimental information was missing, approximate methods of modeling and calculating thermodynamic properties were used. The use of such calculations is described in [47]. In order to compare the experimental and calculated data, the critical nuclei sizes were calculated for the phase formation conditions identical to the actual conditions of nanocrystals synthesis.

2.2. Experiment

Nanocrystalline oxide particles were synthesized by three main methods, which make it possible to use the data from [33, 35–48, 60–69, 90, 91] and obtain nanocrystals of relatively small size and narrow size distribution. The methods of precipitated hydroxides decomposition under hydrothermal conditions and thermal treatment in air were used as soft chemistry methods for synthesizing oxide nanocrystals. The other method for synthesizing oxide nanocrystals was solution combustion. The conditions of nanoparticle synthesis by these methods have been previously described [33, 35–48, 63–66, 77–80, 92–94]. In some cases, the growth of nanocrystals was retarded by applying techniques based on the organization and self-organization of spatial constraints that prevent mass transfer and, consequently, the growth of nanocrystals during the synthesis [63, 72, 77–80].

Crystal sizes in the synthesized phases were determined mainly using the data on the width of the X-ray diffraction lines. The calculations were carried out mainly using the Scherrer formula and assuming the isometric form of crystallites and narrow crystallite size distribution. The possibility of using such calculations for determining the size of crystallites in the considered cases was based on the coincidence of the crystal size data obtained by different methods when analyzing a number of oxide nanocrystals synthesized under the conditions similar to the considered ones [77, 79, 95].

3. Results and discussion

Table 1 presents the calculated values of the critical nucleus size (d_{cr}) of some oxides for different conditions of their formation. The maximum values of the unit cells parameters ($L_{\max}$) of these crystalline phases are given for comparison.

It should be noted that under the considered nucleation conditions, d_{cr} exceed $L_{\max}$ by almost 10-fold for the phases based on zirconia, α-Al_2O_3 and γ-Al_2O_3, while for other compounds, this difference is less significant. For example, in some cases of Cr_2O_3 formation, d_{cr} exceeds $L_{\max}$ only by 2-4-fold. The d_{cr} values calculated for some conditions of α-Fe_2O_3, γ-Fe_2O_3, and TiO_2 (rutile) formation are comparable with those of $L_{\max}$. This result raises great doubts about the legitimacy of using the thermodynamic approach for estimating the minimum values of the dimensions of a stable crystalline phase, since it is impossible to imagine a crystalline phase consisting of a single unit cell. The calculation of d_{cr} for the TiO_2 (anatase) formation yields a result that is absolutely unrealistic for crystalline phases. In this case, $d_{cr} < L_{\max}$ (see Table 1), but the size of a crystalline particle cannot be smaller than the minimum translation unit that forms the crystal, which is the unit cell of the crystal. An analysis of the performed calculations of the critical nucleus size showed that in the case of crystalline phases, the d_{cr} value cannot be regarded as an estimate of the minimum possible size of the forming nanocrystal.

TABLE 1. Calculated values of the critical nucleus size depending on the synthesis conditions

Substance	$L_{\max}$, **nm**	d_{cr}, **nm**	**Synthesis conditions**	
			Initial substance	T,°C / P, **atm**
m-ZrO_2	0.531 [PDF 01-089-9066]	5 – 9 – 40	Amorphous $ZrO(OH)_2$	250 / 1 – 100 – 600
		5 – 10		300 – 200 / 700
t-ZrO_2	0.527 [PDF 00-042-1164]	5 – 12 – 35		250 / 1 – 100 – 300
		8 – 30		300 – 200 / 700
c-ZrO_2	0.509 [PDF 01-072-2742]	8 – 45		250 / 1 – 100
		10 – 40		300 – 200 / 700
TiO_2-rutile	0.459 [PDF 01-089-4202]	0.44 – 0.65 – 0.8	Amorphous $TiO_2 \cdot nH_2O$	375 – 120 – 25 / 1
		0.46 – 1.0 – 0.85		575 – 120 – 25 / 1000
TiO_2-anatase	0.951 [PDF 01-089-4203]	0.5 – 0.6		120 – 25 / 1
		0.6 – 0.75		120 – 25 / 1000
α-Al_2O_3	1.299 [PDF 01-089-7717]	8 – 40	γ-AlOOH	300 – 200 / 20
		5 – 35		500 – 300 / 700
		18 – 50	α-AlOOH	500 – 450 / 20
		30 – 75		500 – 475 / 700
γ-Al_2O_3	0.794 [PDF 01-076-4179]	5 – 40	γ-AlOOH	500 – 300 / 20
		10 – 40		500 – 400 / 700
		10 – 55	α-AlOOH	450 – 350 / 20
α-Fe_2O_3	1.375 [PDF 01-087-1166]	1 – 25	γ-FeOOH	500 – 100 / 1
		2.5 – 15		500 – 250 / 100
γ-Fe_2O_3	2.501 [PDF 00-013-0458]	2 – 25		500 – 200 / 1
		3 – 15		600 – 400 / 100
Cr_2O_3	1.359 [PDF 01-082-1484]	3 – 10	γ-CrOOH	750 – 550 / 1
		5 – 20		850 – 750 / 100

Table 2 presents the experimentally determined sizes (d) of oxide nanocrystals synthesized under different conditions. An analysis of the data in Table 2 shows that $d \gg L_{\max}$ for all the considered methods of synthesis.

Table 2: Nanocrystal sizes in some simple and complex oxides

Composition	$L_{\max}$**, nm**	***d*, nm**
m-ZrO_2	0.531 [PDF 01-089-9066]	15–25*
t-ZrO_2	0.527 [PDF 00-042-1164]	10–30*; 5-10*
c-ZrO_2	0.509 [PDF 01-072-2742]	4–20*(solid solutions with Y_2O_3)
TiO_2-rutile	0.459 [PDF 01-089-4202]	∼4 [96]; ∼30 [97]; ∼10*; 68–80 [98]
TiO_2-anatase	0.951 [PDF 01-089-4203]	7–45*; 5–12 [99]; 10–50 [100]; 10–20 [101],5–10*; 20–27 [98]
TiO_2-brookite	0.918 [PDF 03-065-2448]	∼10*; ∼50 [102]; ∼20 [103]
α-CeO_2	0.539 [PDF 01-073-6318]	6–31 [104]; 6–8 [105]
α-Al_2O_3	1.299 [PDF 01-089-7717]	60–100*, 10 [106]
γ-Al_2O_3	0.794 [PDF 01-076-4179]	16–13 [107]
η-Al_2O_3	0.791[ICSD 28260]	5 [108]
α-Fe_2O_3	1.375 [PDF 01-087-1166]	∼30 (160°C, 15 MPa, 2 h.); 11–32 [104]; 13–14 [105]; 57 [109, 110]; 27–30 [41]
γ-Fe_2O_3	2.501 [PDF 00-013-0458]	6-8 [111]
Cr_2O_3	1.359 [PDF 01-082-1484]	25*
α-Y_2O_3	1.061 [PDF 01-089-5591]	18–20 [41]
$CoFe_2O_4$	0.839 [PDF 01-078-4451]	6–50*; 7–15*; ∼10*
$BiFeO_3$	1.388 [PDF 01-077-9630]	20*(450°C); ∼100*(850°C); 71–72*(550°C); 21–70 [112]; 23 [113]; 26 [113]; 41–75 [114] ; 38 [115] ; 17 [77]
$NdFeO_3$	0.776 [PDF 01-089-6644]	7*; 20*; 40*;75 [116]; 20 [117]; 45 – 75 [118]; 42 [119]; 50 (TEM), 36.8 (XRD) [120]; 88 [121]; 50 [122]; 30–50 [123]; 42±1(XRD), 44±1 (SEM) [124]; 35-45 (HRTEM), 12 (XRD) [125]
o-$YFeO_3$	0.760 [PDF 01-089-2609]	50–70 [41]; 30–52 [126, 127]; 25–35 [45, 128]; 17–40 [65]
o-$LaFeO_3$	0.785 [PDF 01-076-7897]	16–37 [129]
o-$GdFeO_3$	0.768 [PDF 00-047-0067]	18–36 [129]; 21–48 [130]
o-$CeFeO_3$	0.781 [PDF 00-022-0166]	32–51 [104]
o-$EuFeO_3$	0.769 [PDF 01-074-1475]	28–46 [132]
o-$HoFeO_3$	0.761 [PDF 00-046-0115]	20–40 [132]

Continued on next page

Table 2: continued from previous page

Composition	$L_{\max}$, **nm**	d, **nm**
h-$YFeO_3$	1.172 [PDF 00-048-0529]	6–11 [63, 64]; 5–8 [65]
h-$HoFeO_3$	1.172*	5–10*
$Bi_{1-x}Ca_xFeO_{3-\delta}$ ($x = 0.1$–0.56)	—	20–40*(550°C)
$Bi_{1-x}Sr_xFeO_{3-\delta}$ ($x = 0.1$–0.5)	—	50±2*(550°C)
$Bi_4Ti_3O_{12}$ ($m = 3$)	3.28 [PDF 01-089-7500]	35*(450°C); 60*(800°C); 21 [133]; 20–25 [134], 40–70 [134]; 57 [135]
$Bi_5FeTi_3O_{15}$ ($m = 4$)	4.13 [PDF 00-021-0818]	30*(450°C); 82*(800°C); 18–80 [136]
$Bi_6Fe_2Ti_3O_{18}$ ($m = 5$)	4.9 [PDF 01-075-8378]	36*(450°C); 80*(800°C)
$Bi_7Fe_3Ti_3O_{21}$ ($m = 6$)	5.7 [PDF 01-075-8067]	30*(450°C); 63*(800°C)
$Bi_8Fe_4Ti_3O_{24}$ ($m = 7$)	6.5*	28*(450°C); 57*(800°C)
$Bi_9Fe_5Ti_3O_{27}$ ($m = 8$)	7.6 [PDF 00-021-0100]	30*(450°C); 56*(800°C)
$Bi_{10}Fe_6Ti_3O_{30}$ ($m = 9$)	8.1*	24*(450°C); 54*(800°C)
$Bi_xNd_{1-x}FeO_3$ ($x = 0.2$)	0.778*	30*(600°C)
$Bi_xNd_{1-x}FeO_3$ ($x = 0.4$)	0.779*	40*(600°C)
$Bi_xNd_{1-x}FeO_3$ ($x = 0.6$)	0.781 [PDF 00-061-0719]	50*(600°C)
$Bi_xNd_{1-x}FeO_3$ ($x = 0.7$)	0.783*	50*(600°C)
$Bi_xNd_{1-x}FeO_3$ ($x = 0.75$)	0.784*	40*(600°C)
$Bi_xNd_{1-x}FeO_3$ ($x = 0.8$)	1.118*	40*(600°C)
$Bi_xNd_{1-x}FeO_3$ ($x = 0.85$)	1.266 [48]	23 [137]
$Bi_xNd_{1-x}FeO_3$ ($x = 0.9$)	1.381 [48]	33 [137]
$Bi_xNd_{1-x}FeO_3$ ($x = 0.95$)	1.386 [48]	50 [137]
$Bi_xNd_{1-x}FeO_3$ ($x = 1$)	1.386 [48]	74 [137]
$Bi_xNd_{1-x}FeO_3$ ($x = 0.85$)	0.837 [49]	19 [138]
$Bi_xNd_{1-x}FeO_3$ ($x = 0.9$)	1.182 [49]	19 [138]
$Bi_xNd_{1-x}FeO_3$ ($x = 0.95$)	1.373 [49]	24 [138]
$Bi_xNd_{1-x}FeO_3$ ($x = 1$)	1.383 [49]	25 [138]

Note: *– results of the present work; conditions of nanoparticles synthesis, specifics of their composition or the method for crystal size determination are given in parentheses.

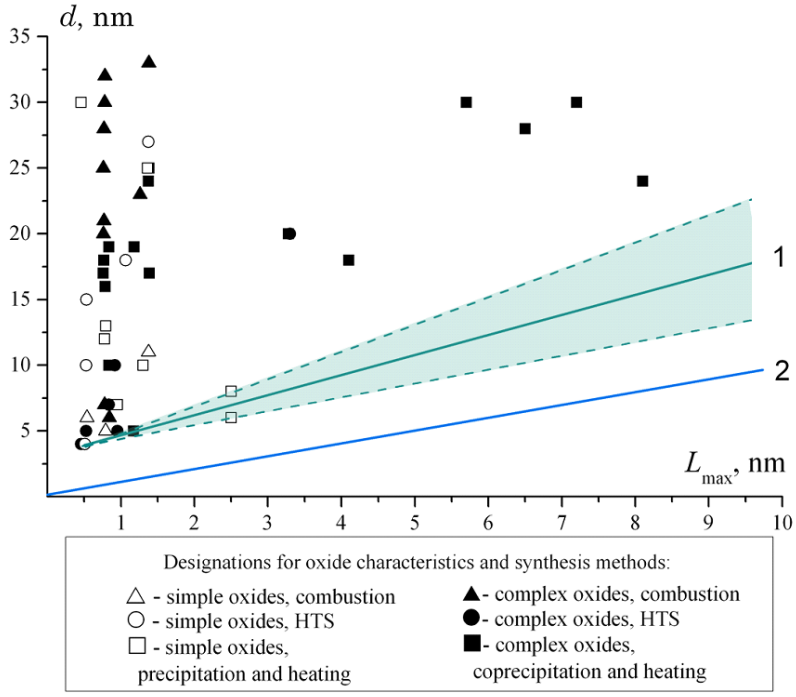

FIG. 1. Dependence of crystallite sizes in synthesized oxide phases (d) on the maximum value of the crystal unit cell parameter ($L_{\max}$) 1 – dependence of the minimum crystal size on the maximum values of the corresponding phase unit cell parameter ($d_{cryst}(L_{\max})$); 2 – $L_{\max} = L_{\max}$ line

The data presented in Fig. 1 show that even the minimal experimentally-obtained values of d (straight line 1) are approximately 3.2 nm above the $L_{\max}$ values (straight line 2).

It should be noted that smaller values of d can more often be achieved in an experiment when synthesizing simple oxides. In this case, the smallest d values for double oxides are observed, as a rule, firstly, when $L_{\max}$ values for these oxides are small, and secondly, when the chosen synthesis conditions limit the mass transfer in the reaction system (see references in Table 2). Mass transfer limitation was achieved either by the synthesis conditions that ensure the presence in the reaction system of structural precursors of the forming crystalline phases and low rates of components diffusion (see, e.g., [37, 45, 77–80]), or by the formation of spatial constraints that inhibit the growth of the formed nanocrystals (see, e.g., [48, 63–65, 72, 139]).

It can be concluded from the data in Table 2 that an increase in the temperature and duration of the synthesis in the absence of spatial limitations in the reaction system leads to a multiple increase in the size of the crystals.

An analysis of experimental and theoretical data demonstrated limitations of the thermodynamic concept of the critical nucleus for estimating the minimum possible size of the synthesized crystalline phases. A comparison of the experimental values of d with the calculated d_{cr} and with the empirical $d_{cryst}(L_{\max})$ dependence shown in Fig. 1 (line 1), allows a conclusion that the minimum size of the synthesized crystals can be determined from the relation:

$$d_{\min} = \max\{d_{cr}, d_{cryst}(L_{\max})\}.$$

The uncertain position of the $d_{cryst}(L_{\max})$ dependence (Fig. 1) seems to be associated with a simplified representation of this dependence as a function of only $L_{\max}$. It can be expected that, depending on the morphology and mechanism of nanocrystals formation, the $d_{\min}$ values will be determined by different parameters of the crystal unit cell. For example, the $d_{\min}$ value may be inconsistent with the proposed dependence in the case of the epitaxial junction of the forming crystal with the crystal matrix. In particular, such cases are possible when the formation of thin layers occurs through the atomic layer deposition (ALD), as was observed in [140].

4. Conclusions

The study has shown that the minimum size of the synthesized crystals can be determined by the critical nucleus size, and also be a function of the crystal unit cell parameters. It is possible to experimentally obtain small size nanocrystals by limiting their growth, which is determined by mass transfer. This can be effectively achieved by

increasing the nucleation rate, or by applying soft chemistry methods for the synthesis, when the process temperature and, therefore, the diffusion rate, are low. Also, it is possible to use synthesis methods, in which spatial constraints (barriers) that form in reaction systems slow down the mass transfer of components to the products of reaction.

Acknowledgements

The present work was supported by the Russian Science Foundation (Project No. 16-13-10252).

References

[1] Tammann G. *Aggregatzustände. Zustandsänderungen der Materie in Abhängikeit von Druck und Temperatur Verlag von Leopold Voss.*, Leipzig, 1922, 237 p.
[2] Volmer M. *Kinetik der Phasenbildung*. T. Steinkopff, Dresden-Leipzig, 1939, 126 p.
[3] Frenkel J. A general theory of heterophase fluctuations and pretransition phenomena. *J. Chem. Phys.*, 1939, **7** (7), P. 538–546.
[4] Zel'dovch Ya. On the theory of new phase formation. Cavitation. *ZhETF*, 1942, **12** (11/12), P. 525–538, (in Russian).
[5] Pound G.M., La Mer V.K. Kinetics of crystalline nucleus formation in supercooled liquid tin. *J. Amer. Chem. Soc.*, 1952, **74**, P. 2323–2332.
[6] Cahn J.W., Hilliard J.E. Free energy of a nonuniform system. III. Nucleation in a two-component incompressible fluid. *J. Chem. Phys.*, 1959, **31** (3), P. 688–700.
[7] Lothe J., Pound G.M. Reconsideration of nucleation theory. *J. Chem. Phys.*, 1962, **36** (8), P. 2080–2085.
[8] Abraham F.F., Pound G.M. Re-examination of homogeneous nucleation theory: statistical thermodynamics aspects. *J. Chem. Phys.*, 1968, **48** (2), P. 732–740.
[9] Reiss H. Treatment of droplike clusters by means of the classical phase integral in nucleation theory. *J. Stat. Phys.*, 1970, **2** (1), P. 83–104.
[10] Kuni F.M., Rusanov A.I. Statistical theory of aggregative equilibrium. *Theor. Math. Phys.*, 1970, **2** (2), P. 192–206.
[11] Blander M., Katz J.L. The thermodynamics of cluster formation in nucleation theory. *J. Stat. Phys.*, 1972, **4** (1), P. 55–59.
[12] Katz J.L., Donohue M.D. A kinetic approach to homogeneous nucleation theory. *Adv. Chem. Phys.*, 1979, **40**, P. 137.
[13] Slezov V.V., Sagalovich V.V. Diffusive decomposition of solid solutions. *Sov. Phys. Usp.*, 1987, **30** (1), P. 23–45.
[14] Ruth V., Hirth J.P., Pound G.M. On the theory of homogeneous nucleation and spinodal decomposition in condensation from the vapor phase. *J. Chem. Phys.*, 1988, **88** (11), P. 7079–7087.
[15] Brener E.A., Marchenko V.I., Formation of nucleation centers in a crystal. *JETP Lett.*, 1992, **56** (7), P. 368–372.
[16] Oxtoby D.W. Nucleation of first-order phase transitions. *Acc. Chem. Res.*, 1998, **31** (2), P. 91–97.
[17] Antonov N.M., Popov I.Yu., Gusarov V.V. Model of spinodal decomposition of phases under hyperbolic diffusion. *Phys. Solid State.*, 1999, **41** (5), P. 824–826.
[18] Gorbachev Yu.E., Nikitin I.S. Evolution of cluster size distribution during nucleation with rapidly changing dynamic gas processes. *Tech. Phys.*, 2000, **45** (12), P. 1538–1548.
[19] Oxtoby D.W. Phase transitions: Catching crystals at birth. *Nature*, 2000, **406**, P. 464–465.
[20] Kuni F.M., Shchekin A.K., Grinin A.P. Theory of heterogeneous nucleation for vapor undergoing a gradual metastable state formation. *Phys. Usp.*, 2001, **44** (4), P. 331–370.
[21] Xu D., Johnson W.L. Geometric model for the critical-value problem of nucleation phenomena containing the size effect of nucleating agent. *Phys. Rev. B*, 2005, **72**, P. 052101.
[22] Kukushkin S.A., Osipov A.V. First-order phase transition through an intermediate state. *Phys. Solid State*, 2014, 56 (4), P. 792–800.
[23] Tolman R.C. The effect of droplet size on surface tension. *J. Chem. Phys.*, 1949, **17** (3), P. 333–337.
[24] Rusanov A.I. Phase equilibria and surface phenomena. Khimiya, Leningrad, 1967, 388 p. (in Russian); German edition: Rusanov A.I. Phasengleichgewichte und Grenzflächenerscheinungen. Akademie-Verlag, Berlin, 1978, 465 p.
[25] Bykov T.V., Shchekin A.K. Surface tension, tolman length, and effective rigidity constant in the surface layer of a drop with a large radius of curvature. *Inorganic Materials*, 1999, **35** (6), P. 641–644.
[26] Gordon P.V., Kukushkin S.A., Osipov A.V. Perturbation methods in the kinetics of nanocluster growth. *Phys. Solid State.*, 2002, **44** (11), P. 2175–2180.
[27] Samsonov V.M., Bazulev A.N., Sdobnyakov N.Y. Rusanov's linear formula for the surface tension of small objects. *Doklady Physical Chemistry*, 2003, **389** (1–3), P. 83–85.
[28] Magomedov M.N. Dependence of the surface energy on the size and shape of a nanocrystal. *Phys. Solid State*, 2004, **46** (5), P. 954–968.
[29] Rekhviashvili S.Sh., Kishtikova E.V. On the size dependence of the surface tension. *Tech. Phys.*, 2011, **56** (1), P. 143–146.
[30] Kukushkin S.A., Osipov O.V. New phase formation on solid surfaces and thin film condensation. *Progress in surface science*, 1996, 5 (1), P. 1–107
[31] Kuni F.M., Rusanov A.I. The homogeneous nucleation theory and the fluctuation of the center of mass of a drop. *Phys. Letters. A*, 1969, **29** (6), P. 337–338.
[32] Kligman F.I., Rusanov A.I. On the thermodynamic equilibrium states of disperse systems with suspended particles. *Koll. Zh.*, 1977, **39** (1), P. 44–47. (in Russian)
[33] Pozhidaeva O.V., Korytkova E.N., Drozdova I.A., Gusarov V.V. Phase state and particle size of ultradispersed zirconium dioxide as influenced by condition of hydrothermal synthesis. *Russ. J. General Chem.*, 1999, **69** (8), P. 1219–1222.
[34] Yau S.-T., Vekilov P.G. Quasi-planar nucleus structure in apoferritin crystallization. *Nature*, 2000, **406** (6795), P. 494–497.
[35] Pozhidaeva O.V., Korytkova E.N., Romanov D.P., Gusarov V.V. Formation of ZrO_2 nanocrystals in hydrothermal media of various chemical compositions. *Russ. J. General Chem.*, 2002, **72** (6), P. 849–853.
[36] Sharikov F.Yu., Almjasheva O.V., Gusarov V.V. Thermal analysis of formation of ZrO_2 nanoparticles under hydrothermal conditions. *Russ. J. Inorg. Chem.*, 2006, **51** (10), P. 1538–1542.
[37] Kuznetsova V.A., Almjasheva O.V., Gusarov V.V. Influence of microwave and ultrasonic treatment on the formation of $CoFe_2O_4$ under hydrothermal conditions. *Glass Phys. Chem.*, 2009, **35** (2), P. 205–209.

[38] Krasilin A.A., Almjasheva O.V., Gusarov V.V. Effect of the structure of precursors on the formation of nanotubular magnesium hydrosilicate. *Inorganic Materials*, 2011, **47** (10), P. 1111–1115.

[39] Bugrov A.N., Almjasheva O.V. Formation of Cr_2O_3 nanoparticles under hydrothermal conditions. *Nanosystems: Physics, Chemistry, Mathematics*, 2011, **2** (4), P. 126–132.

[40] Almjasheva O.V., Gusarov V.V. Metastable clusters and aggregative nucleation mechanism. *Nanosystems: Physics, Chemistry, Mathematics*, 2014, **5** (3), P. 405–417.

[41] Popkov V.I., Almjasheva O.V. Formation mechanism of $YFeO_3$ nanoparticles under the hydrothermal condition. *Nanosystems: Physics, Chemistry, Mathematics*, 2014, **5** (5), P. 703–708.

[42] Popkov V.I., Almjasheva O.V., Gusarov V.V. The investigation of the structure control possibility of nanocrystalline yttrium orthoferrite in its synthesis from amorphous powders. *Russ. J. Appl. Chem.*, 2014, 87 (10), P. 1417–1421.

[43] Vasilevskaya A.K., Almjasheva O.V., Gusarov V.V. Formation of nanocrystals in the ZrO_2 –H_2O system. *Russ. J. Gen. Chem.*, 2015, **85** (12), P. 2673–2676.

[44] Almjasheva O.V., Gusarov, V.V. Prenucleation formations in control over synthesis of CoFe2O4 nanocrystalline powders. *Russ. J. Appl. Chem.*, 2016, **89** (6), P. 851–856.

[45] Popkov V.I., Almjasheva O.V., et al. The role of pre-nucleus states in formation of nanocrystalline yttrium orthoferrite. *Dokl. Chem.*, 2016, **471** (2), P. 356–359.

[46] Komlev A.A., Panchuk V.V., et al. Effect of the sequence of chemical transformations on the spatial segregation of components and formation of periclase-spinel nanopowders in the MgO–Fe_2O_3–H_2O system. *Russ. J. Appl. Chem.*, 2016, **89** (12), P. 1930–1936.

[47] Almjasheva O.V. Formation and structural transformations of nanoparticles in the TiO_2–H_2O system. *Nanosystems: Physics, Chemistry, Mathematics*, 2016, **7** (6), P. 1031–1049.

[48] Almjasheva O.V., Krasilin A.A., Gusarov V.V. Formation mechanism of core-shell nanocrystals obtained via dehydration of coprecipitated hydroxides at hydrothermal conditions. *Nanosystems: Physics, Chemistry, Mathematics*, 2018, **9** (4), P. 568–572.

[49] Gusarov V.V. Fast Solid-Phase Chemical Reactions. *Russ. J. of Gen. Chem.*, 1997, **67** (12), P. 1846–1851.

[50] Gusarov V.V., Malkov A.A., Ishutina Zh.N., Malygin A.A. Phase formation in a nanosize silicon oxide film on the surface of aluminum oxide. *Tech. Phys. Lett.*, 1998, **24** (1), P. 1–3.

[51] Gusarov V.V., Ishutina Zh.N., Malkov A.A., Malygin A.A. Solid-phase reaction of mullite formation in nanosized composite films. *Dokl. Phys. Chem.*, 1997, **357** (1–3), P. 360–363.

[52] Ivanov V.K., Polezhaeva O.S. Synthesis of ultrathin ceria nanoplates. *Rus. J. Inorg. Chem.*, 2009, **54** (10), P. 1528–1530.

[53] Čubová K., Čuba V. Synthesis of inorganic nanoparticles by ionizing radiation – a review. *Radiation Physics and Chemistry*, 2019, **158**, P. 153–164.

[54] Roca A.G., Gutiérrez L., et al. Design strategies for shape-controlled magnetic iron oxide nanoparticles. *Advanced Drug Delivery Reviews*, 2019, **138**, P. 68–104.

[55] Rajeshkumar S., Naik Poonam. Synthesis and biomedical applications of cerium oxide nanoparticles – A Review. *Biotechnology Reports*, 2018, **17**, P. 1–5.

[56] Krl A., Pomastowski P., et al. Zinc oxide nanoparticles: Synthesis, antiseptic activity and toxicity mechanism. *Advances in Colloid and Interface Science*, 2017, **249**, P. 37–52.

[57] Saad W.S., Prud'homme R.K. Principles of nanoparticle formation by flash nanoprecipitation. *Nanotoday*, 2106, **11** (2), P. 212–227.

[58] Calvache-Muñoz J., PradoJorge F.A., Rodríguez-Páez E. Cerium oxide nanoparticles: Synthesis, characterization and tentative mechanism of particle formation. *Colloids and Surfaces A: Physicochemical and Engineering Aspects*, 2017, **529**, P. 146–159.

[59] Byrappa K., Adschiri T. Hydrothermal technology for nanotechnology. *Progress in crystal growth and characterization of materials*, 2007, **53** (2), P. 117–166.

[60] Merzhanov A.G. SHS Process: Combustion Theory and Practice. *Archivum Combustionis*, 1981, **1** (1–2), P. 23–48.

[61] Merzhanov A.G. Theory and Practice of SHS: Worldwide state of the art and the newest results. *Int. J. Self-Prop. High-Temp. Synth.*, 1993, 2 (2), P. 113–158.

[62] Mukasyan A.S., Rogachev A.S. Combustion synthesis: mechanically induced nanostructured materials. *J. Mater. Sci.*, 2017, **52**, P. 11826–11833.

[63] Popkov V.I., Almjasheva O.V., et al. Features of nanosized $YFeO_3$ formation under heat treatment of glycine–nitrate combustion products. *Russ. J. Inorg. Chem.*, 2015, **60** (10), P. 1193–1198.

[64] Popkov V.I., Almjasheva O.V., et al. Crystallization behavior and morphological features of $YFeO_3$ nanocrystallites obtained by glycine-nitrate combustion. *Nanosystems: Physics, Chemistry, Mathematics*, 2015, **6** (6), P. 866–874.

[65] Popkov V.I., Almjasheva O.V., Schmidt M.P., Gusarov V.V. Formation mechanism of nanocrystalline yttrium orthoferrite under heat treatment of the coprecipitated hydroxides. *Russ. J. Gen. Chem.*, 2015. **85** (6), P. 1370–1375.

[66] Lomanova N.A., Tomkovich M.V., Sokolov V.V., Gusarov V.V. Special Features of Formation of Nanocrystalline $BiFeO_3$ via the glycine-nitrate combustion method. *Russ. J. Gen. Chem.*, 2016, **86** (10), P. 2256–2262.

[67] Chen Y., Yang J., et al. Synthesis $YFeO_3$ by salt-assisted solution combustion method and its photocatalytic activity. *J. Ceram. Soc. Japan.*, 2014, **122** (1422), P. 146–150.

[68] Khaliullin Sh.M., Zhuravlev V.D., et al. Solution-combustion synthesis and eletroconductivity of $CaZrO_3$. *Int. J. Self-Prop. High-Temp. Synth.*, 2015, **24** (2), P. 83–88.

[69] Ostroushko A.A., Russkikh O.V. Oxide material synthesis by combustion of organic-inorganic compositions. *Nanosystems: Physics, Chemistry, Mathematics*, 2017, **8** (4), P. 476–502.

[70] Boldyrev V.V. Reactivity of solids. *J. of Thermal Analysis*, 1993, **40** (3), P. 1041–1062.

[71] Kalinin S.V., Vertegel A.A., Oleynikov N.N., Tretyakov Y.D. Kinetics of solid state reactions with fractal reagent. *J. Mater. Synth., Process*, 1998, **6** (5), P. 305–309.

[72] Al'myasheva O.V., Gusarov V.V. Features of the phase formation in the nanocomposites. *Russ. J. Gen. Chem.*, 2010, **80** (3), P. 385–390.

[73] Ashgriz N., Brocklehurst W., Talley D. Mixing mechanisms in a pair of impinging jets. *J. Propul. Power.*, 2001, **17** (3), P. 736.

[74] Handbook of Atomization and Sprays/Ed. N. Ashgriz. Toronto: Springer Science + Business Media, LLC, 2011. Ch. 30., P. 685.

[75] Erkoc E., Fonte C.P., et al. Numerical study of active mixing over a dynamic flow field in a T-jets mixer – Induction of resonance. *Chem. Eng. Res. Design*., 2016, **106**, P. 74.

[76] Ravi Kumar D.V., Prasad B.L.V., Kulkarni A.A. Impinging jet micromixer for flow synthesis of nanocrystalline MgO: Role of mixing/impingement zone. *Ind. Eng. Chem. Res.*, 2013, **52**, P. 17376.

[77] Proskurina O.V., Nogovitsin I.V., et al. Formation of $BiFeO_3$ nanoparticles using impinging jets microreactor. *Russ. J. Gen. Chem.*, 2018, **88** (10), P. 2139–2143.

[78] Proskurina O.V., Abiev R.S., et al. Formation of nanocrystalline $BiFeO_3$ during heat treatment of hydroxides co-precipitated in an impinging-jets microreactor. *Chemical Engineering and Processing – Process Intensification*, 2019, **143**, P. 107598.

[79] Proskurina O.V., Sivtsov E.V., et al. Formation of rhabdophane-structured lanthanum orthophosphate nanoparticles in an impinging-jets microreactor and rheological properties of sols based on them. *Nanosystems: Physics, Chemistry, Mathematics*, 2019, **10** (2), P. 206–214.

[80] Abiev R.S., Almyasheva O.V., Izotova S.G., Gusarov V.V. Synthesis of cobalt ferrite nanoparticles by means of confined impinging-jets reactors. *J. Chem. Tech. App*., 2017, **1** (1), P. 7–13.

[81] Koutzarova T., Kolev S., et al. Microstructural study and size control of iron oxide nanoparticles produced by microemulsion technique. *Phys. Stat. Sol.*, **3** (5), P. 1302–1307.

[82] Ganguli A.K., Ahmad T., Vaidya S., Ahmed J. Microemulsion route to the synthesis of nanoparticles. *Pure Appl. Chem.*, 2008, **80** (11), P. 2451–2477.

[83] Koltsov I., Kimmel G., et al. The new nano-enabled phase map of ZrO_2–Al_2O_3. *Scientific Reports*, 2019, **9**, P. 5540.

[84] Kovalenko A.N., Tugova E.A. Thermodynamics and kinetics of non-autonomous phases formation in nanostructured materials with variable functional properties. *Nanosystems: Physics, Chemistry, Mathematics*, 2018, **9** (5), P. 641–662.

[85] Tauson V.L., Akimov V.V. Effect of crystallite size on solid state miscibility: applications to the pyrite- cattierite system. *Gochimica et Cosmocimica Acta*, 1991, **55** (10), P. 2851–2859.

[86] Emerging materials for energy conversion and storage. Edited by: Cheong K.Y., Impellizzeri G., Amorim Fraga M., 2018, 418 p.

[87] Singh S., Barick K.C., Bahadur D. Functional oxide nanomaterials and nanocomposites for the removal of heavy metals and dyes. *Nanomater. nanotechnol.*, 2013, **3**, 20:2013.

[88] NIST-JANAF Thermochemical Tables. `URL: http://kinetics.nist.gov/janaf/` .

[89] Iorish V.S, Belov G.V. IVTANTHERMO/WIN – database and software for high temperature chemical processes modeling. *9th Int. Conf. on High Temperature Materials Chemistry: Proceedings*, Pennsylvania (USA), 1997. P. 42.

[90] Aruna S.T., Mukasyan A.S., Combustion synthesis and nanomaterials. *Curr. Opin. Solid State Mater. Sci.*, 2008, **12** (3–4), P. 44–50.

[91] Gabala M.A., Al-Solami F., et al. Auto-combustion synthesis and characterization of perovskite-type $LaFeO_3$ nanocrystals prepared via different routes. *Ceramics International*, 2019, **45** (13), P. 16530–16539.

[92] Karpov O.N., Tomkovich M.V., Tugova E.A. Formation of $Nd_{1-x}Bi_xFeO_3$ nanocrystals under conditions of glycine-nitrate synthesis. *Russ. J. Gen. Chem.*, 2018, **88** (10), P. 2128–2133.

[93] Tugova E., Yastrebov S., Karpov O., Smith R. $NdFeO_3$ nanocrystals under glycine nitrate combustion formation. *J. Cryst. Growth*, 2017, **467**, P. 88–92.

[94] Tugova E.A., Gusarov V.V. Structure peculiarities of nanocrystalline solid solutions in $GdAlO_3$–$GdFeO_3$ system. *Nanosystems: Physics, Chemistry, Mathematics*, 2013, **4** (3), P. 352–356.

[95] Almjasheva O.V., Fedorov B.A., Smirnov A.V., Gusarov V.V. Size, morphology and structure of the particles of zirconia nanopowder obtained under hydrothermal conditions. *Nanosystems: Physics, Chemistry, Mathematics*, 2010, **1** (1), P. 26–36.

[96] Klein S.M., Choi J.H., Pine D.J., Lange F.F. Synthesis of rutile titania powders: Agglomeration, dissolution, and reprecipitation phenomena. *J. Mater. Res.*, 2003, **18** (6), P. 1457–1464.

[97] Krishnankutty-Nair P. Kumar Growth of rutile crystallites during the initial stage of anatase-to-rutile transformation in pure titania and titania-alumina nanocomposites. *Scripta Metallurgica et Materialia*, 1995, **32** (6), P. 873–877.

[98] Vasilevskaia A.K., Popkov V.I., Valeeva A.A., Rempel' A.A. Formation of nonstoichiometric titanium oxides nanoparticles Ti_nO_{2n-1} upon heat-treatments of titanium hydroxide and anatase nanoparticles in a hydrogen flow. *Russ. J. Appl. Chem.*, 2016, **89** (8), P. 1211–1220.

[99] Guang M., Xia Y., et al. Controllable synthesis of transparent dispersions of monodisperse anatase-TiO_2 nanoparticles and nanorods. *Materials Chemistry and Physics*, 2019, **224**, P. 100–106.

[100] Macwan D.P., Dave P.N., Chaturvedi S. A review on nano-TiO_2 sol-gel type syntheses and its applications. *J. Mater. Sci.*, 2011, **46** (11), P. 3669–3686.

[101] Li C.-J., Yang G.-J., Wang Z. Formation of nanostructured TiO_2 by flame spraying with liquid feedstock. *Mater. Lett.*, 2003, **57** (13–14), P. 2130–2134.

[102] Kominami H., Kohno M., Kera Y. Synthesis of brookite-type titanium oxide nano-crystals in organic media. *J. Mater. Chem.*, 2000, **10** (5), P. 1151–1156.

[103] Deng Q., Wei M., et al. Brookite-type TiO_2 nanotubes. *Chem. Commun.*, 2008, **31**, P. 3657–3659.

[104] Zaboeva E.A., Izotova S.G., Popkov V.I. Glycine-nitrate combustion synthesis of $CeFeO_3$-based nanocrystalline powders. *Russ. J. Appl. Chem.*, 2016, **89** (8), P. 1228–1236.

[105] Popkov V.I., Tolstoy V.P., Omarov S.O., Nevedomskiy V.N. Enhancement of acidic-basic properties of silica by modification with CeO_2–Fe_2O_3 nanoparticles via successive ionic layer deposition. *Appl. Surf. Sci.*, 2019, **473**, P. 313–317.

[106] Li L., Pu S., et al. High-purity disperse α-Al_2O_3 nanoparticles synthesized by high-energy ball milling. *Adv. Powder Technol.*, 2018, **29** (9), P. 2194–2203.

[107] Tabesh S., Davar F., Loghman-Estarki M.R. Preparation of γ-Al_2O_3 nanoparticles using modified sol-gel method and its use for the adsorption of lead and cadmium ions. *J. Alloys Comp.*, 2018, **730**, P. 441–449.

[108] Kotlovanova N.E., Matveeva A.N., et al. Formation and Acid–Base Surface Properties of Highly Dispersed η-Al_2O_3 Nanopowders. *Inorg. Mater.*, 2018, **54** (4), P. 392–400.

[109] Kuchina Y.A., Subbotin D.I., et al. Metal ferrites synthesis by AC plasma torch. *J. Phys. Conf. Ser.*, 2018, **1135**, P. 012095.

[110] Dudnik Y.D., Safronov A.A., et al. Plasma ways to obtain ultrafine oxides. *J. Phys. Conf. Ser.*, 2019, **1147**, P. 012127.

[111] Elouafi A., Moubah R., et al. Finite size effects on the magnetocaloric properties around blocking temperature in γ-Fe_2O_3 nanoparticles. *Physica A: Statistical Mechanics and Its Applications*, 2019, **523**, P. 260–267.

[112] Hasan M., Islam Md. F., et al. A soft chemical route to the synthesis of $BiFeO_3$ nanoparticles with enhanced magnetization. *Mat. Res. Bull.*, 2016, **73**, P. 179–186.

[113] Ortiz-Quinonez J.L., Diaz D., et al. Easy synthesis of high-purity $BiFeO_3$ nanoparticles: new insights derived from the structural, optical, and magnetic characterization. *Inorg Chem.*, 2013, **52**, P. 10306–10317.

[114] Park T.-J., Papaefthymiou G.C., et al. Size- dependent magnetic properties of single-crystalline multiferroic $BiFeO_3$ nanoparticles. *Nano Lett.*, 2007, **7**, P. 766–772.

[115] Proskurina O.V., Tomkovich M.V., et al. Formation of Nanocrystalline $BiFeO_3$ under Hydrothermal Conditions. *Russ. J. Gen.Chem.*, 2017, **87** (11), P. 2507–2515.

[116] Morales L.A., Sierra-Gallego G., Barrero C.A., Arnache O. Relative recoilless F-factors in $REFeO_3$ (RE = rare-earth La, Pr, Nd and Sm) orthoferrites synthesized by self-combustion method. *Materials Science and Engineering B*, 2016, **211**, P. 94–100.

[117] Luu M.D., Dao N.N., et al. A new perovskite-type $NdFeO_3$ adsorbent: synthesis, characterization, and As(V) adsorption. *Adv. Nat. Sci.: Nanosci. Nanotechnol.*, 2016, **7**, P. 025015.

[118] Chanda S., Saha S., Dutta A., Sinha T.P. Raman spectroscopy and dielectric properties of nanoceramic $NdFeO_3$. *Mater. Res. Bull.*, 2013, **48** (4), P. 1688–1693.

[119] Shanker J., Rao G.N., Venkataramana K., Babu D.S. Investigation of structural and electrical properties of $NdFeO_3$ perovskite nanocrystalline. *Phys.Lett. A*, 2018, **382** (40), P. 2974–2977.

[120] Atta N.F., El-Ads E.H., Galal A. Evidence of Core-Shell Formation between $NdFeO_3$ nano-perovskite and ionic liquid crystal and its application in electrochemical sensing of metoclopramide. *J. Electrochem. Soc.*, 2016, **163** (7), P. B325–B334.

[121] Atta N.F., Galal A., Ali S.M. The Effect of the Lanthanide Ion-Type in $LnFeO_3$ on the Catalytic Activity for the Hydrogen Evolution in Acidic Medium. *Int. J. Electrochem. Sci.*, 2014, **9**, P. 2132–2148.

[122] Atta N.F., Binsabt M.H., El-Ads E.H., Galal A. Synthesis of neodymium-iron nanoperovskite for sensing applications of an antiallergic drug. *Turk. J. Chem.*, 2017, **41** (4), P. 476–492.

[123] Ho T.G., Ha T.D., et al. Nanosized perovskite oxide $NdFeO_3$ as material for a carbon-monoxide catalytic gas sensor. *Adv. Nat. Sci: Nanosci. Nanotechnol.*, 2011, **2**, P. 015012.

[124] Yousefi M., Soradi Zeid S., Khorasani-Motlagh M. Synthesis and characterization of nano-structured perovskite type neodymium orthoferrite $NdFeO_3$. *Curr. Chem. Lett.*, 2017, **6** (1), P. 23–30.

[125] Hao Y.J., Li B., Liu R.H., Li F.T. Synthesis of $NdFeO_3$ perovskites in a reverse microemulsion and its visible light photocatalytic activity. *Adv. Mater. Res.*, 2011, **282–283**, P. 593–596.

[126] Popkov V.I., Almjasheva O.V. Yttrium orthoferrite $YFeO_3$ nanopowders formation under glycine-nitrate combustion conditions. *Russ. J. Appl. Chem.*, 2014, **87** (2), P. 167–171.

[127] Popkov V.I., Almjasheva O.V., et al. Magnetic properties of $YFeO_3$ nanocrystals obtained by different soft-chemical methods. *J. Mater. Sci.: Mater. Electron.*, 2017, **28** (10), P. 7163–7170.

[128] Popkov V.I., Almjasheva O.V., et al. Effect of spatial constraints on the phase evolution of $YFeO_3$-based nanopowders under heat treatment of glycine-nitrate combustion products. *Ceram. Int.*, 2018, **44** (17), P. 20906–20912.

[129] Popkov V.I., Tugova E.A., Bachina A.K., Almyasheva O.V. The formation of nanocrystalline orthoferrites of rare-earth elements $XFeO_3$ (X = Y, La, Gd) via heat treatment of coprecipitated hydroxides. *Russ. J. Gen. Chem.*, 2017, **87** (11), P. 2516–2524.

[130] Gimaztdinova M.M., Tugova E.A., Tomkovich M.V., Popkov V.I. Glycine-nitrate combustion synthesis of $GdFeO_3$ nanocrystals. *Condens. Matter and Interphases*, 2016, **18** (3), P. 422–431.

[131] Martinson K.D., Kondrashkova I.S., Popkov V.I. Synthesis of $EuFeO_3$ nanocrystals by glycine-nitrate combustion method. *Russ. J. Appl. Chem.*, 2017, **90** (8), P. 1214–1218.

[132] Kondrashkova I.S., Martinson K.D., Zakharova N.V., Popkov V.I. Synthesis of nanocrystalline $HoFeO_3$ photocatalyst via heat treatment of products of glycine-nitrate combustion. *Russ. J. Gen. Chem.*, 2018, **88** (12), P. 2465–2471.

[133] Zhi-hui C., Jun-fu Q., et al. Preparation of $Bi_4Ti_3O_{12}$ nanopower by azeotropic co-precipitation and dielectric properties of the sintered ceramic. *Ceram. Intern.*, 2010, **36** (1), P. 241–244.

[134] Chen D., Jiao X. Hydrothermal synthesis and characterization of Bi4Ti3O12 powders from different precursors. *Materials Research Bulletin*, 2001, **36**(1–2), P. 355–363.

[135] Al-Amani U., Sreekantan S., Fauzi A.M.N., Khairunisak A.R., Warapong K. Soft combustion technique: Solution combustion synthesis and low-temperature combustion synthesis; to prepare $Bi_4Ti_3O_{12}$ powders and bulk ceramics. Science of Sintering, 2012, **44** (2), P. 211–221.

[136] Zhang H., Ke H., et al. Crystallisation process of $Bi_5Ti_3FeO_{15}$ multiferroic nanoparticles synthesized by a sol–gel method. *J. Sol-Gel Sci. Technol.*, 2018, **85** (1), P. 132–139.

[137] Gautam A., Singh K., et al. Crystal structure and magnetic property of Nd doped $BiFeO_3$ nanocrytallites. *Mater. Lett.*, 2011, **65**, P. 591–594.

[138] Mishra R.K., Pradhan D.K., Choudhary R.N.P., Banerjee A. Dipolar and magnetic ordering in Nd-modified $BiFeO_3$ nanoceramics. *J. Magn. Magnetic Mater.*, 2008, **320**, P. 2602–2607.

[139] Almjasheva O.V., Smirnov A.V., et al. Structural features of ZrO_2–Y_2O_3 and ZrO_2–Gd_2O_3 nanoparticles formed under hydrothermal conditions. Russ. *J. Gen. Chem.*, 2014, **84** (5), P. 804–809.

[140] Gusarov V.V., Malkov A.A., Malygin A.A., Suvorov V.A. Formations of aluminum titanate in compositions with a high level of spatial and structural conjugation of components. *Russ. J. Gen. Chem.*, 1994, **64** (4), P. 554.

NANOSYSTEMS: PHYSICS, CHEMISTRY, MATHEMATICS, 2019, 10 (4), P. 438–446

The prediction of COOH functionalized carbon nanotube application in melphalan drug delivery

Hadi Lari, Ali Morsali, Mohammad Momen Heravi

Department of Chemistry, Mashhad Branch, Islamic Azad University, Mashhad, Iran

hadilari1359@yahoo.com, almorsali@yahoo.com, drmh45@yahoo.com

PACS 78.67.n; 78.67.Ch **DOI 10.17586/2220-8054-2019-10-4-438-446**

Using quantum chemical calculations, noncovalent functionalization of melphalan drug on the surface of functionalized carbon nanotube (NT) have been examined. Quantum molecular descriptors of noncovalent interactions were investigated. It was concluded that binding of drug melphalan into COOH-functionalized NT (FNT) is exothermic and makes the system stable. Comparison between FNT and COCl functionalized NT ($F'NT$) showed that FNT has more binding energy and may act as a carrier for drug delivery (if the noncovalent functionalization is desired). The OH and NH_2 groups of melphalan may bond to Cl (COCl mechanism) and COOH (COOH mechanism) of $F'NT$ and FNT, respectively. Therefore, four mechanisms for the covalent functionalization have been investigated. The transition states of four pathways were optimized and activation parameters were evaluated. The high barriers of COOH pathway are greater than those of COCl pathway and therefore $F'NT$ is suitable carrier for covalent functionalization.

Keywords: Carbon nanotube, density functional theory, functionalization, melphalan, quantum descriptors.

Received: 14 May 2019

Revised: 28 June 2019

1. Introduction

Despite all efforts to overcome cancer, the old approaches through chemotherapy cause side effects such as vomiting, heart disease, hair loss and etc. [1, 2]. In recent years, the use of targeted methods for drug delivery has been felt [3–6]. For this purpose, organic compounds such as dendrimers [7], drug-polymer conjugates [8] and liposomes [9] and inorganic nanoparticles, such as gold NPs [10], iron oxide NPs [11, 12], silica NPs [13] have been exploited.

Experimental and theoretical studies have recently focused on carbon-based nanoparticles, such as carbon nanotubes and graphene, for drug delivery [14–21]. With a unique set of mechanical, electrical and chemical properties [22–29], carbon nanotubes have many applications in chemical pharmaceutical researches [30–33].

In spite of some deficiencies such as low solubility in aqueous solutions and high toxicity [34–36], carbon nanotubes have been highly regarded in drug delivery due to good cell penetration qualities and high drug loading [37–39]. Using nanotubes as the carrier molecules, lower doses of anticancer drugs are needed, resulting in reduced side effects of the medicine [40–42]. Functionalized carbon nanotubes were used as carriers for different anticancer drugs such as platinum (IV) [43], 6-mercaptopurine [44], doxorubicin [45, 46], paclitaxel [47], Methotrexate [48], gemcitabine [49], camptothecin [50], tamoxifen [51], oridonin [52], sorafenib [53], soyasapogenol [54] and etc. Melphalan or 4-[bis(2-Chloroethyl)amino]-L-phenylalanine is an alkylating agent which has anticancer activities and is extremely effective in the treatment of tumors such as multiple myeloma [55, 56].

Quantum computing is a powerful tool for analyzing drug delivery systems [57–64]. In this work, quantum chemical calculations were used to study the covalent and noncovalent adsorption of the exterior surface of COOH functionalized carbon nanotube (FNT) with melphalan drug. Noncovalent functionalization is more commonly used to carry medicine, but in many cases, such as hydroxycamptothecin, doxorubicin, pirarubicin, platinol, methotrexate, tamoxifen and thalidomide, covalent functionalization has been used [65]. The predictions made in this way can help researchers build and use targeted anticancer drugs and reduce the process of trial and error in the laboratory.

2. Computational details

GAUSSIAN 09 package [66] has been utilized for the optimization of all configurations in gas and solution phases at UB3LYP/6-31G(d,p). Polarized continuum model (PCM) was employed to consider the implicit solvent effects [67, 68]. For the optimization of the molecular configurations, the standard convergence criteria were utilized. All degrees of freedom were optimized for all species. The transition states were confirmed to have only one imaginary frequency of the Hessian. In addition, zero-point corrections were taken into account to obtain the activation energy.

COOH functionalized armchair (5,5) single wall carbon nanotube (FNT) comprising 114 atoms (10 Å) was considered as FNT model. Unrestricted method (U in UB3LYP) is used for molecules with unpaired electrons such as FNT model.

Quantum molecular descriptors may be used to evaluate chemical reactivity and stability. The global hardness (η) demonstrates the resistance of one particle against the modification in its electronic configuration:

$$\eta = \frac{I - A}{2}, \tag{1}$$

where $I = -E_{HOMO}$ and $A = -E_{LUMO}$ are the ionization potential and the electron affinity, respectively. The electrophilicity index (ω) [69] is evaluated by

$$\omega = \frac{(I + A)^2}{8\eta}. \tag{2}$$

3. Results and discussion

Melphalan (M) is an anticancer molecule with NH_2, OH and Cl groups as represented in Fig. 1. The optimized geometries of M, COOH functionalized carbon nanotube (FNT) and COCl functionalized carbon nanotube (F′NT) in aqueous solution have been shown in Fig. 1.

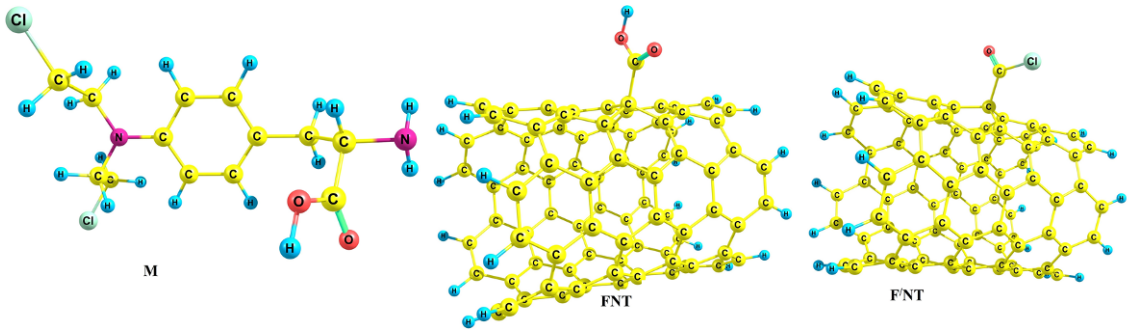

FIG. 1. Optimized geometries of M, FNT and F′NT

The hydrogen bond interactions between M and FNT or F′NT occur via NH_2, OH and Cl groups. These five configurations have been illustrated in Figs. 2 and 3, namely, FNT/M1-3R and F′NT/M1-2R.

The binding energies (ΔE) of M to FNT (in water) and F′NT (in DMF) were calculated using equation (3) and represented in Table 1:

$$\Delta E = E_{FNT(F'NT)/M1-3R} - (E_{FNT(F'NT)} + E_M). \tag{3}$$

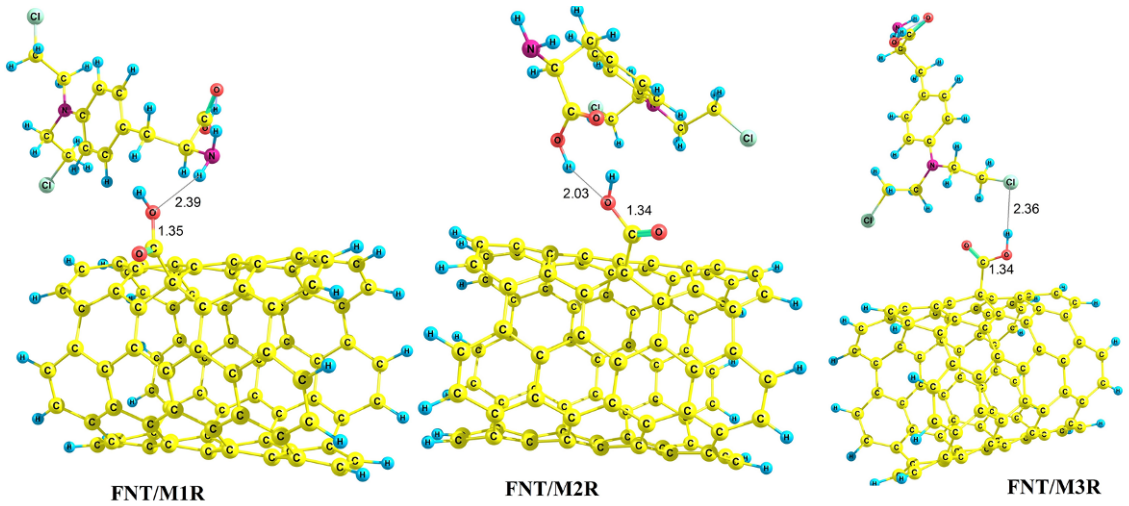

FIG. 2. Optimized geometries of FNT/M1-3R

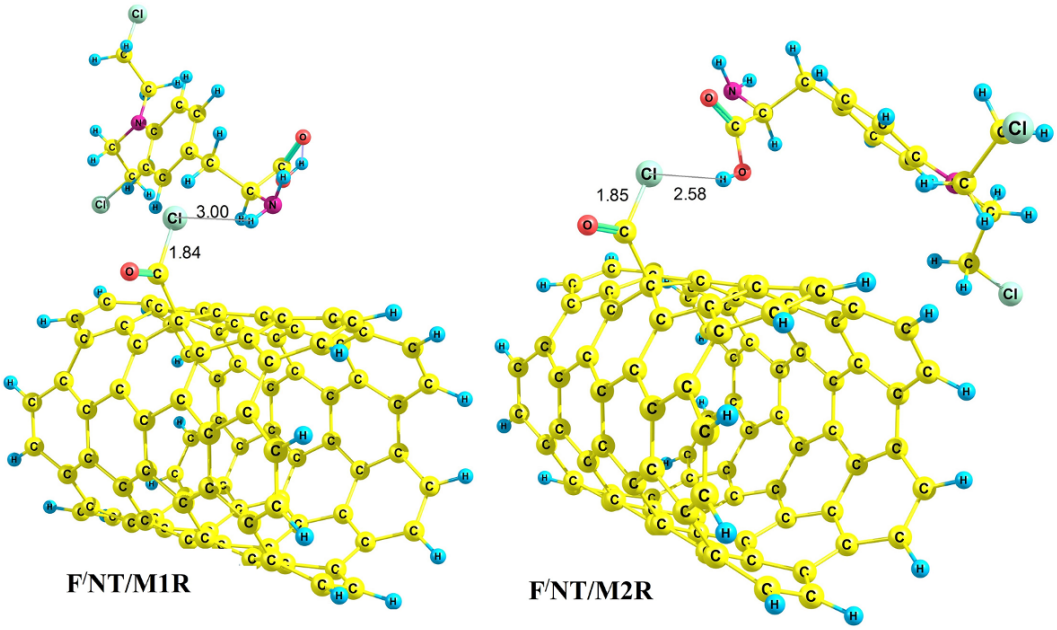

FIG. 3. Optimized geometries of F′NT/M1-2

TABLE 1. Solvation and binding energies of different configurations (kJ·mol^{-1})

Species	Solvation energy	Binding energy	Binding energy
M	−45.02	Solution phase	Gas phase
FNT	−49.00		
FNT/M1R	−84.43	−6.48	−16.07
FNT/M2R	−69.17	−24.26	−49.10
FNT/M3R	−74.48	−12.84	−32.37
F′NT/M1R	—	−2.74	—
F′NT/M2R	—	−7.79	—

Using the calculated ΔE_s of five species in Table 1, these binding energies are negative in gas and solution phases showing M drug is stabilized by FNT and F′NT surfaces. Among the 5 species, FNT/M1-3R are more stable than F′NT/M1-2R. Among the three species of FNT/M1-3R, the second one has more negative energy in gas and solution phases, denoting a stronger hydrogen bonding (from OH group).

Generally, for noncovalent interactions, comparison between FNT and F′NT indicates that using the first one is more favorable because of a stronger hydrogen bonding between M and COOH functionalized single wall carbon nanotube.

The solvation energies (ΔE_{solv}) of all structures have been calculated using the following equation:

$$\Delta E_{solv} = E_{sol} - E_{gas}, \tag{4}$$

where E_{gas} and E_{sol} represent the total energies in the gas and solution phases, respectively. The solvation energies of M, FNT, FNT/M1-3R have been shown in Table 1. Because of the negative values of solvation energies, this process is spontaneous. The calculated solvation energies show that M solubility increases in the vicinity of FNT. After the functionalization of M on FNT, solubility of M increases which is critical to the drug delivery systems. The important feature of M is in having NH_2, OH and Cl groups, creating hydrogen bonds between FNT, solvent molecules and M drug.

Table 2 represents the quantum molecular descriptors for M (H_2O, DMF, GAS), FNT (H_2O, GAS), F′NT (DMF), FNT/M1-3R (H_2O, GAS) and F′NT/M1-2R (DMF). In Table 2, gap of energy between LUMO and HOMO (E_g) was also evaluated. E_g determines a more stable system.

TABLE 2. Binding energies (kJ·mol^{-1}) and quantum molecular descriptors (eV) for optimized species

Species	E_{HOMO}	E_{LUMO}	E_g	η	ω
		H_2O			
M	-5.37	-0.24	5.12	2.56	1.53
FNT	-4.04	-2.74	1.30	0.65	8.86
FNT/M1R	-4.05	-2.76	1.29	0.65	8.96
FNT/M2R	-4.04	-2.74	1.30	0.65	8.86
FNT/M3R	-3.92	-2.73	1.19	0.60	9.26
		GAS			
M	-5.52	-0.35	5.17	2.59	1.66
FNT	-3.90	-2.59	1.31	0.65	8.04
FNT/M1R	-3.96	-2.66	1.30	0.65	8.44
FNT/M2R	-3.92	-2.62	1.30	0.65	8.21
FNT/M3R	-3.92	-2.61	1.31	0.65	8.17
		DMF			
M	-5.37	-0.24	5.12	2.56	1.54
F′NT	-4.07	-2.82	1.26	0.63	9.46
F′NT/ M2R	-4.09	-2.83	1.25	0.63	9.57
F′NT/ M3R	-4.09	-2.84	1.25	0.63	9.62

η and E_g of the M drug are higher than those of FNT/M1-3R and F′NT/M1-2R, demonstrating the reactivity of M increases in the presence of COOH (COCl) functionalized NT. ω of M increases in the vicinity of COOH (COCl) functionalized NT, showing that M is an electron acceptor. The η and E_g values in FNT/ M1-2R are higher than F′NT/ M1-2R, indicating F′NT/ M to be more reactive (less stable) compared to FNT/ M.

In the covalent functionalization, NH_2 and OH groups attack the carbon atom of COOH or COCl to transfer their protons to the OH (Cl) group. We considered these four possible mechanisms for F(F′)NT/M1-2R. In COOH mechanism OH from FNT is substituted by NH (O) from M to give product P(P′)FNT. The optimized products (P(P′)FNT) have been presented in Fig. 4.

Using reactant FNT/M1R and product PFNT, the transition state of this step was obtained (TS1 in Fig. 5). The bond lengths are presented in Figs. 2, 4 and 5.

Relative energies for all structures have been calculated in Table 3 by considering the zero value for electronic plus zero point energy (E), enthalpy (H) and Gibbs free energy (G) of reactants (FNT+M). The activation energy (E_a), activation enthalpy ($\Delta H^{\ddagger}$) and activation Gibbs free energy ($\Delta G^{\ddagger}$) for COOH/M1 mechanism are 200.53, 202.78 and 254.38 kJ·mol^{-1}, respectively (Table 3).

Similar to COOH/M1 mechanism, using FNT/M2R and P′FNT, the transition state (TS2 in Fig. 5) was obtained. E_a, $\Delta H^{\ddagger}$ and $\Delta G^{\ddagger}$ for COOH/M2 mechanism are 125.41, 129.02 and 178.99 kJ·mol^{-1} respectively (Table 3). In room temperature, the activation energies of COOH mechanism are too high to occur.

In the other reactions for the covalent functionalization of M onto COCl functionalized carbon nanotube (COCl mechanism), FNT was firstly converted into alkyl chloride using SOCl2 (F′NT) [70]. M then reacts with F′NT to form covalent bond. F′NT is again converted to FNT in the presence of water. Therefore, this process should take place in a solvent such as DMF. In this mechanism, the attack of NH_2 and OH of M to Cl in the F′NT forms products PF′NT and P′F′NT, respectively (Fig. 6).

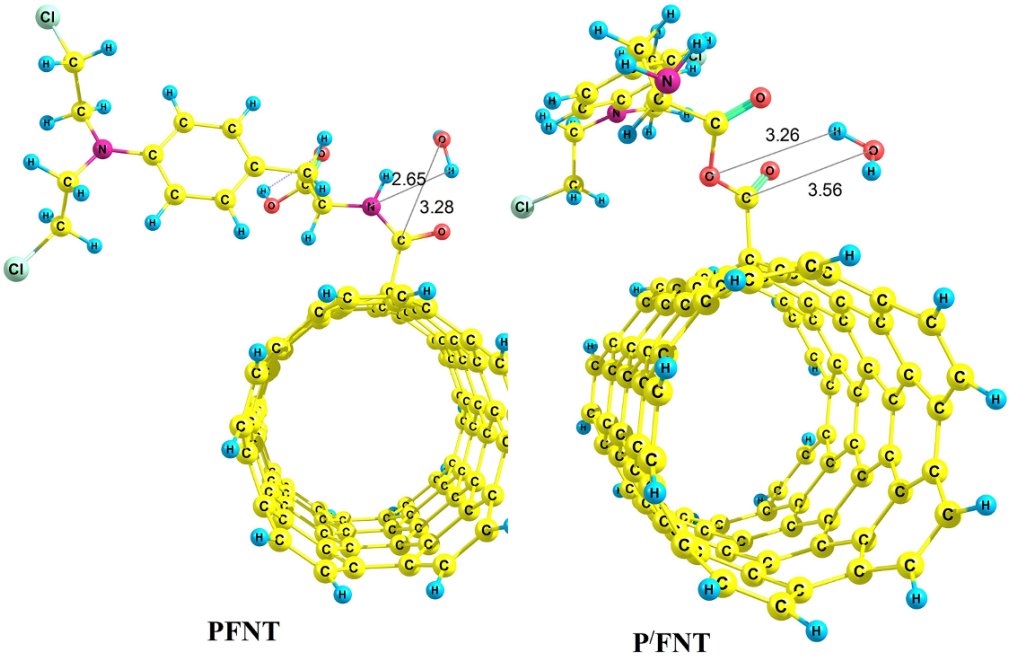

FIG. 4. Optimized geometries of PFNT and P′FNT

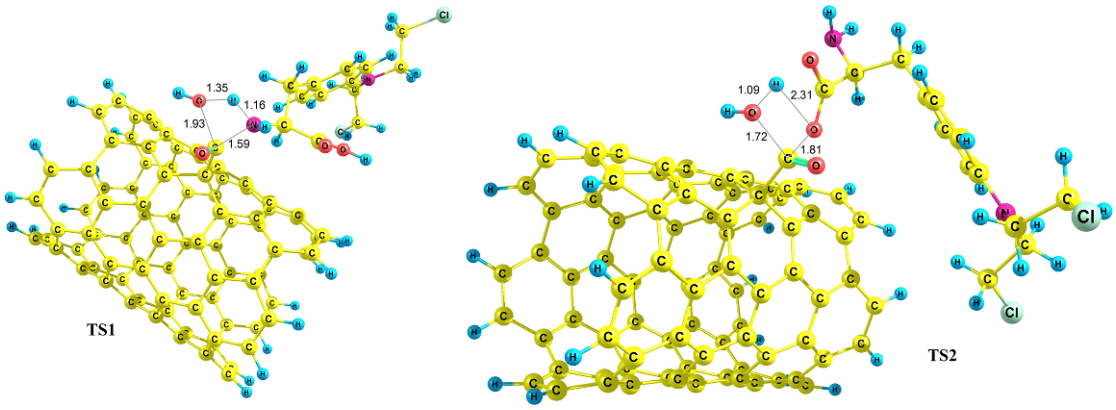

FIG. 5. Optimized geometries of TS1 and TS2

Using F′NT/M1R and PF′NT, TS3 is optimized (Fig. 7). The bond lengths are represented in Figs. 3, 6 and 7. E_a, $\Delta H^{\ddagger}$ and $\Delta G^{\ddagger}$ for COCl/M1 mechanism are 68.10, 74.68 and 95.24 kJ·mol^{-1}, respectively (Table 3). Using reactant F′NT/M2R and product P′F′NT, TS4 was obtained (Fig. 7). E_a, $\Delta H^{\ddagger}$ and $\Delta G^{\ddagger}$ for COCl/M2 mechanism are 86.66, 94.94 and 114.02 kJ·mol^{-1}, respectively (Table 3).

The total E_a for COCl/M1-2 mechanisms are lower than COOH/M1-2 mechanisms by 132.43 and 38.75 kJ·mol^{-1}, respectively. Hence, for the covalent functionalization of CNT by M drug F′NT should be used.

4. Conclusion

Four configurations of noncovalent interactions of drug melphalan (M) onto FNT and F′NT were examined. The binding energies of F′NT are lower than those of FNT, denoting FNT/M configurations have more stability. The HOMO-LUMO energy gap and global hardness of FNT/M species are greater than those of F′NT/M configurations species, showing the reactivity of M increases in the F′NT/M species and its stability decreases.

Four covalent functionalization mechanisms of M onto FNT (COOH mechanism) and F′NT (COCl mechanism) have been examined. M may bond to FNT or F′NT via NH_2 and OH groups. The energy barriers of COOH mechanisms are higher than those of COCl mechanisms. Therefore, COCl mechanisms are suitable for the covalent functionalization.

TABLE 3. Relative energies (kJ·mol^{-1}) for species in COOH and COCl mechanisms

Species	E	H	G
In water	COOH mechanism		
FNT+M	0.00	0.00	0.00
FNT/M1R	−6.48	0.00	26.38
TS1	200.53	202.78	254.38
PFNT	−9.07	−2.57	23.79
FNT/M2R	−24.26	−22.01	28.66
TS2	125.41	129.02	178.99
P′FNT	49.24	51.77	102.44
In DMF	COCl mehanism		
F′NT+M	0.00	0.00	0.00
F′NT/M1R	−2.74	4.07	23.59
TS3	68.10	74.68	95.24
PF′NT	−16.96	−11.43	−3.55
F′NT/M2R	−7.79	−0.90	18.52
TS4	86.66	94.94	114.02
P′F′NT	−22.58	−17.20	−9.41

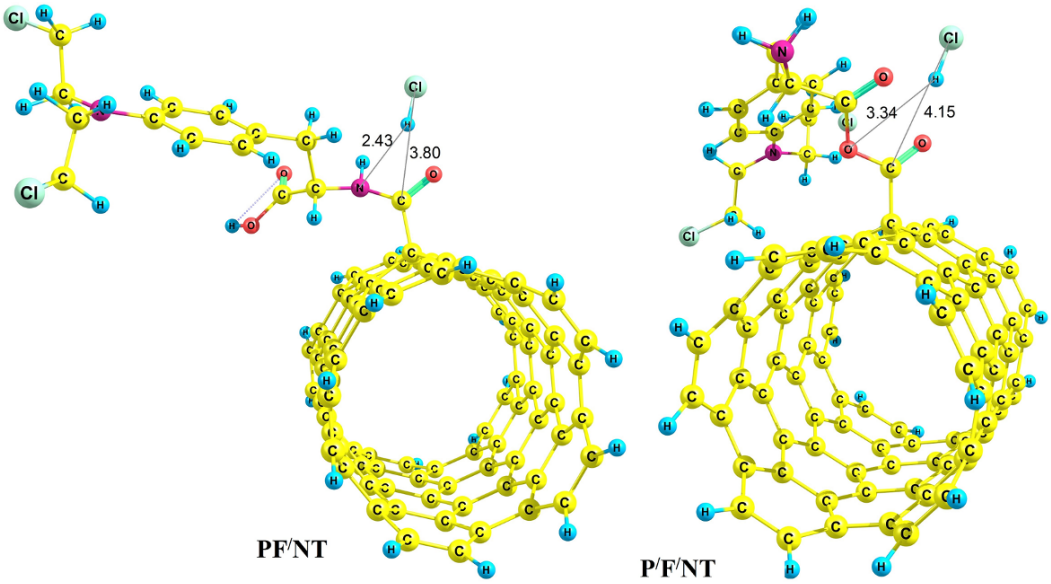

FIG. 6. Optimized geometries of PF′NT and P′F′NT

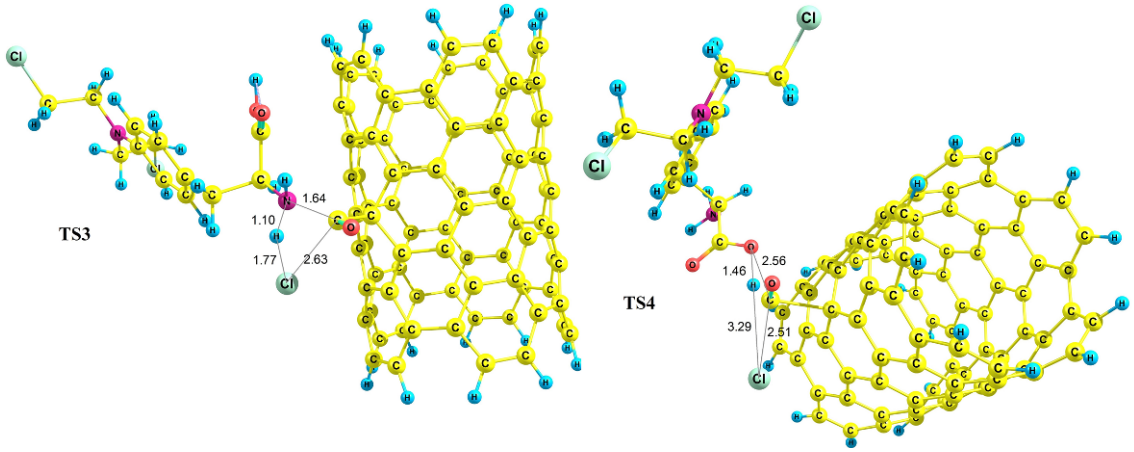

FIG. 7. Optimized geometries of TS3 and TS4

References

[1] Pennock G.D., Dalton W.S., et al. Systemic toxic effects associated with high-dose verapamil infusion and chemotherapy administration. *J. Natl. Cancer Inst.*, 1991, **83** (2), P. 105–110.

[2] Lindley C., McCune J.S., et al. Perception of chemotherapy side effects cancer versus noncancer patients. *Cancer pract.*, 1999, **7** (2), P. 59–65.

[3] Hughes G.A. Nanostructure-mediated drug delivery. *Nanomedicine in Cancer*, Pan Stanford, 2017, P. 47–72.

[4] Mitra S., Sasmal H.S., et al. Targeted drug delivery in covalent organic nanosheets (CONs) via sequential postsynthetic modification. *J. Am. Chem. Soc.*, 2017, **139** (12), P. 4513–4520.

[5] Ramasamy T., Ruttala H.B., et al. Smart chemistry-based nanosized drug delivery systems for systemic applications: a comprehensive review. *J. Controlled Release*, 2017, **258**, P. 226–253.

[6] Liu Q., Das M., Liu Y., Huang L. Targeted drug delivery to melanoma. *Adv. Drug Deliv. Rev.*, 2018, **127**, P. 208–221.

[7] Chauhan A.S. Dendrimers for Drug Delivery. *Molecules*, 2018, **23** (4), 938.

[8] Marasini N., Haque S., Kaminskas L.M. Polymer-drug conjugates as inhalable drug delivery systems: A review. *Curr. Opin. Colloid Interface Sci.*, 2017, **31**, P. 18–29.

[9] Pattni B.S., Chupin V.V., Torchilin V.P. New developments in liposomal drug delivery. *Chem. Rev.*, 2015, **115** (19), P. 10938–10966.

[10] Ghosh P., Han G., et al. Gold nanoparticles in delivery applications. *Adv. Drug Deliv. Rev.*, 2008, **60** (11), P. 1307–1315.

[11] Arami H., Khandhar A., Liggitt D., Krishnan K.M. In vivo delivery, pharmacokinetics, biodistribution and toxicity of iron oxide nanoparticles. *Chem. Soc. Rev.*, 2015, **44** (23), P. 8576–8607.

[12] Etebari N., Morsali A., Beyramabadi S.A. Structural and Mechanistic Studies of γ-Fe_2O_3 Nanoparticle as Capecitabine Drug Nanocarrier. *Chinese J. Struc. Chem.*, 2018, **3**, P. 375–382.

[13] Naghavi F., Morsali A., Bozorgmehr M.R. Molecular mechanism study of surface functionalization of silica nanoparticle as an anticancer drug nanocarrier in aqueous solution. *J. Mol. Liq.*, 2019, **282**, P. 392–400.

[14] Spencer D.S., Puranik A.S., Peppas N.A. Intelligent nanoparticles for advanced drug delivery in cancer treatment. *Current opinion in chemical engineering*, 2015, **7**, P. 84–92.

[15] Bokarev A., Plastun I. Possibility of drug delivery due to hydrogen bonds formation in nanodiamonds and doxorubicin: molecular modeling. *Nanosystems: Phys. Chem. Math.*, 2018, **9** (3), P. 370–377.

[16] Khorram R., Morsali A., et al. Mechanistic, Energetic and Structural Aspects of the Adsorption of Carmustine on the Functionalized Carbon Nanotubes. *Chinese J. Struc. Chem.*, 2017, **10**, 007.

[17] John A.A., Subramanian A.P., et al. Carbon nanotubes and graphene as emerging candidates in neuroregeneration and neurodrug delivery. *Int. J. Nanomedicine*, 2015, **10**, 4267.

[18] Kamel M., Raissi H., Morsali A., Shahabi M. Assessment of the adsorption mechanism of Flutamide anticancer drug on the functionalized single-walled carbon nanotube surface as a drug delivery vehicle: An alternative theoretical approach based on DFT and MD. *Appl. Surf. Sci.*, 2018, **434**, P. 492–503.

[19] d'Amora M., Giordani S. Carbon Nanomaterials for Nanomedicine. *Smart Nanoparticles for Biomedicine*, Elsevier, 2018, P. 103–113.

[20] Mikheev I., Pirogova M., et al. Optimization of the solventexchange process for highyield synthesis of aqueous fullerene dispersions. *Nanosystems: Phys. Chem. Math.*, 2018, **9** (1), P. 41–45.

[21] Shaki H., Morsali A., et al. Mechanistic, energetic and structural studies of single-walled carbon nanotubes functionalized with penicillamine. *J. Serb. Chem. Soc.*, 2018, **83** (2), P. 167–179.

[22] Barnett C.J., Gowenlock C.E., et al. Spatial and contamination-dependent electrical properties of carbon nanotubes. *Nano Lett.*, 2018, **18** (2), P. 695–700.

[23] Kholmanov I.N., Magnuson C.W., et al. Optical, electrical, and electromechanical properties of hybrid graphene/carbon nanotube films. *Adv. Mater.*, 2015, **27** (19), P. 3053–3059.

[24] Il'ina M., Il'in O., et al. The memristive behavior of nonuniform strained carbon nanotubes. *Nanosystems: Phys. Chem. Math.*, 2018, **9** (1), P. 76–78.

[25] Abdalla S., Al-Marzouki F., Al-Ghamdi A.A., Abdel-Daiem A. Different technical applications of carbon nanotubes. *Nanoscale Res. Lett.*, 2015, **10** (1), 358.

[26] Sozykin S., Beskachko V. Optical properties of defective carbon nanotube (7,7). *Nanosystems: Phys. Chem. Math.*, 2018, **9** (1), P. 73–75.
[27] Cheng H.-M., Liu C., Hou P.-X. Field emission from carbon nanotubes. *Nanomaterials Handbook*, Second Edition, CRC Press, 2017, P. 255–272.
[28] Ferreira F., Franceschi W., et al. Dodecylamine functionalization of carbon nanotubes to improve dispersion, thermal and mechanical properties of polyethylene based nanocomposites. *Appl. Surf. Sci.*, 2017, **410**, P. 267–277.
[29] Bocharov G., Egin M., Eletskii A., Kuznetsov V. Filling carbon nanotubes with argon. *Nanosystems: Phys. Chem. Math.*, 2018, **9** (1), P. 85–88.
[30] Chandrasekhar P. CNT Applications in Drug and Biomolecule Delivery. *Conducting Polymers, Fundamentals and Applications*, Springer, 2018, P. 61–64.
[31] Meher J.G., Kesharwani P., et al. Carbon Nanotubes (CNTs): A Novel Drug Delivery Tool in Brain Tumor Treatment. *Nanotechnology-Based Targeted Drug Delivery Systems for Brain Tumors*, Elsevier, 2018, P. 375–396.
[32] Pham-Huy C., Dramou P., et al. Carbon Nanotubes Used as Nanocarriers in Drug and Biomolecule Delivery. *Drug Delivery Approaches and Nanosystems*, **1**, Apple Academic Press, 2017, P. 163–212.
[33] Sciortino N., Fedeli S., et al. Multiwalled carbon nanotubes for drug delivery: Efficiency related to length and incubation time. *Int. J. Pharm.*, 2017, **521** (1–2), P. 69–72.
[34] Karimi M., Solati N., et al. Carbon nanotubes part II: a remarkable carrier for drug and gene delivery. *Expert Opin. Drug Deliv.*, 2015, **12** (7), P. 1089–1105.
[35] Zhang H., Hou L., et al. In vitro and in vivo evaluation of antitumor drug-loaded aptamer targeted single-walled carbon nanotubes system. *Curr. Pharm. Biotechnol.*, 2014, **14** (13), P. 1105–1117.
[36] Unnati S., Shah R. Review: Nano carrier systems for cancer therapy. *Int. J. Pharm. Technol.*, 2011, **3** (2), P. 927–946.
[37] Mehra N.K., Palakurthi S. Interactions between carbon nanotubes and bioactives: a drug delivery perspective. *Drug Discov. Today*, 2016, **21** (4), P. 585–597.
[38] Mehra N.K., Jain K., Jain N.K. Pharmaceutical and biomedical applications of surface engineered carbon nanotubes. *Drug Discov. Today*, 2015, **20** (6), P. 750–759.
[39] Hampel S., Vittorio O., Cirillo G., Makharza S. Physiological and Clinical Considerations of Drug Delivery Systems Containing Carbon Nanotubes and Graphene. *Drug Delivery Approaches and Nanosystems*, **2**, Apple Academic Press, 2017, P. 229–248.
[40] You Y., Wang N., et al. Designing dual-functionalized carbon nanotubes with high blood-brain-barrier permeability for precise orthotopic glioma therapy. *Dalton Trans.*, 2019, **48**, P. 1569–1573.
[41] Samal S.K. Cancer and Carbon Nano Tubes: A Promising Hope of Future. *Scientific Review*, 2018, **4** (7), P. 64–67.
[42] Ménard-Moyon C. Applications of Carbon Nanotubes in the Biomedical Field. *Smart Nanoparticles for Biomedicine*, Elsevier, 2018, P. 83–101.
[43] Feazell R.P., Nakayama-Ratchford N., Dai H., Lippard S.J. Soluble single-walled carbon nanotubes as longboat delivery systems for platinum (IV) anticancer drug design. *J. Am. Chem. Soc.*, 2007, **129** (27), P. 8438–8439.
[44] Karimi-Maleh H., Tahernejad-Javazmi F., et al. A novel DNA biosensor based on a pencil graphite electrode modified with polypyrrole/functionalized multiwalled carbon nanotubes for determination of 6-mercaptopurine anticancer drug. *Industrial & Engineering Chemistry Research*, 2015, **54** (14), P. 3634–3639.
[45] Liu Z., Sun X., Nakayama-Ratchford N., Dai H. Supramolecular chemistry on water- Soluble carbon nanotubes for drug loading and delivery. *ACS Nano*, 2007, **1** (1), P. 50–56.
[46] Wolski P., Nieszporek K., Panczyk T. Pegylated and folic acid functionalized carbon nanotubes as pH controlled carriers of doxorubicin. Molecular dynamics analysis of the stability and drug release mechanism. *PCCP*, 2017, **19** (13), P. 9300–9312.
[47] Lay C.L., Liu H.Q., Tan H.R., Liu Y. Delivery of paclitaxel by physically loading onto poly (ethylene glycol)(PEG)-graftcarbon nanotubes for potent cancer therapeutics. *Nanotechnology*, 2010, **21** (6), 065101.
[48] Samorì C., Ali-Boucetta H., et al. Enhanced anticancer activity of multi-walled carbon nanotubemethotrexate conjugates using cleavable linkers. *Chem. Commun.*, 2010, **46** (9), P. 1494–1496.
[49] Razzazan A., Atyabi F., Kazemi B., Dinarvand R. In vivo drug delivery of gemcitabine with PEGylated single-walled carbon nanotubes. *Mater. Sci. Eng.: C*, 2016, **62**, P. 614–625.
[50] Chae S., Kim D., et al. Encapsulation and Enhanced Delivery of Topoisomerase I Inhibitors in Functionalized Carbon Nanotubes. *ACS Omega*, 2018, **3** (6), P. 5938–5945.
[51] Yi W., Zhang P., et al. Enhanced response of tamoxifen toward the cancer cells using a combination of chemotherapy and photothermal ablation induced by lentinan-functionalized multi-walled carbon nanotubes. *Int. J. Biol. Macromol.*, 2018, **120**, P. 1525–1532.
[52] Wang C., Li W. Preparation, characterization, and in vitro and vivo antitumor activity of oridonin-conjugated multiwalled carbon nanotubes functionalized with carboxylic group. *Journal of Nanomaterials*, 2016, **2016**, 3439419.
[53] Karadas-Bakirhan N., Patris S., et al. Determination of the anticancer drug sorafenib in serum by adsorptive stripping differential pulse voltammetry using a chitosan/multiwall carbon nanotube modified glassy carbon electrode. *Electroanalysis*, 2016, **28** (2), P. 358–365.
[54] Haroun A., Amin H., El-Alim S.A. Immobilization and In vitro Evaluation of Soyasapogenol B onto Functionalized Multi-Walled Carbon Nanotubes. *IRBM*, 2018, **39** (1), P. 35–42.
[55] Facon T., Mary J.Y., et al. Melphalan and prednisone plus thalidomide versus melphalan and prednisone alone or reduced-intensity autologous stem cell transplantation in elderly patients with multiple myeloma (IFM 9906): a randomised trial. *The Lancet*, 2007, **370** (9594), P. 1209–1218.
[56] Horowitz M.E., Etcubanas E., et al. Phase II testing of melphalan in children with newly diagnosed rhabdomyosarcoma: a model for anticancer drug development. *J. Clin. Oncol.*, 1988, **6** (2), P. 308–314.
[57] Lotfi M., Morsali A., Bozorgmehr M.R. Comprehensive quantum chemical insight into the mechanistic understanding of the surface functionalization of carbon nanotube as a nanocarrier with cladribine anticancer drug. *Appl. Surf. Sci.*, 2018, **462** (34), P. 720–729.
[58] Saikia N., Deka R.C. Adsorption of isoniazid and pyrazinamide drug molecules onto nitrogen-doped single-wall carbon nanotubes: an ab initio study. *Struct. Chem.*, 2014, **25** (2), P. 593–605.
[59] Chegini H., Morsali A., Bozorgmehr M., Beyramabadi S. Theoretical study on the mechanism of covalent bonding of dapsone onto functionalised carbon nanotubes: effects of coupling agent. *Prog. React. Kinet. Mech.*, 2016, **41** (4), P. 345–355.
[60] Xu H., Li L., Fan G., Chu X. DFT study of nanotubes as the drug delivery vehicles of Efavirenz. *Comput. Theor. Chem.*, 2018, **1131**, P. 57–68.

[61] Kamel M., Raissi H., Morsali A. Theoretical study of solvent and co-solvent effects on the interaction of Flutamide anticancer drug with Carbon nanotube as a drug delivery system. *J. Mol. Liq.*, 2017, **248**, P. 490–500.
[62] Shahabi D., Tavakol H. DFT, NBO and molecular docking studies of the adsorption of fluoxetine into and on the surface of simple and sulfur-doped carbon nanotubes. *Appl. Surf. Sci.*, 2017, **420**, P. 267–275.
[63] Naderi S., Morsali A., Bozorgmehr M.R., Beyramabadi S.A. Mechanistic, energetic and structural studies of carbon nanotubes functionalised with dihydroartemisinin drug in gas and solution phases. *Phys. Chem. Liq.*, 2018, **56** (5), P. 610–618.
[64] Ketabi S., Rahmani L. Carbon nanotube as a carrier in drug delivery system for carnosine dipeptide: A computer simulation study. *Mater. Sci. Eng.: C*, 2017, **73**, P. 173–181.
[65] Wong B.S., Yoong S.L., et al. Carbon nanotubes for delivery of small molecule drugs. *Adv. Drug Deliv. Rev.*, 2013, **65** (15), P. 1964–2015.
[66] Frisch M., Trucks G., et al. Gaussian 09, Revision B. 01 [computer software]. Wallingford, CT, USA: Gaussian. Inc. Google Scholar, 2010.
[67] Tomasi J., Persico M. Molecular interactions in solution: an overview of methods based on continuous distributions of the solvent. *Chem. Rev.*, 1994, **94** (7), P. 2027–2094.
[68] Coitino E.L., Tomasi J., Cammi R. On the evaluation of the solvent polarization apparent charges in the polarizable continuum model: a new formulation. *J. Comput. Chem.*, 1995, **16** (1), P. 20–30.
[69] Parr R.G., Szentpaly L.v., Liu S. Electrophilicity index. *J. Am. Chem. Soc.*, 1999, **121** (9), P. 1922–1924.
[70] Lin T., Bajpai V., Ji T., Dai L. Chemistry of carbon nanotubes. *Aust. J. Chem.*, 2003, **56** (7), P. 635–651.

NANOSYSTEMS: PHYSICS, CHEMISTRY, MATHEMATICS, 2019, 10 (4), P. 447–455

Investigation of physicochemical properties and radiation resistance of fullerene and endohedral metallofullerene derivatives under the ionizing radiation influence

M. V. Suyasova, A. A. Borisenkova, V. A. Shilin, V. P. Sedov, D. N. Orlova

B. P. Konstantinov Petersburg Nuclear Physics Institute, NRC Kurchatov Institute,
Leningradskaya oblast, Gatchina, 1 mkr. Orlova roshcha, 188300, Russia

suyasova_mv@pnpi.nrcki.ru, borisenkova_aa@pnpi.nrcki.ru, shilin_va@pnpi.nrcki.ru,
victorsedov61@gmail.com, orlova_dn@pnpi.nrcki.ru

PACS 61.48.+c **DOI 10.17586/2220-8054-2019-10-4-447-455**

The radiation resistances of fullerenes C_{60} and C_{70}, end metallofullerenes $Me@C_{2n}$ (n = 30 – 50), derivatives $C_{60}(OH)_{(30)}$ and $Me@C_{2n}(OH)_{30-40}$ (Me = Sm, Eu, Gd, Tb, Ho, Fe, Co), and complexes with biocompatible polymers – polyvinylpyrrolidone and dextrin – $Fe@C_{60}(C_6H_9NO)_n$, $Sm@C_{82}(C_6H_9NO)_n$, $Gd@C_{82}(C_6H_9NO)_n$ and $Fe@C_{60}(C_6H_{10}O_5)_n$ were studied. For the structures irradiated by protons with energies of 100 MeV and 1 GeV, radiation resistance was estimated. The comparison of the results of radiation resistance under irradiation by protons and reactor neutrons at fluencies from 10^{18} to 10^{19} cm^{-2} was carried out. It is shown, that endofullerenols are more stable under the proton and neutron irradiation than initial endofullerenes. The molecules containing Eu, Gd and Sm with large thermal neutron capture cross sections were found to be the most stable under neutron irradiation.The mechanism of rebuilding of secondary endofullerenols Eu, Sm, Gd, as well as other factors' influence on radiation resistance are discussed.

Keywords: fullerenes, endometallofullerenes, fullerenols, fullerene complexes with biopolymers, radiation resistance, proton irradiation, neutron irradiation.

Received: 12 June 2019

Revised: 29 June 2019

1. Introduction

The creation of therapeutic drugs capable of tumor-selective accumulation, currently remains an important task. The most promising in this medicine area are endometallofullerenes (EMF) with a metal atom in a carbon shell that is enclosed and protected from chemical attack of the *in vivo* environment. Furthermore, the irradiation of EMF in the ionizing radiation flow discovers the possibility of creating radiopharmaceuticals for the diagnosis and treatment of cancer.

The currently used chemotherapy methods don't always ensure selective delivery and effective concentration of therapeutic agents in the target tumor tissue. In conjunction with limited monitoring ability to outcome therapeutic procedure results it often leads to complications and also reduces the therapeutic effect.The development of specific tumors MRI contrast agents based on nanotechnology and nanomaterials would increase selectivity and sensitivity of non-invasive tumor-imaging in clinical practice in comparison with traditional imaging methods [1, 2].

Recent studies have found that surface-modified endofullerene $Fe@C_{60}$ with hydroxyl groups are more effective contrast agents than the iron oxide nanoparticles generally used in practical imaging [3–5].

Practical interest in biocompatible iron-containing fullerene-polymer complexes is caused by the possibility of their use for improving resolution in magnetic resonance imaging [5], as well as for molecular-targeted drug delivery in the human body, including for the cancer treatment [6].

However, EMF administration is complicated by the fact that these compounds are insoluble in water in their initial form, so their biomedical application may require modification, such as hydroxylation [7] or synthesis of complexes with water-soluble biocompatible polymers. Polymeric materials are attractive because of number of advantages determining their effectiveness in delivery and therapy techniques – biocompatibility, biodegradability, and interoperability. Basic and the most widely – used compounds for the polymer nanoparticle synthesis are polylactic (PLLA) and polyglycolicacids (PGA), polyethylene glycol (PEG), polycaprolactone (PCL), polyvinylpyrrolidone (PVP). Due to its good solubility in water and the tendency to complex formation, PVP has found wide application in medicine.

In addition, particles of contrast agents should easily penetrate cell membranes. Therefore, control of new potential objects sizes is extremely important for such medical purposes [8].

In this research of fullerene derivatives radiation resistance, fullerene and endometallofullerene complexes with biocompatible polymers have been synthesized. As polymers, the polysaccharide dextrin $(C_6H_{10}O_5)_n$, obtained by

thermal treatment of potato starch, and a synthetic polymer polyvinylpyrrolidone $(C_6H_9NO)_n$ with low molecular weight were chosen.

To develop new generation radiopharmaceuticals, it is also necessary to determine how the properties of water-soluble fullerene and EMF derivatives are altered under radiation exposure. For polymeric materials the effects of ionizing radiation on the physicochemical properties have been well studied [9–12]. However, radiation effect and, most of all, influence of proton irradiation on the fullerenes and EMF polymer complexes has not yet been described.

The main feature of proton irradiation is the possibility of observing a large number of nuclear reactions ((p,α), (p,n), (p,p), (p,γ), (p,d) etc.). The probability of the reactions becomes significant at such proton energy when the permeability of the Coulomb barrier becomes quite large [13, 14]. In this regard, the purpose of our work was to study the radiation resistance of the initial, functionalized by hydroxyl groups and biocompatible polymers (PVP, dextrin) fullerenes and EMF with 3d and 4f-elements under proton and neutron irradiation.

2. Experimental

Thermal evaporation of the composite electrode material, extraction of fullerenes and EMF with an impurity of empty fullerenes $Me@C_{2n}$ + C_{2n} (Me = Sm, Eu, Gd, Tb, Ho, Fe, Co) were carried out according to previously-described methods [12, 15–21].

For fullerene and EMF synthesis, hollow graphite rods with an outer diameter 10 mm and internal diameter 6 mm with different graphite density were used. The electrodes were produced by the Federal State Unitary Enterprise Scientific Research Institute of Electric Carbon Products (graphite density 1.35 g/cm^3) and Chelyabinsk company "Graphite Formula" (1.8 g/cm^3). To obtain EMF composite electrodes were prepared as follows. A powder mixture of metal oxide with graphite was introduced into the cavity of the graphite tube by pressing. The composite electrode was annealed at 1000 °C in vacuum (3 hours) to remove water and organic impurities. The metal content in the composite electrode was in the range 0.8 – 1.0 % at. Thermal vaporization of the composite electrode material was carried out at a constant current of an electric arc (120 – 130 Å) in helium atmosphere (608 mm Hg) according to the methods [18–21].

Figure 1 shows the dependences of higher fullerenes (productivity parameter *PHF*) and endometallofullerenes (productivity parameter *PEMF*) outputs from the helium pressure in the electric arc generator [16]. To determine *PHF* and *PEMF* parameters high performance liquid chromatography (HPLC) data was used. The productive parameter is an integrated value, including the yield of electric arc soot (wt.%), the content of extractable fullerenes (wt.%) and the content of higher fullerenes or EMF according to HPLC. As can be seen from the figure, there are two maxima: the first at 114 mm Hg and the second – in the range of 532 – 684 mm Hg. Therefore, further synthesis was performed at preferred helium pressure – 608 mm Hg. In such a way the values of the *PHF* parameter were increased by 2 – 2.5 times as compared with *PHF* at low pressure.

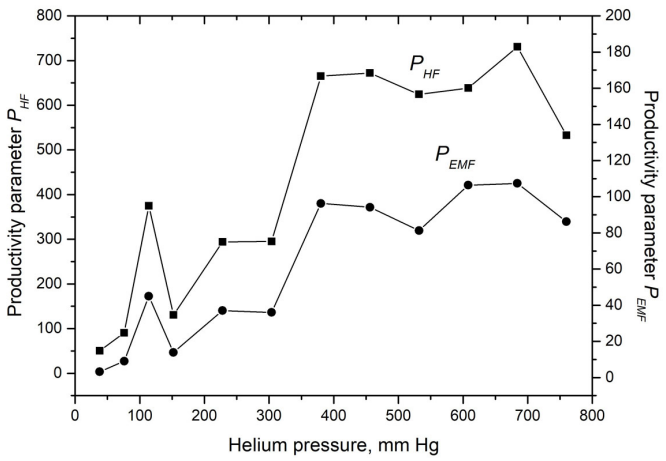

FIG. 1. The dependences of higher fullerenes productivity parameter P_{HF} and endometallo-fullerenes productivity parameter P_{EMF} outputs from the helium pressure [16]

Figure 2 shows the arc current influence on the productivity parameter *PEMF* in the series of EMF synthesis with various elements of the lanthanide group: Sm (1), Gd (2), Dy (3), Eu (4), Ho (5). It can be seen that *PEMF* is influenced by the nature of the metal atom. In the synthesis of EMF with samarium, gadolinium, and europium atoms, the current change in the studied range doesn't lead to changes in the EMF yields. At the same time, for EMF with

dysprosium, the yield decreases, but for holmium, it increases significantly. Thus, the optimum range of the electric arc current at 120 – 130 Å, in which the thermal vaporization of the composite electrode material was stable and accompanied by a high value of the EMF yield (*PEMF*) was established.

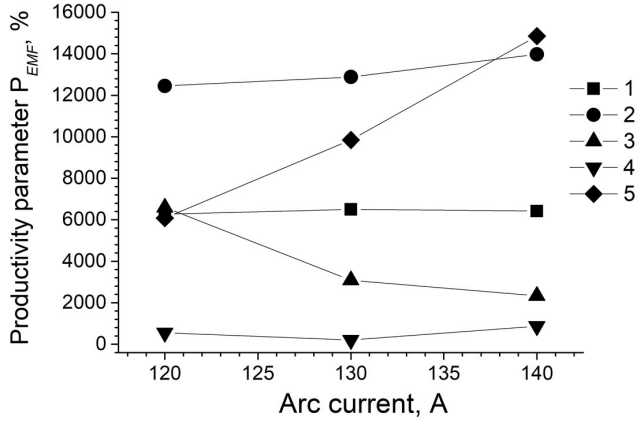

FIG. 2. The arc current influence on the productivity parameter P_{EMF} in the series of EMF synthesis with various elements of the lanthanide group: Sm (1), Gd (2), Dy (3), Eu (4), Ho (5)

For EMF derivatives identification, the IR-spectra of solid samples were obtained by multi-bounce attenuated total reflection FTIR (ATR-FTIR) in the frequency range 400 – 4400 cm^{-1}. The endofullerenol spectra illustrate absorption bands typical for fullerenols [23–25]. Characteristic bands at 1025 – 1150 cm^{-1} can be assigned νC–O bond, reflecting the presence of oxidized units on the carbon cage. The bands at 1340 – 1387 cm^{-1} are assigned to δ_sC–O–H bond. The bands 1515 – 1625 cm^{-1} can be assigned to νC–C and νC=C bonds of the aromatic ring. Valence vibrations of C=O bonds in fullerenols, which formed at the ends of the broken C–C bonds of fullerene are reflected in the range 1647 – 1738 cm^{-1}. The spectra also contain characteristic absorption bands C–C of pure fullerenes C_{60} and C_{70} – 528 and 1428 cm^{-1}.

IR spectra of PVP-complexes are presented at Fig. 3. The spectra demonstrate absorption bands typical for PVP and fullerenes. The bands in the range 1020 – 1097 cm^{-1} are assigned to νC–O bond vibrations. The characteristic bands at 1276 – 1282 cm^{-1} can be referred to the in-plane bending of the C–H bond in PVP. The 1424 cm^{-1} band of scissoring bending of the CH_2 bond in PVP overlaps the 1428 cm^{-1} absorption band of pure fullerene C–C bonds. The double bands at 1502 – 1558 cm^{-1} can be also attributed to the νC–C and νC=C bonds of the aromatic fullerene ring. The band of νC=O group in the PVP lactam at 1657 cm^{-1} is overlapped the band at 1651 – 1662 cm^{-1} of νC=O bonds in fullerenes.

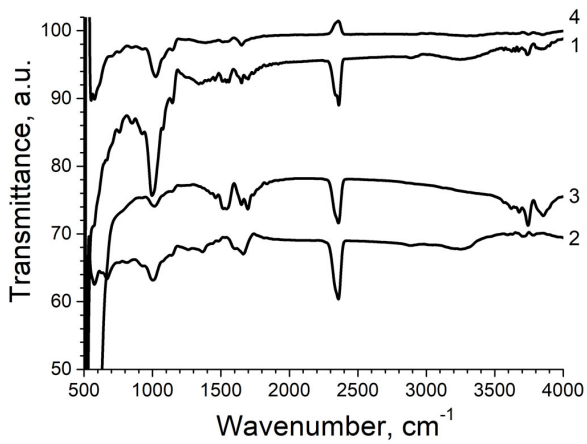

FIG. 3. IR-spectra of pure dextrin $(C_6H_{10}O_5)_n$ (1) and water-soluble dextrin complexes $C_{60}(C_6H_{10}O_5)_n$ (2), Gd@$C_{82}(C_6H_{10}O_5)_n$ (3) and Fe@$C_{60}(C_6H_{10}O_5)_n$ (4)

Similarly, during investigation of dextrin complexes IR-spectra (Fig. 4), the presence of bands that can be attributed both to dextrin and fullerenes was observed. Characteristic band of the polysaccharide molecule skeleton

vibrations shifts from 1001 cm^{-1} to 1007 – 1024 cm^{-1} in the complexes. Strong bands at 1360 – 1387 cm^{-1} in the complexes are referred to δO–H groups in the C–O–H bond. The strong band at 1650 cm^{-1}, caused by the stretching C=O vibrations of non-ionized and ionized acids groups in dextrin, overlaps by stretching vibrations of C=O bonds in fullerenes in the range 1651 – 1662 cm^{-1}. Broad and strong bands in the region of 3253 – 3327 cm^{-1} can be related to the intermolecular hydrogen bonds formation in the complexes.

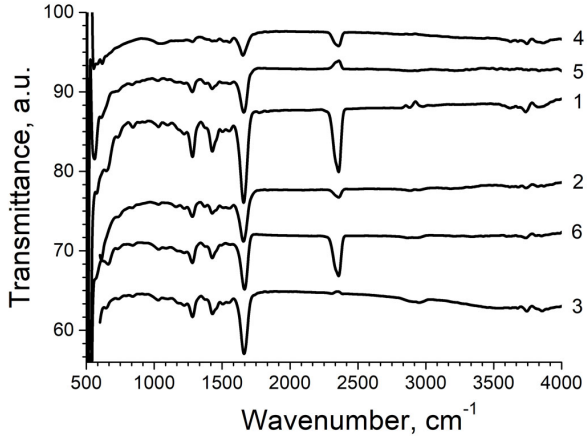

FIG. 4. IR-spectra of water-soluble polyvinylpyrrolidone $(C_6H_9NO)_n$ complexes: $C_{2n}(C_6H_9NO)_n$ (1), Sm@$C_{82}(C_6H_9NO)_n$ (2), Ho@$C_{82}(C_6H_9NO)_n$ (3), Gd@$C_{82}(C_6H_9NO)_n$ (4), Eu@$C_{82}(C_6H_9NO)_n$ (5), Dy@$C_{82}(C_6C_9NO)_n$ (6)

Thus, by the method of IR-spectroscopy it has been able to characterize the obtained compounds and confirm the presence of fullerenes in the synthesized water-soluble complexes.

Earlier studies of the fullerene derivatives radiation resistance under neutron irradiation in the WWR-M reactor zone (NRC "Kurchatov Institute" – PNPI, Gatchina) showed that significant radiation damage and insoluble carbon aggregate formation were observed at fluences exceeding 10^{16} cm^{-2}. In this study, we investigated radiation resistance under proton irradiation on the samples of fullerenes C_{60}, C_{70}, fullerenols $C_{60}(OH)_{30}$, Fe@$C_{60}(OH)_{30}$ and *Me*@$C_{82}(OH)_{38-40}$ (*Me* = Sm, Eu, Gd, Tb, Ho) and complexes Sm@$C_{82}(C_6H_9NO)_n$, Gd@$C_{82}(C_6H_9NO)_n$, Fe@$C_{60}(C_6H_9NO)_n$, Fe@$C_{60}(C_6H_{10}O_5)_n$. The samples were irradiated at the Synchrocyclotron SC-1000 (NRC "Kurchatov Institute" – PNPI, Gatchina) by protons with energies of 100 MeV and 1 GeV (current value was varied from ~0.03 to 1 μA) for a time from 20 to 72 hours. After irradiation, the samples were kept for two months for the decay of short-lived radionuclides.

The γ-spectra of all irradiated samples were recorded using a semiconductor spectrometer with an ultrapure germanium detector (EG&G ORTEC Gamma-X HPGe, detector efficiency at 1 MeV energy – 5 %, resolution – 0.57 keV for 122.06 keV line of ^{57}Co). Unfortunately, it was not possible to identify all γ-lines of reactions (p, x). Therefore, for samples of endofullerenols and EMF complexes, areas of the most intense γ-lines for soluble and insoluble parts were measured. The irradiated samples radiation resistance (S, %) was estimated by the formula:

$$S(\Phi) = \frac{I_{\text{soluble}}}{I_{\text{soluble}} + I_{\text{insoluble}}} \cdot 100\,\%.$$

The radiation resistance (S, %) of samples C_{60}, C_{70}, $C_{60}(OH)_{30}$ was determined as the ratio of the weight of the soluble part to the total weight. It should be noted, that a small amount of impurity elements could present in the irradiated samples. The neutron capture cross section of some of them can be very large. For example, the thermal neutron capture cross section in a natural mixture for Eu isotopes is 4565 barn, for Gd is 48,890 barn and for Sm is 5670 barn [26]. Such impurities were easily identified in the samples irradiated by the neutron, and in some cases by proton irradiation.

3. Results and discussion

Tables 1 and 2 present the radiation resistance of fullerenes C_{60}, C_{70}, EMF *Me*@C_{2n} ($n = 30 - 50$), hydroxylated derivatives $C_{60}(OH)_{30}$ and *Me*@$C_{2n}(OH)_{30-40}$ (*Me* = Sm, Eu, Gd, Tb, Ho, Fe, Co), as well as complexes Fe@$C_{60}(C_6H_9NO)_n$, Sm@$C_{82}(C_6H_9NO)_n$, Gd@$C_{82}(C_6H_9NO)_n$ and Fe@$C_{60}(C_6H_{10}O_5)_n$ under proton irradiation. The capture cross sections for main reactions proceeding at target irradiation by protons was estimated using the semi-empirical method [27] (Table 1).

TABLE 1. Radiation resistance of samples under irradiation by protons of 1 GeV

Formula	Content of $C_{2n}(OH)_{38}$, wt %	Atomic radius, pm [28]	Proton capture cross section σ, barn [26]	Radiation resistance, %
C_{60}	—	—	—	56±4
C_{70}	—	—	—	21±3
$C_{60}(OH)_{30}$	—	—	—	99±1
$Fe@C_{60}(OH)_{30}$	2.4 %	124	0.717	71±1
$Sm@C_{82}(OH)_{38-40}$	3.4 %	181	1.371	41±3
$Eu@C_{82}(OH)_{38-40}$	1.0 %	199	1.378	55±3
$Gd@C_{82}(OH)_{38-40}$	40 %	179	1.414	46±2
$Tb@C_{82}(OH)_{38-40}$	18 %	177	1.420	57±2
$Ho@C_{82}(OH)_{38-40}$	10 %	179	1.456	52±3
$Gd@C_{82}(C_6H_9NO)_n$	—	179	1.414	34±2
$Fe@C_{60}(C_6H_9NO)_n$	—	124	0.717	51±2
$Fe@C_{60}(C_6H_{10}O_5)_n$	—	124	0.717	36±1

TABLE 2. Comparison of radiation resistance for the samples irradiated by 100 MeV and 1 GeV protons

Formula	Radiation resistance, %	
	Proton energy	
	100 MeV	1 GeV
$Fe@C_{60}(OH)_{30}$	44.7±1.0	32±3
$Gd@C_{82}(OH)_{38-40}$	74±4	29±2
$Sm@C_{82}(OH)_{38-40}$	50±2	31±2
$Tb@C_{82}(OH)_{38-40}$	70±2	57±2
$Sm@C_{82}(C_6H_9NO)_n$	39.4±1.5	26±4

As can be seen from Table 1, the cross sections for EMF, including elements Sm, Gd, Eu, during proton irradiation are in the range 1.3 – 1.5 bar. The values of radiation resistance for EMF Sm, Gd, Eu are also varied slightly – 41, 46 and 55 %, respectively. Comparing the radiation resistance values obtained for hydroxylated and polymeric EMF derivatives, it should be noted that the complexes resistance is almost 20 %, and in some cases 30 % less: $Gd@C_{82}(OH)_{38-40}$ (46 %) and $Gd@C_{82}(C_6H_9NO)_n$ (34 %); $Fe@C_{60}(OH)_{30}$ (71 %), $Fe@C_{60}(C_6H_9NO)_n$ (51 %) and $Fe@C_{60}(C_6H_{10}O_5)_n$ (36 %). Probably, the nature of bond formation between polymer and EMF molecules may influence on such difference. It is known, that in the case of a complex with polyvinylpyrrolidone, donor-acceptor interaction is realized, and in the case of a complex with dextrin, a dipole-dipole interaction does [8]. Such complexes turn out to be less resistant to proton irradiation than chemically modified fullerenols with OH-groups. In addition, polymer amorphization at large fluencies can also lead to a decrease their solubility and resistance [29].

Table 2 presents radiation resistance comparison for the samples irradiated by 100 MeV and 1 GeV protons. It has been found that for a series of 1 GeV proton irradiation, the values of radiation resistance are significantly lower than for 100 MeV ones. High-energy protons lead to more damage in the EMF derivatives, which adversely affects the solubility and, as a result, the resistance values.

To compare with the proton irradiation results, the data for neutron irradiation fullerene derivative by fluence $\Phi = 2 \times 10^{18}$ cm^{-2}, at which sample differences appear clearly are shown in the Table 3. As mentioned above, in addition to compounds with 4f-metals, we studied fullerenols with cobalt, obtained for the first time in the synthesis of a new EMFs with paramagnetic 3d-metals [17].

TABLE 3. Radiation resistance of endometallofullerenols under neutron irradiation by fluence $\Phi = 2 \times 10^{18}$ cm^{-2} [30]

Symbol	Formula	Content of $C_{2n}(OH)_{38}$, wt %	Atomic radius, pm	Recoil energy, eV	Neutron capture cross section σ_{th}, barn	Radiation resistance, %
Fe	$Fe@C_{60}(OH)_{30}$	24 %	124	393.3	2.56	47.0±0.5
Sm	$Sm@C_{82}(OH)_{38-40}$	3.4 %	181	260.3	5670	80.1±0.3
Eu	$Eu@C_{82}(OH)_{38-40}$	1.0 %	202	256.1	4565	90.5±0.3
Gd	$Gd@C_{82}(OH)_{38-40}$	40 %	179	136.4	48890	94.1±0.3
Tb	$Tb@C_{82}(OH)_{38-40}$	19 %	177	136.1	23.4	59.3±0.7
Ho	$Ho@C_{82}(OH)_{38-40}$	10 %	176	125.9	64.7	65.6±0.5
Co	$Co@C_{60}(OH)_{38}$	12 %	125	501.5	37.2	48.5±1

The radiation resistance dependence on the accumulated fluence (F) for neutron irradiation of EMF with europium, samarium, thulium, holmium and their water-soluble derivatives are shown at Fig. 5. As a comparison sample, irradiated empty fullerenols $C_{60}(OH)_{30}$ were used. It has been found that for all fullerenols with rare earth elements, the resistance rate is almost an order of magnitude higher than for initial EMFs. The increased radiation resistance of fullerenols $Me@C_{2n}(OH)_{30-40}$ in compare with $Me@C_{2n}$(Me = Sm, Eu, Ho, Co) may be related to EMF becomes more stable and their chemical reactivity decreases with increasing a number of hydroxyls [7]. In addition, resistance depends not only on the number of hydroxyl groups, but also on their distribution on the fullerene shell.

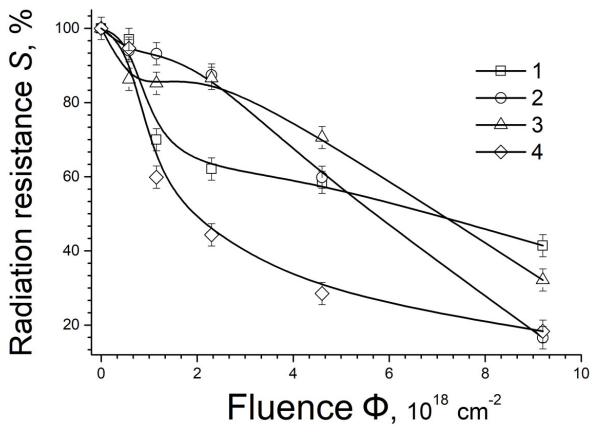

FIG. 5. Dependence of the radiation resistance (S) from fluence (Φ) for irradiated by thermal and fast neutrons fullerenols $C_{60}(OH)_{30}$ (1) and endofullerenols $Eu@C_{82}(OH)_{38-40}$ (2) $Sm@C_{82}(OH)_{38-40}$ (3), $Tm@C_{82}(OH)_{38-40}$ (4)

As shown from the Table 3, it should pay attention to the anomalously high radiation resistance near to 80 % of EMF with samarium, gadolinium and europium, whereas for other EMFs it is about 20 %. Probably, it is due to the electronic properties features of $Sm@C_{2n}$ and $Gd@C_{2n}$ molecules [31, 32].

It is known that $Me^{3+}@C_{2n}^{3-}$ molecules are more stable than $Me^{2+}@C_{2n}^{2-}$. However, captured by a carbon molecule samarium (III) becomes a $Sm^{2+}@C_{76}^{2-}$. Also, among the $Me^{2+}@C_{2n}^{2-}$ molecules, EMF with samarium is the most stable and resistant to external influences, including neutron irradiation. In addition, the EMF with samarium has an important feature – it does not obey the isolated pentagons rule [30]. It is not excluded that this feature may affect the radiation resistance of unique molecule $Sm^{2+}@C_{76}^{2-}$.

The endohedral metallofullerene $Gd@C_{82}$ is also distinguished by high radiation resistance, which may be associated with the anomalouselectronic structure of the molecule [16, 17]. In previous studies [34–36], it was established that Gd^{+3} ion in the carbon cage is located near the hexagonal ring. So EMF molecule $Gd@C_{82}$ acquires the same properties as $La@C_{82}$, $Sc@C_{82}$.

In general, EMF radiation resistance depends on a number of factors: the metal ion radius, shape and size symmetry of EMF molecules, carbon cage electronic structure and incapsulated atom localization, presence of C_{2n} empty fullerenes (see Table 1), and the nonradiative de-excitation of EMF molecules [34, 35]. But none of them explains the high radiation resistance of EMF molecules with Sm, Gd, Eu irradiated by neutrons.

Remarkable that anomalously high resistance ($\sim$80 – 90 %) in the stream of fast and slow neutrons is demonstrated by molecules (Table 2) containing Sm, Eu and Gd elements with large thermal neutrons capture cross sections (5670, 4600, 48,890 barn, respectively). These cross sections are several orders of magnitude larger than cross sections, for example, for Ho, Tb, and Co (64.7, 8.97, 37.2 barn, respectively) [26]. We assumed, that the causes of the anomalously high radiation resistance of EMF with Sm, Eu and Gd could be large cross sections and the secondary processes of EMF reproduction during continued exposure on the samples by thermal neutrons [30].

In this connection, it is of great interest to compare the results of proton and neutron irradiation. As can be seen from Table 1, the cross sections for targets irradiated by protons, including elements Sm, Gd, Eu, are in the range from 1.3 to 1.5 barn, just as for Ho and Tb. The radiation resistance values for EMF Sm, Gd, Eu and Ho, Tb are also not significantly different (41, 46, 55 % and 52, 57, respectively). For samples containing Sm, Eu, Gd, the calculated values of the nuclei recoil energy is approximately 260 eV. Such values are sufficient for the atoms to leave the carbon cage and can penetrate into the surrounding neighboring molecules. Therefore, it can be expected accelerated dissociation of the initial endohedral complexes and, at the same time, new endofullerenol reproduction.

It is interesting to note that the properties of EMF molecules, for example with gadolinium and lanthanum, are the same. Also, the symmetry of the C_{82} cage of $Gd@C_{82}$ is the same as $La@C_{82}$. With all the similarity of gadolinium and lanthanum endofullerenes properties, there is a significant difference – the thermal neutron capture cross section of gadolinium (48,890 barn, unlike lanthanum 8.97 barn) and, as a result, the radiation resistance of gadolinium EMF is much greater than that of lanthanum EMF (80 and 25 %, respectively).

Consequently, it can be argued, that high radiation resistance of Sm, Eu, Gd EMFs in comparison with other EMFs, is associated with a large values of thermal neutrons capture cross sections and new EMFs regeneration during continued exposure on the samples by thermal neutrons. And the influence of electronic structure features of EMF molecules with Sm, Eu, Gd is small or completely absent.

4. Conclusion

Fullerenes, endometallofullerenes $Me@C_{2n}$ (n = 30 – 50) and their hydroxylated water soluble derivatives as $C_{60}(OH)_{30}$, $Me@C_{2n}(OH)_{30-40}$ (*Me* = Sm, Eu, Gd, Tb, Ho, Fe, Co), and also complexes with biocompatible polymers – polyvinylpyrrolidone and dextrin – $Fe@C_{60}(C_6H_9NO)_n$, $Sm@C_{82}(C_6H_9NO)_n$, $Gd@C_{82}(C_6H_9NO)_n$ and $Fe@C_{60}(C_6H_{10}O_5)_n$ have been synthesized and characterized. By the method of IR-spectroscopy, the characteristic bands of water-soluble derivatives have been established and the presence of fullerenes in the new synthesized water-soluble complexes has been confirmed.

In the series of irradiation by neutrons and protons, the radiation resistance evaluation was carried out for fullerenes, EMF, derivatives and complexes: C_{60}, C_{70}, $C_{60}(OH)_{30}$, $Fe@C_{60}(OH)_{30}$ and $Me@C_{82}(OH)_{38-40}$ (*Me* = Eu, H, Sm, Gd, Tb, C), $Fe@C_{60}(C_6H_9NO)_n$, $Sm@C_{82}(C_6H_9NO)_n$, $Gd@C_{2n}$ $(C_6H_9NO)_n$, $Fe@C60(C_6H_{10}O_5)_n$. The values of their radiation resistance under proton irradiation has been determined for the first time. It is shown, that irradiated by protons and neutrons $Me@C_{82}(OH)_{38-40}$ are an order of magnitude more stable than initial EMFs. Thisis probably due to hydroxyl groups that insulate carbon shells and prevent fullerenes carbon-carbon bonding between fullerene molecules.

The irradiation result comparison of Sm, Eu, and Gd EMF-ols with high reactor neutrons capture cross sections (5670, 4600, 48,890 barns, respectively) by neutrons and protons was made. The reaction cross sections for the indicated isotopes of Sm (1.371 barn), Eu (1.378 barn) and Gd (1.414 barn) under proton irradiation are comparable

to Ho (1.456 barn) and Tb (1.420 barn) isotopes. The radiation resistance of fullerenols with Sm, Eu and Gd (41, 55, 46 %.) also differs insignificantly from Ho, Tb and Co (52, 57 %) fullerenols. Consequently, it can unequivocally argued, that high radiation resistance of $Sm@C_{82}(OH)_{38-40}$ and $Gd@C_{82}(OH)_{38-40}$ under neutron irradiation is associated with a large values of thermal neutrons capture cross sections and new EMFs regeneration. In such a way, the influence of electronic structure features of EMF molecules with samarium and gadolinium is small or completely absent.

It can be concluded, at samples variation fundamental differences in the obtained product characteristics haven't been found. It makes it possible using general irradiation conditions for a number of carbon and metal-carbon structures, both initial and water-soluble. It has been established, despite the large proton energy 1 GeV after prolonged irradiation up to 72 hours, up to 50 % EMF molecules remain intact and suitable for the preparation of new radiopharmaceuticals based on fullerenes, EMP and their derivatives for biomedicine.

References

[1] Piotrovsky L.B., Kiselev O.I. *Fullerenes in biology*, Rostock, SPb, 2006, 336 p.

[2] Anokhin Yu.N. Nanotechnologies and nanomaterials for the visualization and therapy of malignant tumors. *The success of modern science*, 2014, **5** (2), P. 14–25.

[3] Lebedev V.T., Kulvelis Yu.V., et al. Biocompatible water-soluble endometallofullerenes: peculiarities of self-assembly in aqueous solutions and ordering under an applied magnetic field. *Nanosystems: physics, chemistry, mathematics*, 2016, **7** (1), P. 22–29.

[4] Lebedev V.T., Szhogina A.A., Bairamukov V.Yu. Small angle neutron and X-ray studies of carbon structures with metal atoms. *J. Phys.: Conf. Series*, 2017, **848**, 012005.

[5] Ferrucci J.T., Stark D.D. Iron oxide-enhanced MR imaging of the liver and spleen: Review of the first 5 years. *Am. J. Roentgenol*, 1990, **155**, P. 943–950.

[6] Kalambur V.S., Longmire E.K. Cellular level loading and heating of superparamagnetic iron oxide nanoparticles. *Langmuir*, 2007, **23**, P. 12329–12336.

[7] Djordjevic A., et al. Review of synthesis and antioxidant potential of fullerenol nanoparticles. *Journal of Nanomaterials*, 2015, **16** (1), 280.

[8] Yevlampieva N.P., et al. Polymer-endofullerene $Fe@C_{60}$ complexes for biomedical applications. *Vestnik SPSU. Physics and chemistry*, 2018, **5** (63).

[9] Aryutkin K.N., et al. Investigation of the structural features of titanium-polymer composite materials irradiated by protons and electrons. *Proceedings of higher educational institutions*, 2011, **1/2**, P. 44–50.

[10] Pavlenko V.I., et al. The phenomena of electrification dielectric polymer composite under the action of a stream of high-energy protons. *Proceedings of the Samara Scientific Center of the Russian Academy of Sciences*, 2010, **12** (4–3), P. 677–681.

[11] Borisov A.M., et al. Modeling the impact of space factors on composite ceramic layers on aluminum alloys. *Physics and chemistry of materials processing*, 2012, **5**, P. 27–30.

[12] Lebedev V.T., et al. Investigation of radiation resistance of fullerenes under irradiation with fast neutrons. *Physics of the Solid State*, 2014, **56** (1), P. 178–182.

[13] Harutyunyan G.S. Acceleration methods for obtaining technetium 99M – technology of preparation and processing of the target and beam control, Diss. for the degree of Ph.D., Yerevan, 2016.

[14] Khmelev A.V., Bakay P.S. Features of 124I cyclotron production for PET diagnostics during proton irradiation of 124TeO film. *Medical Physics*, 2013, **4**, P. 52–59.

[15] Szhogina A.A., Shilin V.A., Sedov V.P., Lebedev V.T. Radiation resistance of endohedral metallofullerenols under neutron irradiation. *Crystallogr. Reports*, 2016, **61** (4), P. 666–669.

[16] Shilin V.A., Lebedev V.T., Sedov V.P., Szhogina A.A. Synthesis and radiation resistance of fullerenes and fullerene derivatives. *Crystallogr. Reports*, 2016, **61** (4), P. 670–674.

[17] Shilin V.A., et al. Fullerenes and Fullerenols survival under irradiation. *Nanosystems: physics, chemistry, mathematics*, 2016, **7** (1), P. 146–152.

[18] Method of producing fullerene C_{70}, Patent.2455230C2 Russia: MPK B01D11/02, B01D15/08, B01D9/00, B82B3/00, B82Y40/00, C01B31/02, Sedov V.P., Kolesnik S.G., N 2010134077/05A, Issue N 19.

[19] Method of producing highly water-soluble fullerenols, Patent.2558121C1 Russia: MPK B82B3/00, B82Y40/00, C01B31/02, C07C29/03, Sedov V.P., Szhogina A.A., N 2014113248/05A, Issue N 21.

[20] Method of producing 3d-metal endofullerene, Patent. 2664133C1 Russia: MPK C01B 32/156, B82B 3/00, B82Y 40/00, Sedov V.P., Szhogina A.A., Suaysova M. V., Lebedev V.T., N 2017108883A, Issue N 23.

[21] Method for producing water-soluble hydroxylated derivatives of endometallofullerenes of lanthanides, Patent. 2659972C1 Russia: MPK C01B 32/156, B82B 3/00, B82Y 40/00, Sedov V.P. Szhogina A.A., Suaysova M.V., Shilin V.A., Lebedev V.T., No. 2016151106A, Issue No. 19.

[22] Shilin V.A., et al. Investigation of the neutron activation of endohedral rare earth metallofullerenes. *Crystallography Reports*, 2011, **56** (7), P. 1192–1196.

[23] Kokubo K., et al. Facile synthesis of highly water-soluble fullerenes more than half-covered by hydroxyl groups. *ACS nano*, 2008, **2** (2), P. 327–333.

[24] Husebo L.O., Sitharaman B., et al. Fullerenols revisited as stable radical anions. *Journal of the American Chemical Society*, 2004, **126** (38), P. 12055–12064.

[25] Chiang L.Y., Upasani R.B., Swirczewski J.W., Soled S. Evidence of hemiketals incorporated in the structure of fullerols derived from aqueous acid chemistry. *Journal of the American Chemical Society*, 1993, **115** (13), P. 5453–5457.

[26] Belanova T.S., Ignatyuk A.V., Pashchenko A.B., Plyaskin V.I. Radiative Neutron. Capture – Handbook. Energoatomizdat, Moscow, 1986, 248 p. (in Russian)

[27] Schmitt C., Schmidt K.-H., Keli'c-Heil A. SPACS: A semi-empirical parameterization for isotopic spallation cross sections. *Physical Review*, 2014, **90** (6), 064605.

[28] Mishenina L.M., Shelkovnikov V.V. Reference materials in chemistry, educational and methodical manual. 2007, URL: https://ido.tsu.ru/schools/chem/data/files/spravochnik.pdf.

[29] Malik B., Panigrahi, S. Effect of amorphization cross-section of polymer due to MeV-proton irradiation. *Applied Physics*, 2012, **1**, P. 20–25.

[30] Dubovskii I.M., et al. Study of the Radiation Resistance of Endohedral Fullerenes of Rare-Earth Elements and Their Water-Soluble Derivatives. *Crystallography Reports*, 2018, **63** (1), P. 132–138.

[31] Dunsch L., Krause M., Noack J., Georgi P. Endohedral nitride cluster fullerenes: Formation and spectroscopic analysis of L3xMxN@ C2n ($0x3$; $N = 39, 40$). *Journal of Physics and Chemistry of Solids*, 2004, **65** (2–3), P. 309–315.

[32] Kobayashi K., Nagase S. Structures and electronic states of M@ C82 (M= Sc, Y, La and lanthanides). *Chemical physics letters*, 1998, **282** (3–4), P. 325–329.

[33] Hao Y., et al. Sm@C2v (19138)-C76: A non-IPR cage stabilized by a divalent metal ion. *Inorganic chemistry*, 2015, **54** (9), P. 4243–4248.

[34] Mizorogi N., Nagase S. Do Eu@C82 and Gd@C82 have an anomalous endohedral structure?. *Chemical physics letters*, 2006, **431** (1–3), P. 110–112.

[35] Liu L., et al. The structural determination of endohedral metallofullerene Gd@C82 by XANES. *Chemical Communications*, 2008, **4**, P. 474–476.

[36] Sebetci A., Richter M. Gd@C82: origin of the antiferromagnetic coupling between endohedral Gd and the free spin on the carbon cage. *The Journal of Physical Chemistry C*, 2009, **114** (1), P. 15–19.

[37] Grushko Y.S., et al. Radioactive metallofullerenes: Hot atom chemistry aspects. *Fullerenes, Nanotubes, and Carbon Nonstructures*, 2006, **14** (2–3), P. 249–259.

[38] Averbukh V., Cederbaum L.S. Interatomic electronic decay in endohedral fullerenes. *Physical review letters*, 2006, **96** (5), 053401.

NANOSYSTEMS: PHYSICS, CHEMISTRY, MATHEMATICS, 2019, 10 (4), P. 456–465

Preparation and properties of CeO_2 sols stabilized by polyvinyl alcohol

S. A. Kuznetsova, A. A. Gordeev, D. A. Fedorishin, V. V. Kozik

Department of Chemistry, Tomsk State University, Tomsk, Siberia, Russia

onm@chem.tsu.ru, gaa1998sukh-mo@mail.ru, strix187@yandex.ru, vkozik@mail.ru

PACS 82.70.Gg **DOI 10.17586/2220-8054-2019-10-4-456-465**

The CeO_2 sols stabilized by polyvinyl alcohol (PVA) were obtained from solution of cerium nitrate (III) in the presence of hydrogen peroxide and ammonia. X-ray diffraction, transmission electron microscopy, the pH metric method, ultraviolet spectroscopy and infrared spectroscopy were used to investigate the compositions and properties of the sols. It was observed that the PVA stabilizes the colloidal solution of cerium dioxide. The stability of the solution depends on the mass content of PVA and pH. The surface of various CeO_2 particles exhibiting the property of an acceptor interacts with OH groups of PVA. CeO_2 sol with 5 wt.% PVA and pH 8.55 (particle size 67 nm) has sun protection properties (UVA/UVB = 0.64) and is characterized by low photocatalytic activity, cytotoxicity and genotoxicity.

Keywords: cerium dioxide sol,sun protection properties, methyl orange, propertiesof sol, polyvinyl alcohol.

Received: 18 July 2019

Revised: 4 August 2019

1. Introduction

Ultraviolet radiation is very important in human life. UV rays have exhibitedanalgesic and sedative effects. Strictly metered-dose UV irradiation stimulates the production of antibodies, thus increasing the resistance of humans to infection.Despite its important role in medicine, the harm of ultraviolet radiation on health exceeds the benefits. The ultraviolet range of the spectrum is conventionally divided into several regions. The most dangerous region of UV-radiation is UV-B radiation with wavelengths ranging from 290 to 320 nm [1]. The long-term effects of UV B on human skin can cause the incidence of skin cancer, including cutaneous melanoma, and photo aging of the skin [2]. Currently, inorganic UV filters based on ZnO and TiO_2 are widely used to protect the skin from well-known carcinogenic effects of ultraviolet light in cosmetic creams, including sunscreen. However, these metal oxides also have some disadvantages; numerous studies have shown that titanium and zinc oxide nanoparticles have high photocatalytic activity [8–10]. The authors of the work [11] showed that titanium dioxide is a photocytotoxic substance to the fibrous region of the skin. Analysis of the literature shows that approximately 20 years ago researchers proposed to use cerium dioxide as an inorganic UV filter [12–14]. This oxide over titanium and zinc oxides has several advantages, among which it should be noted a yellowish color of the substance (close to the skin color), transparency in the visible region of the spectrum, the ability to effectively absorb UV radiation [15,16], decrease in photocatalytic activity with decrease in particle size [17]. Information about CeO_2 photocatalytic activity which provided in the literature is ambiguous. It is believed that CeO_2 has a low photoactivity due to the large band gap (3.19 eV) and rapid recombination of photogenerated charge carriers. Photocatalytic activity is increased due to the addition of metal additives [18] or metal oxides [19–21] in cerium dioxide. The authors of [22] found that CeO_2 nanoparticles reduce oxidative DNA damage caused by UV irradiation. Other authors indicate that cerium dioxide exhibits photocatalytic properties [23–26]. The comparative analysis of literature indicates that state of the oxide surface and the presence of defects [25,26] and Ce^{3+} state [27] in the composition of oxide affect its photocatalytic properties and depend on conditions of its preparation.

Despite the large number of known synthetic methods, today there is an open question related to the development of new methods of producing of CeO_2 sol, which take into account the possibility of high-quality purification from reaction by-products and unreacted substances. Also, important task is searching a new non-toxic stabilizers, allowing obtaining stable sols with biologically relevant pH values. Polyvinyl alcohol (PVA) can be used as such a non-toxic stabilizer, which forms adsorption layers on the surface of dispersed particles and contributes to Van der Waals London interactions. It is known [28, 29] that PVA is usually weakly charged at neutral pH and therefore the stabilization of nanoparticles in the sol is due to electrostatic repulsion.

The aim of this study is obtaining sol of CeO_2 with PVA from cerium (III) nitrate solution and investigating photocatalytic, toxic and sunscreen properties of sol.

2. Experimental procedure

2.1. Materials

Cerium nitrate (III) hexahydrate (purity 99.9 wt.%) was purchased from Novosibirsk plant of rare metals. PVA-16/1 was purchased from company "Nevinnomyssky Azot". The solution of ammonia (25 wt.%) and the solution of hydrogen peroxide (30 wt.%) were purchased in the JSC "Base No. 1". Distilled water was used throughout the experiments. Methyl orange (MO) was purchased from Alfa Aesar.

2.2. Synthesis of CeO_2 sols

Procedure for preparing of light yellow and transparent CeO_2 sols is as follows. The aqueous solution of PVA (5 wt.%) was added to the solution of $Ce(NO_3)_3$ (C = 0.001 M) in a 1:5 volume ratio under magnetic stirring (3 K/min). The aqueous solution of H_2O_2 (30 wt.%) was then added to form a red color of $Ce(OH)_3OOH$. This solution was heated to 90 °C with constant stirring for 45 minutes. The aqueous solution of ammonia (0.03 – 1.5 ml 24 wt.%) was then added and left to mix at 90 °C for more 3 hours. Finally, prepared sol was allowed to air cool. The formation of cerium dioxide can be represented by the following reaction equation:

$$2\mathrm{Ce(NO_3)_3} + \mathrm{H_2O_2} + 6\mathrm{NH_3} \cdot \mathrm{H_2O} = 2\mathrm{CeO_2} + 6\mathrm{NH_4NO_3} + 4\mathrm{H_2O}.$$

The particles of cerium dioxide in the solid phase were obtained by the same method, using 2 wt.% solution of PVA and 0.5 ml solution of ammonia 24 wt.%. After several hours in such light yellow and transparent CeO_2 sol, the oxide particles coagulate and precipitate. The precipitate was filtered, washed with distilled water and dried at room temperature.

2.3. Characterization methods the composition and properties of sols

X-ray diffractograms (XRD) of solid samples (CeO_2) were recorded on a Rigaku Miniflex 600 powder diffractometer (CuKα emission) at a voltage, and current of 40 kV and 15 mA, respectively. The range $2\theta = 10\,^\circ - 90\,^\circ$ at a rate of 2 $^\circ\mathrm{min}^{-1}$ was used to identify the crystalline structure. The samples' phase compositions werefound using the ICSD PDF-2 database. The average crystallite size was calculated from the XRD peak (111) using the Scherer equation: $L = \dfrac{0.9\lambda}{\beta\cos\theta}$. High-resolution images and selected area electron diffraction (SAED) patterns were observed with a JEOL JEM-2100F transmission electron microscope (TEM) operating at 200 kV. The acid–base properties of the CeO_2 surface were studied using a Multitest pH meter by a procedure described in work [30]. The change pH of the cerium dioxide suspension in bidistilled water over time from the moment of formation until reaching the electrochemical equilibrium was detected according to the pH meter readings with the combined glass electrode ESC-10605. IR spectra of PVA, sols of CeO_2 with PVA and dried at 90 °C sols of CeO_2 with PVA were measured on an Agilent Cary 630 FTIR spectrophotometerin the frequency range 400 – 4000 cm^{-1}. The absorption and transmission spectra of sols in the visible region in ultraviolet were removed relative to the aqueous solution of PVA and relative to air (PE-5400 UF spectrophotometer). The average size of cerium dioxide particles in the sol was determined by the "turbidity spectrum" method. The method is based on the use of the Rayleigh equation for colloidal systems with low concentration, the dispersed phase of which does not absorb incident light and is optically isotropic [31].

The photocatalytic activity was evaluated for the decomposition of MO (as a model reaction) under UV light irradiation. For this, we used samples of the dried CeO_2 sol with PVA, as well as samples of CeO_2 particles without PVA, which were separated from the sol with higher oxide content. The 42 ml solution of MO (concentration of 12.760 g/l) and 0.425 g of the sample were placed into a reactor of quartz glass. The mixture was kept in the dark under magnetic stirring for 1 h to reach sorption–desorption equilibrium. Next, the reaction mixture was placed under an I_2 excimer ultraviolet lamp with $\lambda = 342$ nm and exposed to UV radiation for 1 h with constant stirring. Every 10 min, we took an aliquot, which was centrifuged to separate the precipitate, and then the absorbance of the mother liquor was measured. The methyl orange concentration was determined spectrophotometry method on a PE-5400 UF spectrophotometer (cuvette length 10 mm, filming step 1 nm). The wavelength for the measurement was 461 nm, which is the maximum characterized adsorption wavelength of MO. The absolute accuracy limit in the transmission measurement was ± 0.5 %.

In this paper, we performed an analysis of the sun protection characteristics of cerium dioxide sols on middle (UVB) and near (UVA) UV ranges. To assess the effectiveness of skin protection in the UVB range, the UVA/UVB ratio was determined according to [32]:

$$\frac{\mathrm{UVA}}{\mathrm{UVB}} = \frac{\int_{320}^{400} \lg\left(\frac{1}{T(\lambda)}\right) d\lambda / \int_{320}^{400} d\lambda}{\int_{290}^{320} \lg\left(\frac{1}{T(\lambda)}\right) d\lambda / \int_{290}^{320} d\lambda}.$$

TABLE 1. Properties of sols CeO_2 with PVA 5 wt. %

V NH_3 initial, ml	pH value	Particle size, nm	Aggregative stability
0.03	8.11	—	—
0.10	8.31	60	+
0.30	8.46	63	+
0.50	8.55	67	+
1.50	9.49	68	—

The UVA/UVB value is the ratio of the mean absorption in the near and middle UV ranges. The efficiency of the photoprotective action of sol in the UVA range was estimated in units of the critical absorption wavelength [33]:

$$\int_{290}^{c} \lg\left(\frac{1}{T(\lambda)}\right) d\lambda = 0.9 \int_{290}^{400} \lg\left(\frac{1}{T(\lambda)}\right) d\lambda.$$

The study of the sun protection properties of sol was carried out by the method of experimental model of ultraviolet erythema in rats according to the guidelines for preclinical studies of drugs [34]. Male rats (Rattusnorvegicus forma alba) of the Wistar line with an average weight of 250 ± 25 g ($n = 5$) were used as a test system. All rats were divided into two groups – experimental and control. An object of study in the form of an ointment was applied to the hairless area of the skin on the abdomen of animals of the experimental group. On a similar area of the skin of animals of the control group was applied only ointment base c PVA. Acute erythema in experimental animals was caused by irradiation with UV rays of these skin areas at a dose of 1 MED (minimum erythemic dose) [35]. Animals during experimental were under combined etheric-xylazine anesthesia. A laboratory source of ultraviolet radiation with a power of 250 W with a natural ratio of UVA and UVB radiation intensities was used. The irradiated areas were exposed for 10 minutes. The severity of erythema and edema of the skin was assessed visually immediately, after 0.5; 1; 2 and 3 hours, as well as the next day after irradiation on a conditional 4-point scale. The values of scale were: 0 – no erythema, 1 – very weak erythema, 2 – weak erythema, 3 – moderate erythema, 4 – clearly expressed erythema [36].

Genotoxicity of CeO_2 sols with PVA was investigated using Allium cepa test [37]. This technique is based on the influence of the environment on the growth of the roots of Allium cepa bulbs. For the experiment sol of CeO_2 with PVA (prototype), solution of PVA (placebo) and H_2O distilled (control sample) were used. Sol was diluted with water in a ratio of 1:49. The PVA solution was also diluted. Experiments were duplicated 4 times. Bulbs were sprouted for three days while kept at room temperature. On the 4th day the bulbs were taken out. The length of the roots was measured. After that they were fixed with a clamp Clark. For microscopic examination the crushed cytogenetic preparations were prepared by the standard method. The toxic effect was determined by the length of the roots.

The cytotoxicity of the CeO_2sol with PVA was assessed on monocytes isolated from whole blood of a healthy person by magnetic separation using MTT test [38]. CeO_2 tablets of the test substances are poured in to 2 ml of cell suspension and allowed to incubate for 144 hours at 37 °C and 5 % CO_2. For the test, a 96-well plate was used. After 144-hour incubation of monocytes with test substances, 100 μl of cell culture suspension was placed in each well. Before the transfer of cells from the culture cup to the 96-well plate for the MTT test, the cell suspension was re-suspended. Then, 10 μl of MTT working solution was introduced into each well and incubated for another 3 hours in a CO_2 incubator with 5 % CO_2. After 3 hours, the tablet was removed from the CO_2 incubator and the medium in each well was replaced with a DMSO solution. After that, using a tablet reader Tecan Infinite F50, the optical density of each well was determined at 490 nm, and the measured background absorption at 620 nm was subtracted.

3. Results and discussion

3.1. Characteristics sols CeO_2 with PVA

It was found that the stability of sols is influenced by the amount of PVA and the pH value of sols, which is determined by the volume of ammonia. The sols of CeO_2 with PVA up to 5 wt.% and values pH of 8 – 11 are not formed. The oxide particles coagulate in the process of obtaining sols. The stability of CeO_2 sols with 5 wt.% PVA depends on pH values. Some properties of sols and their stability are summarized in Table 1.

The as-prepared sols were light-yellow and transparent. The pH values of the stable sols were slightly basic. The average size of the colloidal particles in such sols was characterized by comparable values. The average colloidal particle size in the filtered sol with pHvalue of 9.49 was 68 nm. Consequently, an increase in the particle size of more than 70 nm in the studied solutions leads to their coagulation. The morphology of the CeO_2 nanocomposites of sols with pH = 8.31 and pH = 8.55 was investigated by the TEM analysis, which is shown in Fig. 1(a, b). Fig. 1 shows that the CeO_2 nanoparticles don't have a pronounced cut and are agglomerated, regardless of the pH of the sols. The degree of agglomeration tends to decrease with increasing of pH sols. Electron diffraction data additionally indicate the polycrystalline nature of nanocomposites. The particle size of CeO_2 in sol with pH = 8.31 is in the range of 2 nm to 4 nm with a narrow particle size distribution. For a sol with pH = 8.55, the size of CeO_2 nanoparticles reaches from 4 nm to 10 nm and particles have a more regular spherical shape.

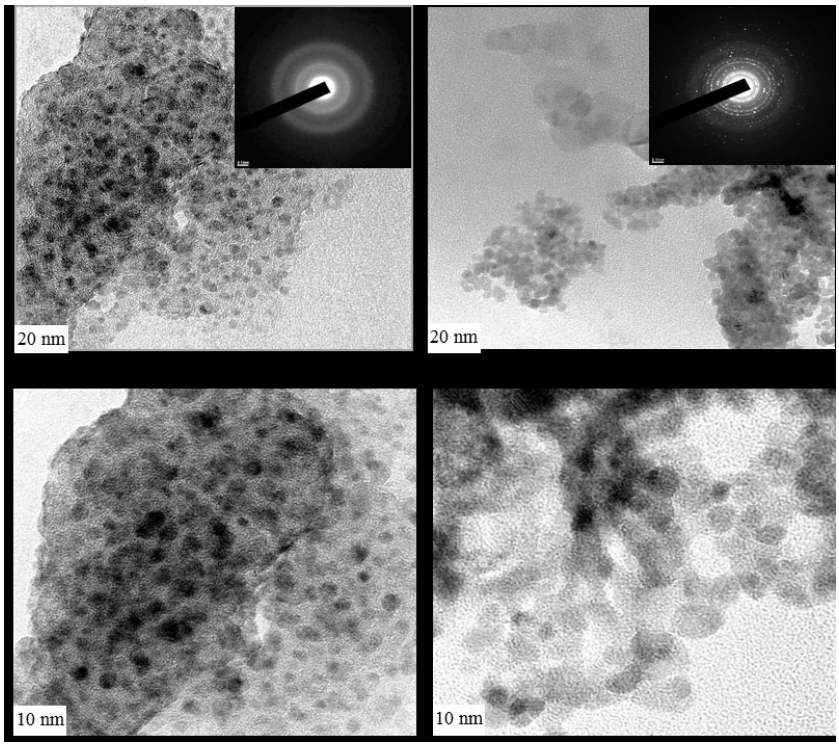

FIG. 1. TEM images of CeO_2 nanoparticles in sols with pH = 8.31 (a) and pH = 8.55 (b)

It is known [39,40], that the sun protection properties increase with increasing the size of particles in the sol. The sol with pH = 8.55 was stable and has a maximum particle size. This sol was investigated in this work.

Figure 2(a) shows the diffraction pattern of CeO_2 particle prepared from sol with PVA 2 wt.%. Diffraction peaks at $2\theta = 28.54352$, 33.09498, 47.46177, 56.349266, 59.089647, 69.44741, 76.61854, 79.03574 and $88.37222°$ correspond to the cubic phase (111), (200), (220), (311), (222), (400) (331) (420) and (422) cerium dioxide (from JCPDS card 00-034-0394).

The average crystallite size is 12.81 nm. Fig. 2(b) shows the diffraction pattern of the dried at 60 °C sol CeO_2 with PVA5 wt.%. (pH = 8.55). This sample contains a lot of amorphous phase. Diffraction peaks are wide and weak. The average crystallite size is 2.07 nm and is comparable with the value of nanocrystallites in sols (TEM).

The analysis of the IR spectra of solid PVA, PVA in an aqueous solution, sol of CeO_2 with PVA and dried at 60 °C sol of CeO_2 with PVA was performed to understand the interaction between CeO_2 and PVA in the sol. Fig. 3(a) shows absorption bands are observed at frequencies characterizing valent O–H bond vibrations (3400 – 3200 cm^{-1}) and C–H bond (2905 cm^{-1}) in the IR spectrum of solid PVA. A wide band of vibrations of O–H bonds indicates the formation of various associates in the solid phase of PVA [41].

The region of vibrations below the frequency of 1500 cm^{-1} corresponds to the valent vibrations of C–O group (1239 cm^{-1}), deformation vibrations of O–H groups (1140 cm^{-1}, 1081 cm^{-1}) and $–CH_2–$ groups of various types: scissors (1414 cm^{-1}); fan and torsion (915 cm^{-1}, 838 cm^{-1} syndio- and isotactic PVA structures, respectively [42] (Fig. 4).

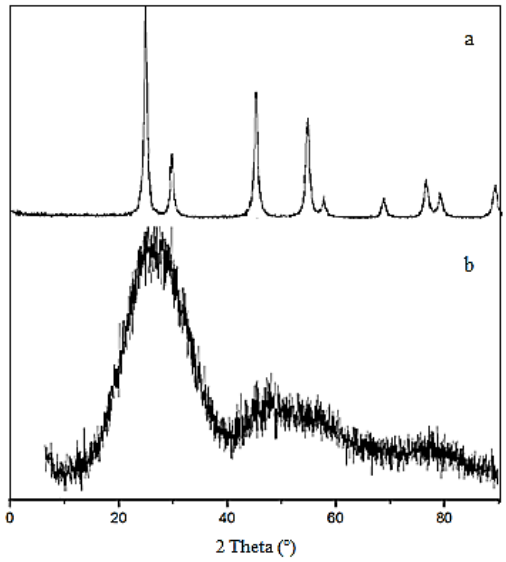

FIG. 2. XRD patterns of coagulated particles CeO_2 (a) and dried sol CeO_2 with PVA (b)

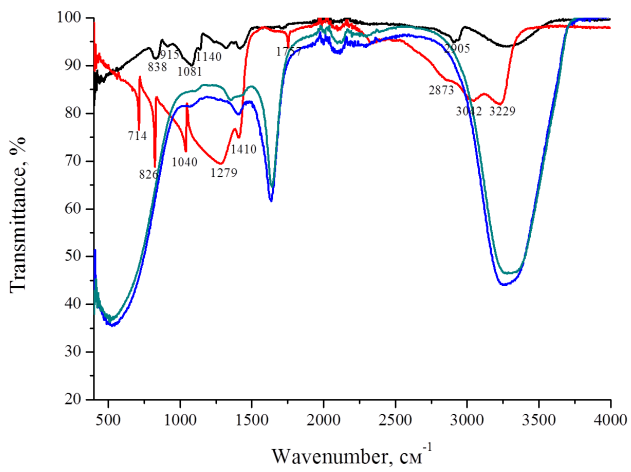

FIG. 3. IR spectra of solid PVA (a —), dried at 60 °C sol of CeO_2 with PVA (b —) PVA in an aqueous solution (c —) and sol of CeO_2 with PVA (d —)

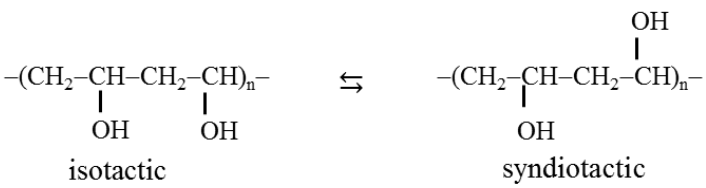

FIG. 4. Structure of the PVA

The frequencies of valent vibration of O–H groups (3042 and 3229 cm^{-1}), C–H group (2873 cm^{-1}), C–O group (1279 cm^{-1}) and deformation vibration of the O–H group (1040 cm^{-1}), $–CH_2$-group of an isotactic structure PVA (826 cm^{-1}) are also observed in the infrared spectrum of the dried sol of CeO_2 with PVA (Fig. 3(b)). In addition, in the IR spectrum of this sample there is apeak at frequency 714 cm^{-1}, which correspond to the deformation vibrations of the $–CH_2–$ group pendulum type. Proof of the interaction of CeO_2 with PVA is a change in the intensity of the observed absorption bands of valent and deformation vibrations and a shift of their wavelengths to the low-frequency region compared to the IR spectrum of PVA without CeO_2, as well as a shift in equilibrium towards the formation of the syndiotactic structure of PVA. The IR spectra of an aqueous solution of PVA and sol of CeO_2 with PVA are less informative because of the very wide absorption bands (Fig. 3(c, d)). However, when comparing them, a difference is also observed, especially in the region of vibrations of $–CH_2–$ groups.

The properties of the surface of CeO_2 were evaluated by the pH-metry method. The samples of CeO_2 obtained from sol with PVA 5 wt.% (pH = 8.11) were placed in bidistilled water and pH values of suspension over time were measured with constant stirring. Fig. 5 shows sharp decrease in pH of an aqueous suspension of CeO_2 to 3.95 during the first 60 seconds.

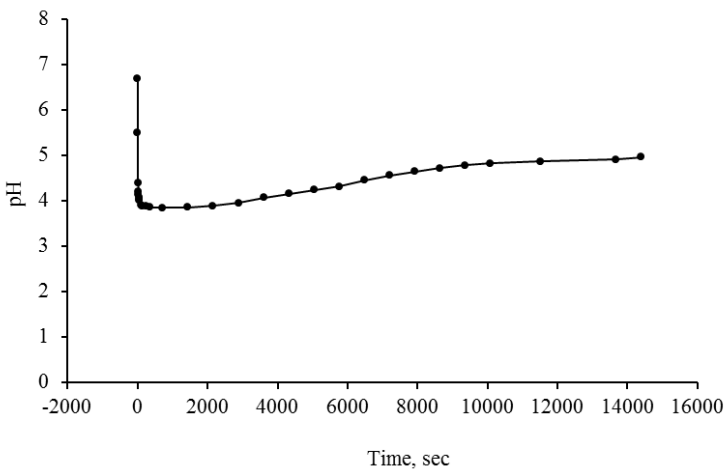

FIG. 5. Changes inpH of CeO_2 suspension over time

Such a change in pH indicates that the process of desorption of adsorbed water molecules from air from the surface of cerium oxide proceeds by the reaction:

$$\mathrm{CeO}_{2-x} \cdot y\mathrm{H}_2\mathrm{O}_{\mathrm{abs}} \leftrightarrows \mathrm{CeO}_{2-x} \cdot y\mathrm{OH}^- + y\mathrm{H}^+.$$

Changing the pH of the aqueous suspension of CeO_2 after 60 seconds isdue to the interaction with the surface of the CeO_2 liquid water by dissociation mechanism. Equilibrium in the reaction of water dissociation on the surface of CeO_2 occurs at pH = 4.96:

$$\mathrm{CeO}_{2-x} + z\mathrm{H}_2\mathrm{O}_{\mathrm{liq.}} \leftrightarrows \mathrm{CeO}_{2-x} \cdot z\mathrm{OH}^- + z\mathrm{H}^+.$$

Consequently CeO_2 is Lewis acid and can hold PVA with donor pairs of OH-group electrons. It is known [43], that part of the oxygen atoms on the surface of CeO_2 are absent in the corresponding crystallographic positions. Oxygen vacancies are formed, the effective degree of oxidation on the cerium atoms decreases to $+3$, and the cerium atoms can exhibit acceptor properties.

Figure 6 shows that in the UV spectrum of sol CeO_2 with PVA there are two broad absorption maxima at 305 and 275 nm, which characterize the content in the oxide not only Ce^{+4} , but also Ce^{+3}, respectively [44], which indirectly indicates the presence of oxygen vacancies in cerium dioxide.

Based on the above, interaction of the PVA with the surface of CeO_2 can be represented following scheme (Fig. 7).

This interaction leads to the fact that the CeO_2 particles are located at a distance from each other and cannot coagulate [45].

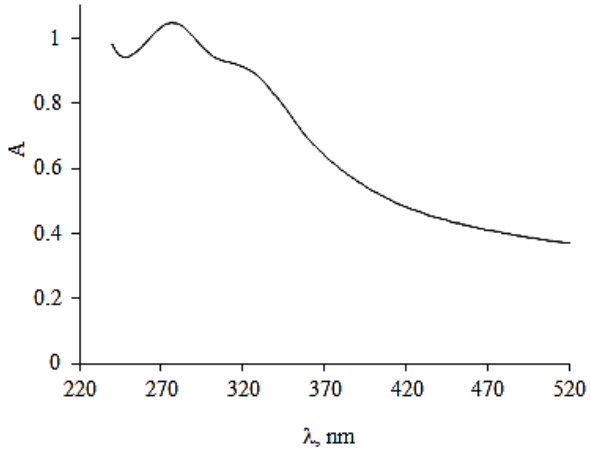

FIG. 6. UV absorption spectrum of sol CeO_2 with PVA

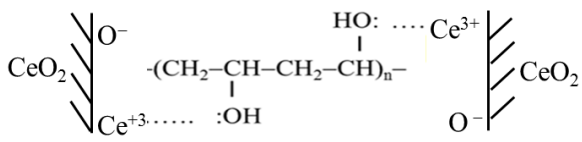

FIG. 7. Scheme of sorption PVA on the surface of colloidal CeO_2 particles

3.2. Photocatalytic, toxic and sunscreen properties sols

Before studying the photocatalytic activity of the samples (dried sol of CeO_2 with PVA and particles CeO_2 without PVA) under ultraviolet radiation, all samples were immersed in the setup reactor and kept in the dark for saturation adsorption. Equilibrium of adsorption was achieved after 60 min. Absorption capacity is possible due to oxygen vacancy defects on the surface of CeO_2, which is confirmed by UV spectroscopy and pH metric analysis. Photocatalytic destruction of an aqueous solution of MO under UV irradiation is shown in Fig. 8.

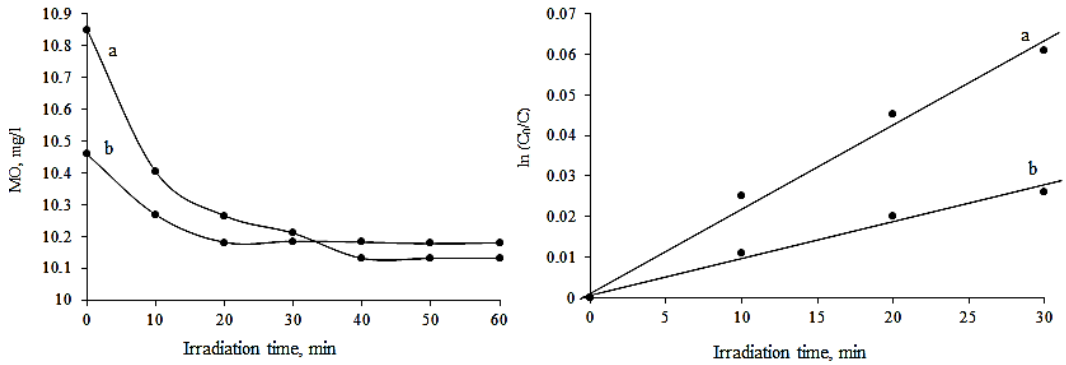

FIG. 8. Photocatalytic degradation of MO aqueous solution by sol CeO_2 with PVA (a) and particles CeO_2 without PVA under UV irradiation

The photocatalytic activity of the dried sol with PVA and particles CeO_2 without PVA obtained from the sol is very small. Fig. 8 shows that the presence of PVA reduces the sorption of MO on CeO_2 particles, but practically doesn't effect on the rate of photocatalysis and the degree of conversion of MO. The destruction of MO in the presence of a sample of CeO_2 with PVA occurs after 40 min and amounts to 6.2 %, and for the sample of CeO_2 without PVA – after 20 minutes is 2.6 %. An increase in the time of exposure to UV radiation (8 h) on the suspension does not lead to further decomposition of MO. Photodegradation reaction MO was adapted to the Langmuir–Hinshelwood model.

The slope of $\ln(C_0/C)$ plotted versus irradiation time (min) indicates the reaction rate constant of the sample. The rate constant of the reaction was measured as $2.2 \cdot 10^{-3}$ min^{-1} for sample with PVA and $0.9 \cdot 10^{-3}$ min^{-1} for sample without PVA. Small photocatalytic activity under UV irradiation is explained by recombination processes [46].

The sol of CeO_2 with PVA is characterized by the value of the critical wave absorption $\lambda_C = 353$ nm, which corresponds to "good" sunscreen properties on the classification of the FDA. Sol TiO_2 1 wt.% is characterized by $\lambda_C = 364$ nm and UVA/UVB = 0.36 [40]. The value of the UVA/UVB for sol CeO_2 with PVA is 0.64. Ultraviolet irradiation of the control areas of the exposed skin of rats for 10 minutes leads to the formation of ultraviolet erythema. Erythema intensity of 4 points is observed in all control areas of the skin with applied ointment base with PVA. After a day, the intensity of erythema drops to 3 points. Irradiation of the test sites applied with ointment base and fill with PVA/CeO_2 causes erythema intensity at 1 point. The absence of erythema (0 points) was observed at all experimental sites a day after irradiation. There were no cases of unscheduled death and complications in animals.

The results of the study of toxicity of sol CeO_2 with PVA and solid CeO_2 obtained from sol are show in Fig. 9. Fig. 9(a) shows, that the sol of CeO_2 with PVA inhibits the growth of the roots of Allium cepa. The results of microscopic examination of the roots of Allium cepa bulbs after their exposure in the sol of CeO_2 with PVA indicate a large number of heterochromatin clumps in the cell nuclei of the experimental samples. This feature is not anomalous, andmay indicate some genotoxic activity forthe sol. Fig. 9(b) shows that the optical density of samples after incubation of monocytes with solid CO_2 is significantly lower than that of intact cells. The average percentage of surviving lymphocytes was only 35.196 %. This indicates the cytotoxicity of cerium dioxide.

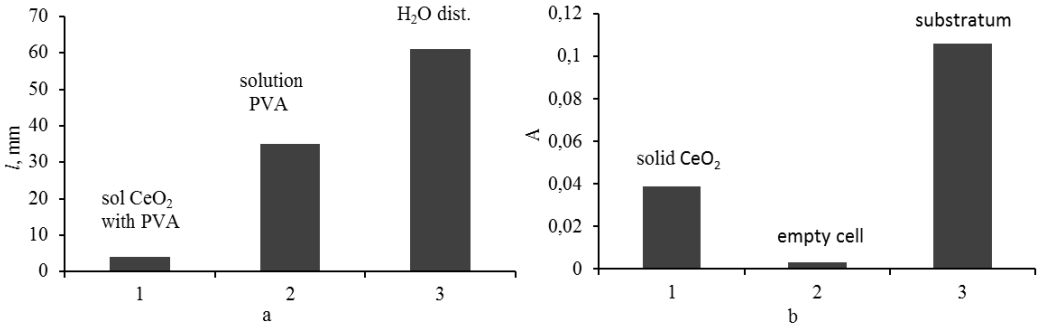

FIG. 9. Toxic properties of samples: the length of the roots of Allium cepa during exposure to samples (a), the optical density of the samples in the MTT test (b)

3.3. Conclusions

The CeO_2 sols stabilized by PVA 5 wt.% were obtained from solution of cerium nitrate (III) in the presence of hydrogen peroxide and different ammonia content. The sol remains stable at pH values ranging from 8.31 to 8.55. The size of colloidal particles in sols increases with increasing pH. The maximum size of the CeO_2 particles, which is not subjected to coagulation in the presence of 5 wt.% PVA is 67 ± 1 nm. The surface of cerium dioxide nanoparticles is characterized by acceptor properties due to the presence of Ce^{+3}. OH-groups of PVA are adsorbed onto the Ce^{+3} surface by a donor-acceptor mechanism. Interaction of PVA with the surface of CeO_2 nanoparticles prevents their agglomeration in the sol.

The sol of CeO_2 stabilized by with 5 wt.% PVA (pH = 8.55) has sun protection properties, which are not inferior to the properties of TiO_2 sols [5]. The sol in anointment base reduces the intensity of erythema in experimental animals irradiated with ultraviolet rays, while displaying low toxicity. The photocatalytic activity of this sol is weakly expressed.

References

[1] Paul J., Meechan C.W. Use of Ultraviolet Lights in Biological Safety Cabinets: A Contrarian View. *Appl. Bios.*, 2006, **11** (4), P. 222–227.

[2] Hirst S.M., Karakoti A.S., et al. Anti-inflammatory properties of cerium oxide nanoparticles. *Small*, 2009, **5** (24), P. 2848–2856.

[3] Bocca B., Caimi S., et al. ICP-MS based methods to characterize nanoparticles of TiO_2 and ZnO in sunscreens with focus on regulatory and safety issues. *Sci. Total. Environ.*, 2018, **630**, P. 922–930.

[4] Serpone N., Dondi D., Albini A. Inorganic and organic UV filters: Their role and efficacy in sunscreens and suncare products. *Inorg. Chem. Acta*, 2007, **360**, P. 794–802.

[5] Barbosa J.S., Neto D.M.A., et al. Ultrafast sonochemistry-based approach to coat TiO_2 commercial particles for sunscreen formulation. *Ultrason. Sonochem.*, 2018, **48**, P. 340–348.

[6] Bairi V.G., Lim J-H., Fong A., Linde Sean W. Size characterization of metal oxide nanoparticles in commercial sunscreen products. *J. Nanopart. Res.*, 2017, **19**, 256.

[7] Reinosa J.J., Docio C.M.Á., Ramírez V.Z., Lozano J.F.F. Hierarchical nano ZnO-micro TiO_2 composites: High UV protection yield lowering photodegradation in sunscreens. *Ceram. Int.*, 2018, **44** (3), P. 2827–2834.

[8] Kryczyk A., Zmudzki P., et al. The impact of ZnO and TiO_2 on the stability of clotrimazole under UVA irradiation: Identification of photocatalytic degradation products and in vitro cytotoxicity assessment. *J. Pharm. Biomed. Anal.*, 2017, **145**, P. 283–292.

[9] Shuwang D., Ling Z., et al. Controllable tartaric acid modified ZnO crystals and their modification determined optical, super hydrophilic/hydrophilic and photocatalytic properties. *J. Alloys Compd.*, 2018, **768**, P. 214–229.

[10] Gu Y., Wang L., et al. Study on Preparation and Functional Finishing of TiO_2 Supported Nano ZnO. *J. Nanosci. and Nanotech.*, 2018, **18** (11), P. 7703–7712.

[11] Wamer W.G., Yin J.J., Wei R.R. Oxidative damage to nucleic acids photosensitized by titanium dioxide. *Free Radical. Biol. Med.*, 1997, **23**, P. 851–858.

[12] Li R., Yabe S., et al. UV-shielding properties of zinc oxide-doped ceria fine powders derived via soft solution chemical routes. *Mat. Chem. Phys.*, 2002, **75**, P. 39–44.

[13] Li R., Yabe S., et al. Synthesis and UV-shielding properties of ZnO- and CaO-doped CeO_2 via soft solution chemical process. *Solid State Ionics*, 2002, **151**, P. 235–241.

[14] Yamashita M.., Kameyama K., et al. Synthesis and microstructure of calcia doped ceria as UV filters. *J. Mat. Sci.*, 2002, **37**, P. 683–687.

[15] Yabe S., Sato T. Cerium oxide for sunscreen cosmetics. *J. Solid State Chem.*, 2003, **171**, P. 7–11.

[16] Herrling T., Seifert M., Jung K. Cerium Dioxide: Future UV-filter in Sunscreen? *SOFW-Journal*, 2013, **139** (5), P. 11–14.

[17] Zholobak N.M., Ivanov V.K., et al. UV-shielding property, photocatalytic activity and photocytotoxicity of ceria colloid solutions. *J. Photochem. Photobiolog. B: Biology*, 2011, **102**, P. 32–38.

[18] Samai B., Chall S., Mati S.S., Bhattacharya S.C. Role of Silver Nanoclusters in the Enhanced Photocatalytic Activity of Cerium Oxide Nanoparticles. *Eur. J. Inorg. Chem.*, 2018, P. 3224–3231.

[19] Apostolescu N., Cernătescu C., et al. Promoting effect of ceria on the catalytic activity of CeO_2–ZnO polycrystalline materials. *Environ. Eng. and Manag. J.*, 2018, **17** (4), P. 765–770.

[20] Usharani S., Rajendran V. RTFM, RTPL and photocatalytic activity of CeO_2/ZrO_2 nanocomposites. *Chin. J. Phys.*, 2017, **55** (6), P. 2588–2596.

[21] Moongraksathum B., Chen Y. CeO_2-TiO_2 mixed oxide thin films with enhanced photocatalytic degradation of organic pollutants. *J. Sol-Gel Sci. Technol.*, 2017, **82**, P. 772–782.

[22] Fujita N., Kamada K. Protective effect of CeO_2 nanoparticles on photo-induced oxidative damage of DNA. *J. Ceram. Soc. Jpn.*, 2014, **122** (1422), P. 141–145.

[23] Laouedj N., Elaziouti A., Benhadria N., Bekka A. CeO_2 nanoscale particles: Synthesis, characterization and photocatalytic activity under UVA light irradiation. *J. Rare Earths.*, 2018, **36** (6), P. 575–587.

[24] Vatanparast M., Saedi L. Sonochemical-assisted synthesis and characterization of CeO_2 nanoparticles and its photocatalytic properties. *J. Mater. Sci. Mater. Electron.*, 2018, **29** (9), P. 7107–7113.

[25] Liu Zh., Li X., et al. Planar-dependent oxygen vacancy concentrations in photocatalytic CeO_2 nanoparticles. *Cryst. Eng. Comm.*, 2018, **20**, P. 204–212.

[26] Gao H., Yang H., Yang G., Wang Sh. Effects of oxygen vacancy and sintering temperature on the photoluminescence properties and photocatalytic activity of CeO_2 nanoparticles with high uniformity. *Mater. Technol.*, 2018, **33** (5), P. 321–332.

[27] Yuán S., Xu B., et al. Development of the visible?Light Response of $CeO_{2?x}$ with a high Ce^{3+} content and Its Photocatalytic Properties. *Chem. Cat. Chem.*, 2018, **10**, P. 1267–1271.

[28] So J-H., Oh M-H., Lee J-D., Yang S-M. Effects of Polyvinyl Alcohol on the Rheological Behavior and Phase Stability of Aqueous Silica Suspensions. *J. hem. ng. Jpn.*, 2001, **34** (2), P. 262–268.

[29] Dippon U., Pabst S., Klitzke S. Colloidal stabilization of CeO_2 nanomaterials with polyacrylic acid, polyvinyl alcohol or natural organic matter. *Sci. Tota. Environ.*, 2018, **645**, P. 1153–1158.

[30] Slizhov Y.G., Matveev T.N., Minakova T.S. Acid-base properties of the surface of chromatographic sorbents modified by metal acetylacetonates. *Russ. J. Phys. Chem. A*, 2012, **86** (3), P. 463–467.

[31] Jalava J., Taavitsaine V., Haario H., Lamberg L. Determination of particle and crystal size distribution from turbidity spectrum of TiO_2 pigments by means of t-matrix. *J. Quant. Spectrosc. Radiat. Transfer*, 1998, **60** (3), P. 399–409.

[32] Department of Health and Human Services. Food and Drug Administration. 21 CFR Parts 347 and 352 [WDocket No. 1978N0038] (formerly Docket No. 78N0038) RIN 0910AF43, Sunscreen Drug Products for Over-the-Counter Human Use; Proposed Amendment of Final Monograph, Federal Register. 2007, **72** (165), P. 49070–49122.

[33] Diffey B.L. A method for broad spectrum classification of sunscreens. *Int. J. Cosmet. Sci.*, 1994, **16**, P. 47–52.

[34] Guo Z., Zhou B., Sun W.L.X., Luo D. Hydrogen – rich saline protects against ultraviolet B radiation injury in rats. *J. Biomed. Res.*, 2012, **26** (5), P. 365–371.

[35] Davies E.K., Boyle Y., et al. Ultraviolet B-induced inflammation in the rat: A model of secondary hyperalgesia? *PAIN*, 2011, **152** (12), P. 2844–2851.

[36] Bishop T., Hewson D.W., et al. Characterisation of ultraviolet-B-induced inflammation as a model of hyperalgesia in the rat. *PAIN*, 2007, **131** (1–2), P. 70–82.

[37] Liman R., Acikbas Y., Ciğerci I.H. Cytotoxicity and genotoxicity of cerium oxide micro and nanoparticles by Allium and Comet tests. *Ecotoxicol. Environ. Saf.*, 2019, **168**, P. 408–414.

[38] Shishatskaya E.I., Dragana N., et al. Short-term culture of monocytes as an in vitro evaluation system for bionanomaterials designated for medical use. *Food Chem Toxicol.*, 2016, **96**, P. 302–308.

[39] Popov A.P., Priezzhev A.V., Lademann J., Myllyla R. TiO_2 nanoparticles as an effective UV-B radiation skin-protective compound in sunscreens. *J. Phys. D*, 2005, **38**, P. 2564–2570.

[40] Cross S.E., Innes B., et al. Human skin penetration of sunscreen nanoparticles: In-vitro assessment of a novel micronized zinc oxide formulation. *Skin. Pharmacol. Physiol.*, 2007, **20** (3), P. 148–154.

[41] Prosanov I.Y., Bulina N.V., Gerasimov K.B. Complexes of polyvinyl alcohol with insoluble inorganic compounds. *Phys. solid state*, 2013, **55** (10), P. 2132–2135.

[42] Prosanov I.Y., Matvienko A.A. Study of PVA thermal destruction by means of IR and RAMAN spectroscopy. *Phys. solid state*, 2010, **52** (10), P. 2203–2206.

[43] Tsunekawa S., Sivamohan R., et al. Structural study on monosize CeO_{2x} nano-particles. *Nanostruct. Mater.*, 1999, **11**, P. 141–147.

[44] Khalipova O.S., Kuznetsova S.A., Kozik V.V. Composition and properties of CeO_2–SiO_2 composite films prepared from film-forming solution. *Russ. J. Inorg. Chem.*, 2014, **59** (9), P. 913–917.

[45] Li Z., Aly Hassan A., Sahle-Demessie E., Sorial G.A. Transport of nanoparticles with dispersant through biofilm coated drinking water sand filters. *Water Res.*, 2013, **47**, P. 6457–6466.

[46] Saadat-Monfared A., Mohseni M. Polyurethane nanocomposite films containing nano-cerium oxide as UV absorber; Part 2: Structural and mechanical studies upon UV exposure. *Colloids Surfaces A*, 2014, **441**, P. 752–757.

NANOSYSTEMS: PHYSICS, CHEMISTRY, MATHEMATICS, 2019, 10 (4), P. 466–474

Photoelectrochemical cell performance Cu doped ZnO photoanode sensitized by xanthene dyes

Deepak Kumbhar[1,4], Sarita Kumbhar[2], Sagar Delekar[3], Rekha Nalawade[3], Avinash Nalawade[4]*

[1]Department of Chemistry, Raje Ramrao Mahavidyalaya, Jath, 416 404,
affiliated to Shivaji University Kolhapur 416004, MS, India
[2]Department of Physics, Rajashri Chhatrapati Shahu College, Kolhapur, 416 005,
affiliated to Shivaji University Kolhapur 416004, MS, India
[3]Department of Chemistry, Shivaji University, Kolhapur, 416 004, MS, India
[4]Department of Chemistry, Lal Bahadur Shastri College, Satara, 415 002,
affiliated to Shivaji University Kolhapur 416004, MS, India
*avinashnalawaderes@gmail.com

DOI 10.17586/2220-8054-2019-10-4-466-474

In this study transition metal Cu is doped into ZnO framework at 1, 3 and 5 mol% concentrations by sol-gel method and Photoelectrochemical performance under sensitization is recorded. Structural analysis XRD and Raman gives information of wurtzite structure formation without any mislaid peaks. It also informs decrement in crystalline size and lattice parameters as doping level increases. SEM and EDAX provide nono structure formation with appropriate compositions. Optical analysis by FTIR and PL gives peaks at expected positions while DRS UV-visible peaks show humps with red shift due to effect of Cu doping. After structural and morphological study NPs are deposited on conducting glass surface of FTO substrate by doctor blade method and sensitized with mixed xanthene dyes (Eosine Y., Rhodamine B., and Rose Bengal) for 12 h and photoelectrochemical cell performance are recorded under solar simulator under standard AM 1.5 one sun illumination in that 1 % Cu/ZnO photoanode shows good performance as compared to other.

Keywords: Sol-gel, Cu doped ZnO NPs, xanthene dyes, sensitization, photoelectrochemical cell.

Received: 2 August 2019

Revised: 10 August 2019

1. Introduction

The role of energy is crucial in the human development in all areas of human activity, such as economic, ecosystem, employment, prosperity and equity. For many years, human have utilized several resources to generate energy and fulfil all needs for better life. But, currently, because of increased population the use of traditional resources for energy are not adequate and this creates an issue of global warming [1,2]. Thus, humanity is continuously in the search of alternative energy sources with environmental friendliness. Many research groups already worked on solar, wind, hydro, bio and geothermal energies and catch beneficial outcomes [3–5]. Still this era is under increased pressure to obtain satisfactory outcomes. Solar energy is considered to be more beneficial as compared to other renewable energy sources due to its key benefits of clean, non-polluting, noise less, low maintenance, long life etc. [6, 7]. To acquire this energy role of PV devices are originated. In that solar cell play role to convert solar radiation into electricity. The desire of human fabricated first to fourth generation solar cells with diverse materials and technologies. In the market silicon based solar cells existing but it has limitation to use in wide range due to environmental and cost consequence. O'Regan and Grätzel in 1991 invented low cost and simple construction based dye sensitized solar cell (DSSC). In comparison to silicon cells, it is still in a state of growth to get high efficiency and stability. Researchers are currently working on this and have formulated a number of nanomaterials [8].

In DSSC type of photoanode, electrolyte and sensitizer are crucial to bring beneficial outcome. TiO_2 is typically used photoanode material however it has limitations of carcinogenic nature, lower electron lifetime and transport rate [9–11]. So, research groups worked on several alternative materials. ZnO is another choice with parallel properties of TiO_2 having wide band-gap of 3.37 eV at room temperature, 60 meV of electron binding energy [12, 13], higher electron mobility, anti-oxidation and chemically stability. However, considerable research has revealed lower performance of ZnO based DSSC due to some limitations of ZnO. To circumvent these limitations, different strategies have been developed such as modified fabrication process, utilization of different morphological materials, mixing of other nanomaterial, utilization of new dyes, co-sensitization method, material increased porosity and use of varied electrolyte in DSSC. Doping is one more strategy that offers an effective means to enhance and control the structural, optical and electrical properties of ZnO NPs. Already different dopants (Al, Mn, Cd, Mg, Ni, Ga, Ag, Cr etc.) in the lattice structure of ZnO utilized to boost its properties [14–18]. Doping is one of the methods to modify the band

gap of ZnO and shift to the large visible spectrum of light by creating energy levels inside the band gap [19–21]. Our study focused on doping of Cu due to its large solubility in ZnO matrix, rich electronic states and close ionic radius. Until now, various researchers studied and reported effect of Cu doping on ZnO with respect to morphological and optical properties [22–27]. Assimilation of Cu dopants in ZnO is carried out at low level i.e. 1, 3 and 5 mol% for decrement of band gap and to improve electron shifting. This was successfully carried out by simple sol-gel approach. After structural, morphological and optical analyses, photoanodes were prepared by reported doctor blade technique. To improve DSSC performance and reduce Zn^{2+}-dye aggregation photoanodes were sensitized in metal free sensitization in xanthene dyes and the photoelectrochemical cell performance measured under solar simulator standard AM 1.5 one sun illumination visible illumination of 100 mW/cm^2. Among employed photoanodes 1 % Cu/ZnO shows notable efficiency of $\eta = 0.1165$ % and proves fruitful effect of doping and Co-sensitization.

2. Experimental section

2.1. Materials

All the chemicals i.e. zinc acetate dihydrate (Sigma-Aldrich), copper acetate monohydrate (Sigma-Aldrich), sodium dodecyl sulfate (SDS of SD Fine), ammonium hydroxide (SD Fine) used in the experiment were of analytical grade without any prior treatment.

2.2. Synthesis of Cu doped ZnO NPs by sol-gel method

For this 0.2 M zinc acetate dihydrate (for doping with stoichiometric doping amount of copper acetate monohydrate) solution was prepared and 0.02 M of SDS mixed into it with continuous stirring. To this solution ammonium hydroxide was added drop wise till pH of solution becomes near to 8.0 ± 0.1. Here formation of zinc hydroxide sol takes place, which was further dried at 80 °C for 9 h to get gel. The obtained gel was calcinated at 350 °C for 3 h in a muffle furnace, results in Cu doped ZnO NPs.

3. Results and discussion

3.1. X-ray diffraction analysis

The XRD spectra (Fig. 1) indicate pure and Cu doped (1, 3 and 5 mol%) ZnO NPs. XRD patterns of both undoped and Cu doped samples were found to be exactly same. This data was found to be of hexagonal wurtzite phase and JCPDS card No. 36-1451 [25, 28, 29]. The peak intensities of (100), (002), (101), (102), (110), (103), (200), (112), (201), (004) and (202) in the XRD spectrum are slightly decreased as doping concentration increases this can be also attributed to the replacement of Zn^{+2} by Cu^{+2}. The crystalline size of Cu doped ZnO NPs were obtained by fitting the XRD data to the Debye Scherrer formula and full-width at half-maximum (FWHM) of the XRD lines [30]:

$$D = \frac{0.9\lambda}{\beta \cos\theta}, \tag{1}$$

where λ is the wavelength of X-ray (1.5406 Å), β is the full-width at half-maximum in radian, and θ is the angle of diffraction. It is seen that average crystalline size (D) decreased from 60 to 31 nm as Cu doping. The variation in

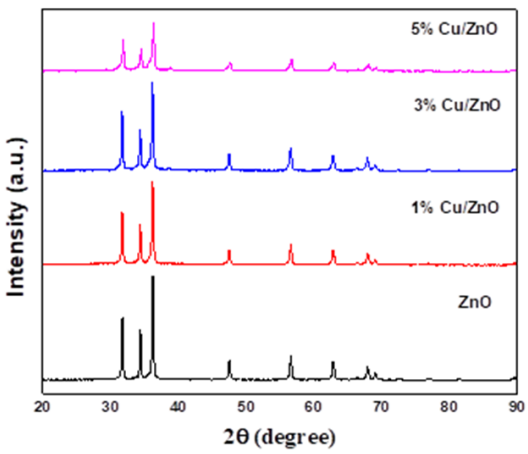

FIG. 1. XRD patterns of pure ZnO and 1, 3, 5 mol% Cu doped ZnO Nanoparticles

the grain size by doping ZnO with Cu^{2+} up to 5 mol% is mainly due to the alteration in the host ZnO lattice, which decreases the nucleation and subsequent growth rate by the addition of Cu concentrations up to 5 mol% as same in some reference [26, 27]. By increasing the Cu content, the carrier concentration and mobility in the conduction band of the semiconductor also increases [31]. The lattice parameters (a, c), volume (V), c/a ratio and crystalline size obtained are given in Table 1. It conclude that values of lattice parameters and volume slightly decreases as doping contartion increases from 1 to 5 mol%. This reduction is due to successful replacement of Zn^{2+} with ionic redii 0.74 Å by Cu^{2+} with ionic redii 0.73 Å [32–35].

TABLE 1. Lattice constant a, c volume of unit cell (V), ratio (c/a) and crystallite size (D) of ZnO and Cu/ZnO sample

Samples	**Lattice Parameter (Å)**		**Volume (Å^3)**	**c/a ratio**	**Crystalline size**
	a	c			**(D) nm**
ZnO	2.9495	5.1065	44.4244	1.732	60
1 % Cu/ZnO	2.9441	5.0993	44.2023	1.732	40
3 % Cu/ZnO	2.9440	5.0961	44.1696	1.732	37
5 % Cu/ZnO	2.9336	5.0811	43.7300	1.732	31

3.2. Raman spectroscopy

Raman spectra in the range of 250 – 600 cm^{-1} of doped and undoped ZnO are showed in Fig. 2. In this range, there are five main bands at 326, 400, 433, 572, 589 cm^{-1}, corresponding to A_1(TO), E_1(TO), E_2(high), E_1(low) and A_1 (low) for ZnO. The strong and sharp band observed at 433 cm^{-1} corresponds to the nonpolar optical phonons E_2 (high) mode of ZnO attribute that incorporation of Cu in ZnO leads to a decrease in crystal quality, but there is no change in wurtzite crystal structure. The features located at 326 and 400 cm^{-1} correspond to the multi-phonon scattering process E_2 (high)–E_2 (low) and A_1 (phonons of ZnO crystal, respectively). The signal located at 572 cm^{-1} could be attributed to the E_1, longitudinal optical phonon (LO) feature, associated with the formation of defects such as oxygen vacancy. According to the literature, as the Cu doping concentration was increased, intensities of spectra decreased and the A_1 transverse optical phonon (TO) mode vanished [36]. It could be successfully explained in terms of resonant anharmonic interaction of the high E_2 mode with a band of combined transverse and longitudinal acoustic modes, as the steep variation of the two-phonon density of states around the high E_2 frequency leads to a distorted phonon line shape [37, 38].

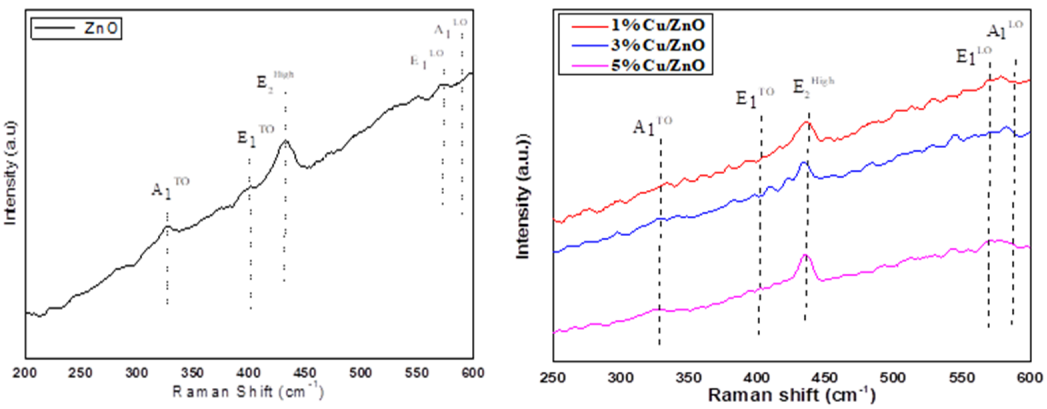

FIG. 2. Raman spectra of the ZnO and Cu doped ZnO NPs

3.3. Scanning electron microscope (SEM) and Energy Dispersive X-Ray Analysis (EDX)

Figure 3 showed that the ZnO and Cu doped ZnO NPs are in regular or almost in granular shape, though some agglomerations have been observed. It was observed that doping of Cu in ZnO slightly affect the size of ZnO NPs, as also suggested by XRD study. It is due to less ionic radii (0.87 Å) of Cu than Zn (0.88 Å) [31]. Fig. 3(b) shows the EDAX spectra of ZnO and Cu doped ZnO nanoparticles. The elements of Zn, O and Cu in doped samples clearly observed. The Compositions are given below (Table 2).

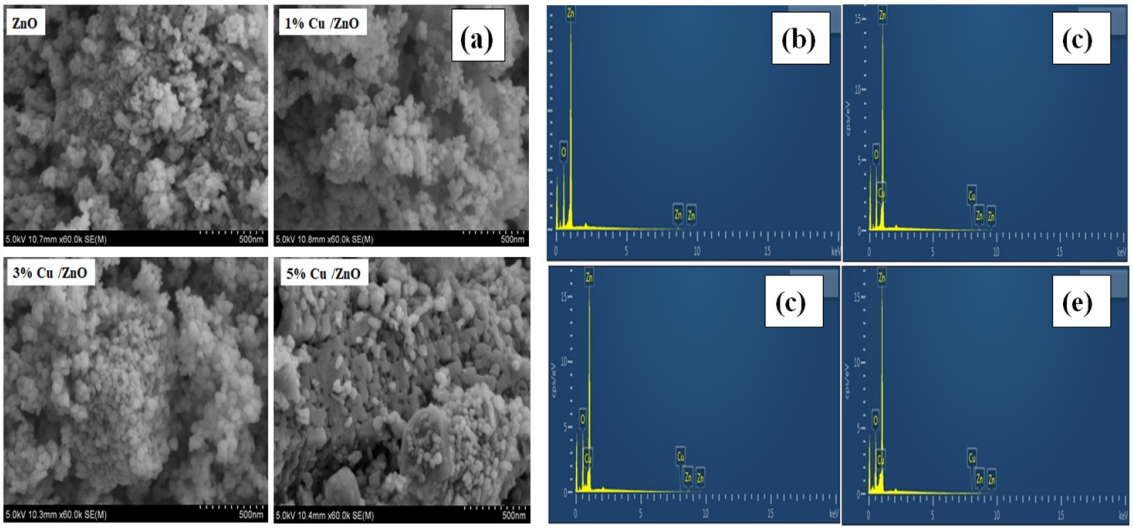

FIG. 3. SEM images of 1, 3 and 5 % Cu/ZnO doped ZnO NPs (a); EDAX images of 1, 3 and 5 % Cu/ZnO doped ZnO NPs (b)

TABLE 2. Composition of ZnO and Cu doped ZnO nanoparticles

Sample	O (Wt %)	Zn (Wt %)	Cu (Wt %)
ZnO	16.84	83.16	—
1 % Cu/ZnO	17.12	82.10	0.87
3 % Cu/ZnO	16.25	81.15	2.60
5 % Cu/ZnO	16.55	79.05	4.40

3.4. Fourier transform infrared spectroscopy (FTIR) studies

The broad absorption peaks in Fig. 4 around 3500 cm^{-1} attributed to normal polymeric O–H stretching vibration of H_2O in Cu–Zn–O lattice and the weak bands from 500 to 881 cm^{-1} are assigned due to the change in the microstructural features Cu doping into Zn–O lattice that shifts frequencies. Copper atom is slightly lighter than Zn atom so, according to the well-established theories of vibrational modes in mixed crystals the substitution should result in an upward shift of the fundamental transverse optical phonon mode. The frequency shift towards the lower side reveals the substitution of Cu^{2+} ion into the Zn–O lattice [39, 40].

3.5. Photoluminescence spectroscopy

ZnO and Cu doped ZnO PL spectra in Fig. 5 displays peaks at ∼300 nm excitation wavelength, in the UV range, which is associated with exciton emission i.e. band edge emission (NBE), another in the visible range at around ∼600 nm, which originates from electron–hole (e–h) recombination at the deep level (DLE) caused by oxygen vacancy or zinc interstitial defect [29, 41]. The lower intensity of UV emission in ZnO than Cu doped ZnO indicated suppression in recombination of photogenerated charge carriers that enhances optical properties [42, 43]. Here 1 % Cu/ZnO samples showed lower recombination rate as compared to other samples.

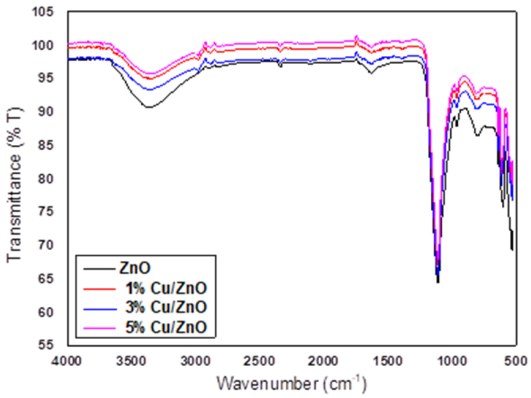

FIG. 4. ATR-FTIR spectra of ZnO and Cu doped ZnO NPs

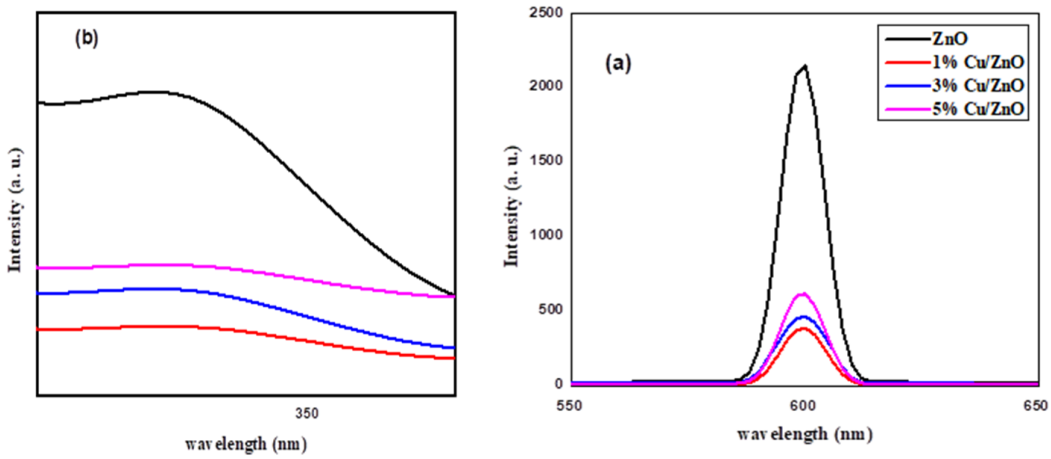

FIG. 5. Photoluminescence spectra of ZnO and Co doped ZnO NPs

3.6. UV-Visible diffuse reflectance spectroscopy studies (DRS UV-Visible) and Tauc plots

The UV-Vis absorption spectra of pure and Cu doped ZnO samples were recorded and presented in Fig. 6(a) The spectra shows increase in absorption ability and red shift with humps as incorporation of Cu content from 1 to 5 mol%. It can be interpreted that there is the formation of new energy levels in the band gap, thereby leading to spectral red shift [23,44]. Therefore the red shift of Cu doped ZnO helps to electron transfer from Zn*3d* to O*2p*. It is observed that the doping effect narrows or shrinks the band gap of ZnO as increasing Cu doping densities.

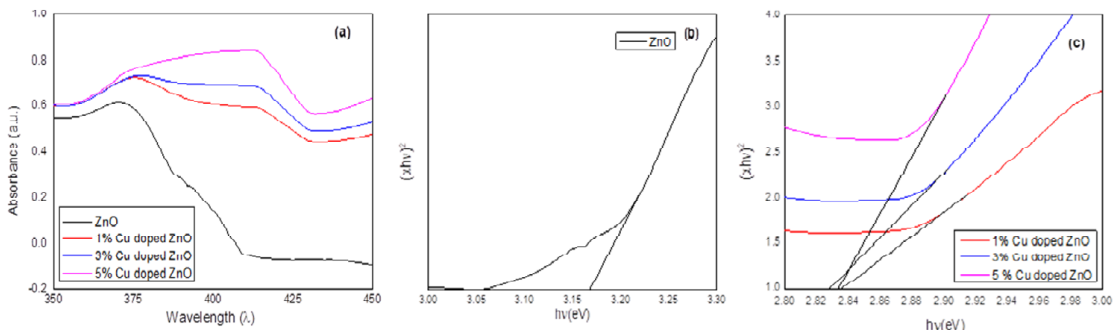

FIG. 6. UV-Visible diffuse reflectance spectrum of ZnO and Cu doped ZnO NPs (a); Tauc plots for band gap determination (b,c)

The Tauc plots Fig. 6(b, c) are drawn using Tauc equation $(\alpha h\nu)^2 = A(h\nu - E_g)$, where, ν is the frequency of light, A is a constant, h is the Planck's constant and E_g is energy band gap of the prepared samples. By extrapolating the line we measure the band gap of prepared ZnO NPs. The computed band gap values are 3.16 for ZnO and 2.84, 2.83, 2.78 eV for 1, 3 and 5 mol% Cu/ZnO respectively i.e. the band gap decreases from 1 to 5 mol%. The absorption edge of samples were associated to the presence of the acceptor level produced by Cu, over the valance band of ZnO [31, 45].

4. Preparationand investigation of dye solution

It is reported that ZnO DSSC are almost unstable in acidic and metal based dyes. Here, we applied sensitization with organic xanthene dyes contain Rose Bengal, Eosin Y. and Rhodamine B. dye. 1:1 proportion of acetonitrile and tert-butanol used to prepare dye solution. UV-Vis absorption investigation Fig. 7 show absorption in visible region at 518, 530, and 535 nm for Eosin Y., Rose Bengal, and Rhodamine-B. Individual dyes have limited absorption so we used mixed dye concept that gives better absorption in the range of 500 – 600 nm which is confirmed by its absorption study [46]. So such sensitization solution is prepared by equal mixing of dyes and sensitization of photoanodes are done.

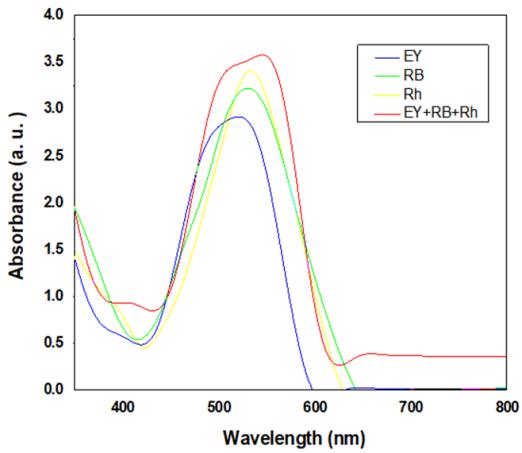

FIG. 7. Optical absorbtion spectra study of single Eosine Y., Rose Bangal, Rhodamine B. dyes and mixed dye in tert-butyl alcohol/acetonitrile

5. Fabrication of photoelectrochemical cell and I–V measurements

5.1. Construction of photoelectrode

Photoelectrodes are prepared by simple doctor blade method [47]. Here NPs were sonicated in alcohol and ethyl cellulose for 30 min. Later α terpineol was added (Sigma-Aldrich) to obtain a better suspension. This suspension deposited on FTO glass surface at conducting side and annealed it at 350 K for 2 h.

5.2. Construction of cell and I–V measurement

The prepared photoanodes are sensitized in dye solution for 12 h and washed with alcohol to remove excess dye. The photoanode of average area 1.0 cm^2 act as working electrode and Pt-coated FTO of similar area were used as the counter electrodes. I–V measurements are taken under under solar simulator standard AM 1.5 one sun illumination visible illumination of 100 mW/cm^2 using a Keithley source meter (model 2460).

First ZnO photoanode without sensitization directly employed in electrolyte solution of 0.1 M lithium iodide and 0.05 M iodine in propylene carbonate then results recorded in dark as well as in light. Later sensitization of ZnO and Cu doped ZnO samples for 12 h carried out and alter I–V measurements are taken Fig. 8. All outcomes i.e. open circuit voltage (V_{oc}), short circuit current density (I_{sc}) and fill factor (FF), efficiency in percentage (η %) are recorded in tabular form in Table 3. It displays worthy efficiency after sensitization i.e. the highest efficiency obtained for 1 % Cu/ZnO of $\eta = 0.1156$ % and other with notable efficiencies 0.0438 and 0.0471 % for 3, 5 % Cu/ZnO respectively.

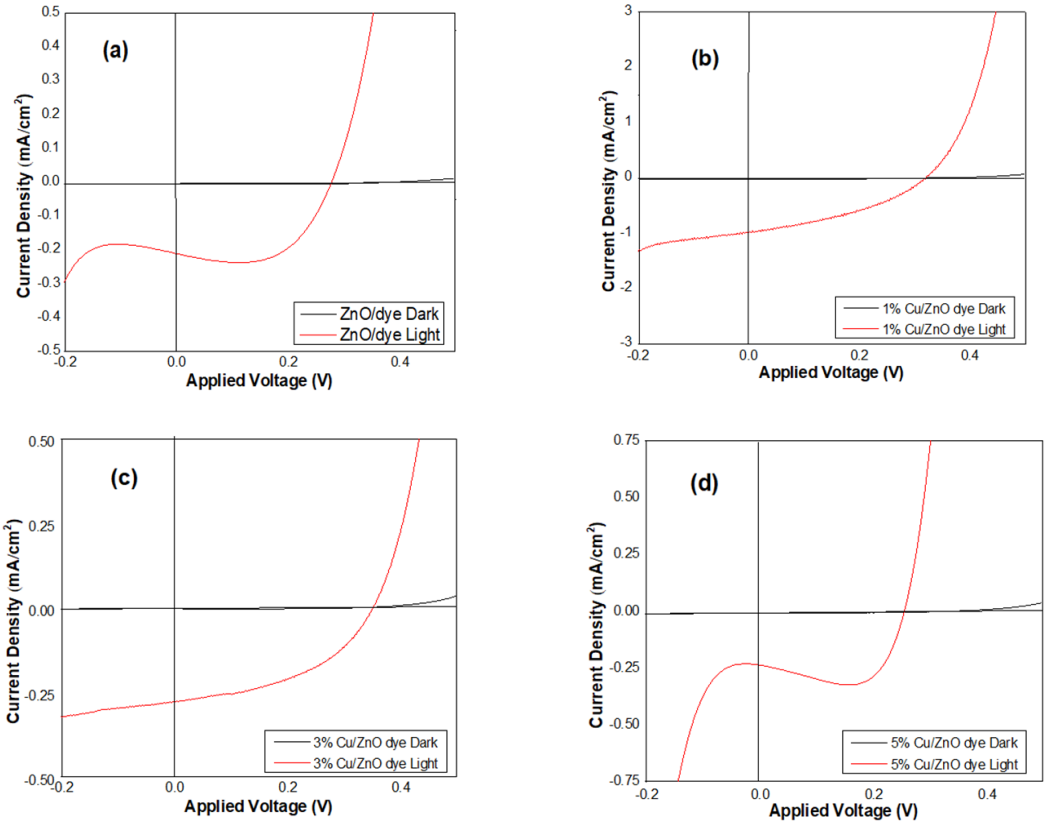

FIG. 8. Photocurrent-voltage curves in I^-/I^{3-} redox electrolyte solution under dark and visible light for: (a) ZnO/dye; (b) 1% Cu/ZnO; (c) 3% Cu/ZnO; (d) 5%Cu/ ZnO with dye

TABLE 3. Photoelectrochemical parameters of the cell

Sample	J_{sc} (mA/cm^2)	Voc (V)	FF	η %
ZnO without dye	0.065	0.262	0.27	0.0045
ZnO/dye	0.211	0.278	0.62	0.0363
1 % Cu/ZnO	0.98	0.319	0.37	0.1156
3 % Cu/ZnO	0.277	0.352	0.45	0.0438
5 % Cu/ZnO	0.236	0.256	0.78	0.0471

6. Conclusion

We effectively employed the effective sol gel technique for the synthesis of Cu/ZnO NPs. The XRD and Raman analysis clearly indicated that Cu/ZnO samples possess a hexagonal wurtzite crystal structure. It also revealed the slight decrement of particles and lattice parameters as Cu doping increses in low concentration. Here, nanograin morphologies are formed with respective elemental compositions. FT-IR studies substantiate the presence of the ZnO peaks into the samples with upward shifting due to Cu doping. Photoluminescence (PL) analysis of all samples of ZnO displays peaks at ∼300 nm in the UV range i.e. band edge emission (NBE), and at ∼600 nm in the visible region i.e. deep level emission (DLE). The UV-Vis absorption spectra depicts an increase in absorption ability and red shift with humps as incorporation of Cu content from 1 to 5 mol% while Tauc equation $(\alpha h\nu)^2 = A(h\nu - E_g)$, computed band gap values indicating band gap decrease from 1 to 5 mol% doping i.e 3.16 for ZnO and 2.84, 2.83, 2.78 eV for 1, 3 and 5 mol% Cu/ZnO respectively. I–V measurements of PEC cell is studied that gives notable results with

highest efficiency of $\eta = 0.1156$ % for 1 % Cu/ZnO photoanode with $J_{sc} = 0.98$ mA/cm^2 and $V_{oc} = 0.319$ V. ZnO photoanode without dye sensitization show low η % value, but when it is sensitized, high increment seen for ZnO and 1 % Cu/ZnO but later for 3 and 5 % values found to be decreased. It is may be due intense color of films for high doping that may affect absorption of photon even after sensitization. Photoluminescence studies also indicate higher electron hole recombination for higher doping These outcomes still very low but doping and co-sensitization such working strategy may give another way to enhance DSSCs outcome in the fast growing solar energy sector.

Acknowledgements

This research was made possible by support given by DST-FIST Analytical Instrumentation Laboratory of Lal Bahadur Shastri College, Satara and Jaysingpur College, Jaysingpur, Maharashtra, India.

References

[1] Halsnæs K., Garg A. Assessing the role of energy in development and climate policiesconceptual approach and key indicators. *World Development*, 2011, **39**, P. 987–1001.
[2] Gielen D., Boshell F., et al. The role of renewable energy in the global energy transformation. *Energy Strategy Reviews*, 2019, **24**, P. 38–50.
[3] Panwar N., Kaushik S., Kothari S. Role of renewable energy sources in environmental protection: A review. *Renewable and Sustainable Energy Reviews*, 2011, **15**, P. 1513–1524.
[4] Verbruggen A., Fischedick M., et al. Renewable energy costs, potentials, barriers: Conceptual issues. *Energy policy*, 2010, **38**, P. 850–861.
[5] Ellabban O., Abu-Rub H., Blaabjerg F. Renewable energy resources: Current status, future prospects and their enabling technology. *Renewable and Sustainable Energy Reviews*, 2014, **39**, P. 748–764.
[6] Kabir E., Kumar P., et al. Solar energy: Potential and future prospects. *Renewable and Sustainable Energy Reviews*, 2018, **82**, P. 894–900.
[7] Kannan N., Vakeesan D. Solar energy for future world:–A review. *Renewable and Sustainable Energy Reviews*, 2016, **62**, P. 1092–1105.
[8] Hamann T.W., Jensen R.A., et al. Advancing beyond current generation dye-sensitized solar cells. *Energy & Environmental Science*, 2008, **1**, P. 66–78.
[9] Ye M., Wen X., et al. Recent advances in dye-sensitized solar cells: from photoanodes, sensitizers and electrolytes to counter electrodes. *Mater Today*, 2015, **18**, P. 155–162.
[10] Susanti D., Nafi M., et al. The preparation of dye sensitized solar cell (DSSC) from TiO_2 and tamarillo extract. *Procedia Chemistry*, 2014, **9**, P. 3–10.
[11] Selvaraj P., Baig H., et al. Enhancing the efficiency of transparent dye-sensitized solar cells using concentrated light. *Sol Energy Mater Sol Cells*, 2018, **175**, P. 29–34.
[12] Kumara K.S., Nagaswarupa H., et al. Synthesis and characterization of nano ZnO and MgO powder by low temperature solution combustion method: studies concerning electrochemical and photocatalytic behavior. *Nanosystems: Physics, Chemistry, Mathematics*, 2016, **7**, P. 662–666.
[13] Karuppannan R., Kulandaivel J., Kandasamy J. Zinc oxide-palladium material an efficient solar-light driven photocatalyst for degradation of congo red. *Nanosystems: Physics, Chemistry, Mathematics*, 2016, **7**, P.740–746
[14] Sengupta D., Das P., Mondal B., Mukherjee K. Effects of doping, morphology and film-thickness of photo-anode materials for dye sensitized solar cell application–A review. *Renewable and Sustainable Energy Reviews*, 2016, **60**, P. 356–376.
[15] Bharat T., Mondal S., et al. Synthesis of Doped Zinc Oxide Nanoparticles: A Review. *Materials Today: Proceedings*, 2019, **11**, P. 767–775.
[16] Daksh D., Agrawal Y.K. Rare earth-doped zinc oxide nanostructures: a review. *Reviews in Nanoscience and Nanotechnology*, 2016, **5**, P. 1–27.
[17] Ugwu E.I. The Effect of Annealing, Doping on the Properties and Functionality of Zinc Oxide Thin Film; Review. In: *Sol-Gel Method-Design and Synthesis of New Materials with Interesting Physical Chemical and Biological Properties*, *Intech. Open*, 2018.
[18] Tang K., Gu S.-L., et al. Recent progress of the native defects and p-type doping of zinc oxide. *Chinese Physics B*, 2017, **26**, P. 047702.
[19] Zhang Q., Dandeneau C.S., Zhou X., Cao G. ZnO nanostructures for dye-sensitized solar cells. *Adv. Mater.*, 2009, **21**, P. 4087–4108.
[20] Vittal R., Ho K.-C. Zinc oxide based dye-sensitized solar cells: A review. *Renewable and Sustainable energy reviews*, 2017, **70**, P. 920–935.
[21] Larina L., Alexeeva O.,et al. Very widebandgap nanostructured metal oxide materials for perovskite solar cells. *Nanosystems: Physics, Chemistry, Mathematics*, 2019, **10**, P. 70–75.
[22] Abass N.K.S., Zainab J.S., Mohammed T.H., Abbas L.K. Fabricated of Cu doped ZnO nanoparticles for solar cell application. *Baghdad Science Journal*, 2018, **15**, P. 198–204.
[23] Horzum S., Torun E., Serin T., Peeters F. Structural, electronic and optical properties of Cu-doped ZnO: experimental and theoretical investigation. *Philosophical Magazine*, 2016, **96**, P. 1743–1756.
[24] Joshi K., Rawat M., et al. Band gap widening and narrowing in Cu-doped ZnO thin films. *J. Alloys Compd.*, 2016, **680**, P. 252–258.
[25] Kumari L., Madhuri R., Sharma P.K. Study of structural, optical and electrical properties of hydrothermally synthesised Cu-doped ZnO nanorods. *AIP Conference Proceedings*, AIP Publishing, 2017, P. 050075.
[26] Thankalekshmi R.D.R., Samwad D., Rastogi A.C. Doping sensitive optical scattering in zinc oxide nanostructured films for solar cells. *Advanced Materials Letters*, 2013, **4**, P. 9–14.
[27] Sajjad M., Ullah I., et al. Structural and optical properties of pure and copper doped zinc oxide nanoparticles. *Results in Physics*, 2018, **9**, P. 1301–1309.
[28] Boukaous C., Benhaoua B., Telia A., Ghanem S.J.M.R.E. Effect of copper doping sol-gel ZnO thin films: physical properties and sensitivity to ethanol vapor. *Materials Research Express*, 2017, **4**, 105024.
[29] Rahmati A., Sirgani A.B., Molaei M., Karimipour M.J.T.E.P.J.P. Cu-doped ZnO nanoparticles synthesized by simple co-precipitation route. *The European Physical Journal Plus*, 2014, **129**, P. 250.
[30] Sharma P.K., Dutta R.K., Pandey A.C. Doping dependent room-temperature ferromagnetism and structural properties of dilute magnetic semiconductor ZnO: Cu2+ nanorods. *Journal of Magnetism and Magnetic Materials*, 2009, **321**, P. 4001–4005.

[31] Tyona M., Osuji R., et al. Highly efficient natural dye-sensitized photoelectrochemical solar cells based on Cu-doped zinc oxide thin film electrodes. *Adv. Appl. Sci. Res.*, 2015, **6**, P. 7–20.

[32] Daratika D.A., Baqiya M.A. Synthesis of $Zn_{1-x}Cu_xO$ Nanoparticles by Coprecipitation and Their Structure and Electrical Property. *IOP Conference Series: Materials Science and Engineering*, IOP Publishing, 2017, P. 012009.

[33] Das B.K., Das T., et al. Structural, bandgap tuning and electrical properties of Cu doped ZnO nanoparticles synthesized by mechanical alloying. *Journal of Materials Science: Materials in Electronics*, 2017, **28**, P. 15127–15134.

[34] Pung S., Ong C., Isha K.M., Othman M.J.S.M. Synthesis and characterization of Cu-doped ZnO nanorods. *Sains Malaysiana*, 2014, **43**, P. 273–281.

[35] Djouadi D., Slimi O., et al. Effects of (Ce, Cu) Co-doping on the Structural and Optical Properties of ZnO Aerogels Synthesized in Supercritical Ethanol. *Journal of Physics: Conference Series*, IOP Publishing, 2018, P. 012008.

[36] Vaiano V., Iervolino G., Rizzo L.J.A.C.B.E. Cu-doped ZnO as efficient photocatalyst for the oxidation of arsenite to arsenate under visible light. *Applied Catalysis B: Environmental*, 2018, **238**, P. 471–479.

[37] Chow L., Lupan O., et al. Synthesis and characterization of Cu-doped ZnO one-dimensional structures for miniaturized sensor applications with faster response. *Sensors and Actuators A: Physical*, 2013, **189**, P. 399–408.

[38] Joshi K., Rawat M., et al. Band gap widening and narrowing in Cu-doped ZnO thin films. *Journal of Alloys and Compounds*, 2016, **680**, P. 252–258.

[39] Abinaya C., Marikkannan M., et al. Structural and optical characterization and efficacy of hydrothermal synthesized Cu and Ag doped zinc oxide nanoplate bactericides. *Materials Chemistry and Physics*, 2016, **184**, P. 172–182.

[40] Muthukumaran S., Gopalakrishnan R. Structural, FTIR and photoluminescence studies of Cu doped ZnO nanopowders by co-precipitation method. *Opt. Mater.*, 2012, **34**, P. 1946–1953.

[41] Moussawi R.N., Patra D. Modification of nanostructured ZnO surfaces with curcumin: fluorescence-based sensing for arsenic and improving arsenic removal by ZnO. *RSC Advances*, 2016, **6**, P. 17256–17268.

[42] Chow L., Lupan O., et al. Synthesis and characterization of Cu-doped ZnO one-dimensional structures for miniaturized sensor applications with faster response. *Sensors and Actuators A: Physical*, 2013, **189**, P. 399–408.

[43] Kuriakose S., Satpati B., Mohapatra S. Highly efficient photocatalytic degradation of organic dyes by Cu doped ZnO nanostructures. *Phys. Chem. Chem. Phys.*, 2015, **17**, P. 25172–25181.

[44] Kadam A., Kim T.G., et al. Morphological evolution of Cu doped ZnO for enhancement of photocatalytic activity. *J. Alloys Compd.*, 2017, **710**, P. 102–113.

[45] Bandyopadhyay P., Dey A., et al. Synthesis and characterization of copper doped zinc oxide nanoparticles and its application in energy conversion. *Current Applied Physics*, 2014, **14**, P. 1149–1155.

[46] Sharma K., Sharma V., Sharma S. Dye-sensitized solar cells: fundamentals and current status. *Nanoscale research letters*, 2018, **13**, P. 381.

[47] Wood C.J., Summers G.H., et al. A comprehensive comparison of dye-sensitized NiO photocathodes for solar energy conversion. *Phys. Chem. Chem. Phys.*, 2016, **18**, P. 10727–10738.

NANOSYSTEMS: PHYSICS, CHEMISTRY, MATHEMATICS, 2019, 10 (4), P. 475–479

Impact of nano-sized ceria particles upon the cyclization kinetics of poly(amic acid) films

I. V. Gofman[1], E. N. Vlasova[1], A. L. Nikolaeva[1], A. V. Yakimansky[1,2],
O. S. Ivanova[3], A. E. Baranchikov[3], V. K. Ivanov[3]

[1]Institute of Macromolecular Compounds, Russian Academy of Sciences,
199004, Bolshoi prospect 31, Saint Petersburg, Russia

[2]Saint Petersburg State University, Institute of Chemistry,
198504, Universitetskii prospect 26, Peterhof, Saint Petersburg, Russia

[3]Kurnakov Institute of General and Inorganic Chemistry, Russian Academy of Sciences,
119991, Leninsky prospect 31, Moscow, Russia

gofman@imc.macro.ru, evl021960@gmail.com, alexandra.l.nikolaeva@gmail.com, yakimansky@yahoo.com,
runetta05@mail.ru, a.baranchikov@yandex.ru, van@igic.ras.ru

PACS 81.07.-b, 62.25.-g **DOI 10.17586/2220-8054-2019-10-4-475-479**

The experimental study was conducted of the impact of ceria nanoparticles introduced into poly(amic acid), the prepolymer of thermally stable aromatic polyimide, upon the kinetics of the thermal cyclization of the film of this prepolymer, the reaction of its transformation to the final polyimide film in the course of its thermal treatment. The nano-filler was shown to accelerate the initial stage of cyclization, occurring at temperatures ranging up to 100–120 °C. A possible way of practical application of this effect was discussed.

Keywords: polymer-inorganic nanocomposites, polyimide, poly(amic acid), ceria, cyclization, mechanical properties.

Received: 5 August 2019

1. Introduction

Among different groups of polymer-inorganic nanocomposite materials that are the subject of extensive studies in last decades, some interesting properties are inherent to the composites obtained by introduction of nano-sized particles of ceria [1, 2] in matrices of thermally stable aromatic polyimides (PIs). It was shown in the previous investigations of these materials that the ceria nanoparticles of quasi-spherical shape do not produce any substantial positive impact on both their mechanical properties and glass transition temperature, but they provoke a sizable variation of the thermal stability of matrix PI [3].

In the communication presented, the results of the following stage of the investigations of PI-ceria nanocomposites are presented, namely the impact of this nano-filler upon the kinetics of synthesis of PI-based film materials is analyzed. The results are examined from a comparative study of the kinetics of the final stage of PI synthesis, the cyclization of prepolymer, a poly(amic acid) (PAA) [4] on one hand, and of the nanocomposite based on this PAA, in which ceria nanoparticles were introduced as an active nano-sized filler, on the other.

2. Materials and methods

A prepolymer used in our work was the PAA of the following structure:

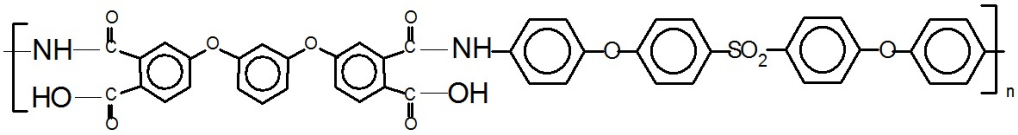

The PAA solution in N-methylpyrrolidone was synthesized in Institute of Macromolecular Compounds, Russian Academy of Sciences. The synthetic protocol was described previously [4].

The thermal treatment of the films of this PAA up to 250–300 °C results in the curing (cyclization) reaction in which the thermally stable aromatic polyimide R-BAPS is formed:

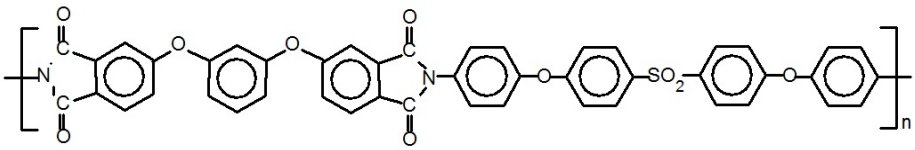

Quasi-spherical ceria nanoparticles with a diameter of ∼3–4 nm, which were used to prepare the nanocomposite, were synthesised at the Kurnakov Institute of General and Inorganic Chemistry, Russian Academy of Sciences. The

protocol for their synthesis is described elsewhere [5]. Briefly, cerium(III) nitrate (0.08 mol/L) in a water/isopropanol (1:1) mixture (180 mL) was added to aqueous ammonia (3 mol/L, 900 mL). The mixture was vigorously stirred for 3 h. Yellow precipitate was washed with distilled water and dried overnight at 60 °C.

To form the nanocomposite film samples, a pre-calculated amount of ceria nanoparticles was sonicated in N-methylpyrrolidone, and then a pre-calculated amount of PAA solution was introduced to the obtained nanoparticle dispersion. The mixture was then subjected to a long-term (24 h) homogenization by a mechanical stirrer (1000 rpm). The layers of homogenized PAA-based nanocomposite solution or of control unfilled PAA solution were cast onto glass plates with the subsequent drying at 80 °C for 24 h in a vacuum to completely remove the solvent. The ceria concentration in PAA-ceria nanocomposite as high as 3 wt.% was chosen for this investigation.

The PAA or PAA-CeO_2 nanocomposite films obtained by this way were subjected to a stepwise thermal treatment at the temperatures of 80, 90, 100, 120, 140, 160, 200 and 250 °C. Each step lasted 30 min. After each step of treatment the IR spectra of films were recorded and the mechanical tests were carried out.

Fourier-transform IR spectra of the films were recorded by using the "Vertex70" spectrometer (Bruker) equipped by a "Pike" micro-unit of singly disturbed total internal reflection with the ZnSe working element. Frequency resolution in these tests was of 4 cm^{-1}, scans number – 30. While registering the spectra, the correction possibility was envisaged to take into account the penetration depth dependence upon the wavelength, but in our experiments the "Pike" micro-fixture used insures the constant sample's pressing value and, hence, the constant penetration depth of IR irradiation into the sample. This makes it possible to carry out direct comparison of the obtained spectra.

The variation of the degree of cyclization of both PAA and PAA–CeO_2 composite films during their heating with the increase of temperature was quantitatively estimated by the increase in the concentration of imide cycles (the rise of the intensity of spectral band at 1778 cm^{-1}, which corresponds to the symmetric valent vibrations of C=O bond) and by the decrease of the concentration of amic acid groups (the fall of the intensity of spectral band 1540 cm^{-1} corresponding to CNH vibrations). Optical density values for the above spectral bands were then normalized to that of the intrinsic standard: the 1015 cm^{-1} band (the vibrations of aromatic ring) that does not vary during the cyclization process [4].

Thermogravimetric tests of the materials to control the residual amount of the solvent in dried films were conducted by a DTG-60 setup (Shimadzu, Japan). Film samples (approximately 5 mg) were heated to 350 °C at a rate of 5 °C/min. The experiments were carried out in an air atmosphere.

The mechanical tests of the films under investigation were carried out in the uniaxial extension mode, at room temperature, using an AG-100kNX Plus universal mechanical test system (Shimadzu, Japan). Strip-like samples with the dimensions 2×30 mm were stretched at a rate of 5 mm/min, according to ASTM D638 requirements. The Young's modulus values E were determined in these tests.

3. Results

IR spectra of PAA film and PAA-ceria nanocomposite one at the early stage of cyclization: after the thermal treatment at 90 °C, are presented in Fig. 1 (Fig. 1a). In the same figure (Fig. 1b), the spectra are presented for the completely cured films – after treatment at 250 °C.

The spectra obtained testify to the acceleration of cyclization process in the PAA film filled with ceria, as compared to that in unfilled PAA film: the concentration of imide rings in the former increases substantially faster along with the increase in temperature than that in the unfilled PAA film. For example, after the thermal treatment of PAA-ceria nanocomposite film at 90 °C the degree of cyclization of PAA-ceria nanocomposite film is three times more than that of the PAA film. The same conclusion was drawn by comparing the speeds of the decrease of the concentrations of amic acid units in the samples studied (Fig. 1a).

But the increased intensity of the process is inherent to the nanocomposite film only at the initial stage of the PAA thermal curing process, namely at temperatures up to 100–120 °C. During the further heating of films of two types, the degrees of cyclization became similar, and up to 250 °C, the PAA conversion to PI completely finishes in both materials (within the accuracy of the conversion degree determination by spectral method).

To confirm the results of IR tests by some other independent method, both the PAA films and PAA-based nanocomposite ones were subjected to the mechanical test after thermal treatment at different temperatures. The value of interest in these tests was the Young's modulus of the film materials. It is known that a system of H-bonds involving the CONH and COOH groups of the amic acid units is formed in the uncured PAA films [4]. But during the cyclization process, these bonds are broken. As a result, there are no H-bonds in the products of cyclization process, the PI films [4]. Under this reason, the cyclization process in PAA is accompanied by some modest decrease of the Young's modulus of the film. This decrease can hardly be fixed as usual at the expense of the incomplete removal of the solvent from the starting polymer volume during the PAA film drying process under standard conditions. This solvent (as a rule it is N,N- dimethylformamide, N,N- dimethylacetamide, or N-methylpyrrolidone) acts as a plasticizer

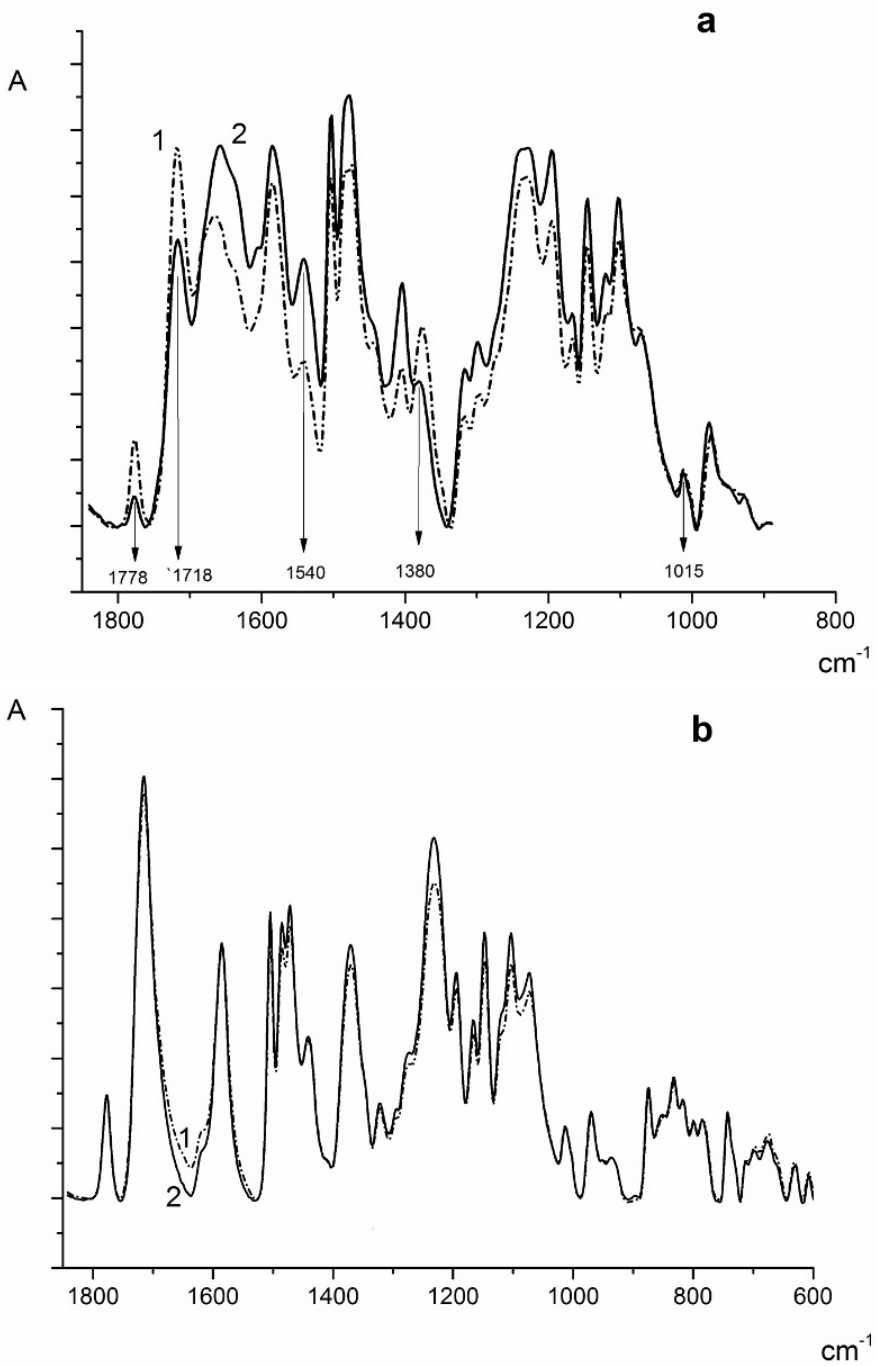

FIG. 1. IR spectra of (a) PAA and PAA-CeO_2 films after heat treatment at 90 °C; (b) PI and PI-CeO_2 films after thermal treatment at 250 °C. (1) – PAA-CeO_2 or PI-CeO_2 nanocomposite films, (2) – PAA or PI films

in the film, which causes a decrease in the initial value of Young's modulus. During the subsequent thermally stimulated PAA cyclization process, the vaporization of this residual solvent occurs causing an increase in the modulus. As a result of the interplay of two processes above – the solvent removal and the destruction of H-bonds during heat treatment of the film – the resulting Young's modulus value of cured film does not decrease and moreover, can slightly increase as compared to that of the PAA film.

To exclude the impact of the deplastification process upon the variation of the Young's modulus during the thermal cyclization, a special pretreatment of both PAA and PAA-based nanocomposite films was carried out; they were subjected to prolonged drying under vacuum (the drying protocol is described above). The completion of the drying process was controlled by TGA tests. The weight losses registered by this method during the heating of pretreated films in the temperature range 80–300 °C were found to be similar to the calculated amount of water, the side product of PAA cyclization reaction. Hence, pretreatment insures the efficient solvent removal from the films and eliminates the impact of deplastification effects upon the results of our tests.

The curves of Young's modulus values of PAA and PAA-ceria nanocomposite films vs. the temperature in the course of the stepwise thermal treatment of the films are presented in Fig. 2.

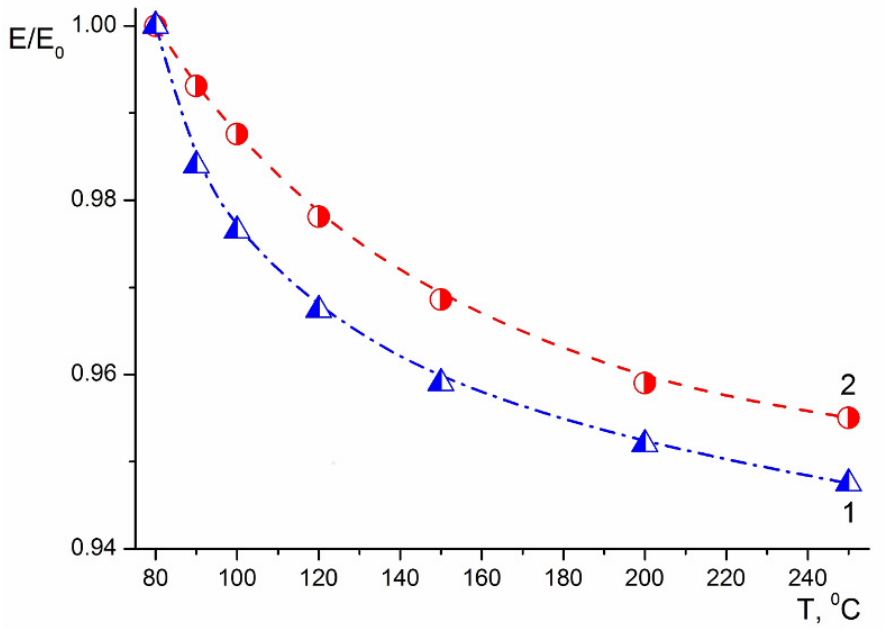

FIG. 2. Young's modulus values of PAA-based composite and PAA films vs. temperature of thermal treatment during the conversion of prepolymer to R-BAPB-based nanocomposite containing 3 wt.% of CeO_2 (1) or to PI R-BAPB (2); E_0 denotes the initial E value of the prepolymer (PAA or PAA-ceria) film pretreated at 80 °C

The results obtained clearly demonstrate the decrease in the Young's modulus values of both PAA and PAA-based nanocomposite films during thermal conversion to PI and PI-based composite ones. At the same time curves in Fig. 2 testify the increased speed of the E depression of nanocomposite film in the initial stage of the process as compared to that of PAA film.

In this way, the data presented evidence the catalytic action of ceria nanoparticles exfoliated in PAA volume on the process of thermally stimulated cyclization of film of this PAA. Indeed, this catalytic impact was registered only at the initial stage of the conversion process: at temperatures ranging up to 100–120 °C. During the further heating of both films the equal degrees of conversion were registered in both films.

At first glance, the effect above is of no practical interest, because it is realized only at the first, initial stage of conversion of PAA to PI. But as a matter of fact, this phenomenon lets us to decrease the severity of the requirements for the initial molecular mass of PAA, which insures the successful fabrication of PI films. Indeed, during the thermal treatment of PAA films, some side reaction takes place along with the cyclization. This is a reaction of thermally stimulated destruction, cleavage of PAA macrochains [4], i.e., the successive decrease of PAA molecular mass. This is a reversible process that occurs at temperatures of 100–150 °C. During the further heating of film, the destruction process gives way to the opposite one, the re-synthesis with the successive increase in the molecular mass of the polymer. Under the optimal conditions of the cyclization process, the full re-synthesis takes place in the temperature

range up to 180–200 °C, resulting in the full restoration of molecular mass up to its initial value [4]. But in the temperature interval 100–150 °C the several fold (up to one order) decrease of molecular mass as compared to its initial value takes place. If this initial value is not very high, the destruction process can provoke the damage of the film in the aforementioned range of temperature at the expense of the local stresses caused by the removal of the solvent.

But if some amount of cured units, of imide rings will be formed in the film up to the development of the destruction process, as in the PAA-ceria nanocomposite film, this can insure the depression of the destruction intensity and hence the possibility increases for successful completion of thermally stimulated cyclization and re-synthesis without the film's damage at the intermediate stages of curing process.

Acknowledgment

The authors acknowledge the help of L.A. Myagkova from the Institute of Macromolecular Compounds, RAS, who synthesised the prepolymer of the matrix polymer R-BAPS.

The work was supported by the Russian Science Foundation (project No. 18-13-00305).

References

[1] Ivanov V.K., Polezhaeva O.S., et al. Synthesis and thermal stability of nanocrystalline ceria sols stabilized by citric and polyacrylic acids. *Russian Journal of Inorganic Chemistry*, 2010, **55**(3), P. 328–332.

[2] Mullins D.R. The surface chemistry of cerium oxide. *Surface Science Reports*, 2015, **70**(1), P. 42–85.

[3] Gofman I., Nikolaeva A., et al. Unexpected selective enhancement of the thermal stability of aromatic polyimide materials by cerium dioxide nanoparticles. *Polymers for advanced technologies*, 2019, 30(6), P. 1518–1524.

[4] Bessonov M.I., Koton M.M., Kudryavtsev V.V., Laius L.A. *Polyimides – thermally stable polymers*. Plenum Publishing Corp., New York, 1987, 327 p.

[5] Ivanov V.K., Kopitsa G.P., et al. Hydrothermal growth of ceria nanoparticles. *Russian Journal of Inorganic Chemistry*, 2009, **54**(12), P. 1857–1861.

NANOSYSTEMS: PHYSICS, CHEMISTRY, MATHEMATICS, 2019, 10 (4), P. 480–487

Layer by layer synthesis of zinc-iron layered hydroxy sulfate for electrocatalytic hydrogen evolution from ethanol in alkali media

D. S. Dmitriev, V. I. Popkov

Ioffe Institute, 194021 Saint Petersburg, 26 Polytechnicheskaya street, Russia

vadim.i.popkov@gmail.com

DOI 10.17586/2220-8054-2019-10-4-480-487

This paper proposes a method for producing nanocomposite electrocatalytic coatings based on zinc-iron layered hydroxy sulfate $Zn_2Fe_4(OH)_{12}SO_4 \cdot 8H_2O$ and iron(III) hydroxide $Fe(OH)_3$ using the successive ionic layer deposition (SILD) method. The obtained materials were investigated with the methods of SEM and EDX, XRD, FTIR spectroscopy, and also were analyzed their electrocatalytic performance. These compounds are formed on the surface of the substrate in nanosheets shape with an average size of 6–17 nm, which self-organized into coral-like agglomerates. It was shown that by varying the anionic component of the reaction solution – NO^{3-}, SO_4^{2-} or Cl^-, effective control of the 2D nanocrystals phase composition is possible. It has been determined that electrocatalytic materials based on $Zn_2Fe_4(OH)_{12}SO_4 \cdot 8H_2O$ and $Fe(OH)_3$ are active in the process of hydrogen evolution from alkaline water-alcohol solutions. In result overpotential value of hydrogen evolution reaction at 10 mA cm^{-2} decreases about $\sim$ 10%, as well as energy consumption to carry out this process reduces about 8–12%. as shown from the decline of the Tafel slope. The developed materials have high cyclic stability and short non-stationary mode, which allows them to be considered as the base of electrocatalysts for the processes of hydrogen evolution from ethanol in an alkaline medium.

Keywords: successive ionic layer deposition, layered hydroxide, electroreforming, hydrogen evolution reaction, electrocatalytic, ethanol reforming.

Received: 13 June 2019

Revised: 18 August 2019

1. Introduction

The reaction of hydrogen evolution (HER) from aqueous and aqueous-alcoholic solutions under the electric current is one of the main processes of modern electrochemical production. This process is especially interesting for the developing fuel cell technology, in which hydrogen is the main source of energy [1–6], as well as for the increasingly popular electroreforming process, where hydrogen is released during electrolysis of aqueous and organic electrolytes at direct current [7–10]. One of the electroreforming applications is the utilization of biomass processing products in water-alcohol solution form, mainly based on methyl and ethyl alcohols (from 2 to 6 mol L^{-1}). For the practical implementation of the electroreforming of such products, it is necessary to increase the electrical conductivity of these solutions, which is usually produced by adding potassium or sodium hydroxides [11–13].

For electroreforming, electrodes from noble metals (Pt, Pd) and iron group metals (Fe, Ni, Co) can be used. The main requirements for electrode materials are high efficiency and low cost, determined, among other parameters, by a slight overpotential of HER. For noble metals, the overpotential value is low (up to 40–60 mV at a current density of 10 mA cm^{-2}), but their high cost restricts their active use as electrodes. Iron group metals are relatively cheaper than noble metals, but their overpotential value is 300–500 mV at a current density of 10 mA cm^{-2} [14–18]. Also, compounds of various classes, called electrocatalysts, are used as electrode materials: oxides (hydroxides), sulfides, phosphides, nitrides, and etc. [19–22]. The advantage of electrocatalysts over pure metals or alloys is their high efficiency at a relatively low cost. Under the effectiveness of electrocatalysts, in addition to low overpotential, they also imply high stability of the material during electrolysis, short non-stationary mode and efficient conversion of electrical energy, determined by the Tafel slope according to its physical meaning [23]. The most common electrocatalytic materials are compounds of molybdenum, tungsten, nickel and cobalt. Some of them, for example, MoS_2 attains an overpotential value of 50–80 mV [24–30]. Therefore, the synthesis of compounds exhibiting electrocatalytic activity in HER at electrochemical reforming as electrode materials is currently an important scientific and practical task.

The work of the electrocatalyst is influenced by the nature of its components as well as the morphology and structure, mainly determined by the conditions and the synthetic route. One of the most promising methods for producing thin film electrocatalysts on the metal surface is the successive ionic layer deposition (SILD) approach, which is one of layer by layer synthesis methods [31]. This method is based on the sequential adsorption of cations and anions, forming a poorly soluble compound from a solution on the surface of a substrate. Automation of parameters allows to adjust the thickness of the electrocatalyst films, the selection of the composition and morphology. This method can be easily scalable for the synthesis of electrocatalytic materials at a standard temperature with simple hardware and the use of low-cost reagents [32–38].

In this paper, a new technique is proposed for producing nanocomposite based on zinc-iron layered hydroxy sulfate (ZF-LHS) as electroreforming materials in an alcohol solution with the aim of hydrogen evolution. The synthesis is carried out in solutions of the Mohr's salt ($(NH_4)_2Fe(SO_4)_2$) and ammonium zinc complexes using $Zn(NO_3)_2$, $ZnSO_4$ and $ZnCl_2$ as a precursor. By varying the ion-contain of the reaction, solutions and additional heat treatment, electrocatalysts with different composition, structure, and morphology are obtained in the form of thin films. The main goal of this work was the nanocomposites ZF-LHS synthesis with the SILD method and to study the effect of the anionic composition on the structural features and electrocatalytic properties during HER in alkaline water-alcohol solution.

2. Experimental technique

2.1. Materials

For the synthesis, glass and silicon plates (substrates) with dimensions of 26×10×1 mm, as well as plates of nickel foil with dimensions of 25×5×0.1 mm were used. Oxides were removed from the nickel foil via abrasion with sandpaper (P120 grit). Immediately before the synthesis, all the substrates were treated with acetone to remove mechanical and chemical impurities. All the reagents were chemically pure. The water for solutions was distilled with a conductivity of 5 MΩ cm.

2.2. Synthesis procedure

For ZF-LHS synthesis by SILD method were used two solutions. The precursor of solution No. 1 was $(NH_4)_2Fe(SO_4)_2$ with a concentration of 0.01 mol L^{-1}. The solution No. 2 was contained an ammonium complex of Zn(II) salts, consisting of zinc salt ($Zn(NO_3)_2$, $ZnSO_4$ or $ZnCl_2$) ($C = 0.01$ mol L^{-1}), NH_4NO_3 ($C = 0.15$ mol L^{-1}) and a dropwise added solution of 1 M NH_4OH to pH = 10.

During the synthesis, the substrate, fixed in the sample holder, was immersed for 30 seconds in chemical beakers with $(NH_4)_2Fe(SO_4)_2$, distilled water, mixed Zn(II) salt, NH_4NO_3, and NH_4OH solution, and again into distilled water. Such processing represented one SILD cycle, which was repeated 30 times (Fig. 1). As a result, nanocomposites with $Zn(NO_3)_2$ (ZF-LHS-1), $ZnSO_4$ (ZF-LHS-2) and $ZnCl_2$ (ZF-LHS-3) reagents were obtained. Also, for a comparative analysis of the effect of heat treatment, the samples were thermally treated for 1 hour at 250 °C in the air (ZF-LHS-1T, ZF-LHS-2T, ZF-LHS-3T).

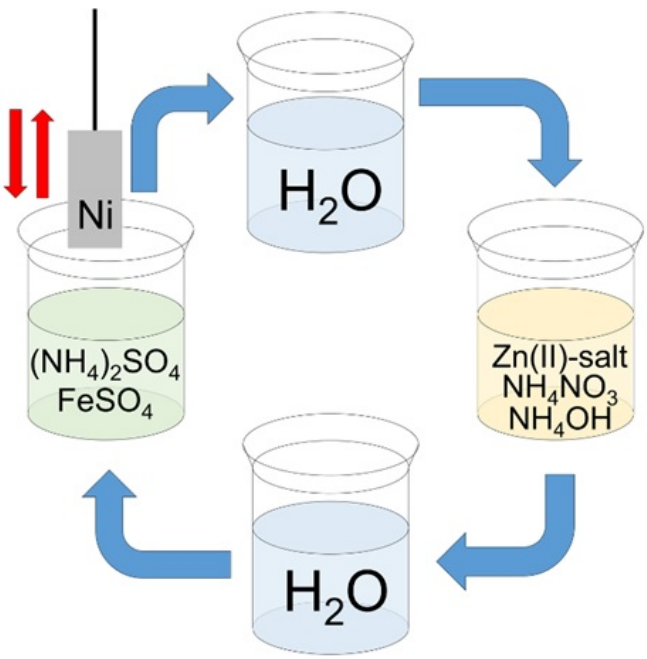

FIG. 1. Scheme of SILD-synthesis of ZF-LHS

2.3. Physicochemical characterization

The elemental composition of the samples and their morphological features were examined by X-ray microanalysis and scanning electron microscopy (SEM) using an FEA Quanta 200 microscope equipped with an EDX attachment. X-ray phase analysis of the samples was carried out by powder X-ray diffraction using a Rigaku SmartLab III multifunctional X-ray diffractometer (Co Kα radiation, $\lambda = 0.179026$ nm). The qualitative X-ray phase composition was determined on the basis of comparing the sample pattern with the data of JCPDS and ICSD. The analysis of the main functional groups located on the surface of the synthesized samples was carried out by the FTIR analysis with spectrophotometer Shimadzu IRTracer-100, equipped with the adapter "Specac". Analysis of the results of FTIR spectroscopy was carried out by comparing the position and intensity of the main absorption bands with the data presented in the literature on similar systems.

2.4. Electrocatalytic performance

Electrocatalytic studies of materials for HER were carried out on an Elins P-20X potentiostat-galvanostat in a three-electrode cell shown in Fig. 2.

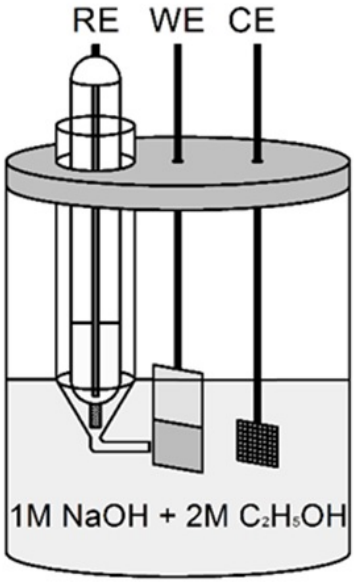

FIG. 2. Three-electrode cell for electrochemical measurements

The working electrode (WE) was a nanocomposite deposited by the SILD method on a nickel substrate with an electroactive surface of 1 cm^2. Ag/AgCl and platinum electrodes were used respectively as a reference electrode (RE) and counter electrode (CE). Overpotential value was calculated according to the Nernst equation for a reversible hydrogen electrode (RHE): $E_{RHE} = E^o_{\mathrm{Ag/AgCl}} + E_{\mathrm{Ag/AgCl}} + 0.059$ pH, where $E^o_{\mathrm{Ag/AgCl}}$ is the standard potential of Ag/AgCl electrode (0.202 mV), $E_{\mathrm{Ag/AgCl}}$ is the potential of the working electrode relative to Ag/AgCl. All measurements were carried out under standard conditions ($T = 25$ °C, $P = 1$ atm.) in an aqueous solution consisting of 2 mole absolute ethanol and 1 mole NaOH (pH = 14). Cyclic CV curves were taken in the potential range from open circuit potential to 1.5 V with a sweep rate of 5 mV s^{-1}. Qualitatively, the working overpotential of the sample was determined from the CV curves at a current density of 10 mA cm^{-2}. Electrochemical measurements were performed without IR-compensation.

3. Results and discussion

As a result of carrying out SILD synthesis according to the method described above, three samples were obtained, differing in the anion type, which was used to prepare the reaction solution No. 2 – zinc nitrate (ZF-LHS-1), zinc sulfate (ZF-LHS-2) and zinc chloride (ZF-LHS-3). The chemical composition of the synthesized samples was studied by the EDX method, the results are shown in Fig. 3a. According to these data, all samples contain oxygen, sulfur, zinc, and iron in their composition. The atomic fraction of iron significantly exceeds the zinc content and this difference from the sample ZF-LHS-1 to the sample ZF-LHS-3 is growing. This is due to a change in the ionic strength of the reaction solution No. 2, depending on the zinc salts. Using various zinc salts leads to different cations sorption (Zn^{2+}

and Fe^{2+}) on the surface of the substrate and the forming varied film of the product. A small number of sulfur atoms, registered in all samples, is apparently due to the occurrence of sulfate groups of the reaction solution No. 1.

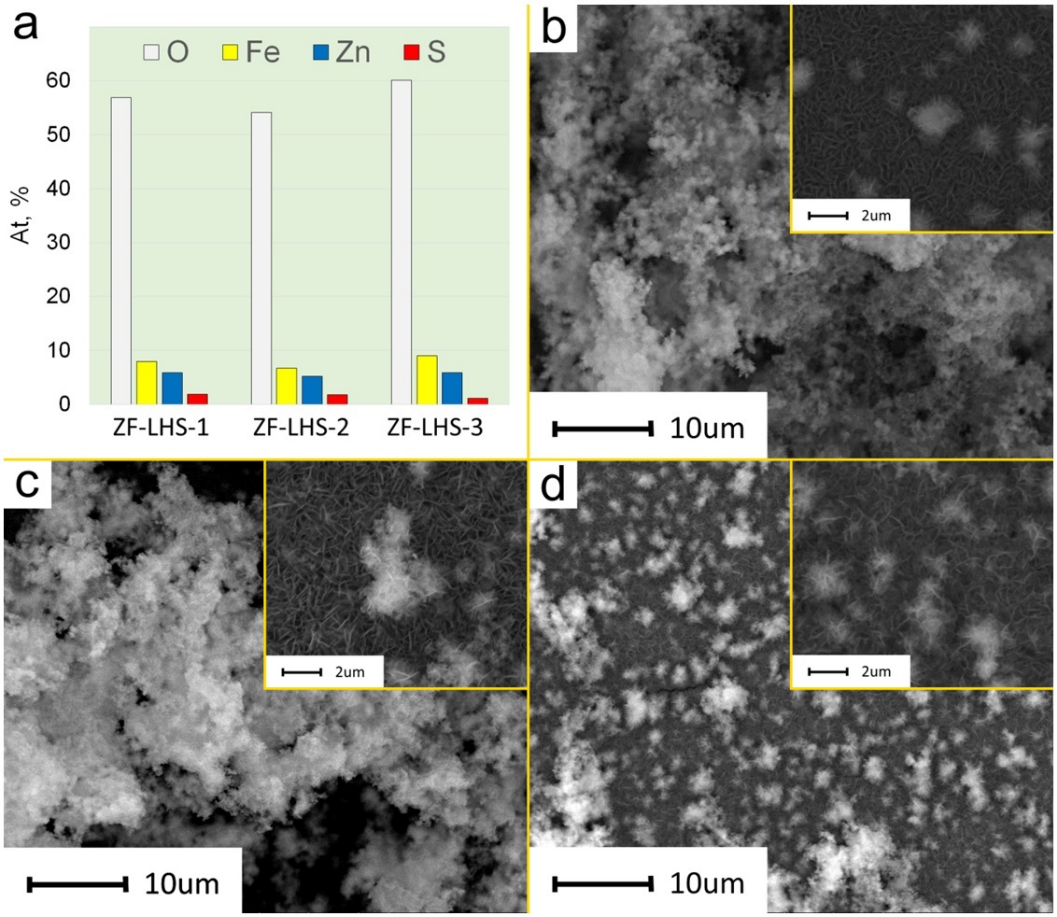

FIG. 3. Results of EDX analysis (a) and SEM micrographs (b–d) of samples ZF-LHS: b – ZF-LHS-1, c – ZF-LHS-2, d – ZF-LHS-3

The morphology of the samples obtained by the SILD method is presented in Fig. 3b-d. According to this data, continuous films consisting of small crystals agglomerated into complex structures of various shapes are deposited on the surface of the Si-substrate. The morphology of individual crystals can be attributed to the morphology of 2D crystals and the effect of the zinc salt anion, apparently, is reduced to the effect on the agglomeration of the forming nanocrystals. The synthesized nanocrystals represent two types of agglomerates – a continuous film on the surface of the Si-substrate and spherical agglomerates on the surface of the continuous film. In some cases, coral-like agglomerates are also observed, which are the result of long-term growth and association of spherical agglomerates. In general, the morphological structure of the obtained compounds is characteristic of the samples are formed by the SILD method [39].

However, differences in the elemental composition, which slightly affect the morphology of nanocrystals, manifest themselves in the results of X-ray diffraction of the samples (Fig. 4). As shown from the data, two phases can be present in the composition of the films: zinc-iron layered hydroxy sulfate $Zn_2Fe_4(OH)_{12}SO_4{\cdot}8H_2O$ (ICSD card No. 9013993) and iron(III) hydroxide $Fe(OH)_3$ (JCPDS card No. 00-013-0092). The ZF-LHS-1 sample contains only the $Zn_2Fe_4(OH)_{12}SO_4{\cdot}8H_2O$ phase, and the ZF-LHS-2 and ZF-LHS-3 samples also contain the $Fe(OH)_3$ phase, whose reflex intensity increases from the ZF-LHS-2 sample to the ZF-LHS-3. This suggests that the increase in the proportion of Fe atoms relative to Zn in the composition of the synthesized samples from ZF-LHS-1 to ZF-LHS-3 leads to the appearance of the second phase of iron (III) hydroxide, which is fixed along with the phase of a zinc-iron layered hydroxy sulfate.

The broadening of the X-ray diffraction lines of the ZF-LHS and iron(III) hydroxide indicates that they are nanostructured, which confirms the results of SEM analyses (Fig. 3c-d). The calculation of the average size of coherent scattering regions for individual reflexes of these phases gives a value from 6 to 17 nm. The uneven broadening of the

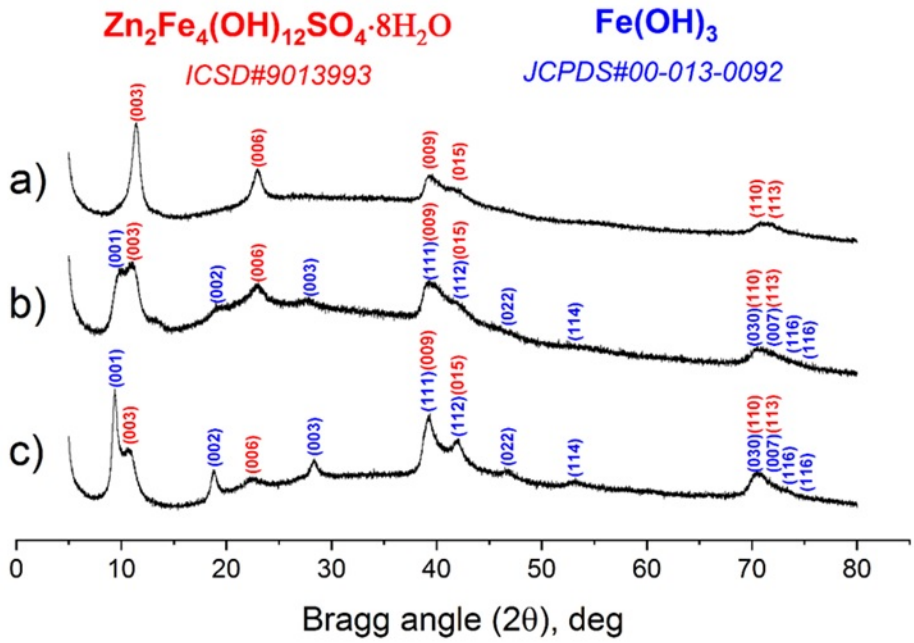

FIG. 4. X-ray diffraction patterns of the samples ZF-LHS: a) ZF-LHS-1, b) ZF-LHS-2, c) ZF-LHS-3

X-ray diffraction lines of the ZF-LHS and iron (III) hydroxides by individual crystallographic directions indicates that the formed crystals have anisotropy of shape and morphology of 2D nanocrystals.

The analysis of the main functional groups located on the surface of the obtained samples was carried out by FTIR, the results are shown in Fig. 5. The absorption bands of 1640 and 3250 cm^{-1} relate, respectively, to the deformation and stretching vibrations of the O–H bond in water molecules adsorbed on the surface of the samples. Since these absorption bands are high-intensity, they shield the absorption bands from vibrations of O–H bonds in the ZF-LHS and iron(III) hydroxide structural groups. The presented spectra also contain a set of absorption bands at 607, 975, and 1090 cm^{-1}, corresponding to the vibrations of the S–O bonds in the sulfate groups of ZF-LHS. In addition, the intense absorption band at 1360 cm^{-1} is clearly visible, which corresponds to the vibrations of the C–O bond in the carbonate group. It's associated with the sorption of CO_2 from the air by the developed surface of the samples [34–40]. The absorption bands of the Zn–O and Fe–O bonds in the wavenumber region of 300–600 cm^{-1} cannot be identified because of their diffuse shape [36]. This is due to the imperfect crystal structure of the main phases – ZF-LHS and iron(III) hydroxide, which are formed as a result of synthesis by the SILD method.

Thus, the surface composition of the obtained compounds is almost completely consistent with the volume composition established on the basis of the results of EDX and PXRD studies, with the exception of components (H_2O and CO_2) that are adsorbed onto the surface of the sample during the synthesis and subsequent storage of the substance.

According to the method presented in the work, coatings were obtained on the surface of nickel electrodes and their electrocatalytic characteristics were studied, the results are shown in Fig. 6. The appearance of the electrodes obtained by deposition of the nanocomposite on the nickel substrate is shown in Fig. 6a. The red color of the precipitate indicates that iron(III) compounds are present in its composition.

Important characteristics in evaluating the effectiveness of electrode material for the hydrogen evolution reaction are the overpotential (η) at some fixed value of the current load (for example, 10 mA cm^{-2}), the slope of Tafel plot ($\log(j) - \eta$) and the stability material, including its short non-stationary mode.

As can be seen from the graph shown in Fig. 6b, the overpotential on a clean nickel substrate at a current density of 10 mA cm^{-2} is 286 mV, which corresponds to the literature data [15]. For ZF-LHS-2 and ZF-LHS-3 nanocomposites, the overpotential value at the same current density is 337 and 365 mV before heat treatment and 278 and 280 mV after (ZF-LHS-2T and ZF-LHS-3T), respectively. Thus, the change in the magnitude of the overpotential for these samples after heat treatment is within the limits of error. However, the ZF-LHS-1 sample after heat treatment (ZF-LHS-1T) shows the best result among the studied samples - the overpotential value at a current density of 10 mA cm^{-2} was 260 mV. Based on this, we can conclude that it is necessary to apply heat treatment after the synthesis of the samples.

Fig. 6c presents the results of the analysis of voltammograms in the Tafel plot for heat-treated samples. The Tafel slope (coefficient b) in these plot indicates a change in overpotential value with a 10-fold increase in current density.

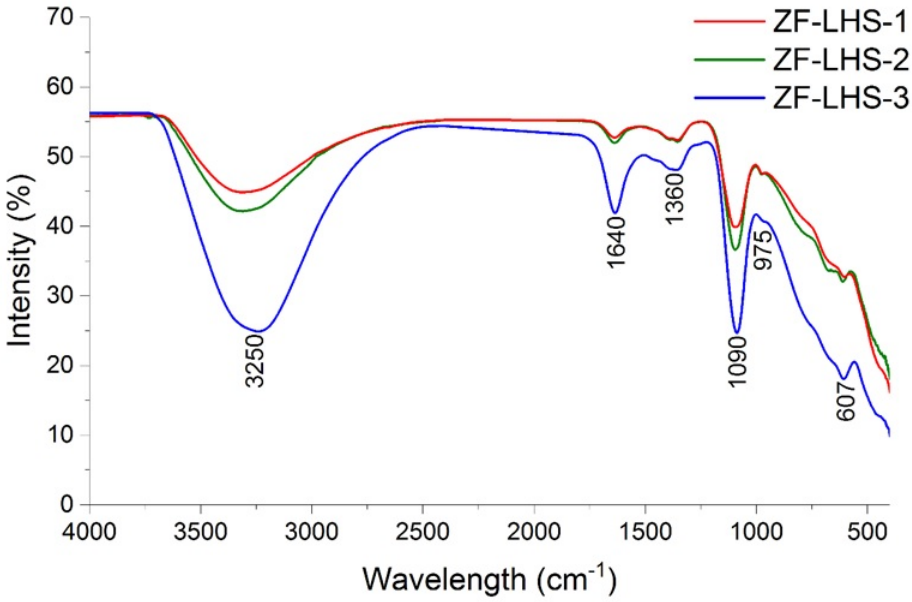

FIG. 5. FTIR spectra of synthesized samples ZF-LHS

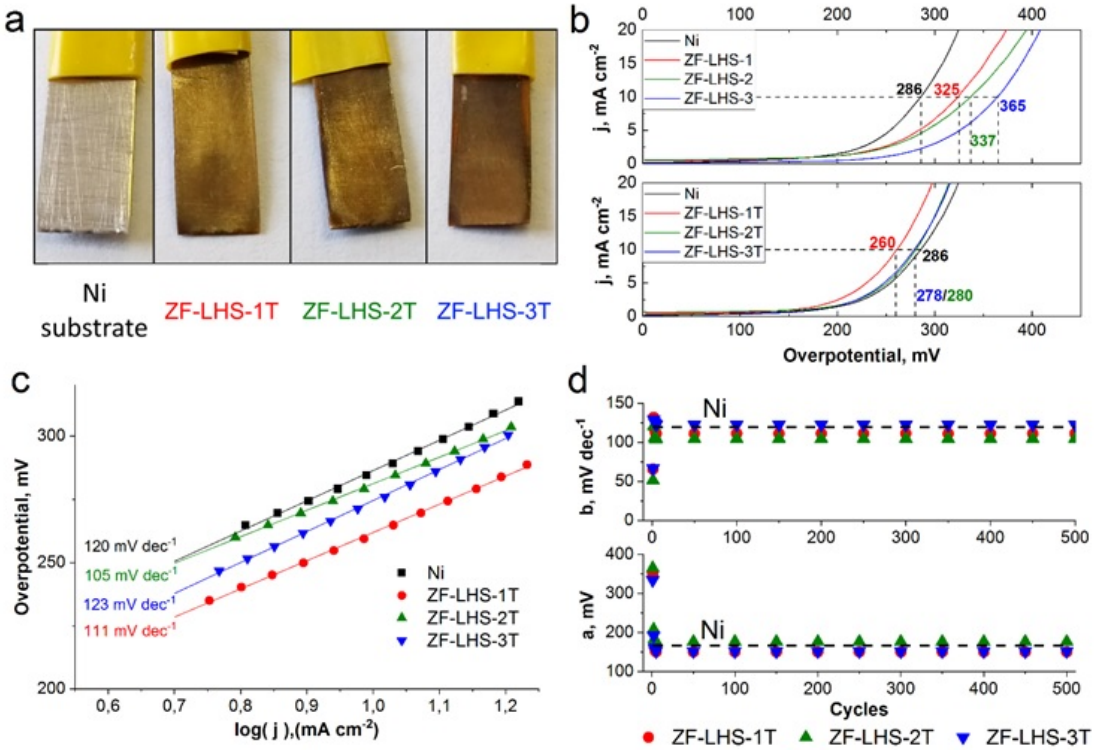

FIG. 6. Electrochemical properties of ZF-LHS: a) Appearance of electrodes; b) CV curves of synthesized nanocomposites; c) Tafel plot of synthesized electrodes; d) Change in the coefficients of the Tafel equation for 500 cycles

Thus, reducing the Tafel slope for ZF-LHS-1T and ZF-LHS-2T samples (111 mV and 105 mV, respectively) relative to pure nickel (120 mV) has an economic advantage in electrochemical reforming, which is 8–12% in terms of power consumption. For the ZF-LHS-3T sample, the Tafel slope value is 123 mV, which is slightly higher than the value for a pure nickel electrode.

The reason for this difference in the electrochemical behavior of electrocatalysts, both between samples and in the presence or absence of heat treatment; this is the result of the structuring degree, which determines the electrical properties of the surface coating. With an increase in the ordering of the structure in the series ZF-LHS-3T – ZF-LHS-2T – ZF-LHS-1T, as can be seen from the microphotographs in Fig. 3b-d, the nanocomposite represents a coral-like structure and its electrochemical characteristics improve: the overpotential of HER is reduced and Tafel slope is decreased. The structuring process is promoted by the proportionality of the anions of zinc salts, to the anions present in solutions No. 1 and No. 2 and participating in the SILD synthesis – NO^{3-} and SO_4^{2-}. In the case of using zinc chloride as a precursor, the structure of the compound (ZF-LHS-3T) is more chaotic and is distributed in a slightly conducting iron oxide (III).

The stability of the work and short non-stationary mode of the electrode materials are presented as a graphical dependence in Fig. 6d. It can be noted that starting from the 5th cycle of operation, the values of the coefficients of the Tafel equation change slightly, and we can speak about the stationary mode. Further cycling of the synthesized electrocatalytic materials up to 500 cycles practically does not change the values of the coefficients a and b, which indicates their high cyclic stability.

4. Conclusion

This paper proposes a simple and effective technique for producing a nanocomposite coating based on $Zn_2Fe_4(OH)_{12}SO_4{\cdot}8H_2O$ and $Fe(OH)_3$ on the surface of a nickel electrode by the SILD method. It was shown that by varying the anionic component of the reaction solution (NO^{3-}, SO_4^{2-} or Cl^-), it is possible to effectively control the phase composition of the nanocomposite coating from pure zinc-iron layered hydroxy sulfate to its equal molar ratio with $Fe(OH)_3$. It was established that the obtained nanocomposite consists of 2D $Zn_2Fe_4(OH)_{12}SO4{\cdot}8H_2O$ and $Fe(OH)_3$ nanocrystals with an average size of 6–17 nm, which cover the nickel electrode and develop its specific surface with the formation of coral-like agglomerates. The synthesized electrode materials were investigated in the process of electrochemical reforming of ethanol in an aqueous medium with the aim of producing hydrogen. It was shown that the developed coatings based on $Zn_2Fe_4(OH)_{12}SO_4{\cdot}8H_2O$ and $Fe(OH)_3$ lead to a decrease in the overpotential value compared to the pure nickel electrode by $\sim$10%, and these coatings also reduce the power consumption for this process by 8–12%. This effect is most pronounced after the heat treatment of these compositions for 1 hour at 250°C in air. Together, with short non-stationary mode and with the high cyclic stability of these materials, the system under investigation can be considered as a promising basis of electrocatalyst for HER processes from ethanol in an alkaline medium.

References

[1] Glebova N.V., Nechitailov A.A., Krasnova A.O., et al. Cathode of hydrogen fuel cell, with modified structure and hydrophobicity. *Russ. J. Appl. Chem.*, 2015, **88**, P. 769–774.

[2] Krasnova A.O., Agafonov D.V., Glebova N.V., et al. Technological Aspects of Hydrogen Fuel Cell Electrodes with Controlled Porosity and Transport Properties. *Altern. Energy. Ecol.*, 2019, **4-6**, P. 51–64.

[3] Mitra M.A. Study on Advances in Hydrogen Fuel Cells. *Electrical Engineering Open Access Open Journal*, 2019, **1**, P. 1–4.

[4] Sharaf O.Z., Orhan M.F. An overview of fuel cell technology: Fundamentals and applications. *Renew. Sustain. Energy. Rev.*, 2014, **32**, P. 810–853.

[5] Akhairi M.A.F., Kamarudin S.K. Catalysts in direct ethanol fuel cell (DEFC): An overview. *Int. J. Hydrogen Energy*, 2016, **41**, P. 4214–4228.

[6] Brandon N.P., Parkes M.A. *Fuel Cells: Materials. Ref. Modul. Mater. Sci. Mater.*, 2016, P. 1–6.

[7] Tuomi S., Santasalo-Aarnio A., Kanninen P., Kallio T. Hydrogen production by methanol-water solution electrolysis with an alkaline membrane cell. *J Power Sources*, 2013, **229**, P. 32–35.

[8] Gutiérrez-Guerra N., Jiménez-Vázquez M., Serrano-Ruiz J.C., et al. Electrochemical reforming vs. catalytic reforming of ethanol: A process energy analysis for hydrogen production. *Chem Eng Process: Process Intensif*, 2015, **95**, P. 9–16.

[9] Hasa B., Vakros J., Katsaounis A.D. Study of low temperature alcohol electro-reforming. *Mater Today Proc*, 2018, **5**, P. 27337–27344.

[10] Hasa B., Vakros J., Katsaounis A.D. Effect of TiO_2 on Pt-Ru-based anodes for methanol electroreforming. *Appl Catal. B Environ*, 2018, **237**, P. 811–816.

[11] Bambagioni V., Bevilacqua M., Bianchini C., et al. Self-sustainable production of hydrogen, chemicals, and energy from renewable alcohols by electrocatalysis. *Chem. Sus. Chem.*, 2010, **3**, P. 851–855.

[12] De Lucas-Consuegra A., Calcerrada A.B., De La Osa A.R., Valverde J.L. Electrochemical reforming of ethylene glycol. Influence of the operation parameters, simulation and its optimization. *Fuel Process Technol*, 2014, **127**, P. 13–19.

[13] Caravaca A., Sapountzi F.M., De Lucas-Consuegra A., et al. Electrochemical reforming of ethanol-water solutions for pure H2 production in a PEM electrolysis cell. *Int J Hydrogen Energy*, 2012, **37**, P. 9504–9513.

[14] Safizadeh F., Ghali E., Houlachi G. Electrocatalysis developments for hydrogen evolution reaction in alkaline solutions - A Review. *Int. J. Hydrogen Energy*, 2015, **40**, P. 256–274.
[15] Nikolic V.M., Maslovara S.L., Tasic G.S., et al. Kinetics of hydrogen evolution reaction in alkaline electrolysis on a Ni cathode in the presence of Ni-Co-Mo based ionic activators. *Appl Catal B Environ*, 2015, **179**, P. 88–94.
[16] Rüetschi P., Delahay P. Hydrogen overvoltage and electrode material. A theoretical analysis. *J. Chem. Phys.*, 1955, **23**, P. 195–199.
[17] Kubisztal J., Budniok A., Lasia A. Study of the hydrogen evolution reaction on nickel-based composite coatings containing molybdenum powder. *Int. J. Hydrogen Energy*, 2007, **32**, P. 1211–1218.
[18] Pêrez-Alonso F.J., Adán C., Rojas S., et al. Ni-Co electrodes prepared by electroless-plating deposition. A study of their electrocatalytic activity for the hydrogen and oxygen evolution reactions. *Int. J. Hydrogen Energy*, 2015, **40**, P. 51–61.
[19] Siddeswara D.M.K., Mahesh K.R.V., Sharma S.C., et al. ZnO decorated graphene nanosheets: an advanced material for the electrochemical performance and photocatalytic degradation of organic dyes. *Nanosyst.: Physics, Chem., Math.*, 2016, **7**, P. 678–682.
[20] Alekseeva O.A., Naberezhnov A.A., Stukova E.V., Popkov V.I. The effect of barium titanate admixture on the stability of potassium nitrate ferroelectric phase in $(1-x)KNO_3+(x)BaTiO_3$ composites. *St. Petersbg. Polytech. Univ. J. Phys. Math.*, 2015, **1**, P. 229–234.
[21] Mylarappa M., Lakshmi V.V., Mahesh K.R.V., et al. Electro chemical and photo catalytic studies of MnO_2 nanoparticle from waste dry cell batteries. *Nanosyst.: Physics, Chem., Math.*, 2016, **7**, P. 657–661.
[22] Gimaztdinova M.M., Tugova E.A., Tomkovich M.V. Synthesis of $GdFeO_3$ nanocrystals via glycine-nitrate combustion. *Condens Phases Interfaces*, 2016, **18**, P. 422–431.
[23] Kodintsev I., Tolstoy V., Lobinsky A. Room temperature synthesis of composite nanolayer consisting of $AgMnO_2$ delafossite nanosheets and Ag nanoparticles by successive ionic layer deposition and their electrochemical properties. *Mater. Lett.*, 2017, **196**, P. 54–56.
[24] Eftekhari A. Electrocatalysts for hydrogen evolution reaction. *Int. J. Hydrogen Energy*, 2017, **42**, P. 11053–11077.
[25] Wang H., Gao L. Recent developments in electrochemical hydrogen evolution reaction. *Curr. Opin Electrochem*, 2018, **7**, P. 7–14.
[26] Zou X., Zhang Y. Noble metal-free hydrogen evolution catalysts for water splitting. *Chem. Soc. Rev.*, 2015, **44**, P. 5148–80.
[27] Mahmood N., Yao Y., Zhang J.W., et al. Electrocatalysts for Hydrogen Evolution in Alkaline Electrolytes: Mechanisms, Challenges, and Prospective Solutions. *Adv. Sci.*, 2018, **5**, P. 1700464.
[28] Voiry D., Yang J., Chhowalla M. Recent Strategies for Improving the Catalytic Activity of 2D TMD Nanosheets Toward the Hydrogen Evolution Reaction. *Adv. Mater.*, 2016, **28**, P. 6197–6206.
[29] Shi Y., Zhang B. Recent advances in transition metal phosphide nanomaterials: Synthesis and applications in hydrogen evolution reaction. *Chem. Soc. Rev.*, 2016, **45**, P. 1529–1541.
[30] Ojha K., Saha S., Dagar P., Ganguli A.K. Nanocatalysts for hydrogen evolution reactions. *Phys. Chem. Chem. Phys.*, 2018, **20**, P. 6777–6799.
[31] Tolstoy V.P. Successive ionic layer deposition. The use in nanotechnology. *Russ. Chem. Rev.*, 2006, **75**, P. 161–175.
[32] Lobinsky A.A., Tolstoy V.P., Kodinzev I.A. Electrocatalytic properties of γ-NiOOH nanolayers, synthesized by successive ionic layer deposition, during the oxygen evolution reaction upon water splitting in the alkaline medium. *Nanosyst.: Physics., Chem., Math.*, 2018, **9**, P. 669–675.
[33] Lobinsky A.A., Tolstoy V.P. Synthesis of 2D Zn-Co LDH nanosheets by a successive ionic layer deposition method as a material for electrodes of high-performance alkaline battery-supercapacitor hybrid devices. *RSC Adv*, 2018, **8**, P. 29607–29612.
[34] Tolstoy V.P., Kuklo L.I., Gulina L.B. Ni(II) doped FeOOH 2D nanocrystals, synthesized by Successive Ionic Layer Deposition, and their electrocatalytic properties during oxygen evolution reaction upon water splitting in the alkaline medium. *J. Alloys. Compd.*, 2019, **786**,P. 198–204.
[35] Pathan H.M., Lokhande C.D. Deposition of metal chalcogenide thin films by successive ionic layer adsorption and reaction (SILAR) method. *Bull. Mater. Sci.*, 2004, **27**, P. 85–111.
[36] Ho S.M. Chemical Science Review and Letters Synthesis of binary metal chalcogenides using SILAR method: Review. *Chem. Sci. Rev. Lett.*, 2015, **4**, P. 1305–1310.
[37] Popkov V.I., Tolstoy V.P., Omarov S.O., Nevedomskiy V.N. Enhancement of acidic-basic properties of silica by modification with CeO_2-Fe_2O_3 nanoparticles via successive ionic layer deposition. *Appl. Surf. Sci.*, 2019, **473**, P. 313–317.
[38] Popkov V.I., Tolstoy V.P., Nevedomskiy V.N. Peroxide route to the synthesis of ultrafine CeO_2-Fe_2O_3 nanocomposite via successive ionic layer deposition. *Heliyon*, 2019, **5**, P. e01443.
[39] Kuklo L.I., Tolstoy V.P. Successive ionic layer deposition of Fe_3O_4@$HxMoO_4 \cdot nH_2O$ composite nanolayers and their superparamagnetic properties. *Nanosyst.: Physics., Chem., Math.*, 2017, **7**, P. 1050–1054.
[40] Nakamoto K. *Infrared and Raman Spectra of Inorganic and Coordination Compounds*. In: Griffiths PR (ed) Handbook of Vibrational Spectroscopy. John Wiley & Sons, Ltd, Chichester, UK, 2006.

NANO Φ&X&M

NANOSYSTEMS:

PHYSICS, CHEMISTRY, MATHEMATICS

INFORMATION FOR AUTHORS

The journal publishes research articles and reviews, and also short scientific papers (letters) which are unpublished and have not been accepted for publication in other magazines. Articles should be submitted in English. All articles are reviewed, then if necessary come back to the author to completion.

The journal is indexed in Web of Science Core Collection (Emerging Sources Citation Index), Chemical Abstract Service of the American Chemical Society, Zentralblatt MATH and in Russian Scientific Citation Index.

Author should submit the following materials:

1. Article file in English, containing article title, the initials and the surname of the authors, Institute (University), postal address, the electronic address, the summary, keywords, MSC or PACS index, article text, the list of references.
2. Files with illustrations, files with tables.
3. The covering letter in English containing the article information (article name, MSC or PACS index, keywords, the summary, the literature) and about all authors (the surname, names, the full name of places of work, the mailing address with the postal code, contact phone number with a city code, the electronic address).
4. The expert judgement on possibility of publication of the article in open press (for authors from Russia).

Authors can submit a paper and the corresponding files to the following addresses: nanojournal.ifmo@gmail.com, popov1955@gmail.com.

Text requirements

Articles should be prepared with using of text editors MS Word or LaTex (preferable). It is necessary to submit source file (LaTex) and a pdf copy. In the name of files the English alphabet is used. The recommended size of short communications (letters) is 4-6 pages, research articles– 6-15 pages, reviews – 30 pages.

Recommendations for text in MS Word:

Formulas should be written using Math Type. Figures and tables with captions should be inserted in the text. Additionally, authors present separate files for all figures and Word files of tables.

Recommendations for text in LaTex:

Please, use standard LaTex without macros and additional style files. The list of references should be included in the main LaTex file. Source LaTex file of the paper with the corresponding pdf file and files of figures should be submitted.

References in the article text are given in square brackets. The list of references should be prepared in accordance with the following samples:

[1] Surname N. *Book Title*. Nauka Publishing House, Saint Petersburg, 2000, 281 pp.
[2] Surname N., Surname N. Paper title. *Journal Name*, 2010, **1** (5), P. 17-23.
[3] Surname N., Surname N. Lecture title. In: Abstracts/Proceedings of the Conference, Place and Date, 2000, P. 17-23.
[4] Surname N., Surname N. Paper title, 2000, URL: http://books.ifmo.ru/ntv.
[5] Surname N., Surname N. Patent Name. Patent No. 11111, 2010, Bul. No. 33, 5 pp.
[6] Surname N., Surname N. Thesis Title. Thesis for full doctor degree in math. and physics, Saint Petersburg, 2000, 105 pp.

Requirements to illustrations

Illustrations should be submitted as separate black-and-white files. Formats of files – jpeg, eps, tiff.

NANOSYSTEMS:

PHYSICS, CHEMISTRY, MATHEMATICS

Журнал зарегистрирован
Федеральной службой по надзору в сфере связи, информационных технологий и массовых коммуникаций
(свидетельство ПИ № ФС 77 - 49048 от 22.03.2012 г.)
ISSN 2220-8054

Учредитель: федеральное государственное автономное образовательное учреждение высшего образования
«Санкт-Петербургский национальный исследовательский университет информационных технологий, механики и оптики»

Издатель: федеральное государственное автономное образовательное учреждение высшего образования
«Санкт-Петербургский национальный исследовательский университет информационных технологий, механики и оптики»

Отпечатано в Учреждении «Университетские телекоммуникации»
Адрес: 197101, Санкт-Петербург, Кронверкский пр., 49

Подписка на журнал НФХМ
На первое полугодие 2020 года подписка осуществляется через
ОАО Агентство «Роспечать»
Подписной индекс 57385 в каталоге «Издания органов научно-технической информации»